KU LEUVEN

ARENBERG DOCTORAL SCHOOL
Faculty of Science

Multi-Fluid Modeling of Magnetic Reconnection in Solar Partially Ionized and Laboratory Plasmas

Alejandro Alvarez Laguna

Supervisors:
Prof. dr. S. Poedts
Prof. dr. ir. H. Deconinck
(VKI)

Dissertation presented in partial fulfillment of the requirements for the degree of Doctor of Science (PhD): Mathematics

December 2017

Multi-Fluid Modeling of Magnetic Reconnection in Solar Partially Ionized and Laboratory Plasmas

Alejandro ALVAREZ LAGUNA

Examination committee:
Prof. dr. L. Decin, chair
Prof. dr. S. Poedts, supervisor
Prof. dr. ir. H. Deconinck, supervisor (VKI)
Prof. dr. R. Keppens
Prof. dr. ir. G. Lapenta

Dr. ir. A. Lani (VKI)
Dr. ir. N. N. Mansour (NASA Ames)
Dr. ir. A. Hakim (Princeton University)

Dissertation presented in partial fulfillment of the requirements for the degree of Doctor of Science (PhD): Mathematics

December 2017

Uitgegeven in eigen beheer, Alejandro Alvarez Laguna, Celestijnenlaan 200A box 2400, B-3001 Leuven (Belgium)

To Pilar, Juanjo, Alberto, and Anne-Flore.

Things could have happened in any other way and, nevertheless, they happened like this.

– *Miguel Delibes*

Acknowledgements

Travel far while still loving your home

– Guillaume Apollinaire

It seems it was yesterday that I started my PhD under the Californian winter sun. Today, almost four years later, with the first snow over the roofs of Brussels, I find myself anchored to my keyboard, finishing this small book that you hold in your hands. These four years were happy and exciting ones for me. During this period, I was surrounded by great people that helped me in many ways to carry out the work of this thesis. I would like to offer them these brief lines of gratitude.

In first place, I would like to thank my promoter, Prof. Stefaan Poedts. Thank you, Stefaan, for all your support, your guidance in this research, and your corrections that largely improved this thesis. Most importantly, I would like to thank you for your endless motivation and positive attitude, which have been an inspiration to me during these years. You have always believed in this project while you supported me for developing my own ideas and skills. Honestly, I could not have imagined having a better advisor and mentor. My sincere thanks also go to my co-promoter, Prof. Herman Deconinck who, together with Dr. Andrea Lani, has supervised my work and always supported me since already six years ago. Your great experience and knowledge helped me to find solutions for the numerical schemes that are presented in this work. Particularly, I would like to thank Dr. Andrea Lani, without whom all this work could not be possible. Thank you, Andrea, for accepting the first application to do an internship at the VKI, for always believing in me, for helping me with COOLFluiD, and for encouraging me to follow a career in research.

The three of them helped me to prepare the proposal for the IWT (Agency for Innovation by Science and Technology) fellowship that opened the door to this PhD. I would like to acknowledge IWT for giving me this wonderful opportunity to developed the independent research that is summarized in this thesis.

I would like to express my gratitude to all the PhD committee: Prof. Leen Decin, Prof. Rony Keppens, Prof. Giovanni Lapenta, Dr. Ammar Hakim, and

Dr. Nagi Mansour for accepting to be part of the jury and for your insightful comments that helped to improve this thesis. Special thanks to Nagi who has supported me since we met, already five years ago, and taught me one of the most valuable lessons that I have ever learned: the passion for science and research. I will carry with me this and many other lessons my entire life.

The results that are presented in this work were obtained together with two colleagues, that are also my friends, Dr. Yana Maneva and Dr. Nataly Ozak, to whom I owe my sincere gratitude. Yana was the first user of the code in the partially-ionized version of it. I would like to thank her for her positive attitude, patience when I needed to fix problems in the code, and support to find solutions to the complex problem of the waves in the chromosphere. I met Nataly two years ago when we were starting to test the code for fully-ionized cases. Her intelligence, professionality, and attention to detail, helped to find countless small bugs in the code. "We finally got the drift waves!". Thank you, Yana and Nataly. This work cannot be understood without you.

During these years, I had the great opportunity of carrying out this research in different places. There, I met most of my friends whom I would like to thank for the countless moments that I will always keep my memory. Firstly, I am deeply indebted to my colleagues in VKI: JB, Anabel (platinum members of the VKI Shuttle), Bruno, Gian Luca, Federico, Marina, Sophia, Fabrizio, Alessandro, Christopher, Alan, Agustin, Julien, Aude, Erik, Jesus, Aurelie, Vincent vdH, Lasse, and Zuheyr. Also, I would like to express my gratitude to Prof. Thierry Magin and Prof. Marc Massot for their interest in my work and their help to understand the transport phenomena in plasmas.

I would like to also thank the fellows at the CmPA group of KU Leuven: Yana, Nataly, Emmanuel, Dimitrios, Fabio, Jo, Irantzu, Christine, Kirit, and Skralan. I appreciated very much the time with you during the days I was teaching at the university.

Finally, I had the great opportunity of developing part of this work at NASA Ames in California. I would like to thank again Dr. Nagi Mansour for his invitation. In the US, I had wonderful time and I enjoyed the beautiful weather and landscapes. I would like to thank Alexandre, Laura, Francesco, Clara, Jorge, Patricia, Jérémie, and Khalil for always opening their doors for my visits. There is not enough Belgian chocolate to pay back your help.

I cannot imagine the city of Brussels without rain nor without Nacho. Thank you Nacho for all your support and nice moments that we lived together. We had great years and I believe the best is yet to come. I will also always remember Tuesday's evening playing with the HuGe Bels fellows: Bernd, Jérôme, Alessia, Pascal, and Imre; and the post-Huge Bel'ers George and Vincent L. Thank you for being the soundtrack of this thesis.

Even though the first time I came to Belgium I was planning to be back in Spain after three months, I delayed my trip back all this time. Thanks to Luis, David, Nacho R., Juan, Diego, Alejandro B., and Adrián for your visits and for keeping our friendship all this time.

There is someone who knows best the person behind this thesis and the feelings behind these thoughts. I admire your intelligence and sensitivity that were an inspiration to me during this time. Thank you, Anne-Flore, for standing beside me and for always being there for me.

Llegado este momento, no puedo más que agraceder a mi familia, Pilar, Juanjo y Alberto, por todo su apoyo. Gracias por enseñarme el valor del trabajo hecho con pasión, humildad y esfuerzo. Gracias, también, por vuestra confianza en mí y por alimentar siempre, desde pequeño, mi curiosidad. Vuestro amor incondicional me alentó en todo momento durante todos estos años.

Summary

Astrophysical and laboratory plasmas host a wide variety of complex phenomena that are caused by the interaction between plasmas and electromagnetic fields. The magnetic field can store large amounts of energy that may be transferred to the plasma by magnetic reconnection. This exchange of energy is responsible for massive eruptions in the solar atmosphere as well as disruptions in magnetic confinement devices for controlled nuclear fusion. Nevertheless, this process is not fully understood as magnetohydrodynamic (MHD) models are not able to completely capture the small-scale phenomena responsible for reconnecting the field lines. Alternatively, kinetic codes represent very accurately the small-scales but are computationally very costly and cannot afford full-domain simulations.

We propose multi-fluid plasma models as a sound alternative to the kinetic and MHD approaches. The multi-fluid plasma model represents the species within the plasma as different interpenetrating fluids that interact among each other by exchanging momentum and energy through elastic collisions, and mass through chemical reactions. Additionally, the charged species interact with the electromagnetic fields. This allows to capture important small-scale phenomena that results from the interplay of the species among themselves and with the electromagnetic fields, while representing the full-scale dynamics.

A novel numerical method that solves for the multi-fluid plasma equations coupled to full Maxwell's equations is developed and implemented into a high performance computing platform. The disparity of time scales contained in the set of equations is a great challenge from the numerical point of view. In order to tackle this problem, we propose an innovative numerical scheme based on the finite volume method on unstructured meshes with implicit time integration. The numerical method proves its versatility in a wide range of plasma conditions – from low-subsonic to supersonic, from reactive partially to fully-ionized, and from collisionally dominated to collisionless and magnetically dominated.

In this dissertation, we focus on the study of two long-standing problems in plasma physics: the role of neutrals in the dynamics of the partially-ionized solar atmosphere and the plasma instabilities inside nuclear fusion devices.

First, we study the complex interaction of the chemical non-equilbrium, ambipolar diffusion, and radiation in magnetic reconnection events under partially-ionized chromospheric conditions. The study shows that the results accounting for radiation show time scales and outflows comparable to these observed in spicules and chromospheric jets. Second, we simulate the propagation of magnetosonic waves across the photosphere and the chromosphere. For the first time, a global multi-fluid simulation of the solar lower atmosphere is performed.

Finally, we analyze the dynamics of a magnetic flux tube under realistic conditions of the DIII-D nuclear fusion reactor. The evolution of the kink instability and the drift-wave instability in a full-scale 3D simulation is studied. Multi-fluid models allow for capturing the influence of the small-scale processes that results of the separation of the motions of the fluids on the macroscopic dynamics.

Samenvatting

In astrofysische en laboratoriumplasma's vindt een grote variteit van complexe fenomenen plaats waarvan de oorzaak te vinden is in de interactie tussen plasma's en electromagnetische velden. Het magnetisch veld kan grote hoeveelheden energie opstapelen die kunnen overgebracht worden naar het plasma door middel van magnetische reconnectie. Deze uitwisseling van energie is verantwoordelijk voor uitbarstingen in de atmosfeer van de zon maar ook voor disrupties in magnetische opsluitingsinstallaties voor gecontroleerde kernfusie. Het reconnectieproces is niet volledig doorgrond omdat de magnetohydrodynamische (MHD) modellen niet in staat zijn om de kleine schaal fenomenen te beschrijven die verantwoordelijke zijn voor de reconnectie van de veldlijnen. Anderzijds zijn de de kinetische methodes die de kleine schalen wel nauwkeurig beschrijven zeer duur in rekentijd zodat ze volledige domeinsimulaties niet veroorloven.

We stellen multi-fluid plasma's voor als een valabel alternatief voor de kinetische en de MHD aanpak. Het multi-fluid plasmamodel behandelt de verschillende species in het plasma als interpenetrerende (vloei)stoffen die met elkaar interageren door uitwisseling van impuls en energie via elastische botsingen, en van massa door middel van chemische reacties. Daarnaast interageren de geladen species ook met de electromagnetische velden. Dit laat toe om belangrijke kleine schaal fenomenen te beschrijven, die voortkomen uit de interacties tussen de species onderling en met de electromagnetische velden, terwijl ook de grote schaal dynamica kan behandeld worden.

Een innovatieve numerische methode werd ontwikkeld en gemplementeerd op een High Performance Computing platform. Deze methode lost de multifluid plasmavergelijkingen op gekoppeld met de volledige Maxwell vergelijkingen. De dispariteit in lengteschalen gevat in deze vergelijkingen is een grote uitdaging op numerisch vlak. Om dit probleem aan te pakken stellen we een innovatief numerisch schema voor gebaseerd op de eindige volume methods op een ongestructureerd rooster en men een impliciete tijdsintegratie. Deze numerische methode bewijst haar diversiteit over een grote waaier van plasmacondities - van laag-subsoon tot supersoon, van partieel reactief tot volledig geoniseerd en van collisievrij tot magnetisich gedomineerd.

In deze doctoraatsverhandeling leggen we de klemtoon op de studie van

twee langbekende problemen in plasmafysica: de rol van neutrale species in de dynamica van de partieel geoniseerde atmosfeer van de zon en de plasma instabiliteiten in kernfusie installaties.

Vooreerst bestuderen we de complexe interactie van de ambipolaire diffusie in chemisch onevenwicht met de straling in magnetische reconnectiefenomenen onder partieel geoniseerde chromosferische condities. Deze studie toont aan dat de simulaties die rekening houden met radiatie, tijdsschalen en uitstroomsnelheden vertonen die vergelijkbaar zijn met deze geobserveerd in spicules en jets in de chromosfeer. Vervolgens berekenen we de voortplanting van magnetosonische golven door de fotosfeer en de chromosfeer. Voor het eerst wordt een globale multi-fluid simulatie uitgevoerd van de lagere atmosfeer van de zon.

Tenslotte analyseren we de dynamica van een magnetische fluxbuis onder realistische condities in de DIII-D nucleaire fusiereactor. We bestuderen de evolutie van de kink-instabiliteit en van de drift-golf instabiliteit in een 3D simulatie op volledige schaal. Multi-fluid modellen laten toe om de invloed te capteren van de klein-schaal processen als gevolg van de scheiding van de speciesstromingen, op de macroscopische dynamica.

Contents

List of Figures

List of Tables

CHAPTER 1

Introduction

[The universe] is written in the language of mathematics, and its characters are triangles, circles, and other geometric figures, without which it is humanly impossible to understand a single word of it; without these, one is wandering about in a dark labyrinth.

– *Galileo Galilei*

1.1 MOTIVATION

The dynamic interaction between magnetic fields and plasmas underlies a great variety of fascinating phenomena that occur in the universe. In some cases, this interplay results in a sudden release of energy that produces a violent eruption of the plasma. Powerful bursts of energy are observed in a wide range of plasma environments – from the atmosphere of the Sun and the magnetosphere of the Earth to man-made laboratory machines. The magnetic field can store the large amounts of energy associated to these eruptions. However, the mechanisms by which the magnetic field energy is transferred to the plasma are still nowadays a major subject of research.

Magnetic reconnection is invoked as the generic process behind these eruptive events. Even though the concept of magnetic reconnection tries to unify a wide range of dynamic phenomena occurring in the universe, it is rich in varieties and subtleties. As noted by Biskamp [13] in his monograph about magnetic reconnection: *"there is hardly a term in plasma physics which exhibits more scents, facets and also ambiguities, and which at times seems to be used with a touch of magic"*.

In a nutshell, magnetic reconnection is a rearrangement of the magnetic field topology that results from a change in connectivity of the field lines [14]. During the restructuring of the topology, the magnetic field configuration undergoes a relaxation that reduces the magnetic tension and thus accelerates the plasma [13]. Although this seems a rather simple concept, it contradicts

the established principle by which the magnetic field lines are "frozen" into ideal electrically conducting fluids and have to move along with it. Therefore, we can conclude that "non-ideal" processes are responsible for magnetic reconnection.

In this thesis we propose a novel numerical approach to study non-ideal processes in magnetized plasmas that is based on the multi-fluid plasma model. We will focus on two main applications: the partially-ionized plasma in the lower solar atmosphere and the fully-ionized plasmas inside magnetically confined nuclear reactors.

1.1.1 The lower atmosphere of the Sun

The atmosphere of the Sun is traditionally divided into three layers with different physical properties. The photosphere is the layer that emits the visible light of the Sun. It has a thickness of around 500 km and the temperature drops from about 6600 K at the bottom of the photosphere to around 4300 K at the top. The chromosphere is 2000 km thick and the temperature in it suffers a dramatic raise from 4300 K to about 10^6 K. The top layer is the corona that stretches out into the heliosphere [15].

The variation with height of the temperature in the Sun's atmosphere [1] is shown in Fig. 1.1. The temperature rises spectacularly within a very thin layer of few hundred km thickness called transition region. This region attracts the attention of the scientific community in order to explain the mechanisms that are responsible for the coronal heating.

Coronal heating remains as one of the biggest enigmas in solar physics [16, 17, 18]. Traditionally, two main models are proposed (e.g., [19, 20, 21, 22]). The first is the propagation of Alfvén waves [23, 24, 25] that may dissipate by phase mixing [26, 27] or by resonant absorption [28, 29]. Drift waves have been also proposed as an alternative wave mechanism that heats the corona [30, 31, 32]. The second is reconnection, by braiding of the magnetic field lines [33, 34] or by impulsive discrete events such as nanoflares [35, 36, 17]. More recent observations suggest that the heating can take place at chromospheric heights associated to chromospheric phenomena [37, 38, 39].

The observations of the lower solar atmosphere provided by the Solar Optical Telecope (SOT) on board Hinode [40], and more recently with the Interface Region Imaging Spectrograph (IRIS) mission [41], show that it is a highly dynamic and complex environment that hosts a wide variety of unsteady processes at different scales. A review of the different types of chromospheric events is given in Chapter 6.

The plasma of the lower atmosphere of the Sun is complex and rich in

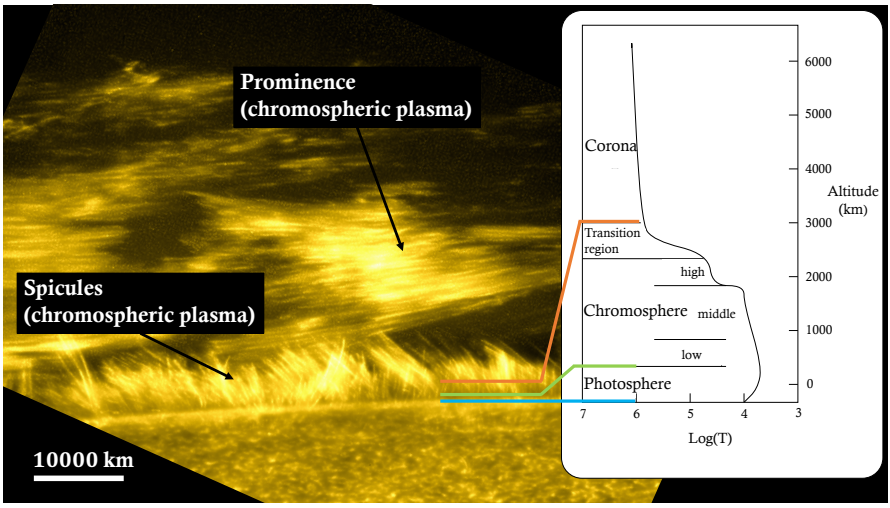

Figure 1.1: Image of the sun atmosphere in Ca II taken by the Solar Optical Telescope (SOT) of Hinode (Credits: JAXA). In the image, taken at the limb of the sun, a prominence is observed in the corona as well as spicules connecting the chromosphere with the corona. The temperature profile for quiet Sun conditions is plotted on the right of the figure [1].

non-ideal processes. In the photosphere, the plasma is weakly ionized and collisionally dominated. The collisional coupling and the presence of neutrals weakens with height [2, 42, 43]. The radiative transfer of energy as well as the ionization and recombination reactions play a fundamental role in the dynamics of the chromospheric plasma that is considered to be out of thermal and chemical equilibrium [44, 45]. The magnetic field topology changes drastically along the atmosphere: from the highly tangled and twisted magnetic field lines in the gas-dominated photosphere to the loop-like structures of the magnetically-dominated corona [46].

Novel mathematical and computational models that are able to capture these complex phenomena together with new observational data will contribute to understand coronal heating.

1.1.2 Magnetic confinement fusion plasmas

Fossil fuel supply is limited and is no longer assured to meet the growing energy needs of a society that increasingly relies on technology. Moreover, the CO_2 emissions that are produced by the combustion of these fuels cause

the global warming that forces our society to look for alternative sources of energy.

Nuclear fusion represents a promising nearly-unlimited source of CO_2-free energy. The fuel that is used in nuclear fusion, i.e., hydrogen isotopes, can be found in water and is so abundant that could supply enough energy to last 10^9 years [47].

Nuclear fusion reactors generate energy through nuclear reactions. The most efficient mechanism is obtained by merging two hydrogen isotopes, deuterium and tritium, into helium and a neutron. This reaction generates 17.6 MeV of which 20% is carried by the helium and 80% by the neutron [15].

Magnetic confinement is an approach to obtain controlled nuclear fusion. A plasma is heated to $1-1.5\cdot10^8$ K, so the particles composing the plasma have enough energy to overcome the repulsive Coulomb forces and obtain a nuclear reaction. Once the reaction occurs, the resulting neutrons are collected in a blanket where the energy is deposited and used to move a turbine that generates electricity. Such a hot plasma is confined by a closed magnetic field geometry that keeps the plasma away from the walls. Tokamaks are a possible design for magnetic confinement where the plasma is confined in a toroidal shape that is obtained by a superposition of a toroidal and a poloidal magnetic field (see Fig. 1.2).

One of the drawbacks of magnetic confinement is that the walls of the vessel become radioactive. However, the radioactive waste that is generated can be considered as short-lived (decay times of 100 years [48]) as compared to the fission radioactive waste (decay times of thousands of years).

Despite all the efforts and developments since the fusion research started after WWII, still nowadays this technology is not mastered. The plasma inside tokamaks contains strong gradients in the density, temperature, and electric current that generate both small-scale turbulence and large-scale global instabilities. The latter can produce disruptions that completely destabilizes the magnetic configuration and prevents from reaching the high temperatures needed for nuclear fusion.

Owing to these difficulties, the so-called plasma energy breakeven point, when the reactor produces as much energy as is consumed, has never been achieved by magnetic confinement devices. The Joint European Torus (JET), holds the record of highest performance after generating 70% of the input power. The ITER (International Thermonuclear Experimental Reactor) tokamak, that is in construction phase, is foreseen to produce a fusion power that is ten times larger than the input power.

The complexity of the plasma inside tokamaks demands models able to capture the instabilities that occur in a wide range of time and space scales.

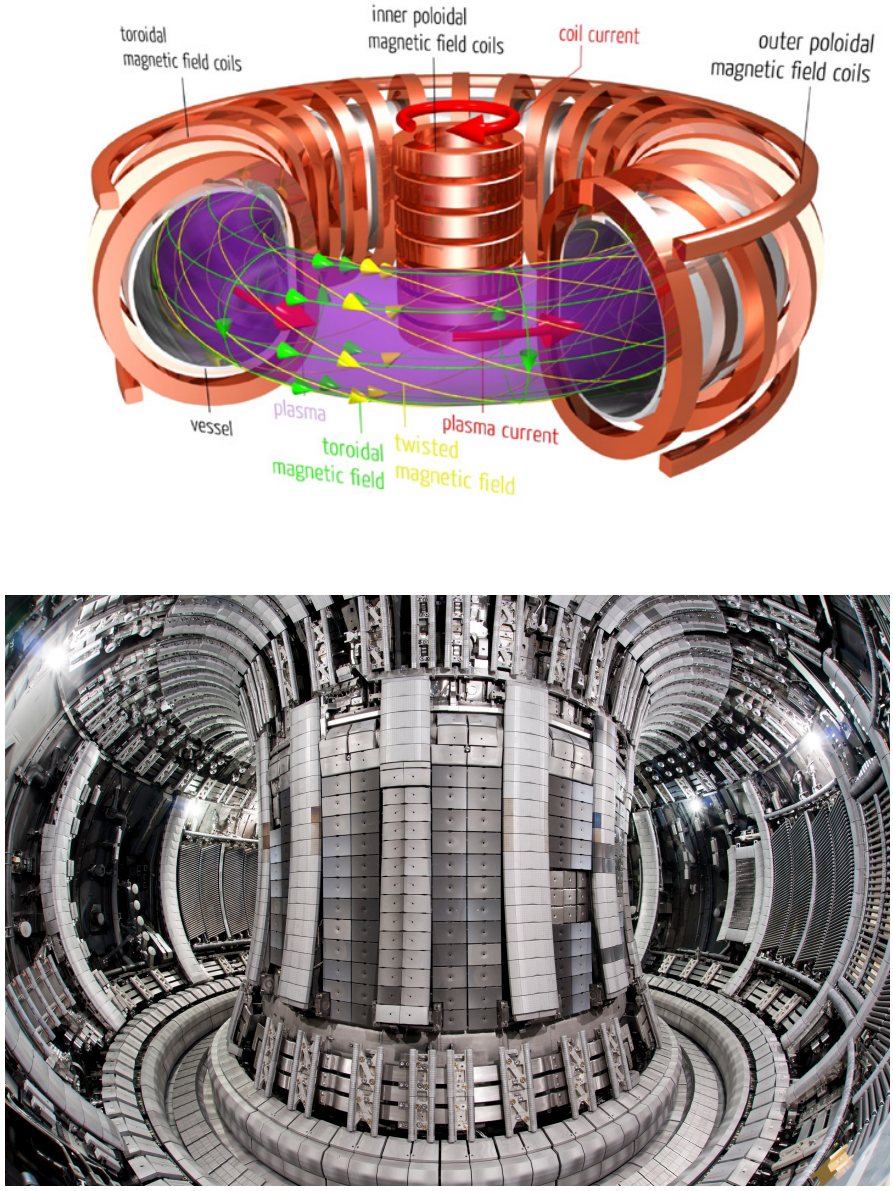

Figure 1.2: Top: Sketch of a tokamak. Bottom: Picture inside the Joint European Torus (JET) tokamak (Credits: EFDA-JET).

1.2 MAGNETIC RECONNECTION

1.2.1 General condition for magnetic reconnection

Previously, we defined magnetic reconnection as a relaxation of the global topology of the magnetic field produced by a local change of connectivity of the field lines. This process results from a decoupling between the plasma and the magnetic field due to non-ideal processes. As magnetic reconnection develops very differently in the chromosphere and in tokamaks, a general criterion for reconnection is discussed below.

The dynamics of the plasma and the magnetic field couples through the so-called Ohm's law that reads in general

$$\vec{E} + \vec{u} \times \vec{B} = \vec{R}, \tag{1.1}$$

where $\vec{E}$ is the electric field, $\vec{u}$ is the macroscopic velocity of the plasma, $\vec{B}$ is the magnetic field, and $\vec{R}$ represents the electric field generated by non-ideal processes in the plasma. These effects include the collisional resistivity, the anisotropy caused by the gyration of ions and electrons around the magnetic fields lines, the decoupling between the motion of the plasma species, the presence of neutral atoms or molecules, turbulent transport, etc.

Schlinder et al. [49] provide a general criterion for a change in the magnetic topology that reads

$$\vec{B} \times \left(\nabla \times \vec{R}_{\parallel} \right) \neq 0. \tag{1.2}$$

Here, $\vec{R}_{\parallel} = \left(\vec{R} \cdot \vec{B} \right) \vec{B}/B^2$ is the component of the electric field generated by non-ideal processes that is parallel to the magnetic field. Owing to that definition, not every non-ideal process leads to changes of the magnetic field topology. Only those that produce electric fields that are parallel to the magnetic field result in reconnection as long as their curl does not vanish.

1.2.2 Reconnection in the solar lower atmosphere

In the Sun lower atmosphere, the first mechanism that can lead to a change of the magnetic field is the magnetic diffusivity due to collisions. The time-scale related to this mechanism is the diffusive decay time $\tau_\eta \sim L^2/\eta$, where L is the characteristic length and η is the so-called Ohmic magnetic diffusivity. Assuming a characteristic length of $L \sim 10^5$ m and the distribution of density and temperature of Vernazza et al. [1], we obtain the decay time shown in Fig. 1.3.

The decay time associated to the collisional diffusivity is very large compared to the observed transient phenomena of the chromosphere that occurs in the scale of tens of second to few minutes (see Chapter 6 for a review of the time-scales associated to chromospheric eruptive phenomena).

Nevertheless, in the chromosphere, the diffusion is important in very thin layers called current sheets where the magnetic field forms sharp gradients. The Sweet-Parker model [50, 51] proposes a long thin current sheet where the scale of the transverse dimension is proportional to the square root of the resistivity. Therefore, the diffusion characteristic time becomes much shorter $\tau_{SP} \sim \tau_A \tau_\eta$, where τ_A is the Alfvénic transit time. However, this mechanism is not short enough to explain the chromospheric phenomena, as shown in Fig. 1.3. Petschek [52], proposed a model that involves slow shocks with a localized reconnection region. The model is able to predict fast energy releases. The presence of shocks is observed in 2D numerical simulations when resistivity is not constant and is enhanced locally [53] or in 3D MHD simulations of eruptive flux ropes [54] with numerical resistivity. However, high-resolution numerical simulations favor the Sweet-Parker model in the case of constant resistivity [13, 55].

Consequently, collisional resistivity is not sufficient to explain the observed reconnection rates in the solar chromosphere. Other mechanisms have been investigated that can accelerate the reconnection rate.

Ambipolar diffusion, produced by the collisions between ions and neutrals, does not reconnect magnetic field lines as it creates an electric field that is perpendicular to the magnetic field [56]. However, it sharpens the magnetic field profile creating conditions that can enhance reconnection [56, 57, 58]. In addition, when the recombination rate is sufficiently high, a loss of ions in the reconnection region is produced, which prevents ion pressure from building up. This results in fast reconnection, independent of the Lundquist number [8, 58, 59, 60, 57]. Similarly, radiative losses cool the plasma, which decreases the pressure inside the current sheet and results in a thinning of the reconnection layer [61, 62].

Resistive current sheets can develop many small-scale magnetic loops inside the reconnection region in the so-called tearing instability. Furth et al. [63] and Bulanov et al. [64] study the stability of this mode for fully-ionized plasmas. Zweibel [65] determined that the growth rate of the tearing mode can be faster than the same process under fully ionized conditions multiplied by a factor of $(\rho_i/\rho)^{1/5}$, where ρ_i is the ion density and ρ is the total density.

When the current sheet width narrows and the Lundquist number is larger than a critical number on the order of 10^3 to 10^4 for fully ionized plasmas [66, 67, 68], the current sheet can break, developing the plasmoid instability.

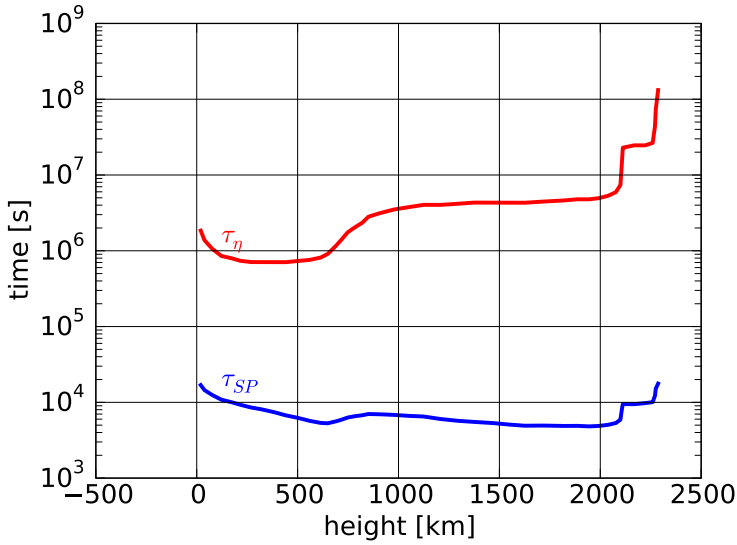

Figure 1.3: Variation of the Ohmic decay time τ_η and the Sweet-Parker model reconnection characteristic time for energy release τ_{SP} as a function of height above the photosphere. The characteristic length is $L = 10^5$ m, the magnetic field model for quite sun from Khomenko et al. [2], and the temperature and density distribution of Vernazza et al. [1].

As noted by Lapenta [69], the formation of magnetic islands is a chaotic and unsteady process that results in reconnections that are faster than the laminar Sweet-Parker model. Similar behaviour is found in partially ionized plasmas in single fluids with ambipolar diffusion [70, 71] and reactive and collisional two-fluid simulations [8, 72, 73].

1.2.3 Reconnection in a tokamak

The temperature inside a tokamak is very high ($T \sim 10$ keV) and therefore the plasma is fully ionized. Under these conditions, the plasma is a very good electrical conductor and the resistivity is thus very low. Owing to that reason, the resistive decay time ($\tau_\eta \sim 24$ s), and the Sweet-Parker model decay time ($\tau_{SP} \sim 8$ ms) are very large compare to the collapse time scales of the oscillations (in the order of tens to hundreds of μs) that are observed in tokamaks [15].

In tokamaks, Ohm's law is dominated by scales that are much smaller than the resistive one. These scales are related to microscopic scales, i.e., ion and electron skin depths, ion and electron gyroradius, and the Debye length. At these scales an important process occurs that is the decoupling of the ion and electron dynamics [13]. Therefore, we cannot consider plasma as one single fluid but as two different fluids.

Depending on the strength of the magnetic pressure as compared to the plasma pressure we can find different regimes. When the pressure is high (high-β regime), the reconnection dynamics are dominated by the Hall term [13]. The Hall term implies that the magnetic field lines are frozen into the electron fluid. Therefore, the Hall term does not produce reconnection of field lines, but sharpens the current sheet and introduces a new dispersive mode, i.e., the whistler mode. Alternatively, when the magnetic pressure is high (low-β regime), the reconnection scales are dominated by a combination of the Hall term and the electron compressibility in the parallel direction to the magnetic field. In this regime, the kinetic Alfvén dispersive mode is introduced. The latter regime is the one that dominates the reconnection dynamics in tokamaks [13].

Reconnection events in tokamaks are associated to the so-called sawtooth oscillations. When the sawtooth instability takes place, the electrons temperature measured in the soft X-ray signal shows a periodic oscillation with a slow increase that is followed by a sudden drop [14]. The oscillations show periods that range miliseconds in small machines to seconds in JET [74].

A sawtooth crash is caused by the helicoidal displacement (kink) of the plasma column in the $m = 1$, $n = 1$ mode (see Chapter 8 for a detailed explanation of this instability). This displacement forces the collision of different magnetic topologies and produces reconnection. However, the kink instability is a macroscopic process. Therefore, during a sawtooth crash, the mutual influence of the macroscopic dynamics and the microscopic phenomena play a fundamental role.

1.3 NUMERICAL MODELING OF PLASMAS

The most complete and universal description of plasma is contained in the kinetic equation that, together with Maxwell's equations, describes the evolution of the distribution function in the phase space for each plasma species. Based on the kinetic equation, Particle-in-Cell (PIC) codes solve for Newton's law of motion of a fraction of the total particles of the system in order to reconstruct the distribution function [75, 76, 77]. They are mostly used

for fully-ionized low-collisional plasmas such as the ones in space weather applications [78] and nuclear fusion plasmas (e.g. [79]). Alternatively, the direct solution to the Vlasov equation ([80] and references therein) in a six-dimensional grid is proposed. However, the numerical solution of the kinetic approach is computationally very expensive and usually restricted to limited domains.

Most of the numerical simulations of magnetized plasmas have focused on solving the Magnetohydrodynamic (MHD) equations. The MHD approach considers plasma as an electrically conducting fluid and solves for mass, momentum, and energy conservation equations coupled to the magnetic induction equation. Numerical codes that solve for the MHD equations have been successfully applied for astrophysical and nuclear confinement plasmas [81]. The MHD approach only deals with large-scale low-frequency phenomena and therefore is not able to represent some of the important phenomena that occur in the partially-ionized lower solar atmosphere or in tokamaks.

Different approaches that modify the MHD equations have been proposed in order to model the different non-ideal effects within the plasma. For the partially-ionized plasma of the chromosphere, the effect of the neutrals is tackled with an ambipolar diffusion (Pedersen dissipation) term in the induction equation [43]. An example of this approach is the simulation code Bifrost [82] that proposes global simulations of the chromosphere with a MHD radiative code that uses a generalized Ohm's law with the ambipolar term while the non-equilibrium effects are accounted for.

For the fully-ionized plasmas inside tokamaks, the Hall-MHD approach extends the induction equation of the MHD equations in order to tackle finite ion gyroradius effects [81]. Other methods that combine the kinetic and the fluid approach are also proposed. Hybrid codes use a hydrodynamic model for the electrons while the ions are represented with a PIC model (e.g., [83]). Alternatively, the two-way coupling of MHD simulations with PIC is recently proposed. In this approach, a limited part of the domain evolves with particle methods whereas the remaining is represented with a MHD approach [84, 85, 86].

In this work, we developed multi-fluid models as an alternative to kinetic and MHD models. The multi-fluid plasma description is obtained by taking moments of the Boltzmann equation for each species. This model is simpler than kinetic models since it averages over the velocity space of each plasma species. It solves for mass, momentum, and energy conservation laws for each species within the plasma. The different species are thus treated as separate fluids that can interact among each other through collisions and reactions, while the charged species interact with the electromagnetic field.

As kinetic models, multi-fluid models are able to capture non-linear processes resulting from the decoupling of the dynamics of the different species in the plasma. Conversely, multi-fluid models are able to tackle high density environments as well as partially-ionized collisional and reactive plasmas in full-domain simulations. In Fig. 1.4, the main differences between one-fluid MHD, multi-fluid and kinetic models are summarized.

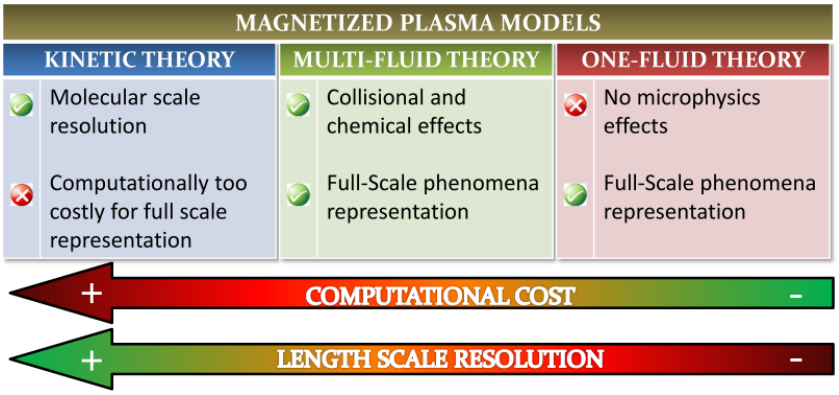

Figure 1.4: Models for magnetized plasma

1.4 OBJECTIVE OF THE DISSERTATION

In this brief introduction, we have seen how processes that occur at microscopic scales can impact the global dynamics of plasma through magnetic reconnection. Understanding the interplay between the small scales and the global dynamics would contribute to shed light on long-standing problems in plasma physics such as the coronal heating or the plasma instabilities in tokamaks.

We propose multi-fluid plasma models as an alternative to the kinetic and the MHD approach. Multi-fluid models are able to capture small-scale phenomena while representing the full-scale dynamics. This dissertation will focus on the study of multi-fluid plasma models for two applications: the lower solar atmosphere and nuclear fusion plasmas.

The core of this thesis is aimed at the development and implementation of a novel numerical method that solves for the multi-fluid plasma equations coupled to the Maxwell's equations. Proposing a numerical method that is able to tackle both the lower solar atmosphere and tokamak conditions is a

great challenge from the numerical point of view. Similarly, the disparity of time scales that results from coupling the multi-fluid and the Maxwell's equations imposes a major difficulty for the time integration. This thesis addresses this problem with an innovative numerical scheme based on the finite volume method with implicit time integration.

The numerical method will be benchmarked in a wide range of plasma conditions. The accuracy of the proposed method will be assessed by comparing the results with analytical solutions. Additionally, the ability of the method to resolve shocks while avoiding spurious numerical instabilities will be evaluated. Finally, the multi-fluid code will be compared to other solutions found in literature as well as other plasma models.

Firstly, we propose a multi-fluid model for studying partially-ionized plasmas in chromospheric conditions. The model is aimed at studying the two main candidates for causing the coronal heating: wave propagation and magnetic reconnection. The goal of this study is to explore the influence of ionization and recombination reactions, anisotropic transport fluxes, frictional exchanges of momentum and energy, and compressibility effects in the dynamics of the solar atmosphere. The model is first used to study the complex interaction of the chemical non-equilibrium, the ambipolar diffusion, and the radiation in magnetic reconnection events under chromospheric conditions. Additionally, the same model is used to study the propagation of magnetosonic waves across the photosphere and the chromosphere in a global 2D simulation of the sun lower atmosphere.

The dynamics of the plasma in tokamaks are studied with the two-fluid (ion+electron) model. The goal of this study is to analyze the influence on the macroscopic dynamics of the small-scale processes that results of the separation of the motions of the two fluids. The evolution of the kink instability and the drift-wave instability in a 3D simulation will be studied.

1.5 OUTLINE OF THE DISSERTATION

In Chapter 2, we derive the multi-fluid equations from the kinetic equation. The general set of equations is presented while taking into account both elastic and inelastic collisions between the particle species. The ideal two-fluid (electron+ion) model is also discussed. The propagation of linear waves in this model is studied in this chapter under different conditions in astrophysical and laboratory plasmas scenarios.

In Chapter 3, the closure for the transport fluxes and the chemical kinetics terms are discussed. A brief description of Grad's method is presented. The

classical transport closure is discussed both for the partially-ionized and the fully-ionized models.

In Chapter 4, the numerical method that solves the system of multi-fluid equations coupled to the full Maxwell's equations is introduced. The benchmarking of the previous numerical scheme is presented in Chapter 5.

In Chapter 6, the effect of radiation on chromospheric magnetic reconnection is studied with a two-fluid partially ionized model. Different ionization levels and radiation models are compared. The non-linear interaction between radiation, the chemical equilibrium, and the ambipolar diffusion changes the properties of the reconnection leading to fast reconnections with time scales that are close to these observed in spicules.

In Chapter 7, a global 2D simulation of the stratified solar atmosphere is presented. For the first time, a global multi-fluid simulation of the partially ionized atmosphere is carried out. The propagation of magnetosonic waves across the chromosphere and the photosphere is studied. We analyze the loss of chemical equilibrium and the heating of the atmosphere due to the compression of the magnetosonic waves.

In Chapter 8, we study the kink and drift-wave instabilities of magnetic flux tubes under the plasma conditions of the DIII-D fusion reactor. The traces of secondary magnetic reconnection are analyzed and discussed.

Finally, in Chapter 9, a discussion of the results and the perspective for future applications and developments of the work are presented.

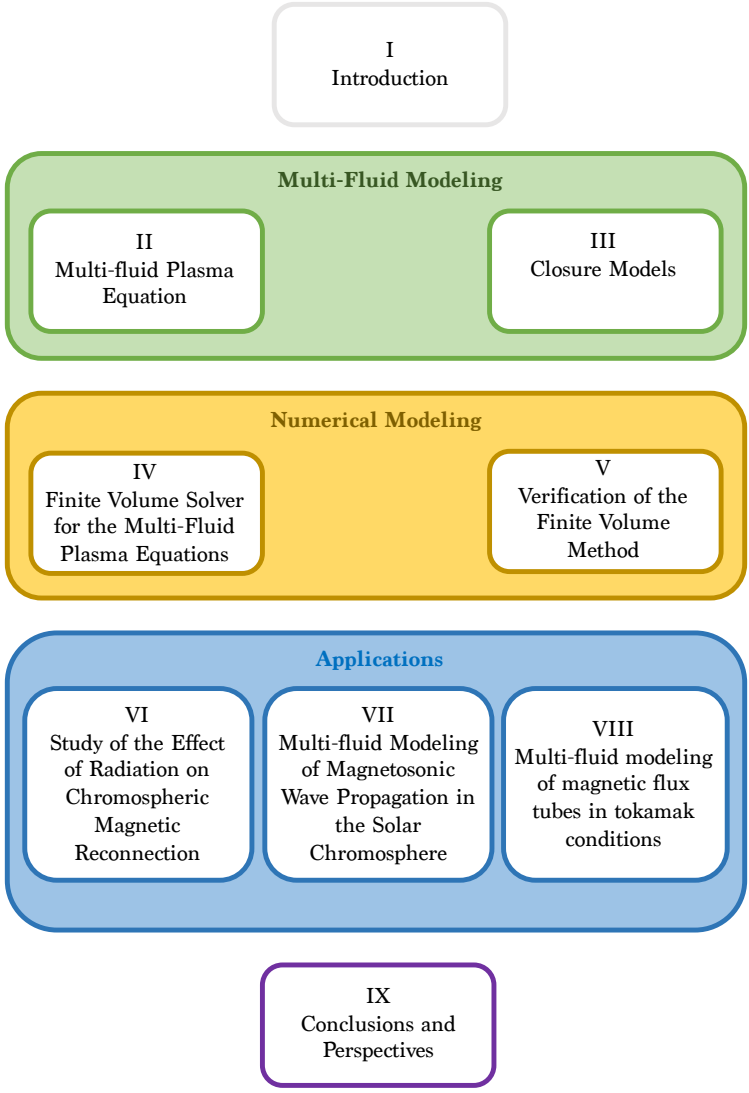
I
Introduction
Multi-Fluid Modeling
II
Multi-fluid Plasma Equation
III
Closure Models
Numerical Modeling
IV
Finite Volume Solver for the Multi-Fluid Plasma Equations
V
Verification of the Finite Volume Method
Applications
VI
Study of the Effect of Radiation on Chromospheric Magnetic Reconnection
VII
Multi-fluid Modeling of Magnetosonic Wave Propagation in the Solar Chromosphere
VIII
Multi-fluid modeling of magnetic flux tubes in tokamak conditions
IX
Conclusions and Perspectives

CHAPTER 2

Multi-Fluid Plasma Equations

In that Empire, the Art of Cartography attained such Perfection that the map of a single Province occupied the entirety of a City, and the map of the Empire, the entirety of a Province.

– *Jorge L. Borges*

We present the general multi-fluid plasma equations within the framework of the classical transport theory. The model is derived from the kinetic equation accounting for elastic and reactive binary collisions. The mass, momentum and energy balance laws correspond to the zeroth, first and second moments of the kinetic equation. A particular multi-fluid model, the ideal two-fluid plasma model that considers ion and electron fluid interacting with the electromagnetic field, is presented. The dispersion relation of this system in a homogeneous background is studied. The closure of the multi-fluid system of equations that considers transport fluxes and unlike-particle interactions will be discussed in a separate chapter.

2.1 MOTION OF A CHARGED PARTICLE IN ELECTROMAGNETIC FIELDS

Plasmas have unique properties as they are strongly affected by electromagnetic fields. The complex influence of an electromagnetic field on a plasma can be illustrated by studying the motion of a single charged particle under the effect of electromagnetic fields.

When a charged particle enters in a region of space permeated by a homogeneous electric field, a uniform acceleration in the direction of the electric field is exerted on the particle. The trajectory followed by the particle is thus a straight line if the particle is initially at rest or its velocity is aligned with the electric field, otherwise it is a parabola.

On the contrary, a charged particle at rest is not affected by magnetic fields. Only when the particle is moving, a force that is perpendicular to both the

velocity and the magnetic field is exerted on the particle. If the magnetic field is homogeneous in space, the particle is deflected describing a helicoidal trajectory around the magnetic field line. The radius of the helix and the frequency of rotation are called *Larmor radius* r_L and *Larmor frequency* Ω, respectively,

$$r_L = \frac{mv_\perp}{qB} \quad \text{and} \quad \Omega = \frac{qB}{m}. \tag{2.1}$$

Here, m is the mass of the particle, q is the electric charge, $v_\perp$ is the velocity component perpendicular to the magnetic field, and B is the modulus of the external magnetic field (see Fig. 2.1).

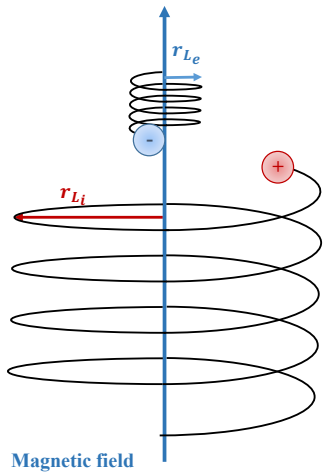

Figure 2.1: Sketch of the gyration of electrons (blue) and ions (red) in a magnetic field.

Conversely, the charges create electromagnetic fields. A moving charge in a magnetic field carries a current that generates a magnetic moment in the direction opposite to the magnetic field. Also, charged particles generate electric fields that attract particles of opposite charge and repel particles of the equal charge.

The degree of complexity increases when the particle moves in the presence of simultaneous magnetic and electric fields. If both fields are homogeneous in space, the Larmor gyration described above is modified. As the particle

gyrates around the magnetic field, the particle is accelerated by the electric field when velocity and electric field are in the same direction and slowed down when they are opposite. Therefore, the perpendicular velocity $v_\perp$ varies with the acceleration produced by the electric field, and consequently the instantaneous gyroradius changes. This effect results in a constant velocity that is perpendicular to both magnetic and electric fields, called *electrical drift velocity*,

$$v_E = \frac{\vec{E} \times \vec{B}}{B^2}. \tag{2.2}$$

This velocity is in the same direction for both negative and positive charges.

Similar effect occurs when, in absence of electric field, the magnetic field varies in space. The instantaneous Larmor radius changes due to the spatial variations of the magnetic field and a drift velocity results in the direction of $\vec{B} \times \vec{\nabla} B$. In this case, the negative and positive charges drift in opposite directions.

As it turns out, the motion of a single charged particle under the effect of simple electromagnetic fields can become extremely complicated. However, in a plasma, not only one but a large number of particles move interacting among each other and with the external electromagnetic fields. The collective motion of the particles have a back reaction on the electromagnetic field. The goal of plasma physics is to understand the behaviour of this intriguing interplay between plasmas and electromagnetic fields. If we were to apply ordinary mechanics to study this system of particles, the number of equations would be as large as the number of particles in the plasma (e.g., 10^{23} inside a tokamak). This approach would provide great accuracy but it would be impractical as we are not able to see the individual particles inside the plasma. On the contrary, we are interested on the plasma properties that we are able to measure such as density, bulk velocity or temperature.

In the present chapter we will discuss the procedure by which we reduce the problem of the evolution of countless invisible microscopic particles into the evolution of a few measurable macroscopic quantities. The chapter is based on the works by Zhdanov [6], Balescu [87], Goedbloed & Poedts [15], and Braginskii [5].

2.2 KINETIC EQUATION

2.2.1 Statistical mechanics and assumptions

A plasma is a system of N charged and neutral particles that interact among each other and with external electromagnetic fields. The system is large ($N \gg 1$) and cannot be tackled by the methods of ordinary mechanics being thus appropriate the *statistical mechanics* approach [87, 15].

In statistical mechanics, the evolution of the system is studied by means of the *distribution function* $f_\alpha(\vec{v}, \vec{x}, t)$ for the particle species α. The distribution function is a positive function in the six-dimensional phase space $(\vec{v}, \vec{x})$, where $\vec{v}$ is the velocity space and $\vec{x}$ is the position. The average number of particles of the species α at time t in the volume element of size $d\vec{x}$ centered in $\vec{x}$ and with a velocity in the interval $d\vec{v}$ centered in $\vec{v}$ is given by $f_\alpha(\vec{v}, \vec{x}, t)d\vec{v}d\vec{x}$.

The evolution in time of the distribution function depends on the external forces and the interaction among the particles. The most general set of equations is known as the BBGKY hierarchy (Bogoliubov-Born-Green-Kirkwood-Yvon), that consists of N coupled equations that accounts for all possible interactions among the particles. In most of the cases of interest, the prevailing interaction is between only two particles, the so-called *binary interaction*. By considering only binary interactions, the problem is largely simplified and the BBGKY hierarchy is truncated to the first equation. The resulting equation is the kinetic equation, also known as *Boltzmann equation*.

In the rest of the chapter, we will use Boltzmann equation to derive the set of equations of conservation of macroscopic quantities. Here, we base the derivation on the *classical transport theory* that assumes the following hypothesis:

1. The theory is based on classical mechanics, i.e., no relativistic or quantum effects are taken into account.

2. The plasma is weakly coupled, i.e., the potential interaction energy (Coulomb interaction) is very small compared to the mean kinetic energy of the particles.

3. The macroscopic parameters weakly change at distances and times of the mean free path and the mean time between collision of particles. That means that the curvature of the electromagnetic field in distances comparable to the mean free path are not considered.

4. Anomalous transport produced by collective effects such as turbulence or instabilities are not taken into account.

5. Excited states are not tracked nor radiation is taken into account.

2.2.2 The kinetic equation

The evolution of the distribution function $f_\alpha(\vec{v}, \vec{x}, t)$ of the species α is described by the Boltzmann kinetic equation,

$$\frac{\partial f_\alpha}{\partial t} + \vec{v} \cdot \vec{\nabla} f_\alpha + \frac{\vec{F}_\alpha}{m_\alpha} \cdot \vec{\nabla}_{\vec{v}} f_\alpha = \left(\frac{\delta f}{\delta t} \right)_{\text{coll}}, \tag{2.3}$$

where $\vec{\nabla}$ and $\vec{\nabla}_{\vec{v}}$ are the gradient operators in $\vec{x}$ and $\vec{v}$ respectively. The left-hand side of Eq. (2.3) represents the substantial derivative in time of the distribution function, whereas the right-hand side is the variation in time of the distribution function produced by binary collisions. The external force exerted on particles α, when the plasma is under the effect of electromagnetic fields, is written as

$$\vec{F}_\alpha = q_\alpha \left(\vec{E} + \vec{v} \times \vec{B} \right), \tag{2.4}$$

where the electric and magnetic field are denoted as $\vec{E}$ and $\vec{B}$ respectively, q_α is the electric charge, and m_α is the mass of the particles α.

The collisional term accounts for two types of contributions,

$$\left(\frac{\delta f}{\delta t} \right)_{\text{coll}} = J_\alpha + J_\alpha^r. \tag{2.5}$$

Here J_α is the elastic collision integral that considers the collision between pairs of particles where the type of particle species is conserved. J_α^r is the inelastic collision integral that considers the collision that lead to formation of new plasma species.

The operator J_α is written as the sum over the binary collisions,

$$J_\alpha = \sum_\beta J_{\alpha\beta}(f_\alpha, f_\beta), \tag{2.6}$$

where $J_{\alpha\beta}(f_\alpha, f_\beta)$ is the collision operator of the binary collision between the species α and β. The partial collisional operator for elastic collisions, can be retrieved under the "molecular chaos" assumption (e.g., [6, 88]) as follows

$$J_{\alpha\beta}(f_\alpha, f_\beta) = \int \int \left(f'_\alpha f'_\beta - f_\alpha f_\beta \right) \sigma_{\alpha\beta} |\vec{v}_\alpha - \vec{v}_\beta| d\hat{\Omega} d\vec{v}_\beta \tag{2.7}$$

where quantities after collisions are denoted with the superscript $'$, $d\hat{\Omega}$ is the solid angle of the scattering after the collision, and $\sigma_{\alpha\beta}$ is the cross section of the collision. The derivation of Eq. (2.7) can be found in Zhdanov [6].

The reactive collisional integral in a bimolecular reaction of the kind

$$A_\alpha + A_\beta \longleftrightarrow A_\gamma + A_\delta, \tag{2.8}$$

reads as follows [89],

$$J^r_\alpha = \frac{1}{2}\sum_{\beta\gamma\delta}\int\int\left(f'_\gamma f'_\delta\left(\frac{m_\alpha m_\beta}{m_\gamma m_\delta}\right)^3 - f_\alpha f_\beta\right)\sigma^r_{\alpha\beta\gamma\delta}|\vec{v}_\alpha - \vec{v}_\beta|d\hat{\Omega}d\vec{v}_\beta. \tag{2.9}$$

General expression of the inelastic collision integral involving more than two atoms/molecules and considering excited states can be found in Giovangigli & Graille [90].

2.3 MACROSCOPIC EQUATIONS

Local macroscopic variables can be obtained from the distribution function by integrating over the velocity space. We define the following macroscopic properties of species α: number density n_α, mass density ρ_α, mean or bulk velocity $\vec{u}_\alpha$, temperature T_α, and internal energy $\mathcal{U}_\alpha$.

$$n_\alpha = \int f_\alpha d\vec{v}, \qquad \rho_\alpha = m_\alpha n_\alpha = \int m_\alpha f_\alpha d\vec{v} \tag{2.10}$$
$$n_\alpha\vec{u}_\alpha = \int \vec{v} f_\alpha d\vec{v}, \qquad \frac{3}{2}n_\alpha k T_\alpha = \mathcal{U}_\alpha = \frac{m_\alpha}{2}\int(\vec{v}-\vec{u}_\alpha)^2 f_\alpha d\vec{v}.$$

Here $k = 1.38 \cdot 10^{23}$ J·K^{-1} is the Boltzmann constant.

The equations describing the evolution of macroscopic variables can be derived from the kinetic equation by taking moments, i.e., integrating the Boltzmann equation over the velocities space of the particles. Consider a variable $\psi_\alpha(\vec{v}_\alpha, \vec{x}, t)$, we define the averaging operator $\langle\cdot\rangle$ as

$$n_\alpha\langle\psi_\alpha\rangle = \int \psi_\alpha f_\alpha d\vec{v}. \tag{2.11}$$

As a result, we multiply Eq. (2.3) by the variable ψ_α and integrate over the

velocities, we obtain the following transport equation:

$$\frac{\partial n_\alpha \langle \psi_\alpha \rangle}{\partial t} + \vec{\nabla} \cdot (n_\alpha \langle \psi_\alpha \vec{v}_\alpha \rangle) - n_\alpha \left[\langle \frac{\partial \psi_\alpha}{\partial t} \rangle + \langle \vec{v} \cdot \vec{\nabla} \psi_\alpha \rangle + \frac{1}{m_\alpha} \langle \vec{F}_\alpha \cdot \vec{\nabla}_{\vec{v}} \psi_\alpha \rangle \right] = \sum_\beta \int \psi_\alpha J_{\alpha\beta} d\vec{v} + \int \psi_\alpha J^r_\alpha d\vec{v}. \quad (2.12)$$

Let the variable ψ_α be the collisional invariants, i.e., $\psi^{(1)}_\alpha = m_\alpha$, $\psi^{(2)}_\alpha = m_\alpha \vec{v}_\alpha$, $\psi^{(3)}_\alpha = m_\alpha v^2_\alpha/2$. Note that using those variables, the terms, $\langle \frac{\partial \psi_\alpha}{\partial t} \rangle$ and $\langle \vec{v} \cdot \vec{\nabla} \psi_\alpha \rangle$ vanish. Using the previous collisional invariants in Eq. (2.12), we obtain mass, momentum and total energy balance equations for the species α, as follows,

$$\frac{\partial \rho_\alpha}{\partial t} + \vec{\nabla} \cdot (\rho_\alpha \vec{u}_\alpha) = \dot{\rho}_\alpha, \quad (2.13)$$

$$\frac{\partial \rho_\alpha \vec{u}_\alpha}{\partial t} + \vec{\nabla} \cdot (\rho_\alpha \vec{u}_\alpha \vec{u}_\alpha + p_\alpha \bar{\bar{I}}) = \vec{\nabla} \cdot \bar{\bar{\pi}}_\alpha + \vec{F}_\alpha + \sum_{\beta \neq \alpha} \vec{R}^{elastic}_{\alpha\beta} + \vec{R}^{react}_\alpha, \quad (2.14)$$

$$\frac{\partial}{\partial t} \left[\mathcal{U}_\alpha + \rho_\alpha \frac{u^2_\alpha}{2} \right] + \vec{\nabla} \cdot \left[\left(\mathcal{U}_\alpha + \rho_\alpha \frac{u^2_\alpha}{2} \right) \vec{u}_\alpha \right] = \vec{\nabla} \cdot (\vec{u}_\alpha \cdot \bar{\bar{\pi}}_\alpha - \vec{q}_\alpha - p_\alpha \vec{u}_\alpha) + \rho_\alpha \vec{F}_\alpha \cdot \vec{u}_\alpha + \sum_{\beta \neq \alpha} \dot{Q}^{elastic}_{\alpha\beta} + \dot{Q}^{react}_\alpha. \quad (2.15)$$

The transport fluxes are defined in terms of the distribution function and the peculiar velocity $\vec{c}_\alpha = \vec{v}_\alpha - \vec{u}_\alpha$. We recall that the peculiar velocity is measured with respect to the macroscopic velocity of the species α, unlike other models, e.g. [88, 6], where the peculiar velocities are taken with respect to the heavy particles mean velocity [88] or the mixture mean velocity [6]. We define the scalar pressure p_α, the stress tensor $\bar{\bar{\pi}}_\alpha$, and the heat flux $\vec{q}_\alpha$ of species α,

$$p_\alpha = \frac{1}{3} \int m_\alpha f_\alpha c^2_\alpha d\vec{v}, \quad \pi_{\alpha_{rs}} = \int m_\alpha f_\alpha \left(c_{\alpha r} c_{\alpha s} - \frac{1}{3} \delta_{rs} c^2_\alpha \right) d\vec{v}, \quad (2.16)$$

$$\text{and} \quad \vec{q}_\alpha = \frac{1}{2} \int m_\alpha c^2_\alpha \vec{c}_\alpha f_\alpha d\vec{v}.$$

The collisional rate of momentum and heat exchange produced by unlike-particle collisions are defined as

$$\vec{R}^{elastic}_{\alpha\beta} = \int m_\alpha \vec{v}_\alpha J_{\alpha\beta} d\vec{v} \quad \text{and} \quad \dot{Q}^{elastic}_{\alpha\beta} = \int m_\alpha v^2_\alpha J_{\alpha\beta} d\vec{v}. \quad (2.17)$$

Similarly, the rate of mass, momentum, and energy exchange produced by the reactive collisions are written as

$$\dot{\rho_\alpha} = \int m_\alpha J_\alpha^r d\vec{v}, \quad \vec{R}_\alpha^{react} = \int m_\alpha \vec{v}_\alpha J_\alpha^r d\vec{v}, \tag{2.18}$$
$$\text{and} \quad \dot{Q}_\alpha^{react} = \int m_\alpha v_\alpha^2 J_\alpha^r d\vec{v}.$$

The system of equations (2.13)-(2.15) is not closed as the variables defined in Eqs. (2.16)-(2.18) are unkowns. Balance equations for the transport fluxes can be obtained by taking higher moments of the kinetic equation. However, these equations involve subsequent higher moments in hierarchical manner. Owing to that reason, an exact closure of the system is impossible to be obtained. In Chapter 3, the approximations that allow for obtaining a closure of the system of equations will be presented.

The previous system of plasma macroscopic quantities is coupled to the equations of the evolution of the electric and magnetic fields. The electric and magnetic fields $\vec{E}$ and $\vec{B}$ are determined by the Maxwell equations as

$$\frac{\partial \vec{B}}{\partial t} + \vec{\nabla} \times \vec{E} = 0, \tag{2.19}$$

$$\frac{\partial \vec{E}}{\partial t} - c^2 \vec{\nabla} \times \vec{B} = -\frac{\vec{j}}{\epsilon_0}, \tag{2.20}$$

$$\vec{\nabla} \cdot \vec{B} = 0, \tag{2.21}$$

$$\vec{\nabla} \cdot \vec{E} = \frac{\rho_c}{\epsilon_0}, \tag{2.22}$$

where $c = 299.8 \cdot 10^6$ m/s is the speed of light, $\epsilon_0^* = 8.854 \cdot 10^{-16}$ F/M is the permittivity of free space, the total electric current density $\vec{j} = \sum_\alpha n_\alpha q_\alpha \vec{v}_\alpha$, and the total charge density $\rho_c = \sum_\alpha q_\alpha n_\alpha$.

2.4 THE IDEAL TWO-FLUID PLASMA MODEL

A particular multi-fluid model is the ideal two-fluid plasma model, also called $5M$ model. This model is especially interesting in order to understand the physical implications of the separation between the dynamics of the fluids. The model considers two plasma species, ions and electrons that are in *local thermodynamic equilibrium* characterised by a different temperature and bulk

velocitie for each of the species. The distribution functions of the fluids are Maxwellian, as follows

$$f_\alpha^{(0)} = n_\alpha \left(\frac{m_\alpha}{2\pi k T_\alpha} \right)^{3/2} \exp\left[-\frac{m_\alpha (\vec{v}_\alpha - \vec{u}_\alpha)^2}{2kT_\alpha} \right]. \tag{2.23}$$

Here $\alpha \in \{e, i\}$ is the subscript that corresponds to electrons and ions, respectively.

Ion and electron fluids can remain in different local thermodynamic equilibrium during long periods of time that are comparable to the macroscopic time. This is due to the difference between the electron and ion masses that causes that the unlike-particle collisions are not equally efficient in exchanging momentum and energy as compared to the like-particle collisions [87, 6].

After enough time, that we refer to as equilibration time τ_{eq}, the velocities and temperatures will tend to equilibrate, i.e., $T_e = T_i$ and $\vec{u}_e = \vec{u}_i$ and both fluids will have the same local thermodynamic equilibrium. Conversely, if the macroscopic time scale related to the free-flow and electromagnetic processes τ_H is of the same order as the equilibration time, the two-fluid description is necessary. In mathematical terms, the condition for the two-fluid regime is $\tau_H \sim \tau_{eq} \gg \tau_i \gg \tau_e$, where τ_i and τ_e are the collisional relaxation times of ions and electrons, respectively.

In general, the two-fluid plasma model considers small deviations from the local thermodynamic equilibrium that are responsible for the transport fluxes, i.e., viscosity and thermal conduction. These fluxes result in the diffusion of the macroscopic quantities, and they can be neglected if the diffusion decay time τ_D is very long compared to the hydrodynamic time. Similarly, the effect of the ion-electron momentum transfer can be neglected if the resistive decay time τ_R is much larger than the hydrodynamic time. Mathematically, these two conditions are written $\tau_D \gg \tau_H$ and $\tau_R \gg \tau_H$. After these simplifications, the resulting system of equations is the so-called ideal two-fluid model, or $5M$ approximation.

Owing to the previous assumptions on the time scales of the problem, the transport fluxes simplify as

$$p_\alpha = n_\alpha k T_\alpha, \quad \pi_{\alpha_{rs}} = 0, \quad \text{and} \quad \vec{q}_\alpha = 0. \tag{2.24}$$

Similarly, the unlike-particle collisional terms simplify as

$$\vec{R}_{\alpha\beta}^{elastic} = \dot{Q}_{\alpha\beta}^{elastic} = \dot{\rho_\alpha} = \vec{R}_\alpha^{react} = \dot{Q}_\alpha^{react} = 0. \tag{2.25}$$

Considering the latter simplifications, the system of equations (2.13)-(2.15) for ions and electrons seems to be uncoupled. However, the fluids are coupled through the electromagnetic fields.

The one-fluid magnetohydrodynamic (MHD) equations can be obtained by combining the two-fluid equations and making certain assumptions on the scales of the problem. The MHD regime requires $\tau_H \gg \tau_{eq}$, thus electrons and ions have the same temperature. Charge separation effects, the displacement current, and the electron inertial terms are neglected. Additionally, the scales of the problem are considered to be much larger than the ion gyroradius, and the relative velocity between ions and electrons to be much smaller than the center of mass velocity [15]. These simplifications might be often violated in regions of the problem where the hydrodynamic and electromagnetic variables vary rapidly, e.g., magnetic reconnection [91], where the drift velocity effects are important [92], or when the plasma deviates from the quasi-neutral state, as observed in tokamaks [93, 94].

2.4.1 Dimensionless ideal two-fluid plasma equations

We normalize the ideal two-fluid plasma equations with the reference length l_0, the reference density ρ_0 equal to the ion reference density, and the reference magnetic field B_0. The rest of the reference magnitudes are computed as a combination of these reference dimensions.

The mass conservation of electrons and ions in dimensionless form reads

$$\frac{\partial \rho_e}{\partial t} + \vec{\nabla} \cdot (\rho_e \vec{u}_e) = 0, \tag{2.26}$$

$$\frac{\partial \rho_i}{\partial t} + \vec{\nabla} \cdot (\rho_i \vec{u}_i) = 0. \tag{2.27}$$

The momentum conservation is written as

$$\frac{\partial \rho_e \vec{u}_e}{\partial t} + \vec{\nabla} \cdot (\rho_e \vec{u}_e \vec{u}_e + p_e) = \frac{\lambda_m}{\hat{r}_L} \rho_e q_e \left(\vec{E} + \vec{u}_e \times \vec{B} \right), \tag{2.28}$$

$$\frac{\partial \rho_i \vec{u}_i}{\partial t} + \vec{\nabla} \cdot (\rho_i \vec{u}_i \vec{u}_i + p_i) = \frac{1}{\hat{r}_L} \rho_i q_i \left(\vec{E} + \vec{u}_i \times \vec{B} \right). \tag{2.29}$$

where $\lambda_m = m_i/m_e$ is the mass ratio, $\hat{r}_L = r_L/l_0 = m_i u_0/B_0 q_0 l_0$ is the non-dimensional ion gyroradius. u_0 is the reference velocity and q_0 is the reference charge, and q_i and q_e are the normalized electric charges of electrons and ions, respectively.

The total energy (kinetic + thermal) is denoted as $\mathcal{E}_\alpha = \mathcal{U}_\alpha + \frac{1}{2}\rho_\alpha u_\alpha^2$. The total energy conservation equation of electrons and ions reads

$$\frac{\partial \mathcal{E}_e}{\partial t} + \vec{\nabla} \cdot \left[(\mathcal{E}_e + p_e)\, \vec{u}_e \right] = \frac{\lambda_m}{\hat{r}_L} \rho_e q_e \vec{E} \cdot \vec{u}_e, \tag{2.30}$$

$$\frac{\partial \mathcal{E}_i}{\partial t} + \vec{\nabla} \cdot \left[\left(\mathcal{E}_i + p_i \right) \vec{u}_i \right] = \frac{1}{\hat{r}_L} \rho_i q_i \vec{E} \cdot \vec{u}_i. \tag{2.31}$$

The temperature of the fluids is computed as a function of the densities following the ideal gas law, in dimensionless form, as $T_e = \frac{p_e}{\lambda_m \rho_e}$ and $T_i = \frac{p_i}{\rho_i}$.

The Maxwell's equations in dimensionless form read

$$\frac{\partial \vec{B}}{\partial t} + \vec{\nabla} \times \vec{E} = 0, \tag{2.32}$$

$$\frac{\partial \vec{E}}{\partial t} - \hat{c}^2 \vec{\nabla} \times \vec{B} = -\frac{1}{\hat{r}_D^2 \hat{r}_L} \left(\rho_i q_i \vec{u}_i + \lambda_m \rho_e q_e \vec{u}_e \right), \tag{2.33}$$

$$\vec{\nabla} \cdot \vec{B} = 0, \tag{2.34}$$

$$\vec{\nabla} \cdot \vec{E} = \frac{1}{\hat{r}_D^2 \hat{r}_L} \left(\rho_i q_i + \lambda_m \rho_e q_e \right), \tag{2.35}$$

where $\hat{c} = \frac{c}{u_0}$ with c as the speed of light, and $\hat{r}_D = \lambda_D / r_L = \epsilon_0 k T_0 m_i / \rho_0 q_0^2$ is the Debye length normalized to the ion's gyroradius.

2.4.2 Linear waves in ideal two-fluid plasmas

We summarize the study presented by Goedbloed & Poedts [15] on the dispersion relation of linear waves traveling in a two-fluid plasma. We consider the waves in a homogeneous background at rest where p_{e_0}, p_{i_0}, $\vec{B}_0$, are constant. The charge neutrality holds in the homogeneous background with $n_{e_0} = n_{i_0}$ that are constant, and therefore, $\vec{E}_0 = 0$. The background is at rest, $\vec{u}_{e_0} = \vec{u}_{i_0} = 0$, and therefore, $\vec{j} = 0$.

We decompose the evolution of the flow variables as $Q(\vec{x}, t) = Q_0 + \tilde{Q} \exp\left[i \left(\vec{k} \cdot \vec{x} - \omega t \right) \right]$ where the perturbations $\tilde{Q}$ are considered to be small. Assuming this solution, the system of equations (2.26)-(2.35) become a system of algebraic equations for the variables $(\tilde{n}_e, \tilde{\vec{u}}_e, \tilde{p}_e, \tilde{n}_i, \tilde{\vec{u}}_i, \tilde{p}_i, \tilde{\vec{E}}, \tilde{\vec{B}})$. Note that the pressure is used as variable instead of the energy, and also, only four electromagnetic variables are independent as a result of the Gauss' laws. Therefore, in total there are 14 independent variables, i.e., so is the number of types of waves we may expect.

First, we change the reference frame where the unit vector $\vec{e}_3$ is on the direction of the propagation of the waves, $\vec{k}$, the vector $\vec{e}_2$ is perpendicular to the plane defined by $\vec{k}$ and $\vec{B}$, and $\vec{e}_1$ perpendicular to $\vec{e}_2$ and $\vec{e}_3$ (see Fig. 2.2), as follows:

$$\vec{e}_1 = \vec{e}_2 \times \vec{e}_3, \qquad \vec{e}_2 = \vec{B} \times \vec{k} / |\vec{B} \times \vec{k}|, \qquad \vec{e}_3 = \vec{k} / |\vec{k}|. \tag{2.36}$$

We also define the angle between the propagation direction and the magnetic field, as θ, and the parameters:

$$\lambda = k_{\parallel}/k = \cos\theta \qquad \text{and} \qquad \tau = k_{\perp}/k = \sin\theta. \tag{2.37}$$

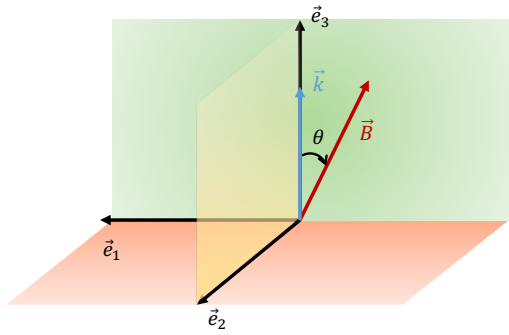

Figure 2.2: Reference frame used in the study of the wave propagation in two-fluid.

In order to simplify the system of 14 variables, we remove the two marginal waves, i.e., $\omega = 0$. These waves correspond to the entropy wave of the ion fluid and the entropy wave of the electron fluid. The marginal waves do not travel, and are responsible for pressure perturbations that balance the electric field, when $\tilde{n}_e \neq 0$ and $\tilde{n}_i \neq 0$. These pressure perturbations are in counterphase, as follows:

$$\tilde{p}_e = -\tilde{p}_i = i\frac{en_e}{k}\tilde{E}_3 = -\frac{e^2 n_e}{\epsilon_0 k^2}\left(\tilde{n}_e - Z\tilde{n}_i\right). \tag{2.38}$$

In order to find the twelve waves remaining, we define the plasma frequency, gyrofrequency and speed of sound as:

$$\omega_{p_{e,i}} = \sqrt{\frac{e^2 n_{e,i}}{\epsilon_0 m_{e,i}}}, \qquad \Omega_{e,i} = \frac{eB}{m_{e,i}}, \qquad a_{e,i} = \sqrt{\frac{\gamma p_e}{n_{e,i} m_{e,i}}}, \tag{2.39}$$

where is the electron charge $e = |q_e|$, $\gamma = 5/3$, and $\mu = \lambda_m^{-1} = m_e/m_i$.

We introduce the following variables for the perturbation that account for the phase difference by the factor i, i.e., the imaginary number.

$$\begin{aligned} \tilde{E}_1 &\equiv i\sqrt{\epsilon_0}\vec{\tilde{E}}\cdot\vec{e}_1 \qquad & \tilde{E}_2 &\equiv \sqrt{\epsilon_0}\vec{\tilde{E}}\cdot\vec{e}_2 \\ \tilde{U}_{e_{1,3}} &\equiv \sqrt{n_e m_e}\vec{\tilde{u}}_e\cdot\vec{e}_{1,3} \qquad & \tilde{U}_{i_{1,3}} &\equiv \sqrt{n_i m_i}\vec{\tilde{u}}_i\cdot\vec{e}_{1,3} \end{aligned} \tag{2.40}$$

Using these variables, the linear system of equations, as given by Goedbloed & Poedts [15], reads

$$\begin{pmatrix} \omega - k^2c^2 & 0 & \omega_{pe}\omega & 0 & -\omega_{pi}\omega & 0 \\ 0 & \frac{\omega^2-k^2c^2}{-\omega_{pe}^2-\omega_{pi}^2} & \lambda\omega_{pe}\Omega_e & \tau\omega_{pe}\Omega_e & \lambda\omega_{pi}\Omega_i & \tau\omega_{pi}\Omega_i \\ \omega_{pe}\omega & \lambda\omega_{pe}\Omega_e & \omega^2 - \lambda^2\Omega_e^2 & -\lambda\tau\Omega_e^2 & 0 & 0 \\ 0 & \tau\omega_{pe}\Omega_e & -\tau\lambda\Omega_e^2 & \frac{\omega^2-k^2a_e^2}{-\omega_{pe}^2-\tau^2\Omega_e^2} & 0 & \omega_{pe}\omega_{pi} \\ -\omega_{pi}\omega & \lambda\omega_{pi}\Omega_i & 0 & 0 & \omega^2 - \lambda^2\Omega_i^2 & -\lambda\tau\Omega_i^2 \\ 0 & \tau\omega_{pi}\Omega_i & 0 & \omega_{pe}\omega_{pi} & -\lambda\tau\Omega_i^2 & \frac{\omega^2-k^2a_i^2}{-\omega_{pi}^2-\tau^2\Omega_i^2} \end{pmatrix} \cdot \begin{pmatrix} \tilde{E}_1 \\ \tilde{E}_2 \\ \tilde{U}_{e_1} \\ \tilde{U}_{e_3} \\ \tilde{U}_{i_1} \\ \tilde{U}_{i_3} \end{pmatrix} = 0. \tag{2.41}$$

Taking the determinant of the previous matrix, we retrieve the twelve order polynomial solution for the dispersion relation $\omega = \omega(\vec{k})$. Since the matrix is symmetric, there are six two-fold degenerate waves propagating in opposite directions, i.e., $\omega < 0$ and $\omega > 0$. The polynomial reads, in general form:

$$F(\bar{k}^2, \bar{\omega}^2) = \sum_{m=0}^{6} \sum_{\max(0,3-m)}^{\min(4,6-m)} \alpha_{mn} \bar{k}^{2n} \bar{\omega}^{2m} = 0, \tag{2.42}$$

where the frequency of the waves and the wave number have been normalized as follows:

$$\bar{\omega} = \omega/\omega_p \quad \text{where} \quad \omega_p = \sqrt{\omega_{pe}^2 + \omega_{pi}^2}, \tag{2.43}$$

$$\bar{k} = \delta k \quad \text{where} \quad \delta = c/\omega_p. \tag{2.44}$$

The 19 coefficients of the polynomial are found in Goedbloed & Poedts [15]. The coefficients depend on the conditions of the background plasma and are a function of the following plasma parameters, $\alpha_{mn} = \alpha_{mn}(\lambda^2, \mu, E^2, v^2, w^2)$, where $E = \Omega_e/\omega_p$, $v = a_e/c$, and $w = a_i/c$.

2.4.3 Two-fluid waves in different astrophysical and laboratory scenarios

In this section, we show the dispersion diagrams for four different astrophysical and laboratory scenarios. In order to compute the diagrams, the solutions to the sixth order polynomial given in Eq. (2.42) are computed numerically. As mentioned above, the waves in two-fluid plasmas depend strongly on the conditions of the background plasma and the direction of propagation. In Table 2.1, we present the conditions used in this study, corresponding to characteristic conditions in the solar wind, the Earth's magnetosphere, a coronal loop and a tokamak.

Table 2.1: Characteristic conditions in the solar wind, the Earth's magnetosphere, a coronal loop, and a tokamak.

	Solar wind	Magnetosphere	Coronal loop	Tokamak
n_0	10^7 m^{-3}	10^{10} m^{-3}	10^{16} m^{-3}	10^{20} m^{-3}
B_0	$6 \cdot 10^{-9}$ T	$3 \cdot 10^{-5}$ T	0.03 T	3 T
T_0	10^5 K	10^4 K	10^6 K	10^8 K
l_0	$1.5 \cdot 10^6$ m	$6 \cdot 10^3$ m	10000 km	1 m

In Figs. 2.3 and 2.4, the dispersion diagrams of the ideal two-fluid plasma model for different astrophysical and laboratory conditions are presented for an oblique propagation at $\theta = 45^o$. In the diagrams, the wavenumber is normalized to the skin depth and the frequency to the plasma frequency.

The following characteristic plasma frequencies and lengths are depicted as black dashed lines: the ion and electron gyroradius r_{L_i} and r_{L_e}, the skin depth δ, the Debye length λ_D, and the plasma frequency ω_p, the ion and electron gyrofrequencies Ω_i and Ω_e. Similarly, the characteristic macroscopic length l_0 and time t_0 are included in the figures, the latter computed as the Alfvénic transit time in one characteristic length.

All the diagrams present the same asymptotic behaviour as $k \to \infty$ and $k \to 0$. Table 2.2 identifies the asymptotic limits and shows the mathematical expression as found in Goedbloed & Poedts [15]. In these limits, different dispersive and non-dispersive waves are present. As depicted in the diagrams, the waves are related to both macroscopic and kinetic regimes.

The regime $k^2 \to 0$ corresponds to long wavelengths that are comparable to macroscopic MHD scales. In this regime, we find three high-frequency dispersive waves: the plasma waves, and the upper and lower hybrid waves (in green, dark blue, and red, respectively). The three low-frequency non-dispersive branches correspond to the MHD waves: Alfvén (purple), fast (light blue), and slow (yellow) magnetosonic waves. The gap between the dispersive and the non-dispersive waves is large in all the conditions studied in Figs. 2.3 and 2.4. This represents an important feature of the two-fluid model that is the breaking of symmetry between the magnetic and electric fields. The high-frequency waves are driven by electric field fluctuations whereas the magnetic field fluctuations are dominant in the low-frequencies. This important property will be used in order to design a numerical scheme for the multi-fluid model.

Table 2.2: Asymptotic limits of the dispersion diagram.

Cutoff $k^2 \to 0$	$\omega^2 = \omega_p^2$ $\omega^2 = \omega_p^2 + \frac{1}{2}(\Omega_e^2 + \Omega_i^2)$ $\pm\lvert\Omega_e - \Omega_i\rvert\sqrt{\omega_p^2 + \frac{1}{4}(\Omega_e + \Omega_i)^2}$	plasma frequency upper and lower cutoff
Resonance $k^2 \to \infty$	$\omega^2 = \lambda^2\Omega_e^2$ $\omega^2 = \lambda^2\Omega_i^2$	electron cyclotron ion cyclotron
Local, high frequency $k^2 \to \infty$, $\omega^2 \to \infty$	$\omega^2 = k^2c^2$ $\omega^2 = k^2a_e^2$ $\omega^2 = k^2a_i^2$	EM waves electron sound ion sound
Global, low frequency MHD $k^2 \to 0$, $\omega^2 \to 0$	$\omega^2 = \lambda^2k^2v_A^2$ $\omega^2 = \frac{1}{2}k^2\left[v_A^2 + v_s^2\right.$ $\left.\pm\sqrt{(v_A^2 + v_s^2)^2 - 4\lambda^2v_A^2v_s^2}\right]$	Alfvén slow and fast m.s. wave

The regime $k^2 \to \infty$ corresponds to short wavelengths related to kinetic scales. Below the Debye length, a different asymptotic limit is found in all conditions of study. Two dispersive waves are present that correspond to the ion and electron cyclotron waves (yellow and light blue, respectively). Similarly, four non-dispersive waves are present: two electromagnetic waves (green and dark blue), and the ion and electron sound waves (purple and red, respectively).

The evolution of the six different branches for finite wavenumbers is an interesting feature of the two-fluid dispersion diagrams. Regarding the three high-frequency branches, the upper hybrid and the plasma waves degenerate into electromagnetic waves for wavelengths of the order of the skin depth. Alternatively, the lower hybrid wave degenerates into the electron cyclotron wave for $k^{-1} \sim \delta$ and into electron sound wave for $k^{-1} \sim \lambda_D$. These waves are related to the so-called O-, X-, and Z-waves for perpendicular propagation and R- and L-waves for parallel propagation.

Concerning the three MHD-wave branches, for $k^{-1} \sim \delta$ the fast magnetosonic waves evolve into the electron cyclotron waves. The Alfvén evolves into the ion cyclotron and ion sound waves for $k^{-1} \sim r_{L_i}$. The slow magnetosonic waves into ion cyclotron waves. For frequencies comparable to the skin depth, these branches are related to the whistler and the ion-whistler waves. As shown in Figs. 2.3 and 2.4, the regime at $k^{-1} \sim \delta$ highly depend on the background conditions and therefore it is a rather unexplored regime in literature as MHD models are not valid.

In summary, the study of the linear wave propagation in ideal two-fluid plasmas illustrates the high potential of the multi-fluid modeling. The multi-fluid model contains the macroscopic MHD modes as well as modes related to Hall-MHD and to kinetic phenomena. Nevertheless, the disparity of scales as well as the presence of dispersive modes involves an important challenge from the numerical point of view.

2.5 SUMMARY

In this chapter, we have derived the general multi-fluid plasma equations from the kinetic equation by taking moments. The model considers each species as a separate fluid and solves for mass, momentum and energy conservation laws for each fluid. The model accounts for the effect of the electromagnetic fields by solving for the Maxwell's equations coupled to the previous system. A particular multi-fluid model is the ideal two-fluid plasma model that considers ions and electrons without collisions nor transport fluxes. The study of the propagation of two-fluid linear waves in a homogenous background shows that a wide range of scales are captured by this model, including both the global MHD, Hall-MHD, and kinetic modes.

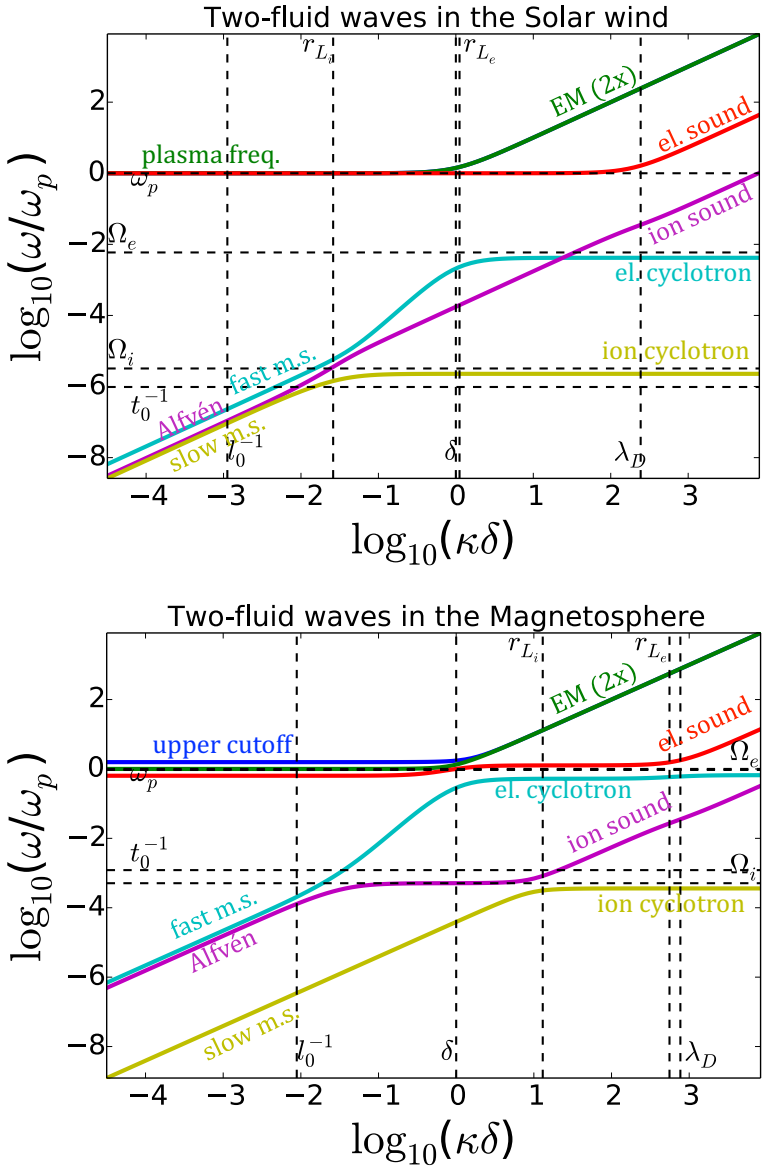

Figure 2.3: Dispersion diagram of the ideal two-fluid system for oblique propagation at $\theta = 45°$ in the solar wind (top) and in the magnetosphere (bottom).

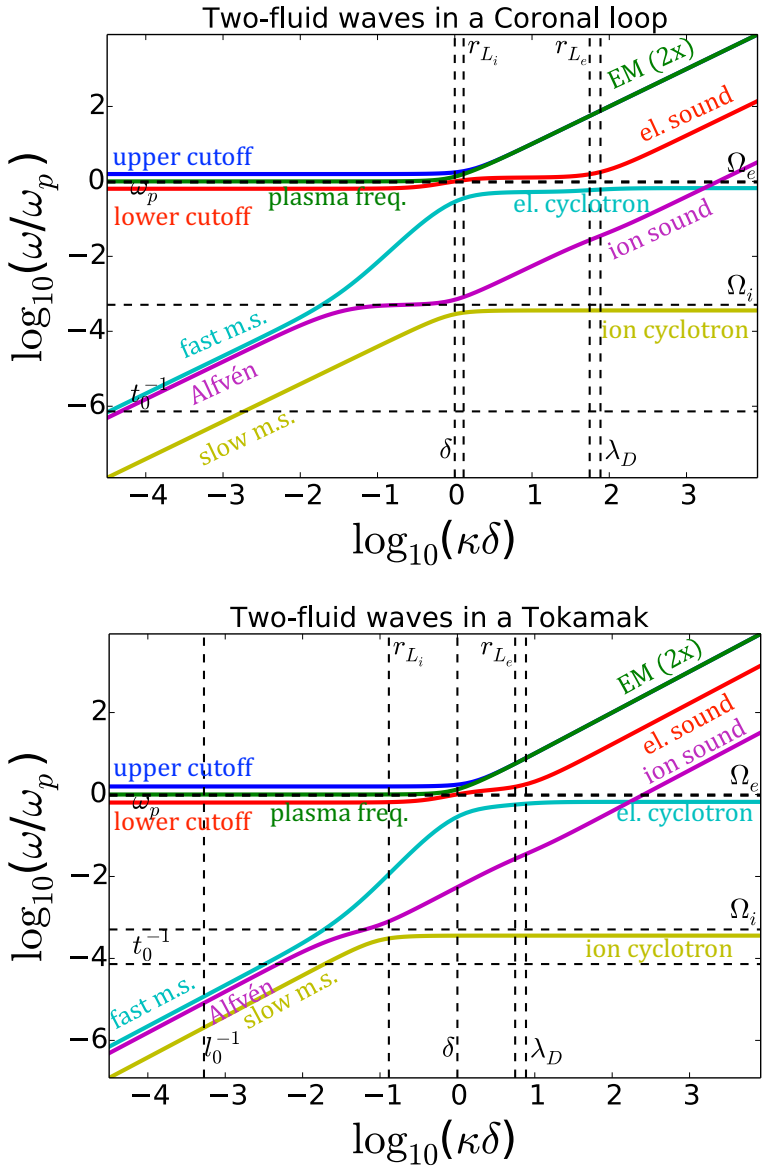

Figure 2.4: Dispersion diagram of the ideal two-fluid system for oblique propagation at $\theta = 45°$ in a coronal loop (top) and in a tokamak (bottom).

CHAPTER 3

Closure models

[The ideal MHD equations] are clearly an approximation to the true plasma equations, but they have so many nice properties that they are the preferred set for describing macroscopic plasma phenomena.

– R. M. Kulsrud

We present two closure models for the partially- and fully-ionized multifluid set of equations. Firstly, Grad's method for obtaining the transport coefficients is described. The model for partially-ionized hydrogen plasmas considers two fluids, one for the charged species (ions and electrons together) and another one describing the neutral species. They interact through ionization and recombination reactions, and elastic collisions that exchange momentum and energy between the fluids. Additionally, two models for optically thin radiation in lower solar atmospheric conditions are presented. Braginskii's classical transport closure [5] for the fully-ionized two-fluid equations is presented and compared to a more recent model derived by Zhdanov [6].

3.1 GRAD'S METHOD

We consider a nonequilibrium state that deviates from the local plasma equilibrium as

$$f_\alpha = f_\alpha^{(0)} \left(1 + \hat{\chi}_\alpha(\vec{v}, \vec{x}, t)\right), \tag{3.1}$$

where the local Maxwellian distribution $f_\alpha^{(0)}$ is defined in Eq. 2.23 and the relative perturbation from equilibrium is considered to be small, in mathematical terms, $|\hat{\chi}_\alpha(\vec{v}, \vec{x}, t)| \ll 1$. In the following, we change the variables as the notation is simplified if we use as independent variable the dimensionless

peculiar velocity

$$\vec{\xi} = \left(\frac{m_\alpha}{kT_\alpha}\right)^{1/2} (\vec{v} - \vec{u}_\alpha)\,. \tag{3.2}$$

The perturbation function $\hat{\chi}_\alpha(\vec{\xi}, \vec{x}, t)$ can be expanded as an infinite series of polynomials. The *irreducible tensorial Hermite polynomials* are a natural choice for this expansion due to their orthogonality properties with respect to a scalar product with the Maxwellian distribution as a weight function [95, 96, 87, 6]. As a result, the perturbation function can be expressed as function of the polynomial $H^{(m)}_{r_1 \ldots r_q}$ of order m and rank q.

As shown in the General Appendix G1 of Balescu [87], $H^{(m)}_{r_1 \ldots r_q}$ can be decomposed into combinations involving lower rank polynomials. Owing to that reason, in the following, we consider three types of Hermite polynomials in the expansion, the scalar Hermite polynomials $H^{(m)}(\vec{\xi})$, the vectorial Hermite polynomials $\vec{H}^{(m)}(\vec{\xi})$, and the traceless tensorial Hermite polynomials $\bar{\bar{H}}^{(m)}(\vec{\xi})$. The expansion of the perturbation function reads

$$\begin{aligned}\hat{\chi}_\alpha(\vec{\xi}, \vec{x}, t) = \sum_{n=1}^{\infty} \Big[& h^{(2n+2)}_\alpha(\vec{x}, t) H^{(2n+2)}(\vec{\xi}) \\ & + \vec{h}^{(2n+1)}_\alpha(\vec{x}, t) \cdot \vec{H}^{(2n+1)}(\vec{\xi}) + \bar{\bar{h}}^{(2n)}_\alpha(\vec{x}, t) : \bar{\bar{H}}^{(2n)}(\vec{\xi}) \Big]\,. \end{aligned} \tag{3.3}$$

Here, $h^{(m)}_\alpha(\vec{x}, t)$, $\vec{h}^{(m)}_\alpha(\vec{x}, t)$, and $\bar{\bar{h}}^{(m)}_\alpha(\vec{x}, t)$ are the *dimensionless scalar, vectorial, and traceless tensorial Hermitian moments*. These coefficients are unknown and need to be calculated by averaging the Hermite polynomials with the distribution function, as follows,

$$h^{(m)}_{\alpha_{r_1 \ldots r_q}} = \int d\vec{\xi} \frac{f_\alpha}{n_\alpha \left(\frac{m_\alpha}{2\pi k T_\alpha}\right)^{3/2}} H^{(m)}_{r_1 \ldots r_q}. \tag{3.4}$$

The first dimensionless Hermitian moments are related to the transport fluxes by simple relations as

$$h^{(2)}_{\alpha_{rs}} = \frac{\sqrt{2}}{2} \frac{\pi_{\alpha_{rs}}}{p_\alpha} \quad \text{and} \quad h^{(3)}_{\alpha_r} = \sqrt{\frac{2}{5}} \left(\frac{m_\alpha}{kT_\alpha}\right)^{1/2} \frac{q_{\alpha_r}}{p_\alpha}. \tag{3.5}$$

Evolution equations for the moments $h^{(m)}_{\alpha_{r_1 \ldots r_q}}$ can be obtained by applying the transport equation (2.12) with $\psi_\alpha = H^{(m)}_{r_1 \ldots r_q}$. The complete set of equations for all the moments is an infinite hierarchy of non-linear partial

differential equations. The solution of this system is equivalent to the solution of the kinetic equation [87]. An approximate truncation of the system of moment equations is necessary in order to provide a closure for the system of plasma macroscopic equations. The accuracy of the method depends on the number of Hermite polynomials taken for the closure. The expansion of the distribution function in the $13M^*$, $21M$, and $29M$-moment approximations reads

$$f_\alpha^{(13M)} = f_\alpha^{(0)} \left(1 + h_{\alpha_r}^{(3)} H_r^{(3)} + h_{\alpha_{rs}}^{(2)} H_{rs}^{(2)}\right), \tag{3.6a}$$

$$f_\alpha^{(21M)} = f_\alpha^{(0)} \left[1 + \sum_{n=1}^{2} \left(h_{\alpha_r}^{(2n+1)} H_r^{(2n+1)} + h_{\alpha_{rs}}^{(2n)} H_{rs}^{(2n)}\right)\right], \tag{3.6b}$$

$$f_\alpha^{(29M)} = f_\alpha^{(0)} \left[1 + \sum_{n=1}^{3} \left(h_{\alpha_r}^{(2n+1)} H_r^{(2n+1)} + h_{\alpha_{rs}}^{(2n)} H_{rs}^{(2n)}\right)\right]. \tag{3.6c}$$

As described by Zhdanov [6], the convergence of the solution with the numbers of polynomials depends on the type of collisions taken into account. In fully ionized plasma, an accuracy higher than the $13M$-moment approximation is necessary when Coulomb collisions between charged particles are taken into account. The $13M$-moment approximation does not provide the desired accuracy when the electrons are highly magnetized but the ions are weakly magnetized [87, 6]. This same fact was taken into account by Braginskii [5] that considers the $29M$-moment approximation. Balescu [87] shows that the actual difference between the $21M$ and $29M$-moment approximation is very small.

In the case of partially ionized plasmas, the $13M$-moment aproximation is sufficient if the ion-atom and electron-atom effective cross-sections are not function of the velocity (as in the hard elastic spheres model) or do not decrease abruptly with growing velocities [6].

The classical transport theory studies the transport processes in the collisional limit. The dimensionless number that compares the collisional relaxation time to the hydrodynamic relaxation time is the so-called Knudsen number

$$\mathrm{Kn} = \mathrm{Max}\left(\frac{\tau_\alpha}{\tau_H}\right), \tag{3.7}$$

*In the $13M$ approximation, for each species, one considers 5 hydrodynamic moments,i.e., ρ_α,$\vec{u}_\alpha$, and T_α, (that are contained in $f_\alpha^{(0)}$), plus the three components of the heat flux $h_{\alpha_r}^{(3)}$, plus the five independent components of the pressure tensor $h_{\alpha_{rs}}^{(2)}$.

where τ_α is the collisional relaxation time of the particles α and τ_H is the hydrodynamical relaxation time that takes into account both electromagnetic and fluid dynamics. The *linear transport regime* makes the assumption on the scale of the dimensionless perturbation function $\hat{\chi}_\alpha(\vec{\xi}, \vec{x}, t)$ that is considered to be at most of order $\mathcal{O}(\mathrm{Kn}) \ll 1$.

In this regime, the evolution equations of the Hermitian moments are largely simplified. As shown by Balescu [87] and Zhdanov [6], if we disregard the terms of order $\mathcal{O}(\mathrm{Kn})^2$ the time derivative of the equations disappears and we obtain a set of equations where the transport fluxes depend linearly on the so-called thermodynamic forces (temperature gradient, current, strain tensor, etc). After performing algebraic transformations, the transport system takes the form

$$J_n = \sum_m L_{nm} X_m, \tag{3.8}$$

where J_n are the transport fluxes (or Hermitian moments), X_m are the thermodynamic forces, and L_{nm} is the transport matrix that contains the transport coefficients. Therefore, these transport coefficients are a combination of the collisional integrals that appear in the Hermitian moments balance equations.

3.2 REACTIVE, COLLISIONAL, AND RADIATIVE TWO-FLUID PARTIALLY-IONIZED MODEL

To our knowledge, the literature on partially ionized multi-fluid models lacks a model that considers both elastic and inelastic collisional interactions and is rigorously based on Grad's method as explained above. Worth mentioning are the recent contributions towards this goal by Zhdanov [97, 89]. However, only the general set of equations and the electron properties are discussed in these references.

Nevertheless, the importance of the transport fluxes is restricted to regions with sharp gradients and the assumption of the high collisionallity of the plasmas and slow variation of the magnetic field is not fulfilled by many cases of interest in astrophysical and laboratory plasmas. Because of this reason, simplified models that do not require the complex derivation of the Grad or Chapman-Engskog methods, while containing the main physical processes, are widely used.

In this work, we consider the two-fluid model for partially ionized plasmas that is discussed in Meier & Shumlak [98], Leake et al. [8, 72], and Murphy & Lukin [73]. A similar model is proposed in Khomenko et al. [2]. The

model considers neutrals and charged species, i.e., ions and electrons, as two separate fluids, accounting for electron impact ionization and radiative recombination as well as elastic collisions that interchange momentum and energy between the fluids. The simplification that considers the charged species, ions and electrons, together as one conducting fluid is motivated when the coupling between the charged particles is stronger than the one between ions and neutrals [99]. This assumption is valid in the solar atmosphere for heights above 1000 km [2, 99, 100].

We also consider different radiative cooling models, namely, the optically thin model proposed by Leake et al. [8], and alternatively, a more realistic model for the chromospheric conditions proposed by Goodman & Judge [3] based on the CHIANTI database.

3.2.1 Normalized two-fluid (ion+neutral) equations

The normalized set of equations of the two-fluid model from Leake et al. [8] and Meier & Shumlak [98] is presented in this section. We normalize with ρ_0, l_0, and B_0. The rest of variables are computed as a combination of the previous ones. The conservation of mass of ions and neutrals reads:

$$\frac{\partial \rho_i}{\partial t} + \vec{\nabla} \cdot (\rho_i \vec{u}_i) = m_i(\Gamma_i^{ion} + \Gamma_i^{rec}), \tag{3.9}$$

$$\frac{\partial \rho_n}{\partial t} + \vec{\nabla} \cdot (\rho_n \vec{u}_n) = m_n(\Gamma_n^{ion} + \Gamma_n^{rec}). \tag{3.10}$$

The reaction rates of electron impact ionization and radiative recombination, $\Gamma_{i,n}^{ion}$ and $\Gamma_{i,n}^{rec}$, are computed by approximating the reactive collisional cross-section in the integral of Eq.(2.9). Approximations for this integrals in Hydrogen plasmas are given below.

Voronov [101] provides fitting formulas for the electron impact ionization rates for the first 28 elements (from H to Ni). The model for Hydrogen in dimensional units reads

$$\Gamma_i^{ion} = -\Gamma_n^{ion} = n_n \nu^{ion}, \tag{3.11}$$

with the ionization frequency,

$$\nu^{ion} = n_e A \frac{1}{X + \phi_{ion}/T_e^*} \left(\frac{\phi_{ion}}{T_e^*}\right)^K e^{-\phi_{ion}/T_e^*}, \tag{3.12}$$

where $n_{i,n,e}$ is the number density of the ions, neutrals, and electrons, T_e^* is the electrons temperature in eV, $A = 2.91 \cdot 10^{-14}$ m^3 s^{-1}, $K = 0.39$,

$X = 0.232$, and $\phi_{ion} = 13.6$ eV. Voronov [101] provides the level of accuracy of the model as compared to experimental data. For Hydrogen, the formula provides accuracy within 5% for electron temperatures between 1 eV to 20 eV.

An approximation for the radiative recombination rate is given by McWhirter [102] for ions with charge Z recombining from a ground state to a charge state to charge state $Z-1$. The model for $Z=1$, in dimensional units is

$$\Gamma_n^{rec} = -\Gamma_i^{rec} = n_i \nu^{rec}, \tag{3.13}$$

with the recombination frequency,

$$\nu^{rec} = 2.6 \cdot 10^{-19} n_e \frac{1}{\sqrt{T_e^*}}. \tag{3.14}$$

The formula is valid for electron temperatures from 1 eV to 15 eV [102].

The normalized momentum conservations of plasma and neutrals read

$$\begin{aligned} \frac{\partial \rho_i \vec{u}_i}{\partial t} + \vec{\nabla} \cdot \left(\rho_i \vec{u}_i \vec{u}_i + (p_i + p_e) \bar{\bar{I}} \right) = \frac{1}{\mathrm{Re}_i} \vec{\nabla} \cdot \bar{\bar{\epsilon}}_i + \\ \vec{j} \times \vec{B} + \vec{R}_i^{in} + \Gamma_i^{ion} m_i \vec{u}_n - \Gamma_n^{rec} m_i \vec{u}_i, \end{aligned} \tag{3.15}$$

$$\begin{aligned} \frac{\partial \rho_n \vec{u}_n}{\partial t} + \vec{\nabla} \cdot \left(\rho_n \vec{u}_n \vec{u}_n + p_n \bar{\bar{I}} \right) = \frac{1}{\mathrm{Re}_n} \vec{\nabla} \cdot \bar{\bar{\epsilon}}_n \\ -\vec{R}_i^{in} - \Gamma_i^{ion} m_i \vec{u}_n + \Gamma_n^{rec} m_i \vec{u}_i, \end{aligned} \tag{3.16}$$

where the Reynolds number of ions and neutrals is $\mathrm{Re}_{i,n} = \rho_0 v_0 l_0 / \xi_{i,n}$, where $\xi_{i,n}$ is the viscosity. They are approximated as

$$\xi_\alpha = \frac{n_\alpha k T_\alpha}{\nu_{\alpha\alpha}}, \tag{3.17}$$

where the collisional frequencies are computed as

$$\nu_{nn} = n_n \Sigma_{nn} \sqrt{\frac{16 k T_n}{\pi m_n}} \quad \text{and} \quad \nu_{ii} = \frac{4}{3} n_i \Sigma_{ii} \sqrt{\frac{2 k T_i}{\pi m_i}}, \tag{3.18}$$

with $\Sigma_{nn} = 7.73 \cdot 10^{-19}$ m^2 [72], and $\Sigma_{ii} = \lambda \pi r_{D_i}^2 10^{-19}$ m^2 and λ the Coulomb logarithm.

The strain tensor reads $\bar{\bar{\epsilon}}_{i,n} = \left[\vec{\nabla} \vec{v}_{i,n} + (\vec{\nabla} \vec{v}_{i,n})^T \right]$, and the normalized collisional momentum exchange reads

$$\vec{R}_\alpha^{\alpha\beta} = m_{\alpha\beta} n_\alpha \nu_{\alpha\beta} (\vec{v}_\beta - \vec{v}_\alpha), \tag{3.19}$$

with the frequency of the collisions between α and β particles,

$$\nu_{\alpha\beta} = n_\beta \Sigma_{\alpha\beta} \sqrt{\frac{8 k_B T_{\alpha\beta}}{\pi m_{\alpha\beta}}}. \tag{3.20}$$

Here $m_{\alpha\beta} = m_\alpha m_\beta/(m_\alpha + m_\beta)$, and $T_{\alpha\beta} = (T_\alpha + T_\beta)/2$. The elastic collision cross-section, $\Sigma_{\alpha\beta}$, is in general a function of the temperature [103, 104]. We chose it to be constant here: $\Sigma_{in} = \Sigma_{ni} = 1.41 \cdot 10^{-19}$ m^2, as in [8], in order to compare the results to the latter reference.

The total energy conservation of plasma and neutrals reads

$$\begin{aligned}\frac{\partial}{\partial t}\left(\mathcal{E}_i + \frac{p_e}{\gamma_e - 1}\right) + \vec{\nabla}\cdot\left(\mathcal{E}_i \vec{u}_i + \frac{\gamma_e p_e}{\gamma_e - 1}\vec{u}_i + p_i \vec{u}_i\right) = \\ \frac{1}{\mathrm{Re}_i}\left(\vec{\nabla}\cdot\bar{\bar{\epsilon}}_i\right)\cdot\vec{u}_i - \vec{\nabla}\cdot\vec{q}_i - \vec{\nabla}\cdot\vec{q}_e + \vec{j}\cdot\vec{E} + \vec{u}_i\cdot\vec{R}_i^{in} \\ + Q_i^{in} - \Gamma_n^{rec}\frac{1}{2}m_i u_i^2 - Q_n^{rec} + \Gamma_i^{ion}\frac{1}{2}m_i u_n^2 + Q_i^{ion} - Q_R,\end{aligned} \tag{3.21}$$

$$\begin{aligned}\frac{\partial \mathcal{E}_n}{\partial t} + \vec{\nabla}\cdot\left(\mathcal{E}_n \vec{u}_n + \vec{u}_n p_n\right) = \\ \frac{1}{\mathrm{Re}_n}\left(\vec{\nabla}\cdot\bar{\bar{\epsilon}}_n\right)\cdot\vec{u}_n - \vec{\nabla}\cdot\vec{q}_n - \vec{u}_n\cdot\vec{R}_i^{in} + \\ Q_n^{in} + \Gamma_n^{rec}\frac{1}{2}m_i u_i^2 + Q_n^{rec} - \Gamma_i^{ion}\frac{1}{2}m_i u_n^2 - Q_i^{ion},\end{aligned} \tag{3.22}$$

where the total (thermal + kinetic) energy is $\mathcal{E}_{i,n} = \frac{p_{i,n}}{\gamma - 1} + \frac{1}{2}\rho_{i,n} u_{i,n}^2$ with the adiabatic constant $\gamma_{i,e,n} = 5/3$. The fluids obey the ideal gas law, i.e., $p_\alpha = n_\alpha k T_\alpha$. The ion and electron heat flux, $\vec{q}_{i,e}$, are taken from Braginskii [5] and are explained in the following section; the heat flux of the neutrals follows the Fourier law, $\vec{q}_n = -\kappa_n \vec{\nabla} T_n$, with the thermal conductivity approximated as

$$\kappa_n = \frac{4 p_n k}{\nu_{nn} m_n}. \tag{3.23}$$

The collisional energy exchange is

$$Q_\alpha^{\alpha\beta} = \frac{1}{2}\vec{R}_\alpha^{\alpha\beta}\cdot(\vec{v}_\beta - \vec{v}_\alpha) + 3\frac{m_{\alpha\beta}}{m_\alpha} n_\alpha \nu_{\alpha\beta} k (T_\beta - T_\alpha); \tag{3.24}$$

the thermal energy exchange terms due to the chemical reactions are

$$Q_n^{rec} = \frac{3}{2}\Gamma_n^{rec} k T_i \text{ and } Q_i^{ion} = \frac{3}{2}\Gamma_i^{ion} k T_n; \tag{3.25}$$

and the effective radiative cooling losses Q_R are discussed in the following section.

The electric current follows the generalized Ohm's law, as follows,

$$\vec{E} + \vec{u}_i \times \vec{B} = \frac{1}{\mathrm{S}}\vec{j} + \hat{\delta}_i \frac{\vec{j} \times \vec{B}}{n_i} - \hat{\delta}_i \frac{\nabla \cdot \bar{\bar{P}}_e}{n_i} - \frac{\nu_{en}}{\Omega_e}\left(\vec{u}_i - \vec{u}_n\right), \tag{3.26}$$

where the Lundquist number $\mathrm{S} = v_0 \mu_0 l_0 / \eta$, and the normalized ion skin depth $\hat{\delta}_i = \delta_i / l_0$. The resistivity is computed as

$$\eta = \frac{m_e n_e \left(\nu_{ei} + \nu_{en}\right)}{\left(e n_e\right)^2}, \tag{3.27}$$

with

$$\nu_{ei} = \frac{4}{3} n_i \Sigma_{ei} \sqrt{\frac{2kT_e}{\pi m_e}} \quad \text{and} \quad \nu_{en} = \frac{4}{3} n_n \Sigma_{en} \sqrt{\frac{2kT_{en}}{\pi m_{en}}}, \tag{3.28}$$

where $\Sigma_{en} = 10^{-19}$ m^2 [72].

The current is computed with the magnetic field as

$$\vec{j} = (\vec{\nabla} \times \vec{B})/\mu_0. \tag{3.29}$$

3.2.2 Radiation model

Two different radiation models are considered. The first, from Meier & Shumlak [98], and Leake et al. [8], represents an approximation of the optically thin radiative losses. This simplified model represents the radiative losses that are due to atomic physics such as the radiative recombination. In this approximation, excited states are not tracked, and instead, an effective potential is assumed [98, 105]. The model reads

$$Q_R^{(1)} = \Gamma^{ion} \phi_{eff}, \tag{3.30}$$

where the $\phi_{eff} = 33$ eV is the effective potential accounting for the electron binding energy plus the excitation energy of the ionization reaction. Yusupaliev [105] computes the effective ionization potential of a gas molecule by applying the dimension theory methods to the experimental data on static electric gas breakdown. ϕ_{eff} is considered as the mean energy expended by the electrons to ionization of one molecule, based on the study of elementary processes with participation of metastable levels of atoms and molecules under the optimum electron multiplication condition.

The second model used in the present work is the effectively thin radiative loss rate presented in Goodman & Judge [3]. The model is computed using the OPACITY project and CHIANTI databases. Goodman & Judge [3] showed that the model radiates the same energy as a plasma with solar photosphere trace element abundances with an accuracy of $\sim 10\%$, for $T \leq 1.5 \cdot 10^4$ K. The function represents a physical fit to a three-level hydrogen atom with two excited levels. The expression of the effectively loss rate in erg cm^{-3} s^{-1} reads

$$Q_R^{(2)} = n_e \left(n_n + n_i\right) 8.63 \cdot 10^{-6} C_E T^{-1/2} \sum_{i=1}^{2} E_i \Upsilon_i \exp(-eE_i/k_B T), \tag{3.31}$$

where $C_E = 1.6022 \cdot 10^{-12}$ erg eV^{-1}, the excited level energies are $E_1 = 3.54$ eV and $E_2 = 8.28$ eV; and the quantities $\Upsilon_1 = 0.15 \cdot 10^{-3}$ and $\Upsilon_2 = 0.065$. The temperature is given in Kelvin and the number densities in cm^{-3}.

In Fig. 3.1, we show the cooling curve defined as $\Lambda = Q_R^{(2)}/n_e \left(n_n + n_i\right)$. The curve is compared to this of Schure et al. [4]. The differences might be due to different composition of the plasma considered in the two models.

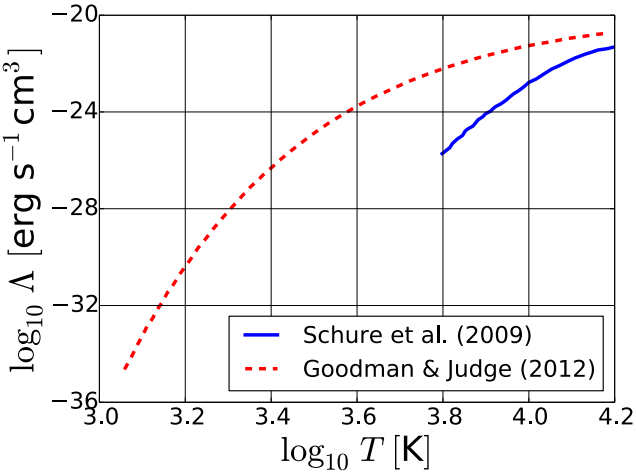

Figure 3.1: Cooling function of the model developed by Goodman & Judge [3] (dashed red) compared to the model develped by Schure et al. [4] (solid blue).

3.3 CLASSICAL TRANSPORT CLOSURE FOR FULLY IONIZED PLASMA

The fully ionized case considers the system of equations (2.13) - (2.15) for $\alpha = i, e$ and no reactions, i.e., $\vec{R}_\alpha^{react} = 0$ and $\dot{Q}_\alpha^{react} = 0$. The model implemented is the $29M$-moments approximation developed by Braginskii [5]. This model is compared to a more recent version calculated independently by Zhdanov [6].

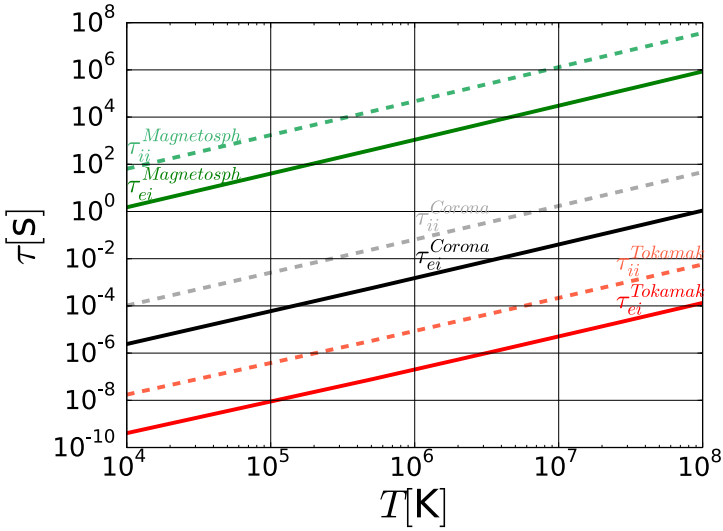

Figure 3.2: Ion-ion (dashed line) and electron-ion (solid line) collisional time as function of the temperature in the magnetosphere (green), the corona (black), and a tokamak (red).

The model neglects all the terms that are of the order $m_e/m_i \ll 1$. As a result, the transport equations of ions and electrons are independent, and only two collisional times are meaningful for the plasma, i.e., the electron-ion and the ion-ion. The collisional times in the conditions of Table 2.1 as a

function of temperature are depicted in Fig. 3.2. They are calculated as

$$\tau_{ei} = \frac{1}{6\epsilon_0^2} n_i \left[\frac{Z^4 e^4}{m_e^{1/2} \left(\pi k T_e\right)^{3/2}} \right] \ln \Lambda, \quad \text{and}$$

$$\tau_{ii} = \frac{1}{6\epsilon_0^2} n_i \left[\frac{Z^4 e^4}{m_i^{1/2} \left(\pi k T_i\right)^{3/2}} \right] \ln \Lambda \quad (3.32)$$

with

$$\Lambda = \frac{12\pi\epsilon_0}{|Ze^2|} k \left(\frac{T_e + T_i}{2} \right) r_D, \quad \text{and} \quad r_D^{-2} = \sum_{\alpha=e,i} \frac{n_\alpha q_\alpha^2}{\epsilon_0 k T_\alpha}. \quad (3.33)$$

In Fig. 3.2, one can observe that for a given density, the electron-ion collision time is shorter than this of the ion-ion collisions. Additionally, the collisional time increases as the temperature increases. The temperature in tokamaks is of the order of $T \sim 10^8$ K and the Alfvénic travel time of $t_A \sim 10^{-6}$ s. Therefore, the plasma inside tokamaks can be considered as collisionless since the collisional time is much larger than the dynamic timescales. Similarly, the plasma in the magnetosphere is collisionless as the temperature is $T \sim 10^4$ K and the Alfvénic travel time of $t_A \sim 1$ s comparable to the electron-ion collisional time. On the contrary, in a coronal loop, the Alfvénic time is $t_A \sim 10$ s and the temperature $T \sim 10^6$ K, and therefore the time between collisions is much smaller than the macroscopic dynamics timescales.

3.3.1 Electron Transport

The electron-ion friction force can be divided into two-parts, one produced by the presence of the electric current and another driven by the gradients in temperature.

$$\vec{R}_{ei} = \vec{R}_{ei}^{w} + \vec{R}_{ei}^{T} \quad (3.34)$$

where

$$\vec{R}_{ei}^{w} = -\frac{\rho_e}{\tau_{ei}} \left[\alpha_\parallel \vec{w}_\parallel + \alpha_\perp \vec{w}_\perp - \alpha_\wedge \left(\vec{b} \times \vec{w} \right) \right] \quad (3.35)$$

with $\vec{w} = \vec{u}_e - \vec{u}_i$.

$$\vec{R}_{ei}^{T} = -n_e k \left(\beta_\parallel \vec{\nabla}_\parallel T_e + \beta_\perp \vec{\nabla}_\perp T_e + \beta_\wedge \left(\vec{b} \times \vec{\nabla} T_e \right) \right). \quad (3.36)$$

The dimensionless coefficients are function of the electron Hall parameter defined as $\beta_e = \Omega_e \tau_{ei}$ and the ionization degree of the ions. In this work, we consider single ionized ions, i.e., $Z = 1$. The coefficients as found in Braginskii [5] read

$$\begin{aligned} &\alpha_\parallel = 0.5129, \quad \alpha_\perp = 1 - \tfrac{6.416\beta_e^2+1.837}{\Delta_e}, \quad \alpha_\wedge = \beta_e \tfrac{1.704\beta_e^2+0.7796}{\Delta_e}, \\ &\beta_\parallel = 0.7110, \qquad \beta_\perp = \tfrac{5.101\beta_e^2+2.681}{\Delta_e}, \qquad \beta_\wedge = \beta_e \tfrac{1.5\beta_e^2+3.053}{\Delta_e}. \end{aligned} \tag{3.37}$$

with $\Delta_e = \beta_e^4 + 14.79\beta_e^2 + 3.7703$. The ion-electron friction reads $\vec{R}_{ei} = -\vec{R}_{ie}$.

The electron heat flux vector is calculated as

$$\vec{q}_e = \vec{q}_e^{\,w} + \vec{q}_e^{\,T}, \tag{3.38}$$

where

$$\vec{q}_e^{\,w} = p_e \left(\beta_\parallel \vec{w}_\parallel + \beta_\perp \vec{w}_\perp + \beta_\wedge \left(\vec{b} \times \vec{w} \right) \right), \tag{3.39}$$

$$\vec{q}_e^{\,T} = -\frac{p_e k}{m_e} \tau_{ei} \left(\lambda_{e_\parallel} \vec{\nabla}_\parallel T_e + \lambda_{e_\perp} \vec{\nabla}_\perp T_e + \lambda_{e_\wedge} \left(\vec{b} \times \vec{\nabla} T_e \right) \right). \tag{3.40}$$

The electron heat conduction coefficients read

$$\lambda_{e_\parallel} = 3.1616, \quad \lambda_{e_\perp} = \tfrac{4.664\beta_e^2+11.92}{\Delta_e}, \quad \lambda_{e_\wedge} = \beta_e \tfrac{2.5\beta_e^2+21.67}{\Delta_e}. \tag{3.41}$$

The electron viscous tensor is computed as

$$\bar{\bar{\pi}}_e = p_e \tau_{ei} \left(\eta_e^{(0)} \bar{\bar{W}}_e^{(0)} + \eta_e^{(1)} \bar{\bar{W}}_e^{(1)} + \eta_e^{(2)} \bar{\bar{W}}_e^{(2)} - \eta_e^{(3)} \bar{\bar{W}}_e^{(3)} - \eta_e^{(4)} \bar{\bar{W}}_e^{(4)} \right), \tag{3.42}$$

where the viscosity coefficients are

$$\begin{aligned} \eta_e^{(0)} &= 0.733, \\ \eta_e^{(4)} &= \tfrac{2.05\beta_e^2+8.50}{\delta_e}, \quad \eta_e^{(1)} = \eta_e^{(2)} \left[2\beta_e \right], \\ \eta_e^{(4)} &= -\beta_e \tfrac{\beta_e^2+7.91}{\delta_e}, \quad \eta_e^{(3)} = \eta_e^{(4)} \left[2\beta_e \right]. \end{aligned} \tag{3.43}$$

with $\delta_e = \beta_e^4 + 13.8\beta_e^2 + 11.6$.

3.3.2 Ion transport

In this section, we take into account the difference in the relaxation time of the ions between Braginskii's transport coefficients [5] and Eq. (3.32), i.e., $\tau_i^{Br} = 2\tau_{ii}$. The ion heat flux vector reads

$$\vec{q}_i = -\frac{p_i k}{m_i}\tau_{ii}\left(\lambda_{i_\parallel}\vec{\nabla}_\parallel T_i + \lambda_{e_\perp}\vec{\nabla}_\perp T_i + \lambda_{e_\wedge}\left(\vec{b}\times\vec{\nabla}T_i\right)\right). \tag{3.44}$$

with the ion heat conduction coefficients

$$\lambda_{i_\parallel} = 7.812, \quad \lambda_{i_\perp} = 2\tfrac{4\beta_i^2+2.645}{\Delta_i}, \quad \lambda_{i_\wedge} = 4\beta_i\tfrac{5\beta_i^2+4.65}{\Delta_i}, \tag{3.45}$$

with $\Delta_i = 16\beta_i^4 + 10.8\beta_i^2 + 0.677$.

The ion viscous tensor reads

$$\bar{\bar{\pi}}_i = p_i\tau_{ii}\left(\eta_i^{(0)}\bar{\bar{W}}_i^{(0)} + \eta_i^{(1)}\bar{\bar{W}}_i^{(1)} + \eta_i^{(2)}\bar{\bar{W}}_i^{(2)} - \eta_i^{(3)}\bar{\bar{W}}_i^{(3)} - \eta_i^{(4)}\bar{\bar{W}}_i^{(4)}\right), \tag{3.46}$$

where the ion viscosity is calculated as

$$\begin{aligned} \eta_i^{(0)} &= 1.92, \\ \eta_i^{(4)} &= 2\tfrac{4.8\beta_i^2+2.23}{\delta_i}, \quad \eta_i^{(1)} = \eta_i^{(2)}\left[2\beta_i\right], \\ \eta_i^{(4)} &= 2\beta_i\tfrac{4\beta_i^2+2.38}{\delta_i}, \quad \eta_i^{(3)} = \eta_e^{(4)}\left[2\beta_i\right], \end{aligned} \tag{3.47}$$

with $\delta_i = 16\beta_i^4 + 16.12\beta_i^2 + 2.33$.

The components of the viscous stress tensor are defined as function of the traceless rate of strain tensor

$$W_{ij} = \frac{\partial u_i}{\partial x_j} + \frac{\partial u_j}{\partial x_i} - \frac{2}{3}\frac{\partial u_k}{\partial x_k}\delta_{ij} \tag{3.48}$$

The tensors for arbitrary orientation of the magnetic field [106] are defined as

$$W_{ij}^{(0)} = \frac{3}{2}\left(b_i b_j - \frac{1}{3}\delta_{ij}\right)\left(b_k W_{kl} b_l\right) \tag{3.49}$$

$$W_{ij}^{(1)} = \delta_{i\mu}^{\perp} W_{\mu\nu}\delta_{\nu j}^{\perp} + \frac{1}{2}\delta_{ij}^{\perp} b_\mu W_{\mu\nu} b_\nu \tag{3.50}$$

$$W_{ij}^{(2)} = \delta_{i\mu}^{\perp} W_{\mu\nu} b_\nu b_j + b_i b_\mu W_{\mu\nu}\delta_{\nu j}^{\perp} \tag{3.51}$$

$$W_{ij}^{(3)} = -\frac{1}{2}\delta_{i\mu}^{\perp} W_{\mu\nu} Z_{\mu j} + \frac{1}{2} Z_{i\mu} W_{\mu\nu}\delta_{\nu j}^{\perp} \tag{3.52}$$

$$W_{ij}^{(4)} = Z_{i\mu} W_{\mu\nu} b_\nu b_j - b_i b_\mu W_{\mu\nu} Z_{\nu j} \tag{3.53}$$

Finally, the transfer of energy (internal + kinetic) in unlike-particle elastic collisions reads,

$$\dot{Q}_{ie}^{elastic} = \frac{3k}{\tau_{ei}} \frac{m_e n_e}{m_i} (T_e - T_i) - \vec{R}_{ei} \cdot \vec{u}_i, \tag{3.54}$$

and

$$\dot{Q}_{ei}^{elastic} = \frac{3k}{\tau_{ei}} \frac{m_e n_e}{m_i} (T_i - T_e) + \vec{R}_{ei} \cdot \vec{u}_i. \tag{3.55}$$

The non-dimensional coefficients of the fully-ionized two-fluid model are shown as function of the magnetization in Fig. 3.3. The solid line corresponds to Braginskii's model [5], which was implemented, whereas the dashed line corresponds to the model derived in Zhdanov [6]. The differences between the two models are very small and only visible by naked eye in the electron properties that are parallel to the magnetic field. Nevertheless, the work of Zhdanov [6] has a remarkable value as he provides a detailed derivation of the model whereas Braginskii [5] gives a summary of the results.

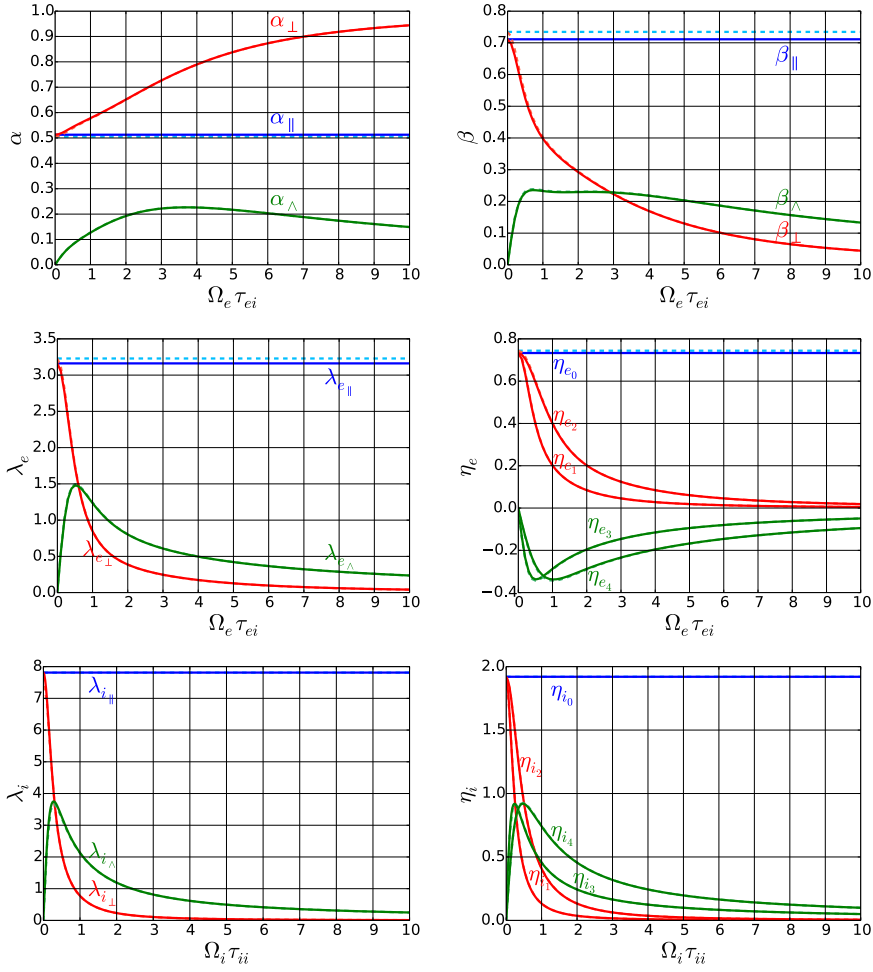

Figure 3.3: Dimensionless transport coefficients of the fully-ionized two-fluid model. The model derived by Braginskii [5] (solid line) is compared to this of Zhdanov [6] (dashed line).

3.4 SUMMARY

We have presented two closures for partially- and fully-ionized multi-fluid models. Firstly, the Grad's method has been described in order to illustrate the complexity that the transport theory requires. The classical transport theory relies on the assumption that the Knudsen number is small (the plasma is collisional), and that the distribution function of the species follows a Maxwellian distribution with a small perturbation. Similarly, effects that are produced by the variation of the magnetic field in mean-free-path scales are not accounted for by this theory. These assumptions might not be fulfilled inside tokamaks.

The multi-fluid model for partially ionized hydrogen plasmas considers two fluids, one for the neutrals and another for the charged species. The fluids interact through elastic collisions that exchange momentum and energy and ionization and recombination reactions. An approximation for the properties is given. Although it is not based on the Grad's method, it contains the main physical phenomena that occur in partially ionized plasmas.

The fully-ionized multi-fluid model considers ions and electrons as two separate fluids. The classic closure derived by Braginskii [5] is presented and compared with a more recent derivation by Zhdanov [6]. The difference between the two models is minimal.

CHAPTER 4

Finite Volume Solver for the Multi-Fluid Plasma Equations

If we suppose that we know all the physical laws perfectly, of course we don't have to pay any attention to computers.

– *Richard P. Feynman*

A finite volume method for the multi-fluid plasma equations, including diffusive, reactive, and collisional terms, coupled to the full Maxwell's equations is presented. We propose an innovative approach that proves to be versatile, representing a wide range of plasma parameters from ideal and resistive MHD to reactive and collisional ion-neutral and ideal ion-electron models. The method couples the multi-fluid equations in the most general formulation to the full Maxwell's equations. We propose a second order TVD spatial discretization and second order fully-implicit time stepping scheme. The electromagnetic field solver uses the hyperbolic divergence method to control the error in the divergence of the fields and an upwind scheme with scaled numerical diffusion. The fluids use a flux vector splitting approach with corrections to solve flows at all speed regimes, from subsonic to supersonic.

Part of this chapter has been published in:

1. A. Alvarez Laguna, A. Lani, H. Deconinck, N. N. Mansour, and S. Poedts, **A fully-implicit finite-volume method for multi-fluid reactive and collisional magnetized plasmas on unstructured meshes**, *Journal of Computational Physics, 318, pp. 252-276, 2016.*
2. A. Alvarez Laguna, N. Ozak, A. Lani, H. Deconinck, and S. Poedts, **Fully-implicit finite volume method for the ideal two-fluid plasma model**, *Computational Physics Communications, under review, 2017.*

4.1 LITERATURE REVIEW ON MULTI-FLUID NUMERICAL MODELS

The mathematical structure of the set of equations that was presented in the previous chapter imposes a major challenge to the numerical modeling. The multi-fluid equations capture phenomena that comprise a wide range of time and space scales, chiefly, the electromagnetic scales, the convective and diffusive scales of each fluid, and the collisional and chemical reaction scales. The disparity of scales in a system of PDEs is known as *stiffness* and usually is related to stability problems in the time integration which implies small time steps. Additionally, the multi-fluid and Maxwell's equations are coupled through source terms that, unlike MHD equations, cannot be written as fluxes. This can lead to errors in the conservation of momentum and energy at the numerical level. Owing to that reason, dedicated numerical methods are to be proposed in order to tackle the particular difficulties of the multi-fluid equations.

An increasing number of numerical methods for solving for the multi-fluid equations coupled to the Maxwell's equations have been recently developed for different multi-fluid approaches. For the fully-ionized ideal two-fluid (electron+ion) model, the first pioneering simulations correspond to the ANTHEM code [107, 108]. More recently, different explicit and semi-implicit methods discretizing the ideal two-fluid set of equations coupled to the Maxwell's equations have been proposed: High-order discontinuous Galerkin methods have been developed by Loverich & Shumlak [109], Loverich et al. [10], Srinivasan & Shumlak [110], and Sousa & Shumlak [111]. Finite difference methods have been presented by Baboolal [112], Baboolal & Bharuthram [113], and Kumar & Mishra [114]. Finite volume discretizations are presented by Shumlak & Loverich [115], and Hakim et al. [116]. An alternative approach is the quasi-neutral two-fluid that suppresses the plasma waves and results in a less stiff system. Finite volume discretizations of the latter are introduced by Amano [117], and Balsara et al. [118] for relativistic flows. As well, a three-fluid model considering electrons, protons, and O^{5+} ions and the effects of the anisotropy introduced by the magnetic field on the transport fluxes, is studied by Ofman et al. [119, 120]. However, very little pioneering work has been devoted to solving multi-fluid equations for characterizing reactive, collisional, partially ionized plasma. A two-fluid model that considers neutrals and ionized particles as separate fluids, interacting by means of chemical reactions, collisional momentum and energy exchanges is presented by Meier [98] and numerical solutions in chromospheric conditions are obtained by Leake et al. [8, 72] and Murphy & Lukin [73].

In this chapter we present a novel numerical method for the simulation of laboratory and/or space plasmas, which solves for the multi-fluid model coupled to the purely hyperbolic full Maxwell's equations [121]. The numerical method proves to be versatile, able to reproduce efficiently ideal MHD, resistive MHD, reactive and collisional ion-neutral, and ideal ion-electron models. Compared to the previous multi-fluid plasma finite volume schemes, this scheme proposes the following novelties:

- The time discretization is a fully-implicit three-point Backward Euler scheme. The eigenvalue structure of the numerical flux has characteristic speeds ranging from the speed of light to the ion speed of sound. Additionally, the source term that couples the electromagnetic fields with the fluids can introduce very short time scales. Consequently, the coupled system is very stiff and results in a very restrictive Courant-Friedrichs-Lewy (CLF) condition in the time step for explicit discretizations. In the present work, all the terms are treated implicitly, resulting in a stable discretization without CFL condition.

- The numerical fluxes of the fluids are discretized by means of an advection upstream splitting method (i.e., AUSM$^+$-up) for all speeds [122, 123, 124]. This flux vector splitting method is designed to achieve shock resolution, monotonicity, positivity and entropy-satisfying properties, as well as accuracy at low Mach number. The latter is an important property since the Mach number of ions and electrons is very different as the electron speed of sound is much greater than that of ions. In addition, unlike the characteristic-based schemes such as Roe's that involve $\mathcal{O}(n^2)$ operations per discretization point, the flux vector scheme AUSM$^+$-up involves only $\mathcal{O}(n)$, where n is the number of equations.

- The Maxwell's equations are discretized using a modified-CIR (Courant-Isaacson-Rees) scheme [125] with scaled dissipation. The exact solution of the Riemann problem of the Maxwell's equations coupled to the two-fluid plasma is unknown as it depends on the source terms, i.e., on the dynamics of the fluids. An approximate Riemann solver constructed without taking into account the coupled problem may result in an over dissipative scheme. In this work, we rescale the numerical dissipation based on the physics of the coupled problem. This approach allows for solving the Maxwell's equations both in the charge-neutrality limit and when charge separation is considered.

- The second-order reconstruction in space uses a limiter suitable for near-constant regions of the flow. We find this to be important for the ideal two-fluid plasma model as the solutions contain dispersive waves that result in regions with small oscillations where the limiter can reduce the order of accuracy.

All developments discussed in this thesis have been implemented within COOLFluiD [126, 127, 128, 129, 130, 131], a world-class open source object-oriented platform for scientific high-performance computing. COOLFluiD consists of a set of plug-in libraries that can be linked at run-time to a C++ kernel where the basic parallel data structure, functionalities and abstract interfaces are defined. The framework is currently able to handle parallel multi-physics simulations including, in particular, complex compressible/incompressible flows in thermochemical equilibrium or nonequilibrium [132, 133, 134, 135, 136, 137] and astrophysical plasmas [138, 139, 140] with a wide range of spatial discretization algorithms and time marching methods.

4.2 HYPERBOLIC DIVERGENCE CLEANING FOR MAXWELL'S EQUATIONS

One of the main concerns when the electromagnetic field is solved numerically, either in the induction equation in the MHD approach or solving the full Maxwell's equations, is to fulfill the divergence constraints for the electromagnetic field. While the MHD approach only needs to consider the divergence free condition for the magnetic field, the full Maxwell system needs also to account for Gauss' law for the electric field. Different methods for enforcing these constraints are found in the literature, a good review of them can be found in [141]. The hyperbolic divergence cleaning (HDC) method introduced by Munz et al. [121] has shown to be an efficient and flexible method to control the divergence constraints, i.e., Eq. (2.34) and Eq. (2.22), in parallel solvers for finite volume calculations on unstructured grids. This method introduces two additional degrees of freedom that couple Gauss' law and the divergence-free condition for the magnetic induction with the evolution equations. This model, called Generalized Lagrange Multiplier Maxwell system, results in a purely hyperbolic system of equations that enforces the divergence constraints. Since the new system continues being hyperbolic, it can be solved using the same numerical methods as the regular hyperbolic system of partial differential equations. The latter can be considered an advantage compared to other methods that involve the solution of stiff Poisson problems or the use of staggered grids [142].

The system proposed by the HDC method is also called the purely hyperbolic Maxwell's equations. Two Lagrange multipliers Φ and Ψ are added to the original Maxwell equations as follows

$$\frac{\partial \vec{B}}{\partial t} + \vec{\nabla} \times \vec{E} + \gamma^2 \vec{\nabla} \Psi = 0, \tag{4.1}$$

$$\frac{\partial \vec{E}}{\partial t} - c^2 \vec{\nabla} \times \vec{B} + (\chi c)^2 \vec{\nabla} \Phi = -\frac{\vec{j}}{\mu_0}, \tag{4.2}$$

$$\frac{\partial \Psi}{\partial t} + c^2 \vec{\nabla} \cdot \vec{B} = 0, \tag{4.3}$$

$$\frac{\partial \Phi}{\partial t} + \vec{\nabla} \cdot \vec{E} = \frac{\rho_c}{\epsilon_0}. \tag{4.4}$$

Artificial waves are introduced at speeds γc and χc that remove the errors in the fulfillment of the constraints. Therefore, the two scalar parameters γ and χ should be chosen to be ≥ 1. In this work, we use $\gamma = \chi = 1$ in the results, so there are no waves that are faster than the speed of light, which avoids increasing the stiffness to the problem.

4.3 FINITE VOLUME FORMULATION

We can write the purely hyperbolic Maxwell equations (4.1)-(4.4) coupled to the general multi-fluid equations (2.13)-(2.15) in conservation form, as follows

$$\frac{\partial \mathbf{U}(\mathbf{P})}{\partial t} + \vec{\nabla} \cdot \vec{\mathbf{F}}^{(c)} = \vec{\nabla} \cdot \vec{\mathbf{F}}^{(d)} + \mathbf{S}, \tag{4.5}$$

where $\mathbf{U}$ are the conservative variables and $\mathbf{P}$ are the variables in which we actually store and update the solution. For Maxwell's equation system, we consider:

$$\mathbf{U} = \mathbf{P} = \begin{pmatrix} \vec{B} \\ \vec{E} \\ \Psi \\ \Phi \end{pmatrix}, \quad \vec{\mathbf{F}}^{(c)} = \begin{pmatrix} \bar{\bar{I}} \times \vec{E} + \gamma^2 \Psi \bar{\bar{I}} \\ -c^2 \bar{\bar{I}} \times \vec{B} + (\chi c)^2 \Phi \bar{\bar{I}} \\ c^2 \vec{B}^T \\ \vec{E}^T \end{pmatrix},$$

$$\text{and } \mathbf{S} = \begin{pmatrix} 0 \\ -\frac{\vec{j}}{\epsilon_0} \\ 0 \\ \frac{\rho_c}{\epsilon_0} \end{pmatrix}. \tag{4.6}$$

For the multi-fluid equations for each species s, we have:

$$\mathbf{U}_s = \begin{pmatrix} \rho_s \\ \rho_s \vec{u}_s \\ \rho_s \mathcal{E}_s \end{pmatrix}, \; \mathbf{P}_s = \begin{pmatrix} \rho_s \\ \vec{u}_s \\ T_s \end{pmatrix},$$

$$\vec{\mathbf{F}}_s^{(c)} = \begin{pmatrix} \rho_s \vec{u}_s \\ \rho_s \vec{u}_s \vec{u}_s + p_s \bar{\bar{I}} \\ \rho_s H_s \vec{u}_s \end{pmatrix}, \; \vec{\mathbf{F}}_s^{(d)} = \begin{pmatrix} 0 \\ \bar{\bar{\pi}}_s \\ \vec{u}_s \cdot \bar{\bar{\pi}}_s - \vec{q}_s \end{pmatrix},$$

$$\text{and } \mathbf{S}_s = \begin{pmatrix} \dot{\rho}_s \\ Q_s \vec{E} + \vec{j}_s \times \vec{B} + \dot{\rho}_s \vec{u}_s + \sum_{j \neq s}^{j \in N_s} \vec{R}_s^{sj} \\ \vec{j}_s \cdot \vec{E} + \frac{1}{2} \dot{\rho}_s u_s^2 + \sum_{j \neq s}^{j \in N_s} \dot{Q}_s^{sj} \cdot \vec{u}_s + \sum_{j \neq s}^{j \in N_s} H_s^{sj} + \dot{Q}_s \end{pmatrix}. \quad (4.7)$$

In order to apply the finite volume method, we divide the domain into N non-overlapping cells of area $|\Omega_i|$, each of them bounded by the closed surface $\partial\Omega_i$ with outward normal $\vec{n}$. The boundary $\partial\Omega_i$ consists of n faces of area $|\partial\Omega_{ij}|$, with $j \in \mathscr{D}_i$, the set of neighboring cells of cell i. Equation (4.5) for the cell Ω_i can be written in integral form as:

$$\frac{d}{dt} \int_{\Omega_i} \mathbf{U}(\mathbf{P}) \, d\Omega + \oint_{\partial\Omega_i} \vec{\mathbf{F}}^{(c)} \cdot \vec{n} \, d\Sigma = \oint_{\partial\Omega_i} \vec{\mathbf{F}}^{(d)} \cdot \vec{n} \, d\Sigma + \int_{\Omega_i} \mathbf{S} \, d\Omega. \quad (4.8)$$

We apply the discretization:

$$\frac{d\mathbf{U}(\mathbf{P}_i)}{dt} |\Omega_i| + \sum_{j \in \mathscr{D}_i} \mathbf{H}_{ij} |\partial\Omega_{ij}| = \sum_{j \in \mathscr{D}_i} \mathbf{G}_{ij} |\partial\Omega_{ij}| + \mathbf{S}_i |\Omega_i|, \quad (4.9)$$

where the cell average $\mathbf{P}_i$ is the actual array of unknowns and $\mathbf{H}_{ij}$ and $\mathbf{G}_{ij}$ are the numerical inviscid and diffusive fluxes at the interface between cells i and j, respectively. The numerical inviscid flux can be approximated with a numerical flux function as $\mathbf{H}_{ij} = \mathscr{H}(\mathbf{U}_i, \mathbf{U}_j, \vec{n}_{ij})$, such that it fulfills the consistency condition $\mathscr{H}(\mathbf{U}, \mathbf{U}, \vec{n}) = \vec{\mathbf{F}}^{(c)} \cdot \vec{n} = \mathbf{H}(\mathbf{U})$. In the following sections we will present the numerical schemes used in the present work, i.e., modified-CIR for Maxwell's equations and a generalization of the AUSM$^+$-up for multi-fluid plasma equations.

4.4 SECOND-ORDER RECONSTRUCTION

The numerical fluxes $\mathbf{H}_{ij} = \mathscr{H}(\mathbf{U}_i, \mathbf{U}_j, \vec{n}_{ij})$ that were introduced in the previous section are first order space accurate upwind schemes, as they only

depend on the values of the cells U_i and U_j. In order to obtain second-order accuracy in space, we use a weighted linear least square reconstruction [143] with Venkatakrishnan's limiter [144]. Weights are based on inverse of the distances between cell-centers of neighboring cells in the reconstruction stencil. The limited reconstructed values of the variables of $\mathbf{U}_i$ and $\mathbf{U}_j$ at the Gauss quadrature point of the cell face are computed from the reconstructed $\mathbf{P}$ variables, which are the ones that are actually stored and to which the least square approach is directly applied:

$$\begin{aligned} \mathbf{U}_i^{rec-limited} &= \mathbf{U}(\mathbf{P}_i^{rec-limited}) \equiv \mathbf{U}_L, \\ \mathbf{U}_j^{rec-limited} &= \mathbf{U}(\mathbf{P}_j^{rec-limited}) \equiv \mathbf{U}_R, \end{aligned} \tag{4.10}$$

where

$$\begin{aligned} \mathbf{P}_i^{rec-limited} &= \mathbf{P}_i + \phi_i \vec{\nabla}\mathbf{P}_i \cdot (\vec{r}_{ij} - \vec{r}_i) \equiv \mathbf{P}_L, \\ \mathbf{P}_j^{rec-limited} &= \mathbf{P}_j + \phi_j \vec{\nabla}\mathbf{P}_j \cdot (\vec{r}_{ij} - \vec{r}_j) \equiv \mathbf{P}_R. \end{aligned} \tag{4.11}$$

Working directly with $\mathbf{P}$ variables instead of $\mathbf{U}$ is more convenient especially for computing gradients needed by transport fluxes (in velocity and temperature), but also when considering more complex nonlinear thermodynamic models for the different species energies (which are not considered here but are planned to be used in future work). In Eq. (4.10), $\mathbf{U}(\mathbf{P})$ is a straightforward analytical variable transformation. In Eq. (4.11), $\vec{r}_{ij}$ is the position vector of the Gauss quadrature point on the cell face $\partial\Omega_{ij}$, $\vec{r}_i$ and $\vec{r}_j$ are the position vectors of the cell center of the cells i and j, respectively. The expression for the limiter ϕ can be found in Venkatakrishnan [144]. In this work, for each variable of $\mathbf{P}$, the limiter corresponding to a cell is computed as the minimum over all the quadrature points on the faces for that variable. For the sake of clarity, in the following the reconstructed values at the interface between the two cells, $\mathbf{U}_i^{rec-limited}$ and $\mathbf{U}_j^{rec-limited}$ will be referred to as $\mathbf{U}_L$ and $\mathbf{U}_R$, respectively.

4.4.1 Venkatakrishnan limiter for smooth region flows

The expression for the limiter ϕ is found to be of remarkable importance for ideal two-fluid plasma model due to the presence in the solution of dispersive waves, e.g., plasma waves or ion/electron cyclotron waves. If the limiter is not properly designed, these oscillations can be detected by the limiter as spurious and the unexpected behaviour of the limiter can damage the accuracy of the numerical scheme. We adopt the limiter presented by Venkatakrishnan [144], which proposes a correction for nearly smooth regions, as follows:

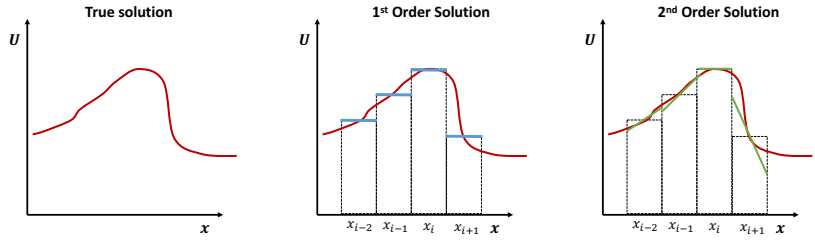

Figure 4.1: Sketch of piece-wise first-order and second-order numerical solutions.

$$\phi_i = \begin{cases} \Phi\left(\frac{\max(\mathbf{P}_i, \mathbf{P}_{k\in\mathscr{D}_i}) - \mathbf{P}_i}{\nabla\mathbf{P}_i\cdot(\vec{r}_{ij}-\vec{r}_i)}\right) & \text{if} \quad \nabla\mathbf{P}_i\cdot(\vec{r}_{ij}-\vec{r}_i) > 0 \\ \Phi\left(\frac{\min(\mathbf{P}_i, \mathbf{P}_{k\in\mathscr{D}_i}) - \mathbf{P}_i}{\nabla\mathbf{P}_i\cdot(\vec{r}_{ij}-\vec{r}_i)}\right) & \text{if} \quad \nabla\mathbf{P}_i\cdot(\vec{r}_{ij}-\vec{r}_i) < 0 \\ 1 & \text{if} \quad \nabla\mathbf{P}_i\cdot(\vec{r}_{ij}-\vec{r}_i) = 0 \end{cases} \tag{4.12}$$

The limiter function reads

$$\Phi\left(\frac{\Delta_+}{\Delta_-}\right) = \frac{1}{\Delta_-}\left[\frac{(\Delta_+^2+\epsilon^2)\Delta_- + 2\Delta_-^2\Delta_+}{\Delta_+^2 + 2\Delta_-^2 + \Delta_-\Delta_+ + \epsilon^2}\right] \tag{4.13}$$

where $\epsilon^2 = (K\Delta x)^3$, $\Delta_- = \nabla\mathbf{P}_i\cdot(\vec{r}_{ij}-\vec{r}_i)$ and $\Delta_+ = \max(\mathbf{P}_i, \mathbf{P}_{k\in\mathscr{D}_i}) - \mathbf{P}_i$. Using this correction, the limiter is not activated for oscillations that are $|\nabla\mathbf{P}_i\cdot(\vec{r}_{ij}-\vec{r}_i)| < (K\Delta x)^{3/2}$. Therefore, by choosing the proper value of $K > 0$, we avoid to limit the slope in the regions without discontinuities but where dispersive waves are present. In this work, each variable uses a different value of K. Typical values used in this work are $K \in (0.1, 1)$.

Figure 5.26 shows the difference in the results for a simulation of magnetic reconnection (see details in Chapter 5) where two different limiters have been used. The solution on the top shows the ion temperature (left) and the corresponding limiter to this variable (right) obtained in the code using a Barth and Jespersen limiter [145], while the figure on the bottom shows also the ion temperature and the value of the limiter at the same solution time using the Venkatakrishnan limiter adopted for the simulations in the validation of our code. From the figures on the right, one can see that the Venkatakrishnan limiter does a better job capturing the shocks, while the reconnection region is not limited. This is possible, since the limiter is not activated in the entire region, where plasma oscillations are present. On the other hand, the Barth and Jespersen limiter is more dissipative in the

domain, especially in the current sheet, and even induced the growth of a spurious plasmoid in the center of the current sheet, which it is not present when using the Venkatakrishnan limiter.

4.5 MODIFIED-CIR SCHEME WITH SCALED NUMERICAL DIFFUSION FOR MAXWELL'S EQUATIONS WITH HDC

We first analyze the original CIR scheme [125] applied to the HDC Maxwell's equations. The original version of the scheme takes into account only the eigenvalue structure of the flux. However, the influence of the motion of the fluids in the electromagnetic equations is driven by the current $\vec{j}$ and the charge density ρ_c that appear in Eq. (4.2) and Eq. (4.4). As it will be shown, if we apply the original CIR scheme and we disregard the scales that are consequence of the fluid-electromagnetics coupled problem, the numerical dissipation is based on a purely electromagnetics flux, which results in an overestimated numerical diffusion.

The original CIR scheme for the HDC Maxwell's equations is constructed as follows. Considering the system of Eq. (4.6), in the 3D case, the flux $\vec{\mathbf{F}}^{(c)}$ projected onto the normal can be written as:

$$\mathbf{H}(\mathbf{U}) = \vec{\mathbf{F}}^{(c)} \cdot \vec{n} = \begin{pmatrix} \gamma^2\Psi n_x + E_z n_y - E_y n_z \\ -E_z n_x + \gamma^2\Psi n_y + E_x n_z \\ E_y n_x - E_x n_y + \gamma^2\Psi n_z \\ \hline \chi^2 c^2 \Phi n_x - c^2 B_z n_y + c^2 B_y n_z \\ c^2 B_z n_x + \chi^2 c^2 \Phi n_y - c^2 B_x n_z \\ -c^2 B_y n_x + c^2 B_x n_y + \chi^2 c^2 \Phi n_z \\ \hline c^2 B_x n_x + c^2 B_y n_y + c^2 B_z n_z \\ E_x n_x + E_y n_y + E_z n_z \end{pmatrix}. \tag{4.14}$$

Since the matrix $\mathbf{H}(\mathbf{U})$ depends linearly on $\mathbf{U}$, we can write $\mathbf{H}(\mathbf{U}) = \frac{\partial \mathbf{H}}{\partial \mathbf{U}}\mathbf{U} = \mathbf{A}_n\mathbf{U}$. Where $\mathbf{A}_n$ is linear with real eigenvalues $\lambda = \pm c, \pm c, \pm\gamma c, \pm\chi c$. Therefore, the system is hyperbolic and the first-order upwind space discretization, a.k.a., CIR scheme, can be obtained immediately by writing the numerical flux $\mathbf{H}_{ij} = \mathscr{H}(\mathbf{U}_L, \mathbf{U}_R, \vec{n}_{ij})$ as:

$$\mathbf{H}_{ij} = \mathbf{A}_n^+\mathbf{U}_L + \mathbf{A}_n^-\mathbf{U}_R = \frac{\mathbf{H}(\mathbf{U}_L) + \mathbf{H}(\mathbf{U}_R)}{2} - \frac{1}{2}|\mathbf{A}_n|(\mathbf{U}_R - \mathbf{U}_L), \tag{4.15}$$

where $\mathbf{A}_n^{\pm} = \mathbf{L}\mathbf{\Lambda}_{\pm}\mathbf{L}^{-1}$ and $\mathbf{\Lambda}_{\pm}$ is the diagonal matrix that contains either the positive or negative eigenvalues of $\mathbf{\Lambda}$ respectively. The matrix $|\mathbf{A}_n| =$

$\mathbf{L}|\mathbf{\Lambda}|\mathbf{L}^{-1}$ where $|\mathbf{\Lambda}| = \frac{\mathbf{\Lambda}_+ - \mathbf{\Lambda}_-}{2}$. Expression of the matrices $\mathbf{A}_n^{\pm}$ can be found in Munz et al. [121].

As it can be seen from Eq. (4.15), the CIR scheme consists of a central scheme with a numerical dissipation term. The numerical dissipation is fundamental in order to obtain a monotone scheme, as stated in Godunov's theorem. In this particular set of equations, the matrix responsible for the numerical dissipation reads

$$|\mathbf{A}_n| = \left[\begin{array}{c|c|c} |\mathbf{A}_n|^B & 0 & 0 \\ \hline 0 & |\mathbf{A}_n|^E & 0 \\ \hline 0 & 0 & |\mathbf{A}_n|^{HDC} \end{array}\right] \tag{4.16}$$

where

$$|\mathbf{A}_n|^B = c\mathbf{D}^B, \text{ with } \mathbf{D}^B = \begin{bmatrix} 1+n_x^2(\gamma-1) & n_xn_y(\gamma-1) & n_xn_z(\gamma-1) \\ n_xn_y(\gamma-1) & 1+n_y^2(\gamma-1) & n_yn_z(\gamma-1) \\ n_xn_z(\gamma-1) & n_yn_z(\gamma-1) & 1+n_z^2(\gamma-1) \end{bmatrix} \tag{4.17}$$

$$|\mathbf{A}_n|^E = c\mathbf{D}^E, \text{ with } \mathbf{D}^E = \begin{bmatrix} 1+n_x^2(\chi-1) & n_xn_y(\chi-1)c & n_xn_z(\chi-1) \\ n_xn_y(\chi-1) & 1+n_y^2(\chi-1) & n_yn_z(\chi-1) \\ n_xn_z(\chi-1) & n_yn_z(\chi-1) & 1+n_z^2(\chi-1) \end{bmatrix} \tag{4.18}$$

and

$$|\mathbf{A}_n|^{HDC} = c\mathbf{D}^{HDC}, \text{ with } \mathbf{D}^{HDC} = \begin{bmatrix} \gamma & 0 \\ 0 & \chi \end{bmatrix}. \tag{4.19}$$

With the previous matrix, we get the following expression for the numerical flux function that will depend on the reconstructed values of $\mathbf{U}$ of the left (L) and right (R) neighbouring cell to the face with normal $\vec{n}$ pointing from

the left state to the right state:

$$\mathscr{H}(\mathbf{U}_L,\mathbf{U}_R,\vec{n}) = \frac{1}{2}\left(\begin{array}{c} \gamma^2(\Psi_L+\Psi_R)n_x + (E_{z_L}+E_{z_R})n_y - (E_{y_L}+E_{y_R})n_z \\ -(E_{z_L}+E_{z_R})n_x + \gamma^2(\Psi_L+\Psi_R)n_y + (E_{x_L}+E_{x_R})n_z \\ (E_{y_L}+E_{y_R})n_x - (E_{x_L}+E_{x_R})n_y + \gamma^2(\Psi_L+\Psi_R)n_z \\ \hline \chi^2c^2(\Phi_L+\Phi_R)n_x - c^2(B_{z_L}+B_{z_R})n_y + c^2(B_{y_L}+B_{y_R})n_z \\ c^2(B_{z_L}+B_{z_R})n_x + \chi^2c^2(\Phi_L+\Phi_R)n_y - c^2(B_{x_L}+B_{x_R})n_z \\ -c^2(B_{y_L}+B_{y_R})n_x + c^2(B_{x_L}+B_{x_R})n_y + \chi^2c^2(\Phi_L+\Phi_R)n_z \\ \hline c^2(B_{x_L}+B_{x_R})n_x + c^2(B_{y_L}+B_{y_R})n_y + c^2(B_{z_L}+B_{z_R})n_z \\ (E_{x_L}+E_{x_R})n_x + (E_{y_L}+E_{y_R})n_y + (E_{z_L}+E_{z_R})n_z \end{array}\right) \underbrace{- \frac{1}{2}\left(\begin{array}{c} c(Bx_R-Bx_L)+c(\gamma-1)[(\vec{B}_R-\vec{B}_L)\cdot\vec{n}]n_x \\ c(By_R-By_L)+c(\gamma-1)[(\vec{B}_R-\vec{B}_L)\cdot\vec{n}]n_y \\ c(Bz_R-Bz_L)+c(\gamma-1)[(\vec{B}_R-\vec{B}_L)\cdot\vec{n}]n_z \\ \hline c(Ex_R-Ex_L)+c(\chi-1)[(\vec{E}_R-\vec{E}_L)\cdot\vec{n}]n_x \\ c(Ey_R-Ey_L)+c(\chi-1)[(\vec{E}_R-\vec{E}_L)\cdot\vec{n}]n_y \\ c(Ez_R-Ez_L)+c(\chi-1)[(\vec{E}_R-\vec{E}_L)\cdot\vec{n}]n_z \\ \hline \gamma c(\Psi_R-\Psi_L) \\ \chi c(\Phi_R-\Phi_L) \end{array}\right)}_{\mathscr{D}(\mathbf{U}_L,\mathbf{U}_R,\vec{n})} \tag{4.20}$$

The first vector is a central difference discretization of the flux, whereas the second term represents the numerical dissipation, denoted as $\mathscr{D}(\mathbf{U}_L,\mathbf{U}_R,\vec{n})$.

In order to illustrate how the numerical dissipation affects the finite volume discretization of the Maxwell's equations, we define $\Delta\vec{B} = \vec{B}_R - \vec{B}_L$, $\Delta\vec{E} = \vec{E}_R - \vec{E}_L$, $\Delta\Psi = \Psi_R - \Psi_L$, and $\Delta\Phi = \Phi_R - \Phi_L$. We also define the distance between the centroids of the left and the right cell as $\Delta l = |\vec{r}_i - \vec{r}_j|$. We rearrange the terms of the magnetic and electric field into the component perpendicular to the face $|\partial\Omega_{ij}|$, i.e., $\Delta\vec{B}_\perp = (\Delta\vec{B}\cdot\vec{n}_{ij})\vec{n}_{ij}$, and the parallel one, $\Delta\vec{B}_\parallel = \Delta\vec{B} - (\Delta\vec{B}\cdot\vec{n}_{ij})\vec{n}_{ij}$.

With these definitions, we can write the numerical dissipation, $\mathscr{D}(\mathbf{U}_L,\mathbf{U}_R,\vec{n})$ in a more compact way:

$$\mathscr{D}(\mathbf{U}_L,\mathbf{U}_R,\vec{n}) = \frac{1}{2}\left(\begin{array}{c} c\Delta l\left(\frac{\Delta\vec{B}_\parallel}{\Delta l} + \gamma\frac{\Delta\vec{B}_\perp}{\Delta l}\right) \\ \hline c\Delta l\left(\frac{\Delta\vec{E}_\parallel}{\Delta l} + c\chi\frac{\Delta\vec{E}_\perp}{\Delta l}\right) \\ \hline \gamma c\Delta l\frac{\Delta\Psi}{\Delta l} \\ \chi c\Delta l\frac{\Delta\Phi}{\Delta l} \end{array}\right). \tag{4.21}$$

The equivalent integral equation including the numerical diffusion is:

$$\frac{d}{dt}\int_{\Omega_i}\begin{pmatrix}\vec{B}\\ \vec{E}\\ \hline \Psi\\ \Phi\end{pmatrix}d\Omega+\oint_{\partial\Omega_i}\begin{pmatrix}\bar{\bar{I}}\times\vec{E}+\gamma^2\Psi\bar{\bar{I}}\\ -c^2\bar{\bar{I}}\times\vec{B}+(\chi c)^2\Psi\bar{\bar{I}}\\ \hline c^2\vec{B}^T\\ \vec{E}^T\end{pmatrix}\cdot\vec{n}\;d\Sigma$$
$$+\oint_{\partial\Omega_i}\begin{pmatrix}c\frac{\Delta l}{2}\left(\vec{\nabla}\vec{B}_{\parallel}+\gamma\vec{\nabla}\vec{B}_{\perp}\right)\\ c\frac{\Delta l}{2}\left(\vec{\nabla}\vec{E}_{\parallel}+\chi\vec{\nabla}\vec{E}_{\perp}\right)\\ \hline \gamma c\frac{\Delta l}{2}\vec{\nabla}\Psi\\ \chi c\frac{\Delta l}{2}\vec{\nabla}\Phi\end{pmatrix}\cdot\vec{n}\;d\Sigma=\int_{\Omega_i}\begin{pmatrix}0\\ -\frac{\vec{j}}{\epsilon_0}\\ \hline 0\\ \frac{\rho_c}{\epsilon_0}\end{pmatrix}d\Omega. \quad (4.22)$$

In the previous equation one can note that the system tends asymptotically to the Eq. (4.6) as the grid size tends to zero, i.e., $\Delta l \to 0$. However, as the numerical dissipation scales as $c\Delta l$ for all the equations, it might be much larger than the rest of the terms since the speed of light is very large compared to the characteristic speeds of the fluids. An overdissipative method results in an important loss of accuracy of the numerical scheme. In the following subsections, we propose a solution to this problem by scaling the dissipation matrix in Eq. (4.16) with a proper value that is based on the coupled fluid-electromagnetic field physics. We propose two versions of the scheme that depend on the particularities of the multi-fluid model: (1) Numerical flux function in the charge neutrality limit for ideal/resistive MHD model, and the reactive and collisional ion-neutral model, (2) Numerical flux function with charge separation for the ideal electron-ion two-fluid model.

4.5.1 Scaling of the numerical dissipation with the charge-neutrality assumption

As mentioned by MacCormack [146], the numerical dissipation of the original CIR scheme is out of balance for a MHD problem. In MHD, the current usually follows Ohm's law: $\vec{j}=\sigma(\vec{E}+\vec{u}\times\vec{B})$. In those cases, the displacement current is very small and the characteristic electric field would be of the order of magnitude $\mathcal{O}(E_c)=\mathcal{O}(u_cB_c)$, where B_c and u_c are the characteristic magnetic field and velocity of the fluid, respectively. However, one can see that the numerical dissipation term of the Faraday's law, equation (4.1) is of the order $\mathcal{O}(cB_c)$ whereas the flux is: $\mathcal{O}(u_cB_c)$. Therefore, the numerical dissipation compared to the flux is $\mathcal{O}(c/u_c)$, i.e., too large.

On the other hand, the numerical dissipation of the Ampere's law, equation (4.2), is $\mathcal{O}(cE_c) = \mathcal{O}(u_c c B_c)$, whereas the terms of the flux are $\mathcal{O}(c^2 B_c)$. In this case, the numerical dissipation compared to the flux is $\mathcal{O}(u_c/c)$, i.e., too low.

Similarly, in the equation for the Lagrange multipliers Ψ and Φ, i.e., equations (4.3) and (4.4) the numerical dissipation is unbalanced. One can deduce that the Lagrange multiplier $\mathcal{O}(\Psi) = \mathcal{O}(\gamma^2 E_c) = \mathcal{O}(\gamma^2 u_c B_c)$. Therefore, in equation (4.3), the numerical dissipation compared to the flux is $\mathcal{O}(\gamma^3 u_c/c)$. Since γ usually is taken to be of order unity, we can deduce that the numerical dissipation is too small in this case. Finally, in equation (4.4), knowing that $\mathcal{O}(\Phi) = \mathcal{O}(\chi^2 B_c)$ we can deduce that in this case the numerical dissipation is of $\mathcal{O}(\chi^3 c/u_c)$, therefore too large.

To solve this problem, we can scale the numerical dissipation, as it is shown in the following. We multiply the flux $\mathbf{H}(\mathbf{U})$ by the scaling matrix $\mathbf{R}$, $\mathbf{H}'(\mathbf{U}) = \mathbf{R}\mathbf{H}(\mathbf{U}) = \mathbf{A}'_n\mathbf{U}$, where

$$\mathbf{R} = \left[\begin{array}{ccc|ccc|cc} r^2 & 0 & 0 & 0 & 0 & 0 & 0 & 0 \\ 0 & r^2 & 0 & 0 & 0 & 0 & 0 & 0 \\ 0 & 0 & r^2 & 0 & 0 & 0 & 0 & 0 \\ \hline 0 & 0 & 0 & s^2 & 0 & 0 & 0 & 0 \\ 0 & 0 & 0 & 0 & s^2 & 0 & 0 & 0 \\ 0 & 0 & 0 & 0 & 0 & s^2 & 0 & 0 \\ \hline 0 & 0 & 0 & 0 & 0 & 0 & s^2 & 0 \\ 0 & 0 & 0 & 0 & 0 & 0 & 0 & r^2 \end{array}\right] \tag{4.23}$$

We apply the CIR method to the scaled flux $\mathbf{H}'$, obtaining the numerical flux function $\mathscr{H}'$. Following the procedure described in MacCormack [146], we choose $r = \sqrt{c}$ and $s = \frac{1}{\sqrt{c}}$, so $\mathbf{A}_n$ and $\mathbf{A}'_n$ have the same eigenvalues. The flux function with scaled diffusion is obtained, $\mathscr{H}^{mod-CIR} = \mathbf{R}^{-1}\mathscr{H}'$. We obtain:

$$\mathscr{H}^{mod}(\mathbf{U}_L, \mathbf{U}_R, \vec{n}) = \frac{1}{2}\begin{pmatrix} \gamma^2(\Psi_L+\Psi_R)n_x + (E_{z_L}+E_{z_R})n_y - (E_{y_L}+E_{y_R})n_z \\ -(E_{z_L}+E_{z_R})n_x + \gamma^2(\Psi_L+\Psi_R)n_y + (E_{x_L}+E_{x_R})n_z \\ (E_{y_L}+E_{y_R})n_x - (E_{x_L}+E_{x_R})n_y + \gamma^2(\Psi_L+\Psi_R)n_z \\ \hline \chi^2c^2(\Phi_L+\Phi_R)n_x - c^2(B_{z_L}+B_{z_R})n_y + c^2(B_{y_L}+B_{y_R})n_z \\ c^2(B_{z_L}+B_{z_R})n_x + \chi^2c^2(\Phi_L+\Phi_R)n_y - c^2(B_{x_L}+B_{x_R})n_z \\ -c^2(B_{y_L}+B_{y_R})n_x + c^2(B_{x_L}+B_{x_R})n_y + \chi^2c^2(\Phi_L+\Phi_R)n_z \\ \hline c^2(B_{x_L}+B_{x_R})n_x + c^2(B_{y_L}+B_{y_R})n_y + c^2(B_{z_L}+B_{z_R})n_z \\ (E_{x_L}+E_{x_R})n_x + (E_{y_L}+E_{y_R})n_y + (E_{z_L}+E_{z_R})n_z \end{pmatrix}$$
$$- \frac{1}{2}\begin{pmatrix} (Bx_R - Bx_L) + (\gamma-1)[(\vec{B}_R - \vec{B}_L)\cdot\vec{n}]n_x \\ (By_R - By_L) + (\gamma-1)[(\vec{B}_R - \vec{B}_L)\cdot\vec{n}]n_y \\ (Bz_R - Bz_L) + (\gamma-1)[(\vec{B}_R - \vec{B}_L)\cdot\vec{n}]n_z \\ \hline c^2(Ex_R - Ex_L) + c^2(\chi-1)[(\vec{E}_R - \vec{E}_L)\cdot\vec{n}]n_x \\ c^2(Ey_R - Ey_L) + c^2(\chi-1)[(\vec{E}_R - \vec{E}_L)\cdot\vec{n}]n_y \\ c^2(Ez_R - Ez_L) + c^2(\chi-1)[(\vec{E}_R - \vec{E}_L)\cdot\vec{n}]n_z \\ \hline \gamma c^2(\Psi_R - \Psi_L) \\ \chi(\Phi_R - \Phi_L) \end{pmatrix}. \quad (4.24)$$

One can see that the new dissipation which has been introduced numerically is balanced with the terms of the flux of Maxwell's equations, as follows:

$$\frac{d}{dt}\int_{\Omega_i}\begin{pmatrix} \vec{B} \\ \vec{E} \\ \hline \Psi \\ \Phi \end{pmatrix} d\Omega + \oint_{\partial\Omega_i}\begin{pmatrix} \bar{\bar{I}}\times\vec{E} + \gamma^2\Psi\bar{\bar{I}} \\ -c^2\bar{\bar{I}}\times\vec{B} + (\chi c)^2\Psi\bar{\bar{I}} \\ \hline c^2\vec{B}^T \\ \vec{E}^T \end{pmatrix}\cdot\vec{n}\, d\Sigma$$
$$+ \oint_{\partial\Omega_i}\begin{pmatrix} \frac{\Delta l}{2}(\nabla\vec{B}_{\parallel} + \gamma\nabla\vec{B}_{\perp}) \\ \frac{c^2\frac{\Delta l}{2}(\nabla\vec{E}_{\parallel} + \chi\nabla\vec{E}_{\perp})}{\gamma c^2\frac{\Delta l}{2}\nabla\Psi} \\ \chi\frac{\Delta l}{2}\nabla\Phi \end{pmatrix}\cdot\vec{n}\, d\Sigma = \int_{\Omega_i}\begin{pmatrix} 0 \\ -\frac{\vec{j}}{\epsilon_0} \\ \hline 0 \\ \frac{\rho_c}{\epsilon_0} \end{pmatrix} d\Omega. \quad (4.25)$$

The numerical scheme $\mathscr{H}^{mod}(\mathbf{U}_L, \mathbf{U}_R, \vec{n})$ presented in equation (4.24), is a novel formulation of the 3D FV solver for the Maxwell's equations on unstructured meshes presented in Munz et al. [121], with scaled numerical dissipation for plasma simulations using HDC. The method proposed in MacCormack [146] has been generalized for unstructured meshes and extended to incorporate the HDC approach.

4.5.2 Scaling of the numerical dissipation with charge separation in the ideal two-fluid plasma model

For the ideal electron-ion model, we base the rescaling of the numerical dissipation matrix on the linear wave structure that was presented in Section

2.4.2. As discussed in that section, the symmetry between the magnetic and electric field waves that is present in the MHD limit, disappears in the ideal two-fluid plasma model. For large scales, the magnetic field waves follow the MHD limit, while the electric field follows the plasma waves and the upper and lower cutt-off frequencies. Owing to that reason, the numerical dissipation of the electric and magnetic field are designed to be different.

The characteristic speed defined by the first two terms of Eq. (4.2) is the speed of light, since the displacement current is responsible for the electromagnetic waves. Here, the order of the numerical dissipation $|\mathbf{A}_n|^E$ is balanced with the flux terms of this equation. Similarly, the hyperbolic divergence cleaning variables are designed to correct the errors in the divergence constraints by introducing waves at speeds γc and χc [121] and consequently the numerical dissipation $|\mathbf{A}_n|^{HDC}$ is balanced accordingly.

Due to the asymmetry between the scales of magnetic and electric fields mentioned above, we must propose a better scaling for the numerical diffusion of the induction equation. To accomplish this we analyze the scales of the two terms in Eq. (4.1): The smallest spatial variations of the electric field, which are produced by the plasma waves are in the scale of the Debye length, i.e., $l_c \sim \mathcal{O}(r_D)$. In the two-fluid plasma model quasi-neutrality is not imposed and charge separation is one of the main drivers for the creation of electric fields present in the model. On the other hand, the time variation in the magnetic field is in the MHD scales. Therefore, we can take $t_c \sim \mathcal{O}(\tau_A)$, with the Alfvén transit time defined as $\tau_A = l_0/v_A$. The length and time scales of Faraday's law define the characteristic velocity $v_c = l_c/t_c \sim O(r_D v_A/l_0)$, which is, in general, much smaller than the speed of light used in other methods.

Thus, the modified matrix for the Faraday's law numerical dissipation is:

$$|\mathbf{A}_n|^B = \hat{r}_D^* v_A \mathbf{D}^B \tag{4.26}$$

where $\hat{r}_D^* = \max(r_D/l_0, \Delta x/l_0)$. As the Debye length can be much smaller than the size of the mesh, an effective scale of the variations of the electric field is applied in the previous equation. The coefficients in Eq. (4.26) are chosen to be constant in all the domain, i.e., the value of $\hat{r}_D^*$ and v_A are set to characteristic values in the simulation. By doing this, we keep the linearity of the equations and we find this to be beneficial to the convergence of the method.

The numerical flux function with this modification reads:

$$\mathscr{H}^{mod}(\mathbf{U}_L,\mathbf{U}_R,\vec{n}) = \frac{1}{2}\begin{pmatrix} \gamma^2(\Psi_L+\Psi_R)n_x + (E_{z_L}+E_{z_R})n_y - (E_{y_L}+E_{y_R})n_z \\ -(E_{z_L}+E_{z_R})n_x + \gamma^2(\Psi_L+\Psi_R)n_y + (E_{x_L}+E_{x_R})n_z \\ (E_{y_L}+E_{y_R})n_x - (E_{x_L}+E_{x_R})n_y + \gamma^2(\Psi_L+\Psi_R)n_z \\ \hline \chi^2c^2(\Phi_L+\Phi_R)n_x - c^2(B_{z_L}+B_{z_R})n_y + c^2(B_{y_L}+B_{y_R})n_z \\ c^2(B_{z_L}+B_{z_R})n_x + \chi^2c^2(\Phi_L+\Phi_R)n_y - c^2(B_{x_L}+B_{x_R})n_z \\ -c^2(B_{y_L}+B_{y_R})n_x + c^2(B_{x_L}+B_{x_R})n_y + \chi^2c^2(\Phi_L+\Phi_R)n_z \\ \hline c^2(B_{x_L}+B_{x_R})n_x + c^2(B_{y_L}+B_{y_R})n_y + c^2(B_{z_L}+B_{z_R})n_z \\ (E_{x_L}+E_{x_R})n_x + (E_{y_L}+E_{y_R})n_y + (E_{z_L}+E_{z_R})n_z \end{pmatrix} - \frac{1}{2}\begin{pmatrix} \hat{r}^*_D v_A(Bx_R - Bx_L) + (\gamma-1)[(\vec{B}_R-\vec{B}_L)\cdot\vec{n}]n_x \\ \hat{r}^*_D v_A(By_R - By_L) + (\gamma-1)[(\vec{B}_R-\vec{B}_L)\cdot\vec{n}]n_y \\ \hat{r}^*_D v_A(Bz_R - Bz_L) + (\gamma-1)[(\vec{B}_R-\vec{B}_L)\cdot\vec{n}]n_z \\ \hline c(Ex_R - Ex_L) + c^2(\chi-1)[(\vec{E}_R-\vec{E}_L)\cdot\vec{n}]n_x \\ c(Ey_R - Ey_L) + c^2(\chi-1)[(\vec{E}_R-\vec{E}_L)\cdot\vec{n}]n_y \\ c(Ez_R - Ez_L) + c^2(\chi-1)[(\vec{E}_R-\vec{E}_L)\cdot\vec{n}]n_z \\ \hline \gamma c(\Psi_R - \Psi_L) \\ \chi c(\Phi_R - \Phi_L) \end{pmatrix}. \quad (4.27)$$

The equivalent integral equation can be written as

$$\frac{d}{dt}\int_{\Omega_i}\begin{pmatrix} \vec{B} \\ \vec{E} \\ \hline \Psi \\ \Phi \end{pmatrix} d\Omega + \oint_{\partial\Omega_i}\begin{pmatrix} \bar{\bar{I}}\times\vec{E} + \gamma^2\Psi\bar{\bar{I}} \\ -c^2\bar{\bar{I}}\times\vec{B} + (\chi c)^2\Psi\bar{\bar{I}} \\ \hline c^2\vec{B}^T \\ \vec{E}^T \end{pmatrix}\cdot\vec{n}\, d\Sigma$$
$$+ \oint_{\partial\Omega_i}\begin{pmatrix} \hat{r}^*_D v_A\frac{\Delta l}{2}(\nabla\vec{B}_\parallel + \gamma\nabla\vec{B}_\perp) \\ c\frac{\Delta l}{2}(\nabla\vec{E}_\parallel + \chi\nabla\vec{E}_\perp) \\ \hline \gamma c\frac{\Delta l}{2}\nabla\Psi \\ \chi c\frac{\Delta l}{2}\nabla\Phi \end{pmatrix}\cdot\vec{n}\, d\Sigma = \int_{\Omega_i}\begin{pmatrix} 0 \\ -\frac{\vec{j}}{\epsilon_0} \\ \hline 0 \\ \frac{\rho_c}{\epsilon_0} \end{pmatrix} d\Omega. \quad (4.28)$$

4.6 MULTI-FLUID EXTENSION OF THE AUSM$^+$-UP SCHEME

As it was done before with the Maxwell's equations, we discretize the system of equations in Eq. (4.7) using the finite volume method. In order to discretize the inviscid flux projected into the normal, $\mathbf{H}_s$, of each of the species s, the numerical flux used in the present work is the AUSM$^+$-up scheme [122, 147, 123]. The essence of the AUSM method is to split the flux into advective and pressure flux terms, as follows:

$$\mathbf{H}_s(\mathbf{U}) = \vec{\mathbf{F}}_s^{(c)} \cdot \vec{n} = \begin{pmatrix} \rho_s \vec{u}_s \cdot \vec{n} \\ \rho_s \vec{u}_s \vec{u}_s \cdot \vec{n} + p\vec{n} \\ \rho_s H_s \vec{u}_s \cdot \vec{n} \end{pmatrix} =$$
$$\vec{u}_s \cdot \vec{n} \begin{pmatrix} \rho_s \\ \rho_s \vec{u}_s \\ \rho_s H_s \end{pmatrix} + p_s \begin{pmatrix} 0 \\ \vec{n} \\ 0 \end{pmatrix} = M_s a_s \begin{pmatrix} \rho_s \\ \rho_s \vec{u}_s \\ \rho_s H_s \end{pmatrix} + p_s \begin{pmatrix} 0 \\ \vec{n} \\ 0 \end{pmatrix}, \quad (4.29)$$

where $M_s = \vec{u}_s \cdot \vec{n}/a_s$. The AUSM scheme discretize the numerical flux for species s at the interface $|\partial\Omega_{ij}|$ as:

$$\mathbf{H}_{ij,s} = \mathbf{H}_{ij,s}^{(A)} + \mathbf{H}_{ij,s}^{(P)}, \quad (4.30)$$

where $\mathbf{H}_{ij,s}^{(A)}$ and $\mathbf{H}_{ij,s}^{(P)}$ are the upwinded advective and pressure fluxes, respectively. The former reads:

$$\mathbf{H}_{ij,s}^{(A)} = M_{1/2,s} a_{1/2,s} \begin{cases} \begin{pmatrix} \rho_s \\ \rho_s \vec{u}_s \\ \rho_s H_s \end{pmatrix}_L, & M_{1/2,s} > 0 \\ \begin{pmatrix} \rho_s \\ \rho_s \vec{u}_s \\ \rho_s H_s \end{pmatrix}_R, & \text{otherwise.} \end{cases} \quad (4.31)$$

Where $M_{1/2,s}$ and $a_{1/2,s}$ are the numerical Mach number and the numerical speed of sound at the cell interface. They can take different forms. In the present work, they are implemented as follows:

$$a_{1/2,s} = \min(\hat{a}_{L,s}, \hat{a}_{R,s}), \text{ where } \hat{a}_{L/R,s} = \left(\frac{a_{,s}^{*^2}}{\max(a_{,s}^{*^2}, u_{n,s})} \right)_{L/R}$$
$$\text{and } a_{,s}^{*^2} = \frac{2(\gamma_s - 1)}{\gamma_s + 1} H_s, \quad (4.32)$$

from Liou [124]. Where $H_s = \frac{1}{2}u_s^2 + c_{p,s}T$ and $u_{n,s} = \vec{u}_s \cdot \vec{n}$. In this work, the numerical Mach speed at the interface is evaluated as:

$$M_{1/2,s} = \mathcal{M}_{(4)}^{+}(M_{L,s}) + \mathcal{M}_{(4)}^{-}(M_{R,s}) - M_{p,s}, \quad (4.33)$$

where the function $\mathcal{M}_{(4)}^{\pm}$ is defined as:

$$\mathcal{M}^{\pm}_{(4)}(M) = \begin{cases} \mathcal{M}^{\pm}_{(1)} & \text{if } |M| \geq 1 \\ \mathcal{M}^{\pm}_{(2)}(1 \mp 16\beta\mathcal{M}^{\mp}_{(2)}) & \text{otherwise,} \end{cases} \tag{4.34}$$

with

$$\mathcal{M}^{\pm}_{(1)}(M) = \frac{1}{2}(M \pm |M|), \text{ and } \mathcal{M}^{\pm}_{(2)}(M) = \pm\frac{1}{4}(M \pm 1)^2. \tag{4.35}$$

The parameter β can be modified as a matter of choice, but it was set to the recommended default value $\beta = 1/8$ in all our simulations. The discussion of the influence of this parameter is omitted herein, but it can be found in Liou [122]. The term $M_{p_{,s}}$ is the pressure diffusion term that is introduced in order to enhance the behavior of the numerical scheme at low Mach number. It is defined in Liou [124] as:

$$M_{p_{,s}} = \frac{K_p}{f_{a_{,s}}}\max(1 - \sigma\bar{M_{,s}}^2, 0)\frac{p_{R_{,s}} - p_{L_{,s}}}{\rho_{1/2_{,s}} a^2_{1/2_{,s}}}, \tag{4.36}$$

where

$$\rho_{1/2_{,s}} = \tfrac{\rho_{R,s}-\rho_{L,s}}{2},\ f_{a_{,s}} = M_{o_{,s}}(2 - M_{o_{,s}})$$

$$M_o^2 = \min(1, \max(\bar{M}^2_{,s}, M_{\infty_{,s}})),\ \bar{M}^2_{,s} = \tfrac{(u^2_{n_{L,s}} + u^2_{n_{R,s}})}{2a^2_{1/2_{,s}}},\ M_{L/R_{,s}} = \tfrac{u_{n_{L/R,s}}}{a_{1/2_{,s}}}, \tag{4.37}$$

where $u_{n_{,s}} = \vec{u}_s \cdot \vec{n}$. The parameters K_p, σ and $M_{\infty_{,s}}$ should be chosen and specified in the input file. The values should satisfy the following conditions, $0 \leq K_p \leq 1$, $\sigma \leq 1$. They are used to control the discretization in regions of low speed flow, when the local Mach number is $M^2 \leq 1/\sigma$, for greater Mach numbers, they have no influence.

The numerical pressure flux of the species s at the interface ij is calculated as suggested in Liou [124]:

$$\mathbf{H}^{(P)}_{ij_{,s}} = p_{1/2_{,s}} \begin{pmatrix} 0 \\ \vec{n}_{ij} \\ 0 \end{pmatrix}, \tag{4.38}$$

where $p_{1/2_{,s}}$ is the numerical flux that can be discretized as:

$$p_{1/2_{,s}} = \mathcal{P}^{+}_{(5)}(M_{L,s}) + \mathcal{P}^{-}_{(5)}(M_{R,s}) - p_{u,s}, \tag{4.39}$$

where $p_{u_{,s}}$ is the so-called velocity diffusion, defined as:

$$p_{u_{,s}} = -K_u \mathcal{P}^{+}_{(5)}(M_{L,s}) \mathcal{P}^{-}_{(5)}(M_{R,s})(\rho_{L,s} + \rho_{R,s}) a_{1/2_{,s}} (u_{R,s} - u_{L,s}), \quad (4.40)$$

and

$$\mathcal{P}^{\pm}_{(5)}(M) = \begin{cases} \frac{1}{M}\mathcal{M}^{\pm}_{(1)} & \text{if } |M| \geq 1 \\ \mathcal{M}^{\pm}_{(2)}[(\pm 2 - M) \mp 16\alpha M \mathcal{M}^{\mp}_{(2)}] & \text{otherwise} \end{cases} \quad (4.41)$$

with

$$\alpha = \frac{3}{16}(5 f^2_{a_{,s}} - 4), \quad (4.42)$$

the coefficient f_a was previously defined in the equation (4.37). The coefficient K_u can be chosen in the simulation in order to control the numerical dissipation, always satisfying the condition: $0 \leq K_u \leq 1$. In this work, the results are obtained with the following coefficients, $K_p = 0.25$, $K_u = 0.75$, and $\sigma = 1$.

4.7 DISCRETIZATION OF DIFFUSIVE FLUXES AND SOURCE TERMS

The discretization of diffusive fluxes $\mathbf{G}_{ij}$ in Eq. 4.9 is based on a deferred correction approach [148] for the calculation of gradients of the relevant variables (e.g. velocity, temperature). At a cell face with outward normal $\vec{n}$, the gradient of some variable w can be written as:

$$\nabla w = (\nabla w \cdot \vec{n})\vec{n} + (\nabla w - (\nabla w \cdot \vec{n})\vec{n})). \quad (4.43)$$

Following this relation, if we indicate with $\vec{e}$ the unit vector of edge joining the cell centers on both sides L and R of the considered face and d_{LR} their distance, the gradient at the interface can be computed as:

$$(\nabla w)^{LR} = \frac{w^R - w^L}{d_{LR}}(\vec{e} \cdot \vec{n})\vec{n} + \frac{1}{2}(\mathbf{I} - \vec{n} \otimes \vec{n}) \left((\nabla w)^L + (\nabla w)^R \right), \quad (4.44)$$

where $(\nabla w)^{L,R}$ are the weighted least squares gradients computed at the left and right cell-centers, already used for the solution reconstruction described in Section 4.4. This method is particularly efficient since it does not require

the integration on some locally defined control volumes, while reusing pre-computed gradients. Moreover, it is known to preserve accuracy in meshes with high-aspect-ratio cells, as needed in our case. As far as source terms are concerned, they are evaluated pointwise at the cell centers.

4.8 IMPLICIT TIME INTEGRATION STRATEGY

The system of discretized equations shown in (4.9) can be re-written as follows:

$$\mathbf{S}(\mathbf{P}) = \frac{d\mathbf{U}(\mathbf{P})}{dt} + \mathbf{R}(\mathbf{P}) = \mathbf{0}, \tag{4.45}$$

where $\mathbf{S}(\mathbf{P})$ is the pseudo-steady residual array and includes the full space-time discretization, $\mathbf{U}$ are the conservative variables, $\mathbf{P}$ are the actual variables used to store/update the solution that in our case are chosen to be $\mathbf{P} = (\vec{B} \;\; \vec{E} \;\; \Psi \;\; \Phi \;\; \rho_s \;\; \vec{u}_s \;\; T_s)^T$, $\mathbf{R}(\mathbf{P})$ is the residual array resulting from the spatial discretization. The choice of the different time integrator defines the actual discretized expression for $\frac{d\mathbf{U}(\mathbf{P})}{dt}$. In this work, we use one- and three-point Backward Euler schemes for steady and unsteady cases, respectively. In the following discussion, we will only focus on the three-point Backward Euler scheme, which reads:

$$\mathbf{S}(\tilde{\mathbf{P}}) = \frac{3\mathbf{U}(\tilde{\mathbf{P}}) - 4\mathbf{U}(\mathbf{P}^n) + \mathbf{U}(\mathbf{P}^{n-1})}{2\Delta t} + \mathbf{R}(\tilde{\mathbf{P}}), \tag{4.46}$$

where $\tilde{\mathbf{P}}$ is obtained through an iterative process using the Newton method. The pseudo-steady residuals are linearized using Taylor expansion around $\mathbf{P}^k$, as follows:

$$\mathbf{S}(\mathbf{P}^{k+1}) = \mathbf{S}(\mathbf{P}^k) + \frac{\partial \mathbf{S}(\mathbf{P}^k)}{\partial \mathbf{P}} \Delta \mathbf{P}^k = \mathbf{0}, \tag{4.47}$$

where $\mathbf{P}^{k+1} = \mathbf{P}^k + \Delta \mathbf{P}^k$ and the Jacobian matrix of the pseudo-steady residuals with respect to the array of solution variables is given by:

$$\frac{\partial \mathbf{S}}{\partial \mathbf{P}} = \frac{3}{2\Delta t} \frac{\partial \mathbf{U}}{\partial \mathbf{P}} + \frac{\partial \mathbf{R}}{\partial \mathbf{P}}. \tag{4.48}$$

In our implementation, the linear variable transformation matrix $\frac{\partial \mathbf{U}}{\partial \mathbf{P}}$ can be computed analytically while the spatial residual jacobian $\frac{\partial \mathbf{R}}{\partial \mathbf{P}}$ is calculated numerically, by means of one-sided finite differentiation and using only the

face neighbors as stencil (despite involving all cell-vertex neighbors in the solution reconstruction to compute the residual $\mathbf{R}$). The Newton method is applied starting at the solution of the previous time-step, i.e., $\mathbf{P}^0 = \mathbf{P}^n$, leading to solve the following linear system:

$$\frac{\partial \mathbf{S}(\mathbf{P}^k)}{\partial \mathbf{P}}(\mathbf{P}^{k+1} - \mathbf{P}^k) = -\mathbf{S}(\mathbf{P}^k), \tag{4.49}$$

until convergence is reached (i.e., $||\Delta \mathbf{P}^k|| < \epsilon$) at each time step. Note that in this work, that the L_1 norm considering all the variables is used for $||\Delta \mathbf{P}^k||$ in the convergence criterium. After the iterative process, the value of the last solution of the Newton method is assigned to the solution at the new time-step, i.e., $\mathbf{P}^{n+1} = \mathbf{P}^{k+1}$. In steady simulations, since time accuracy is not a concern, only one Newton subiteration is run. The linear system in Eq. (4.49) is solved by the GMRES algorithm complemented with the parallel ASM preconditioner provided by the PETSc library [149].

Time discretization of the divergence cleaning equations

In order to correctly handle the divergence cleaning method in unsteady simulations, we use the method explained in Yalim et al. [139], extending it from ideal MHD to full Maxwell's equations. The method proposes to converge the equations of the evolution of the Lagrange multipliers, i.e., Eqs. (2.34) and (2.22), to steady state at each time step. Therefore, for these equations we solve a pure Newton iteration procedure.

$$\mathbf{S}_{\Psi,\Phi}(\tilde{\mathbf{P}}) = \mathbf{R}_{\Psi,\Phi}(\tilde{\mathbf{P}}), \tag{4.50}$$

where $\mathbf{S}_{\Psi,\Phi}$ and $\mathbf{R}_{\Psi,\Phi}$ are respectively the array of unsteady residuals and the array of residuals from the spatial discretization of the equations for the Lagrangian multipliers, i.e., (2.34) and (2.22). This is equivalent to removing the time derivative ($\Delta t = \infty$) of Eqs. (2.34) and (2.22), resulting in an elliptic correction as explained in Dedner et al. [150]. However, with this method, the system continues being hyperbolic, having γc and χc as eigenvalues, which is important for the upwind hyperbolic finite volume method. Using this method, the solenoidal constraint will be satisfied at each time step up to machine accuracy, but without solving a computationally costly Poisson equation as done in classical projection schemes [151].

4.9 SUMMARY

In this chapter, we presented a finite volume method coupling the Maxwell's equations to multi-fluid equations including chemical reactions, collisional effects and anisotropic transport fluxes. In order to fulfill the divergence constraints for magnetic and electric fields contained in Maxwell's equations, we use the HDC method. A new numerical approach extending previous work [121, 146, 152] is proposed for the purely hyperbolic form of the Maxwell's equations, rescaling the numerical dissipation of the spatial discretization in order to have it in balance when the dominant time scales are imposed by the flow motions. Two different approaches are proposed for the limit when the charge neutrality is assumed and when charge separation between ions and electrons is not enforced. For the multi-fluid dynamics equations, the AUSM$^+$-up method is extended to multi-fluid equations. Implicit time discretization is used in order to deal with the stiffness of the system resulting of coupling Maxwell's equations to the multi-fluid equations. Second order reconstruction is used together with Venkatakrishnan's limiter with the correction for smooth flow regions.

CHAPTER 5

Verification of the Finite Volume Method

The simple sailors of today have learned the opposite of the opinion of the philosophers by true experience.

– *Jacques Cartier*

This chapter summarizes the verification of the numerical method previously presented. The method is benchmarked in a number of plasma ranges: ideal MHD, resistive MHD, partially-ionized reacting and collisional ion-neutral model, and fully-ionized ideal ion-electron model. The accuracy in space of the numerical method is assessed in two scenarios, an ideal MHD case that assumes charge neutrality and a two-fluid ion-electron case. The method for plasmas in the charge neutrality limit is verified on the Hartmann flow (including comparison with its analytical solution), two ideal MHD cases with strong shocks, namely, Orszag-Tang and the MHD rotor, and a two-fluid magnetic reconnection under solar chromospheric conditions. For the latter, a comparison with pioneering results available in literature is provided. For the ideal electron-ion model, the two-fluid Briu-Wu shock tube is simulated for different non-dimensional ion gyroradius. Similarly, the magnetic reconnection under magnetotail conditions is reproduced and compared to other plasma models.

Part of this chapter has been published in:

1. A. Alvarez Laguna, A. Lani, H. Deconinck, N. N. Mansour, and S. Poedts, **A fully-implicit finite-volume method for multi-fluid reactive and collisional magnetized plasmas on unstructured meshes**, *Journal of Computational Physics, 318, pp. 252-276, 2016.*
2. A. Alvarez Laguna, N. Ozak, A. Lani, H. Deconinck, and S. Poedts, **Fully-implicit finite volume method for the ideal two-fluid plasma model**, *Computational Physics Communications, under review, 2017.*

5.1 ACCURACY ANALYSIS

The numerical solver here presented uses the second-order reconstruction algorithm described in Section 4.4. The same reconstruction scheme, which is rather standard for unstructured FV solvers, has been previously verified also for ideal multi-dimensional MHD cases [139, 140]. Firstly, The multi-fluid solver that considers charge neutrality is verified with the study of a magnetized isodensity vortex in two dimensions, as proposed in [153, 154, 155, 156, 157]. The test reproduces the evolution of a magnetized vortex in a perfectly conducting flow that advects the vortex diagonally to the domain. Secondly, the method for the ideal two-fluid plasma model without the charge-neutrality assumption is assessed with the propagating circularly polarized Alfvén wave test.

5.1.1 Accuracy analysis of the model with the charge-neutrality assumption

We solve the multi-fluid equations (2.13)-(2.15) for one fluid in ideal conditions, i.e., without chemical reaction nor viscosity nor heat conduction. In order to couple the fluid equations with full Maxwell's system, we consider Ohm's law with large conductivity since we want to reproduce an ideal MHD case. Note that the multi-fluid and Maxwell's equations are coupled through the source terms and therefore Ohm's law is needed. In the test presented below, the value of the conductivity has been set up to $\sigma = 1.25 \cdot 10^{14}$, in non-dimensional units. In ideal MHD cases, low values of conductivity can damage the order of the reconstruction, especially on the magnetic field variables, whereas extremely large values of conductivity result in stiff source terms that are difficult to solve by the linear system of the implicit time integrator.

The MHD iso-density vortex simulation is carried out in a two-dimensional domain of [-5, 5]×[-5, 5] size with periodic boundaries in all directions. The vortex is in dynamical balance, i.e., the magnetic pressure is balanced by the gas pressure. At the initial time, it is located in the center of the domain. The flow carries the vortex at 45° to the horizontal direction and after 10 time units it returns to the initial position. The imposed initial field reads:

$$\mathbf{P}(\vec{x}, t=0) = \begin{cases} \vec{B} = (-y, x, 0)\kappa e^{q(1-r^2)} \\ \vec{E} = (0, 0, -(x+y))\kappa\mu e^{2q(1-r^2)} \\ \Psi = 0 \\ \Phi = 0 \\ \rho = 1 \\ \vec{u} = (1,1) + (-y, x)\mu e^{q(1-r^2)} \\ T = 1 + \frac{1}{4q}\left[\mu^2(1-2qr^2) - \kappa^2\right] e^{2q(1-r^2)} \end{cases} \tag{5.1}$$

where $r = \sqrt{x^2+y^2}$. For this test, we choose the ratio of specific heats to be $\gamma = 5/3$, the parameters of the vortex $\kappa = \mu = 1/2\pi$ and $q = 1/2$. In order to assess the accuracy of the numerical scheme, we compare the solution at $t = 10$ with the analytical solution, given in Eq. 5.1. We study the L_1 and L_2 norms of the B field, E_z, u field, and the array $\mathbf{P}$ holding all the primitive variables.

Number of cells	B field		E_z component	
	L_1	Order	L_1	Order
25×25	$1.1825{\cdot}10^{-2}$		$6.9151{\cdot}10^{-3}$	
50×50	$5.1004{\cdot}10^{-3}$	1.21	$2.4076{\cdot}10^{-3}$	1.52
100×100	$1.8854{\cdot}10^{-3}$	1.44	$7.0596{\cdot}10^{-3}$	1.77
200×200	$4.7460{\cdot}10^{-4}$	1.98	$1.9339{\cdot}10^{-3}$	1.87
Number of cells	u field		Primitive variables	
	L_1	Order	L_1	Order
25×25	$1.1526{\cdot}10^{-2}$		$4.2156{\cdot}10^{-2}$	
50×50	$4.5092{\cdot}10^{-3}$	1.35	$1.7179{\cdot}10^{-2}$	1.30
100×100	$1.3289{\cdot}10^{-3}$	1.76	$5.7558{\cdot}10^{-3}$	1.58
200×200	$3.3447{\cdot}10^{-4}$	1.99	$1.4956{\cdot}10^{-3}$	1.94

Table 5.1: L_1 norm of the accuracy analysis for the 2D isodensity MHD vortex problem.

Number of cells	B field		E_z component	
	L_2	Order	L_2	Order
25×25	$1.2586{\cdot}10^{-3}$		$1.0315{\cdot}10^{-3}$	
50×50	$3.6888{\cdot}10^{-4}$	1.77	$3.0693{\cdot}10^{-4}$	1.75
100×100	$1.1195{\cdot}10^{-4}$	1.72	$9.0927{\cdot}10^{-5}$	1.76
200×200	$2.9749{\cdot}10^{-5}$	1.91	$2.4743{\cdot}10^{-5}$	1.88
Number of cells	u field		Primitive variables	
	L_2	Order	L_2	Order
25×25	$7.2229{\cdot}10^{-3}$		$2.5047{\cdot}10^{-3}$	
50×50	$2.2567{\cdot}10^{-3}$	1.68	$1.7179{\cdot}10^{-3}$	1.65
100×100	$6.1232{\cdot}10^{-4}$	1.88	$7.0464{\cdot}10^{-4}$	1.83
200×200	$1.5374{\cdot}10^{-4}$	1.99	$1.8174{\cdot}10^{-4}$	1.95

Table 5.2: L_2 norm of the accuracy analysis for the 2D isodensity MHD vortex problem.

Tables 5.1 and 5.2 show that the proposed method achieves second order accuracy on the finest mesh tested with 200×200 elements. As it can be seen, it is obtained in all variables. As mentioned in Shen et al. [156], the initial magnetic field has a small jump on the periodic boundaries. This discontinuity produces problems in the coarser meshes since the initial field is not divergence free on the boundaries. Due to this fact, the order of the magnetic field reconstruction is more affected on the coarser meshes than in the rest of variables as it can be seen in Table 5.1.

5.1.2 Accuracy analysis of the ideal two-fluid plasma model

Now, we solve for the ideal two-fluid (ion+electron) plasma model, i.e., Eqs. (2.26)-(2.35) of Section 2.4.1. A frequently used benchmark in codes is a propagating circularly polarized Alfvén wave of constant amplitude propagating along the background magnetic field B_0. We derive the analytical solution for the two-fluid plasma model. We consider the following dispersion relation for two-fluid plasma:

$$1 + \left(\frac{\omega_{pi}}{kc}\right)^2 \frac{\omega}{\omega + \Omega_i} + \left(\frac{\omega_{pe}}{kc}\right)^2 \frac{\omega}{\omega + \Omega_e} - \frac{\omega^2}{k^2 c^2} = 0 \tag{5.2}$$

From this dispersion relation we may solve for the corresponding wave frequency given our choice of wavenumber k, where Ω_s is the gyrofrequency of the species, ion or electrons, keeping in mind that Ω_e will have a negative sign

due to the negative charge dependence. We have the following eigenvectors:

$$\vec{B} = (B_0,\ \varepsilon B_0 \cos(kx - \omega t),\ \varepsilon B_0 \sin(kx - \omega t)) \tag{5.3}$$

$$\vec{u}_{i,e} = (0,\ \varepsilon V_s \cos(kx - \omega t),\ \varepsilon V_s \sin(kx - \omega t)) \tag{5.4}$$

where

$$V_s = \frac{\varepsilon \Omega_s}{\omega + \Omega_s} \frac{\omega}{k}.$$

Here, ε is the amplitude of the wave, which is chosen to be small ($\varepsilon = 0.1$) in order to prevent non-linear instabilities from forming.

For the simulations we use a rectangular computational domain with length ranging from $-L \leq x \leq L$ and height ranging from $-L/2 \leq y \leq L/2$ with periodic boundaries in all sides. We adapt the initial set-up found in [117] for our computation with a mass ratio of $m_i/m_e = 256$, $v_0/c = 1/10$, and $\beta = p_{tot} 2\mu_0 / B_0^2 = 0.1$, with both fluids initially at the same temperature. We test the grid convergence of the code, by running the simulation with grid resolution $N \times N/2$, with $N = 16, 32, 64$, and 128 for all the cases presented here. In all cases we ran the simulation for five wave periods. As commonly done in these tests, we perform simulations initially with the grid aligned such that $\vec{k}$ is parallel to the x-axis and then rotate the initial conditions by an angle $\alpha = \tan^{-1}(0.5)$ (labeled "rotated configuration" in the figures). This means that we perform a rotation such that $x' = x\cos(\alpha) + y\sin(\alpha)$.

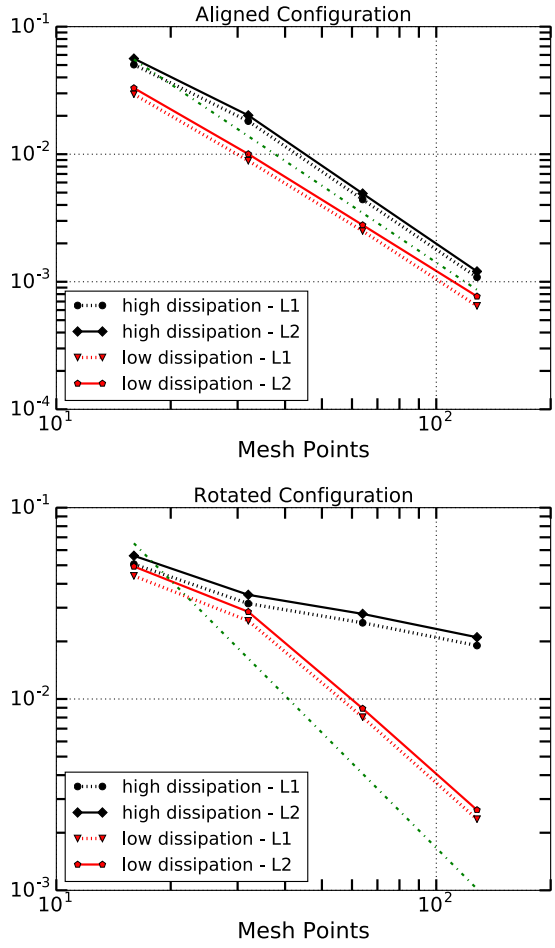

Figure 5.1: Mesh convergence of the error for L_1 error (dashed lines) and L_2 (solid lines) for traveling circularly polarized wave in a domain of size $L/\lambda = \pi$. We compare cases with high and low magnetic field dissipation after five periods. The green line shows the theoretical second-order error for comparison. We show the results for the aligned (left) and the rotated (right) mesh configurations.

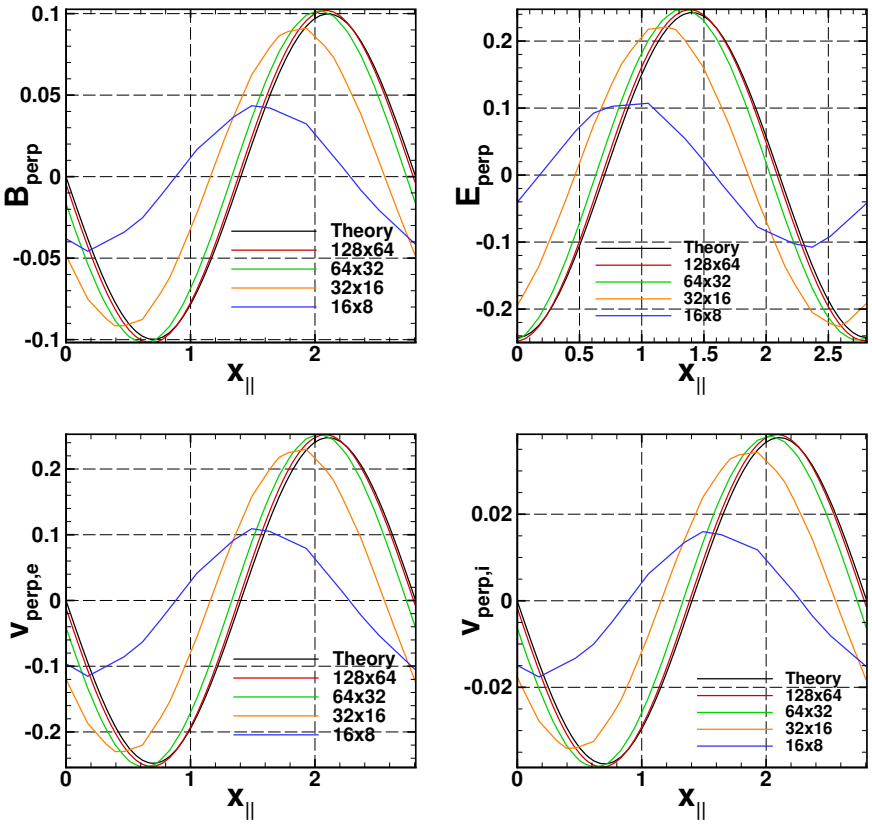

Figure 5.2: Perpendicular component of the magnetic field (top left), electric field (top right), electron velocity (bottom left), and ion velocity (bottom right) for different mesh resolutions $N \times N/2$ with $N = 128, 64, 32, and 16$. This case shows the result for a box size $L/\lambda = \pi$ for the rotated configuration after five periods.

We first run our simulation in a domain with size $L = 2\pi$ using a 'high' ($|\mathbf{A}_n|^B = c\mathbf{D}^B$) and a 'low' ($|\mathbf{A}_n|^B = 10^{-3}c\mathbf{D}^B$) value of the magnetic numerical dissipation in order to illustrate its effect in the final result. We calculate the mesh convergence for L_1 and L_2 errors in the magnetic field.

Fig. 5.1 shows the errors in this simulation as a function of the mesh size for the aligned and rotated configurations. The green line indicates the slope of a second-order solver for comparison purposes, showing that too

much dissipation reduced the order of the solver. For the case with the wave traveling in the rotated configuration the effect of the higher dissipation has larger impact, since the resolution along the diagonal is lower.

In order to test the performance of the code in different regimes relevant to the two-fluid model we continue to follow the approach of Amano [117]. As in their paper, we choose the size of our domain to be $L/\lambda_i = \pi, 2\pi$, and 10π, which corresponds to the wave numbers $k\lambda_i \approx 2.2, 1.1$, and 0.2 and frequencies $\omega \approx 5.4, 1.9$, and 0.25 obtained from the dispersion relation. We define the Courant-Friedrich-Levy number as CFL= $\Delta t c/\Delta x$, where c is the speed of light (the fastest wave of the system), Δt is the time step, and Δx is the length interval computed as $\Delta x = |\Omega_i|/\sum_{j\in\mathscr{D}_i} |\partial\Omega_{ij}|$. The CFL number is fixed in the simulations to CFL $= 1, 0.7, 0.5$ in the simulations with L/λ_i $= 10\pi, 2\pi$, and π, respectively. We run the transverse wave case, using this time the magnetic dissipation as calculated by our scheme (see Eq. (4.26)).

Fig. 5.2 shows the profiles of the perpendicular components of the magnetic field ($B_\perp$), electric field ($E_\perp$), and electron and ion velocities ($u_{\perp,e}$, $u_{\perp,i}$) for the case with the transverse wave in the box size $L/\lambda = \pi$ (corresponding to $k\lambda_i \approx 2.2$) using each of the different mesh resolutions. One can see that with the more refined grid, the solution converges close to the exact solution (shown in black, labeled "Theory") for all the cases. For this case, we have used the magnetic dissipation given by our formulation in Eq. (4.26) and the result shows that the electromagnetic dissipation chosen does not affect the resulting wave. Fig. 5.3 shows the L_2 error for the perpendicular components of the magnetic and electric fields, as well as for the electron and ion velocities for each of the wavelength cases (different box sizes) in the rotated configuration (transverse wave). We see that indeed, our scheme converges to second order accuracy in all variables and wavelengths, which gives us extra confidence in our choice of dissipation of the electromagnetic fields and the ability of the code to solve the equation system correctly.

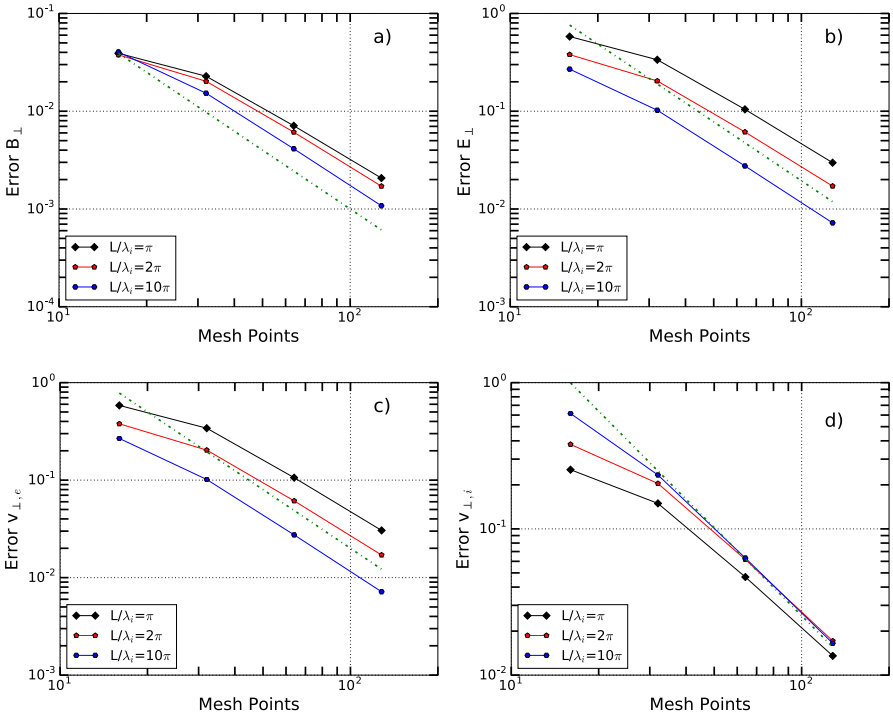

Figure 5.3: L_2 error of the perpendicular component of a) the magnetic field, b) the electric field, c) the electron velocity, and d) the ion velocity for different mesh resolutions $N \times N/2$ with $N = 128, 64, 32$, and 16. Each line represents a different wavelength obtained by changing the box size L as indicated in the label. The green dotted line represents the theoretical second-order error slope for comparison.

5.2 VERIFICATION TESTS

Firstly, the Hartmann flow is solved in order to validate coupling between the numerical method discretizing Maxwell's and the fluid equations in a resistive MHD viscous flow. Secondly, two ideal MHD cases that validate the performance of the numerical scheme in the presence of shocks, namely, the Orszag-Tang vortex and the MHD rotor. Thirdly, a case that studies the magnetic reconnection in a weakly ionized plasma in order to assess the performance of the overall numerical model in a two-fluid MHD flow considering chemical reactions, collisional terms and transport fluxes including anisotro-

pic heat flux. Fourthly, the ideal two-fluid (electron+ion) is validated for different ion gyroradius in the two-fluid version of the Brio-Wu shock tube. Finally, the ideal two-fluid model is compared to Hall-MHD, Hybrid, and PIC models in a magnetic reconnection with magnetospheric conditions.

5.2.1 Hartmann flow

The Hartmann flow [158] considers a viscous, electrically conductive fluid running between two plates separated by a distance $2L$ under an imposed constant pressure gradient. An external electromagnetic field is applied as follows: a magnetic field B_{y_0} contained in the plane of the movement that is perpendicular to the velocity of the fluid, and an electric field E_{z_0} that is perpendicular to the plane of the movement (Fig. 5.4). Due to the electromagnetic forces, the profile of the velocity changes compared to the parabolic Poiseuille flow. Moreover, due to the movement of the conducting fluid, an electric current is created, inducing a magnetic field in the x-direction. Due to symmetry considerations, half channel is simulated in a 250×40 grid. The length of the channel is chosen to be $20L$. The Hartmann number, defined as, $\mathrm{Ha} = B_{y_0} L \sqrt{\frac{\sigma}{\eta}}$, is set to $\mathrm{Ha} = 10$. The streamwise pressure gradient is imposed to $\partial p/\partial x = -7.277$ Pa/m. The mass flow rate is $\dot{m} = 3.6$ kg/s and the Mach number $M = 0.1$. The flow considered is at atmospheric pressure at $T = 288$ K. The properties of viscosity η and heat flux coefficient are those of air at this given temperature and pressure. The electrical conduction is chosen to be $\sigma = \eta(\frac{\mathrm{Ha}}{B_{y_0} L})^2$.

In order to avoid having non-divergence free initial magnetic fields, the initial electromagnetic field is set to zero, as well as the scalar potential field Ψ. Due to the geometry of the problem, the electric field is divergence free, since only the component E_z is created. Therefore, the equation for the potential Φ, controlling the errors in the fullfillment of the Gauss' law, is not solved.

The boundary conditions are subsonic inlet imposing the velocity and temperature of the flow at the LHS boundary (extrapolating pressure from inside the domain), subsonic outlet imposing the pressure at the RHS boundary, isothermal non-slip electrically insulated wall at the top boundary, symmetry condition for the flow and perfect conducting wall at the bottom boundary. Since the steady solution is studied, a first-order in time Backward Euler scheme is applied, while second-order accuracy in space is retrieved using the weighted linear least squares reconstruction of the solution as explained in Section 4.4.

The solution in terms of velocity and magnetic field in the x-direction are presented in Fig. 5.5 and Fig. 5.6 respectively. Both results are mirrored in order to represent the full channel, considering symmetry for the flow and anti-symmetry for the magnetic field with respect to the x-axis. In Fig. 5.8a, the results of normalized velocity and induced magnetic field are compared to the analytical solution showing great agreement. The profile is taken at $x/L = 10$. The solution of the velocity is normalized with the mean velocity, defined as:

$$U_0 = \left(\frac{\sigma B_{y_0} E_{z_0} - p_x}{\sigma B_{y_0}^2} \right) \left(1 - \frac{\sinh \mathrm{Ha}}{\mathrm{Ha} \cosh \mathrm{Ha}} \right). \tag{5.5}$$

The magnetic field is normalized with the characteristic value: $B_0 = -\mu_0(p_x + \sigma B_{y_0} E_{z_0})$. The simulation has converged in approximately 500 iterations using CFL $= 10^9$, as shown in Fig. 5.7b. The performance of the divergence cleaning is shown in Figs. 5.8a and 5.8b. The divergence cleaning method for Maxwell's equations with scaled numerical dissipation presented in this work, using $\chi = 1$, is able to reduce the errors in $\nabla \cdot \vec{B}$ by 4-5 orders of magnitude. The solution of the B_x component of the magnetic field shows good agreement with the analytical solution when no divergence cleaning is used. However, in the latter case, a spurious component of magnetic field B_y is created, as shown in Fig. 5.8b, while this component is completely removed when the divergence cleaning is applied. Even though the impact of the divergence cleaning on the overall solution for the Hartmann problem is relatively small, in more complex problems as the one presented in the next section, the appearance of spurious components of magnetic field can lead to completely erroneous solutions and an effective divergence cleaning method becomes mandatory.

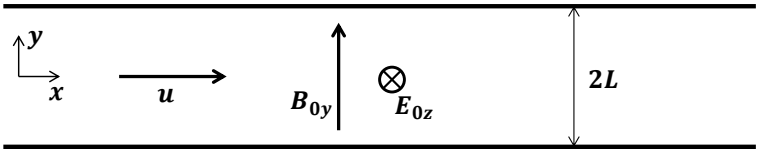

Figure 5.4: Hartmann flow.

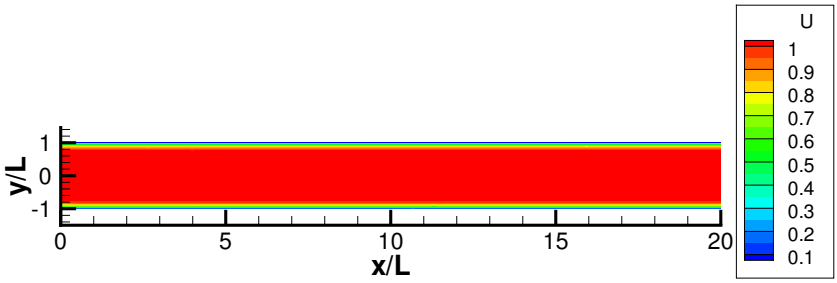

Figure 5.5: Contour plot of the normalized horizontal velocity.

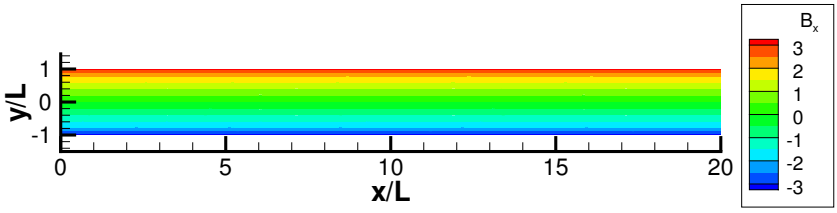

Figure 5.6: Contour plot of the normalized x-component of magnetic field.

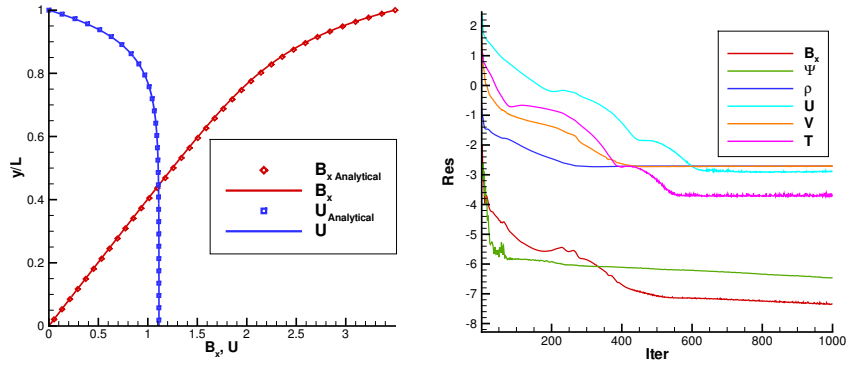

(a) **(b)**

Figure 5.7: (a) Comparison of the numerical results with the analytical solution of the Hartmann flow for the section at $x/L = 10$. (b) Convergence history of the Hartmann flow simulation

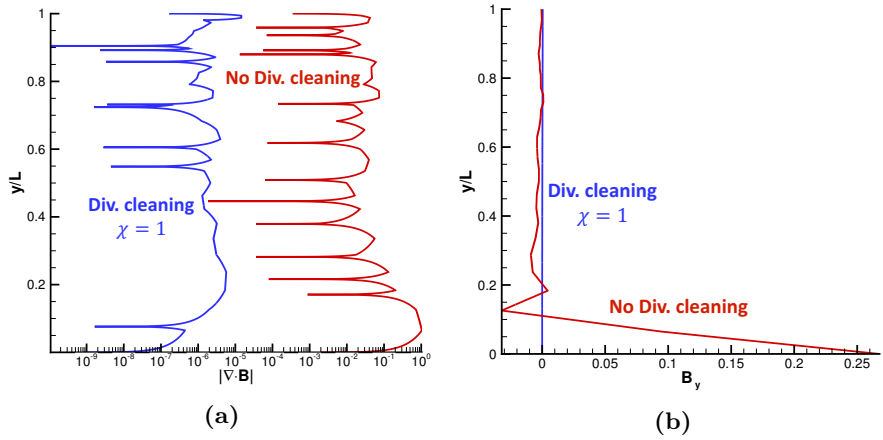

Figure 5.8: (a) Comparison of the numerical results with the analytical solution of the Hartmann flow for the section at $x/L = 10$. (b) Values of B_y with and without divergence cleaning in the Hartmann flow for the section at $x/L = 10$.

5.2.2 Orszag-Tang Vortex

The Orszag-Tang vortex [159, 160] has been computed in order to verify the ability of the proposed numerical solver to tackle MHD shocks and shock-shock interactions. This test represents a transition to 2D supersonic MHD turbulence and is widely used to validate compressible MHD solvers. The present solver is not an ideal MHD solver, therefore the system of equations solved in this test is the same as explained in Section 5.1.1, coupling full Maxwell and inviscid one-fluid equations.

The computational domain used in the present test is $[0, 2\pi] \times [0, 2\pi]$ with periodic boundary conditions in both directions. The non-dimensional initial condition reads:

$$\mathbf{P}(\vec{x}, t = 0) = \begin{cases} \vec{B} = (-\sin y, \sin 2x, 0) \\ \vec{E} = (0, 0, \sin 2x \sin y - \sin x \sin y) \\ \Psi = 0 \\ \Phi = 0 \\ \rho = \gamma^2 \\ \vec{u} = (-\sin y, \sin x) \\ T = 1/\gamma \end{cases} \tag{5.6}$$

where the reference values for the electric field and the temperature are $E_0 = u_0 B_0$ and $T_0 = u_0^2 / R_{gas}$. The specific heat ratio is taken to be $\gamma = 5/3$. The

speed of light is reduced to $c = 10^4$ and the electrical conductivity $\sigma = 10^6$, both in non-dimensional units. Note that Ohm's law is needed in order to couple the dynamics of the flow with the Maxwell's equations.

The test is run in a 200×200 grid mesh, using a time step of $\Delta t = 3 \cdot 10^{-3}$, i.e., CFL = 9.5. The simulation is undertaken until $t = 3$.

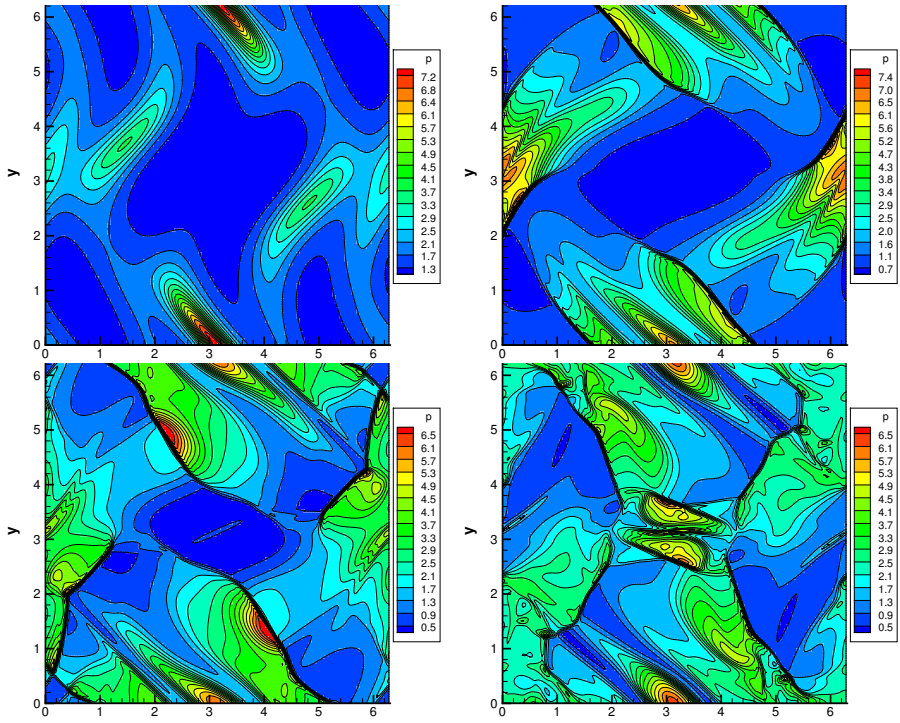

Figure 5.9: Evolution of the thermal pressure at t = 0.6, t = 1.5, t = 2.1 and t =3 on a mesh with 200×200 elements.

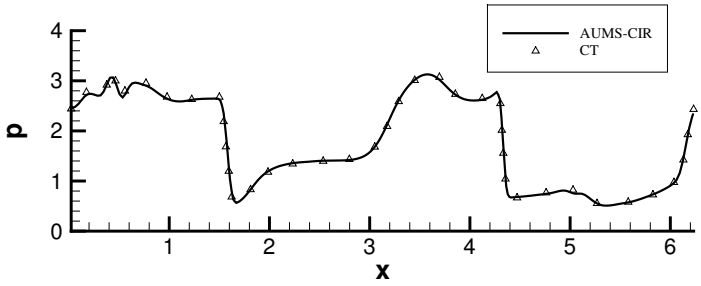

Figure 5.10: Thermal pressure at t = 3 over a line at $y = 0.625\pi$ on a mesh 200×200 compared to a constrained transport solution [7].

In Fig. 5.9, the evolution of the computed thermal pressure is shown using 16 equally-spaced contours in each snapshot. Our results are in good agreement with the reference MHD solution (e.g [139, 7, 141]). Additionally, in Fig. 5.10, the value of the thermal pressure along the line located at $y = 0.625\pi$ at time $t = 3$ shows agreement with the solution of Christlieb et al. [7], the latter using finite difference WENO with constrained transport.

5.2.3 MHD rotor

The proposed method is tested on another ideal MHD case with presence of strong shocks. The 2D MHD rotor problem [161] studies the evolution of strong torsional Alfvén waves in ideal MHD. Initially, a high-density disk spins at large velocity inside a constant pressure background with constant magnetic in the x-direction. The initial state is not in equilibrium and as the rotor spins, the magnetic field wraps up the rotating flow, exchanging angular momentum with the ambient flow through torsional Alfvén waves. The initial circular shape of the rotor changes into an oval as the magnetic pressure builds up. The computational domain is $[0, 1] \times [0, 1]$ using superfast boundary conditions in all directions. The initial field reads:

$$\mathbf{P}(\vec{x}, t=0) = \begin{cases} \vec{B} = (2.5/\sqrt{4\pi}, 0, 0) \\ \vec{E} = (0, 0, B_x u_y) \\ \Psi = 0 \\ \Phi = 0 \\ \rho = 1 + 9f(t) \\ u_x = \begin{cases} -2f(r)y/0.1, & r < 0.1 \\ -2f(r)y/r, & r \geq 0.1 \end{cases} \\ u_y = \begin{cases} 2f(r)x/0.1, & r < 0.1 \\ 2f(r)x/r, & r \geq 0.1 \end{cases} \\ T = 0.5/(1 + 9f(t)) \end{cases} \tag{5.7}$$

where

$$f(r) = \begin{cases} 1, & r < 0.1 \\ (200/3)(0.115 - r), & 0.1 \leq r \leq 0.115 \\ 0, & r > 0.115 \end{cases} \tag{5.8}$$

As in the previous case, the specific heat ratio is $\gamma = 5/3$, the speed of light is $c = 10^4$ and the electrical conductivity $\sigma = 10^6$. The structured mesh has 400×400 grid points and the time step is $t = 1.18 \cdot 10^{-3}$, i.e., CFL = 4720.

In Fig 5.11, the computed density, thermal pressure, Mach number and magnetic pressure at $t = 0.2962$ are shown. The results present 30 equally spaced contours in the ranges, $0.532 < \rho < 10.83$, $0.007 < p < 0.776$, $0 < M < 3.64$ and $0.007 < B^2/2 < 0.702$, as done in Yalim et al. [139]. The results show good agreement with the accepted solution (e.g.[139, 141]).

We would like to remark that, even though the present numerical method is not specifically designed for ideal MHD problems, it is also able to tackle these problems with large time steps despite maintaining the displacement current in Maxwell's equations. Note that the time steps used here are comparable to the ones used by implicit ideal MHD solvers. Those properties can be regarded as valuable assets of the present numerical method.

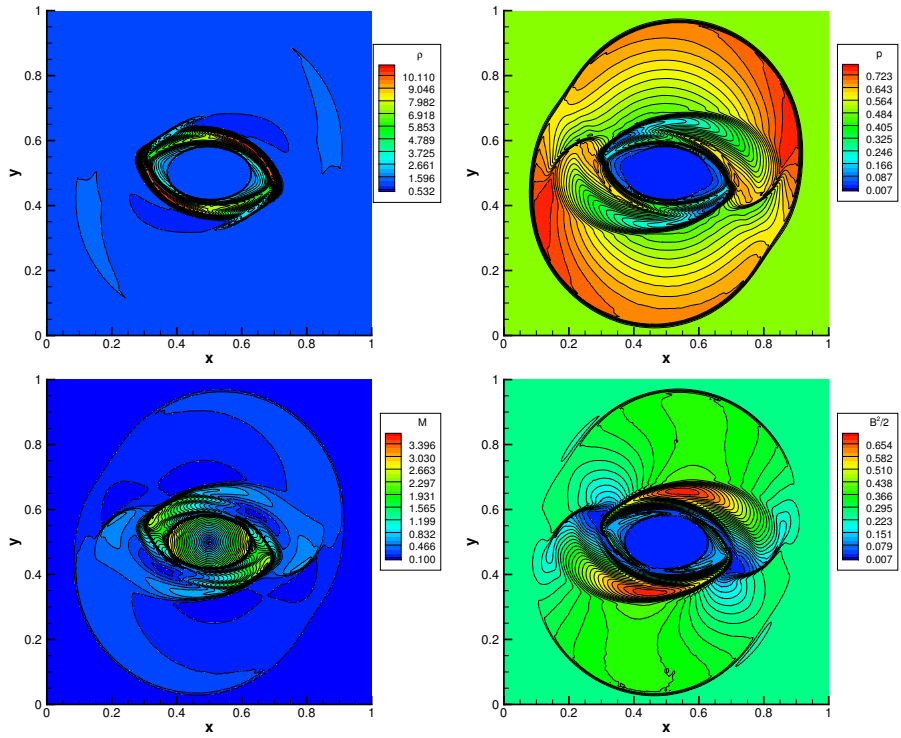

Figure 5.11: density, thermal pressure, Mach and magnetic pressure at t = 0.2962 on a mesh 400 × 400.

5.2.4 Magnetic reconnection in a weakly ionized reacting plasma

In this section we present the results using the two-fluid, reactive collisional model presented in Section 3.2.1. In the literature, only a few examples of simulations reproducing self-consistent partially ionized reactive and collisional multi-fluid models can be found. In order to assess the numerical method explained in this work, we reproduce the results of a magnetic reconnection in a weakly ionized plasma comparing our results with those of Leake et al. [8].

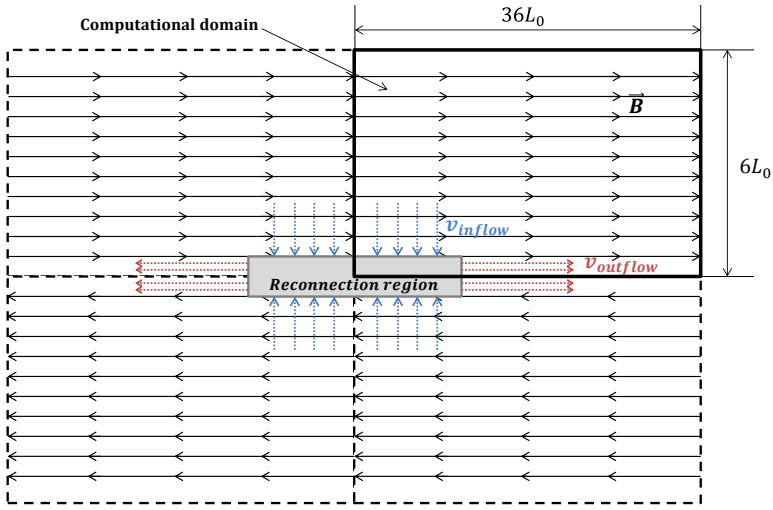

Figure 5.12: Geommetry of the reconnection. Using the symmetries of the problem, only one quarter is simulated.

The parameters used in our simulation of magnetic reconnection in a weakly ionized plasma are taken from Leake et al. [8]. The reference length scale is $L_0 = 10^5$ m. Using characteristic values of the chromospheric plasma, the number density $n_0 = 3.3 \cdot 10^{16}$ m^{-3} and the magnetic field $B_0 = 10^{-3}$ T. With the latter, we obtain the following reference values: the characteristic Alfvén speed is $v_0 = B_0/\sqrt{\mu_0 m_p n_0}$, reference pressure $P_0 = B_0^2/\mu_0$, reference temperature $T_0 = P_0/n_0 k_B$ and reference time $t_0 = L_0/v_0$. The temperature at this level of the solar chromosphere is $T_c = 5 \cdot 10^{-3} T_0$.

Initially, we consider a magnetic field configuration consisting of anti-parallel field lines forming a Harris current sheet (Fig. 5.12). A small perturbation for the magnetic field is introduced in the center in order to force the reconnection to occur in the center of the domain. The initial ionization degree is set to $\psi_i = n_i/(n_i + n_n) = 0.5\%$. Both fluids are initialized in force balance: a perturbation in the pressure is introduced in order to balance the magnetic pressure, and a small velocity is introduced in the ionized fluid in order to produce a frictional force that equilibrates the forces between the fluids. As, presented in Fig. 5.12, using the symmetries of the problem, only one quarter of the domain is simulated. The simulations are carried out in a domain of $36L_0 \times 6L_0$.

Taking the values of the perturbation as $\epsilon = 0.01 B_0 L_0$ and $F = 0.01 P_0$,

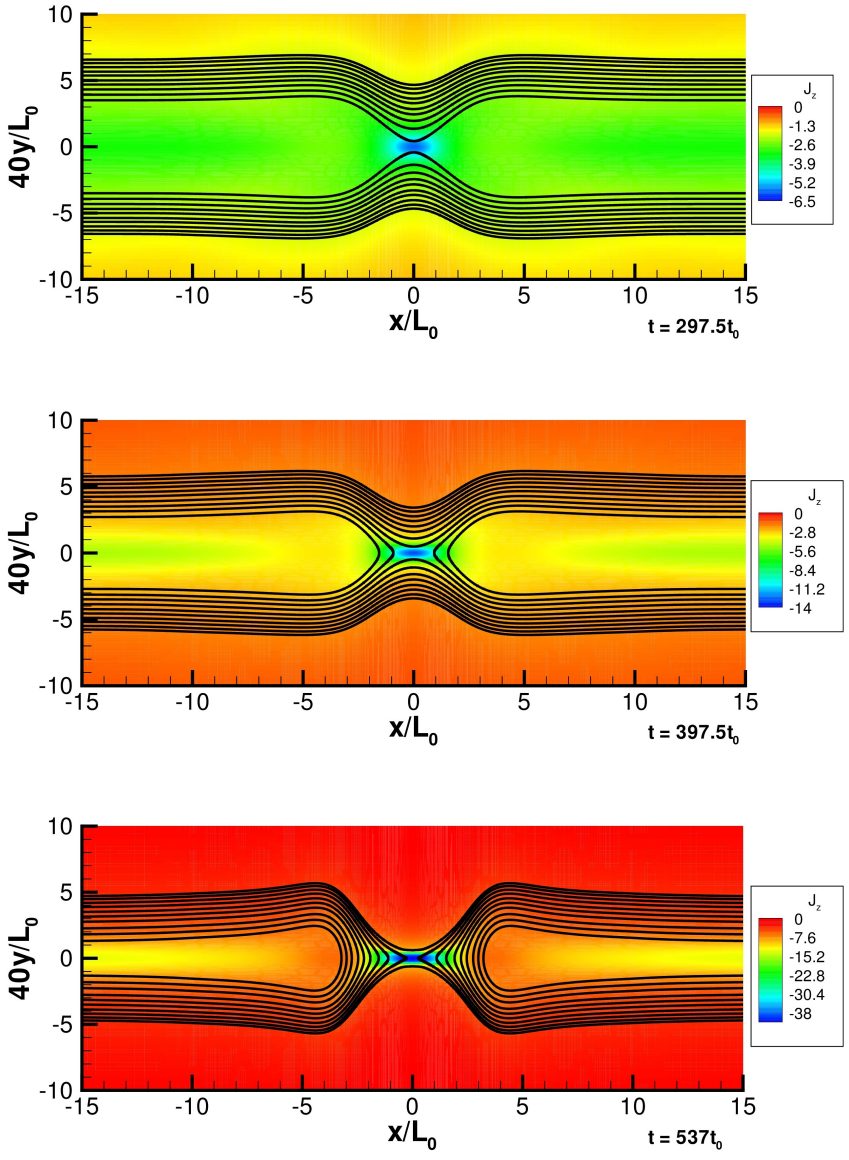

Figure 5.13: Results obtained with the present numerical method that show the evolution of the current sheet and magnetic field lines during the magnetic reconnection for different time steps: $297.5t_0$ (top), $397.5t_0$ (middle) and $537.5t_0$ (bottom).

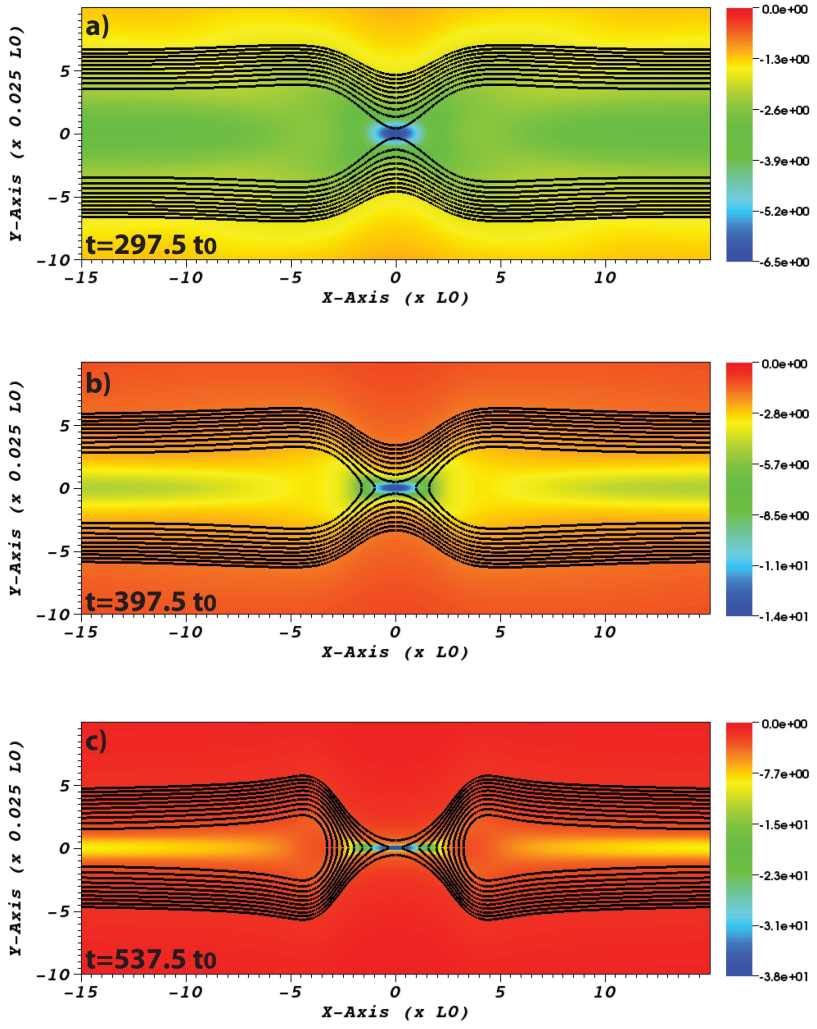

Figure 5.14: Results obtained by Leake et al. [8] method that show the evolution of the current sheet and magnetic field lines during the magnetic reconnection for different time steps: $297.5t_0$ (top), $397.5t_0$ (middle) and $537.5t_0$ (bottom).

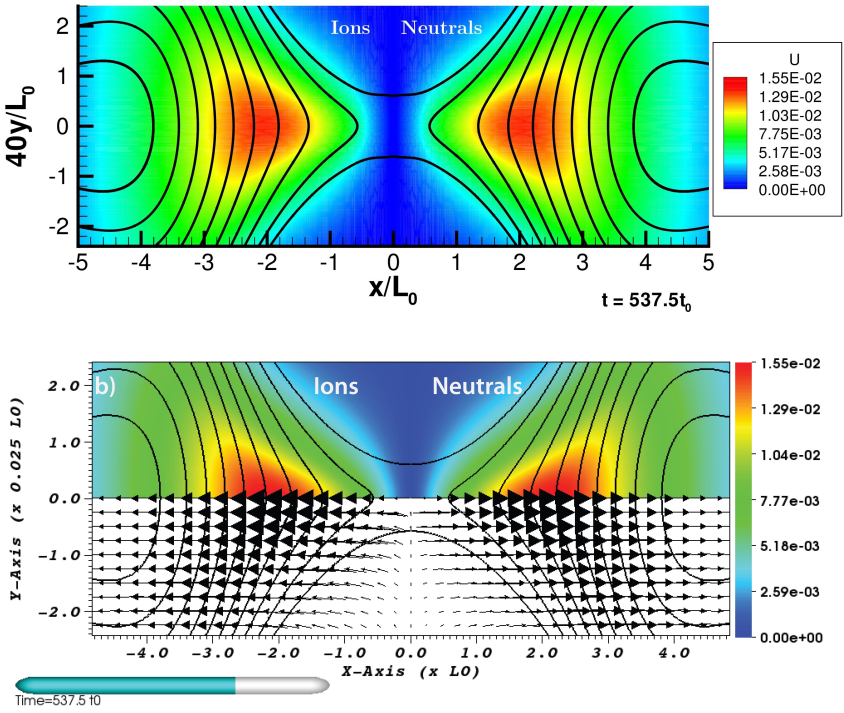

Figure 5.15: Horizontal velocity at $t = 537.5t_0$. The results obtained with our numerical method (top) are compared to those of Leake et al. [8] (bottom). For each plot, the left half represent the horizontal velocity of the ions and the left half the one of the neutrals. Only the top quarter is simulated, therefore, the rest of quarters are mirrored.

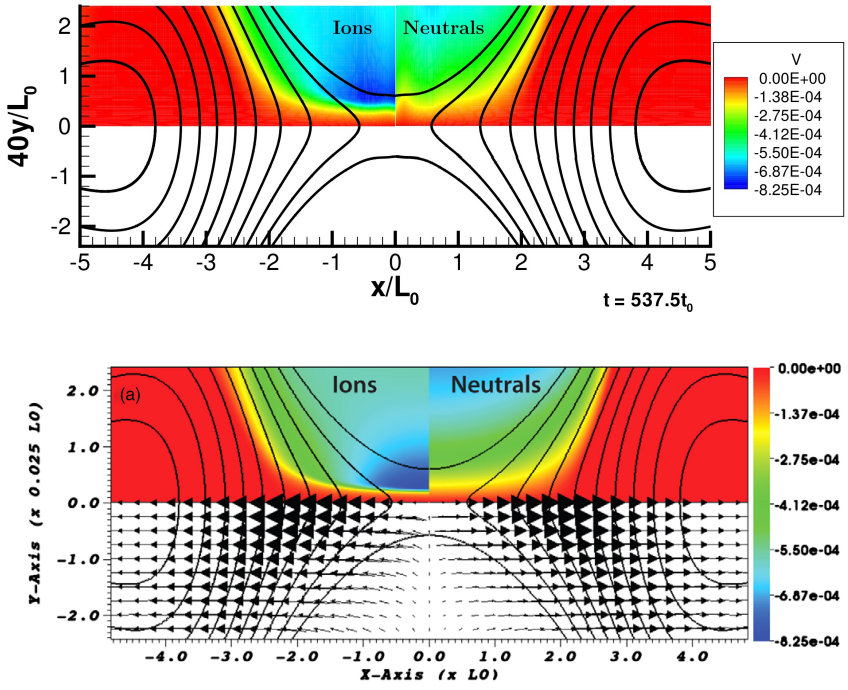

Figure 5.16: Vertical velocity at $t = 537.5t_0$. The results obtained with our numerical method (top) are compared to those of Leake et al. [8] (bottom). For each plot, the left half represent the vertical velocity of the ions and the left half the one of the neutrals. In the left plot, the bottom half is blanked in order to better compare the results. Only the top quarter is simulated, therefore, the rest of quarters are mirrored.

and the perturbation characteristic length as $\lambda_\Psi = 0.5L_0$, the initial field reads:

$$\mathbf{P}(\vec{x}, t=0) = \begin{cases} \vec{B} = (B_0 \tanh(y/\lambda_\Psi) - 2\epsilon \frac{y}{\lambda_\Psi^2} e^{-(\frac{x}{4\lambda_\Psi})^2 - (\frac{y}{\lambda_\Psi})^2}, \\ \qquad \epsilon \frac{x}{8\lambda_\Psi^2} e^{-(\frac{x}{4\lambda_\Psi})^2 - (\frac{y}{\lambda_\Psi})^2}, 0) \\ \vec{E} = (0, 0, \mu_0 \frac{\vec{\nabla} \times \vec{B}_0}{\eta} - v_{i_0} B_{x_0}) \\ \Psi = 0 \\ \Phi = 0 \\ \rho_i = m_p n_0 + \frac{F}{4R_i T_c \cosh^2(y/\lambda_\Psi)} \\ \rho_n = 200 m_n n_0 + \frac{P_0 - F}{2R_n T_c \cosh^2(y/\lambda_\Psi)} \\ \vec{u}_i = (0, \frac{F - P_0}{m_{in} n_i \nu_{in_0}} \frac{\tanh(y/\lambda_\Psi)}{\lambda_\Psi \cosh^2(y/\lambda_\Psi)}) \\ \vec{u}_n = (0, 0) \\ T_i = T_c \\ T_n = T_c \end{cases} \tag{5.9}$$

Where the collisional frequency ν_{in} and m_{in} are defined in Eq. (3.20).

The physical properties used in the simulation are as follows. The specific heat ratio of the ionized fluid and the neutrals is $\gamma = 5/3$. The electrical resistivity is $\eta = 0.5 \cdot 10^5 \mu_0 L_0 v_0$. The ions and neutrals viscosity $\xi_i = \xi_n = 10^{-3} m_p n_0 L_0 v_0$. The neutrals heat conduction coefficient $\kappa_n = 4 \cdot 10^{-3} m_p n_0 L_0 v_0^3 / T_0$. In order to artificially increase the CFL condition for the coupled Maxwell/two-fluid system without comprimising the accuracy of the results, the speed of light is reduced to $c = 30 v_0$, similar value as Hakim et al. [116]. Also, $c = 100 v_0$ was used without noticing major changes in the results. In fact, using $c = 30 v_0$, the ratio between the speed of light and the maximum speed of the fluids is $(c/v_{max})^2 \sim 10^6$, not high enough to have any visible influence in the solution.

The simulations are reproduced in a mesh of 750×400 elements where the distance between the elements stretch in both directions towards the left-bottom corner, being the size of the smallest element $(20 \times 5) \cdot 10^{-5} L_0$, i.e., 20×5 m. In order to simulate only one quarter, we impose boundary conditions simulating the symmetry/anti-symmetry of the problem, as follows. On the boundary conditions at $x = 0$, $x = 36L_0$, and $y = 0$, we impose insulating wall for Maxwell's equations and mirror boundary condition for the fluids, as follows:

$$\begin{pmatrix} \vec{B}_G \\ \vec{E}_G \\ \Psi_G \\ \Phi_G \end{pmatrix} = \begin{pmatrix} -\vec{B}_I + 2(\vec{B}_I \cdot \vec{n})\vec{n} \\ \vec{E}_I - 2(\vec{E}_I \cdot \vec{n})\vec{n} \\ \Psi_I \\ -\Phi_I \end{pmatrix}$$

$$\text{and} \quad \begin{pmatrix} \rho_{G,s} \\ \vec{u}_{G,s} \\ T_{G,s} \end{pmatrix} = \begin{pmatrix} \rho_{I,s} \\ \vec{u}_{I,s} - 2(\vec{u}_{I,s} \cdot \vec{n})\vec{n} \\ T_{I,s} \end{pmatrix}. \quad (5.10)$$

At $y = 6L_0$ perfectly conducting wall for Maxwell equations and subsonic outlet imposing the pressure for the fluids, as follows:

$$\begin{pmatrix} \vec{B}_G \\ \vec{E}_G \\ \Psi_G \\ \Phi_G \end{pmatrix} = \begin{pmatrix} \vec{B}_I - 2(\vec{B}_I \cdot \vec{n})\vec{n} \\ -\vec{E}_I + 2(\vec{E}_I \cdot \vec{n})\vec{n} \\ \Psi_I \\ -\Phi_I \end{pmatrix} \text{ and } \; p_{G,s} = 2p_{0,s} - p_{I,s}, \quad (5.11)$$

where $p_{0,s}$ is the imposed pressure of the different fluids at the boundary that is taken to be as the initial pressures, i.e., for the ions $p_{0,i} = n_0 k_B T_c$ and for the neutrals $p_{0,n} = 200 n_0 k_B T_c$.

The simulations have been carried out using second-order spatial discretization with the numerical schemes described in the present article, i.e., modified-CIR scheme for the Maxwell's equations with divergence cleaning and the extension of AUSM$^+$-up for multi-fluid equations. For the time discretization, second-order three-point Backward Euler has been used, as described previously. As explained in Section 4.8, the equation for the evolution of the Lagrangian multiplier is converged to steady state at every iteration in order to drop the time derivative of the equation.

The time step used in our simulations is $\Delta t = 0.024 t_0$ ($\Delta t = 0.02$ s). The CFL number corresponding to this simulation parameters is CFL $\sim$ 1900. The number of subiterations of the Newton method in each iteration is around 80. Each time step takes a wall time of 1.35 s while running in 320 Intel Xeon X5670 processors with a speed of 2.93 GHz.

Contour spatial plots of the evolution of the current sheet and the magnetic field lines are presented in Fig. 5.13. The results are compared to those of Leake et al. [8] (Fig. 5.14), who used a spectral Finite Element spatial discretization and implicit second-order time integration, also employing PETSc [149] for solving the resulting linear systems. Since Leake et al. [8] were using

a higher order discretization in space than the second-order results presented herein, this could have led to a different topology during the reconnection, i.e. featuring magnetic islands, as explained by Loverich et al. [10]. However, in Fig. 5.13, our results are in good agreement with those of Leake et al. [8], both in the topology of the magnetic field lines and the value of the current, probably because our computational mesh was fine enough to (partially) compensate for the relative lack of spatial accuracy in comparison with our reference's spectral solver. The vertical axis has been expanded by a factor of 40 in order to see better the width of the current sheet, as done by Leake et al. [8].

In Fig. 5.15, the horizontal velocity field is presented at $t = 537.5t_0$, both for ions (left half) and neutrals (right half). Also, the horizontal velocity field shows good agreement with the reference results. During the reconnection, the ions are accelerated by the Lorentz force and in their motion they drag the neutrals by means of collisions. As a result, the horizontal velocity of ions and neutrals are very similar.

In Fig. 5.16, the vertical velocity is presented. In the top left quarter, the one of the ions is shown and in the top right quarter, the one of the neutrals. The bottom half of the plot has been blanked in order to compared with the reference results. The vertical velocity of ions differs from the one of the neutrals, being the latter, almost the half of the ions. This is due to the fact that the ions vertical motion is much slower than the horizontal movement and the collisional momentum in the vertical direction is not transferring as much momentum as in the horizontal direction. The results of the vertical velocity compared to the reference solution are quantitatively similar, although some differences appear probably due to the different order of the spatial discretization of the solutions. We observe the largest difference in the velocity of the neutrals close to the left boundary. The difference is caused by the initiation of the plasmoid instability that is triggered earlier in our computations than in the reference solution.

5.2.5 Two-fluid (ion+electron) Brio-Wu Shock tube

In this section, we use the ideal two-fluid (ion+electron) equations (described in Section 2.4.1). We describe our results for a Brio-Wu type shock tube. For this setup, we adopt the conditions for the two-fluid electromagnetic plasma shock, which is an extension of the Brio-Wu shock tube problem from ideal MHD to two-fluid, as done in other models, e.g., [117, 115, 116, 10]. In this test, we would like to see the effect that the normalized ion gyroradius has in the results. We expect that for $\hat{r}_L \gg 1$ the solution will resemble a

gas dynamic solution with a rarefaction wave, a contact discontinuity, and a shock, since the fluids are not magnetized. On the other hand, for $\hat{r}_L \ll 1$ we expect the solution to resemble an MHD regime solution with a fast rarefaction, a slow compound wave, a contact discontinuity, a slow shock, and a fast rarefaction wave. For all the shock tube tests we use the following initial conditions:

$$\begin{pmatrix} B_x \\ B_y \\ B_z \\ \rho_e \\ \rho_i \\ p_e \\ p_i \end{pmatrix}_{\text{left}} = \begin{pmatrix} 0.75 \\ 1.0 \\ 0. \\ \frac{m_e}{m_i} \\ 1.0 \\ 0.5 \times 10^4 \\ 0.5 \times 10^4 \end{pmatrix}, \qquad \begin{pmatrix} B_x \\ B_y \\ B_z \\ \rho_e \\ \rho_i \\ p_e \\ p_i \end{pmatrix}_{\text{right}} = \begin{pmatrix} 0.75 \\ -1.0 \\ 0. \\ 0.125\frac{m_e}{m_i} \\ 0.125 \\ 0.5 \times 10^3 \\ 0.5 \times 10^3 \end{pmatrix}. \tag{5.12}$$

All other quantities were set to zero for the initial condition. For our first tests, we use a mass ratio $m_i/m_e = 100$ in order to use a coarser grid and speed up the computational time for our simulations. We assume that the polytropic index $\gamma = 5/3$ for each fluid and the temperatures are found using the ideal gas law. For this test we assume $v_0/c = 1/100$. We use a domain with $0 < x/l_0 < 1$ in normalized units and set the initial discontinuity in the center of the domain. For all cases we set the normalized Debye length $\hat{r}_D = r_D/r_L = 0.01$ and we vary the ion gyroradius $\hat{r}_L \in [10^{-3}, 10^{-2}, 10^{-1}, 1, 10]$. The change in the gyroradius is equivalent to changing the charge over mass ratio q_i/m_i since $\hat{r}_L \propto q_i/m_i$, as it is commonly done in other models. The time step in the simulation is chosen to be $\Delta t = 0.1\Omega_i$ since we want to resolve as well the cyclotron oscillations in our results.

Figure 5.17 shows the ion density for $\hat{r}_L = 10^{-3}$ at $t\omega_{pi} = 0.1$ and the corresponding ion and electron velocities in x and y at $t\omega_{pi} = 0.02$ using a grid of N = 6400 and a mass ratio of 100. The density compares very well to the results obtained by Hakim et al. [116] (Figure 5 in their paper) and Loverich et al. [10] (Figure 12 in their paper), which used a real mass ratio and hence a much finer mesh and longer computational time was requiered. As in their paper, our model is able to capture the complex structure of the dispersive waves, as well as the formation of the rarefaction waves and the contact discontinuity, which also appear in the correct locations. A similar result is also obtained by Amano [117] using the quasi-neutral two-fluid plasma model (Figure 1 in their paper). We may compare the velocities to the results of this last paper. One can note that there are slight differences compared to the model of Amano [117] in the oscillations observed in the electron velocity, particularly. The reason for this difference is due to the plasma

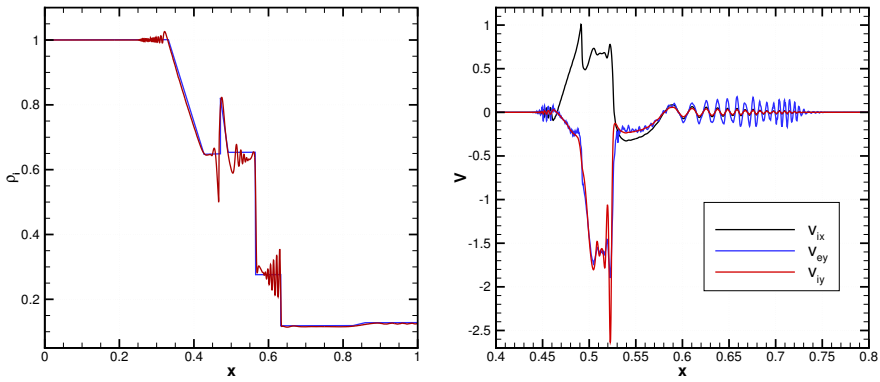

Figure 5.17: Ion density (left) at $t\omega_{pi} = 0.1$ for a normalized ion gyroradius $\hat{r}_L = 10^{-3}$ using a grid with N = 6400 and a mass ratio of 100. The two-fluid solution (red) is plotted with the ideal MHD (blue) solution. The figure on the right shows the ion velocities v_{ix} (black) and v_{iy} (red) and the electron velocity v_{ey} for that same case at $t\omega_{pi} = 0.02$.

waves produced by charge separation, which are included here whereas they are neglected by Amano [117].

Figure 5.18 shows the results of the ion density at $t\omega_{pi} = 0.1$ for the different gyroradii ($\hat{r}_L \in [10, 1, 10^{-1}, 10^{-2}]$). As we decreased the gyroradius, we had to increase our mesh resolution from 400 grid points for $\hat{r}_L = 10, 1, 0.1$ to 1600 points for $\hat{r}_L = 10^{-2}$ in order to be able to capture the different oscillations that develop in the model. One can clearly see the evolution of the solution changing from the gas regime for large $\hat{r}_L$ to the MHD regime for small $\hat{r}_L$. We have omitted the electron density, since the solution just followed the ion density solution exactly (taking into account the mass ratio factor). We have also done some tests with a mass ratio $m_i/m_e = 1832$ and $\hat{r}_L = 0.1$; and show the result of the ion and electron densities in Figure 5.19. Here, one can clearly see that the dynamics of electrons and ions decouple because of the charge separation and the electron plasma waves.

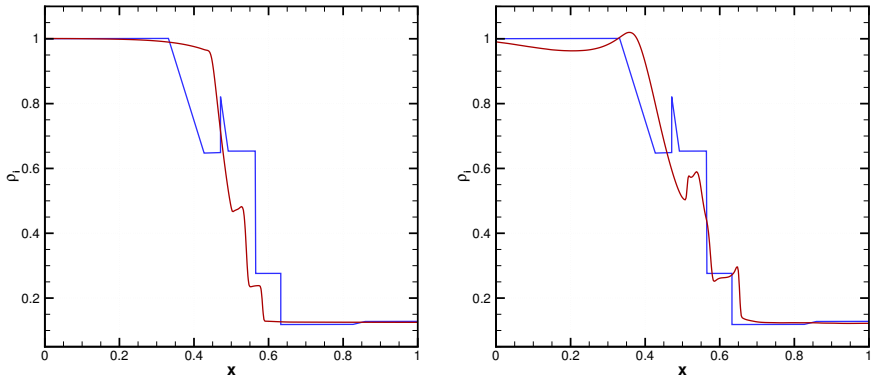

(a) $\hat{r}_L = 10$ **(b)** $\hat{r}_L = 1$

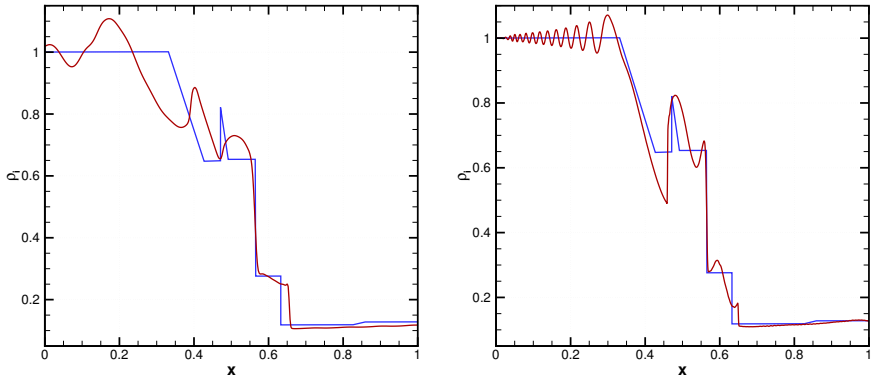

(c) $\hat{r}_L = 10^{-1}$ **(d)** $\hat{r}_L = 10^{-2}$

Figure 5.18: Ion density at $t\omega_{pi} = 0.1$ for different gyroradii, starting with a) $\hat{r}_L = 10$, b) $\hat{r}_L = 1$, c) $\hat{r}_L = 10^{-1}$, and d) $\hat{r}_L = 10^{-2}$. The two-fluid solution is plotted in red and compared to the ideal MHD solution, in blue.

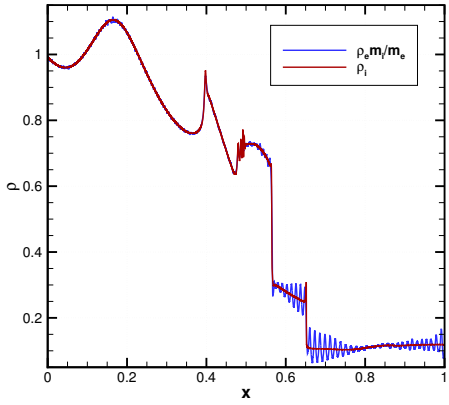

Figure 5.19: Ion and electron density at $t\omega_{pi} = 0.1$ for $\hat{r}_L = 10^{-1}$ and $m_i/m_e = 1832$.

5.2.6 Two-fluid collisionless GEM challenge in the plane perpendicular to the current

Next, we test the GEM challenge reproducing the reconnection taking place in the magnetotail using our ion-electron two-fluid model. We assume an initial Harris equilibrium given by Birn et al. [9] and a current sheet thickness $\lambda = 0.5l_0$ where the reference length is the ion skin depth ($l_0 = \delta_i$). Our initial conditions as function of the reference units are summarized as follows:

$$\mathbf{P}(\vec{x}, t=0) = \begin{cases} \vec{B} = (B_0 \tanh(y/\lambda) - B' \frac{l_0 \pi}{L_y} \cos(2x\pi/L_x) \sin(y\pi/L_y), \\ \qquad 2B' \frac{l_0 \pi}{\pi L_x} \sin(2x\pi/L_x) \cos(y\pi/L_y), 0) \\ \vec{E} = (0,0,0) \\ \Psi = 0 \\ \Phi = 0 \\ \rho_e = m_p n_0 \left(1/5 + \operatorname{sech}^2(y/\lambda)\right) \\ \rho_i = m_e n_0 \left(1/5 + \operatorname{sech}^2(y/\lambda)\right) \\ \vec{u}_e = (0, 0, \frac{2k_B T_e}{\lambda q B_0} \frac{\operatorname{sech}^2(y/\lambda)}{(1/5 + \operatorname{sech}^2(y/\lambda))}) \\ \vec{u}_i = (0, 0, -\frac{2k_B T_i}{\lambda q B_0} \frac{\operatorname{sech}^2(y/\lambda)}{(1/5 + \operatorname{sech}^2(y/\lambda))}) \\ T_e = \frac{5}{12\mu_0} \frac{B_0^2}{n_0 k_B} \\ T_i = \frac{1}{12\mu_0} \frac{B_0^2}{n_0 k_B} \end{cases} \tag{5.13}$$

The magnetic field is balanced by a current given by the ion and electron densities $n_i(y) = n_e(y) = n_0(1/5 + \operatorname{sech}^2(y/\lambda))$ and the drift velocities $v_{z,e}$ and $v_{z,i}$. We obtain pressure equilibrium using $n_0 k_B(T_e + T_i) = \frac{B_0^2}{2\mu_0}$. In the initial equilibrium ($t = 0$) we add a small perturbation in the magnetic field $B'/B_0 = 0.1$, forming two magnetic islands and satisfying the divergence free condition of the magnetic field (see B_y and B_z components above). In the present simulation, we use a mass ratio of $m_i/m_e = 25$, a temperature ratio $T_e/T_i = 5$, and $\gamma = 5/3$, following the GEM challenge parameters. The unit length scale (l_0) chosen is the ion skin depth and the unit of time is the ion cyclotron frequency Ω_i. For the simulation we set up a double current sheet and use a square domain ranging from $-L_x \leq xlL_x$ in x and in y from $-L_y \leq y \leq L_y$, where $L_x = L_y = 25.6l_0$. This allows us to use periodic boundary conditions in all four boundaries. For the simulations presented in this case we use a grid of 512 x 512, but we show only one current sheet in the results. The time step is chosen to be $\Delta t = 0.0025\omega_{pi}$.

We compute the normalized reconnected flux as

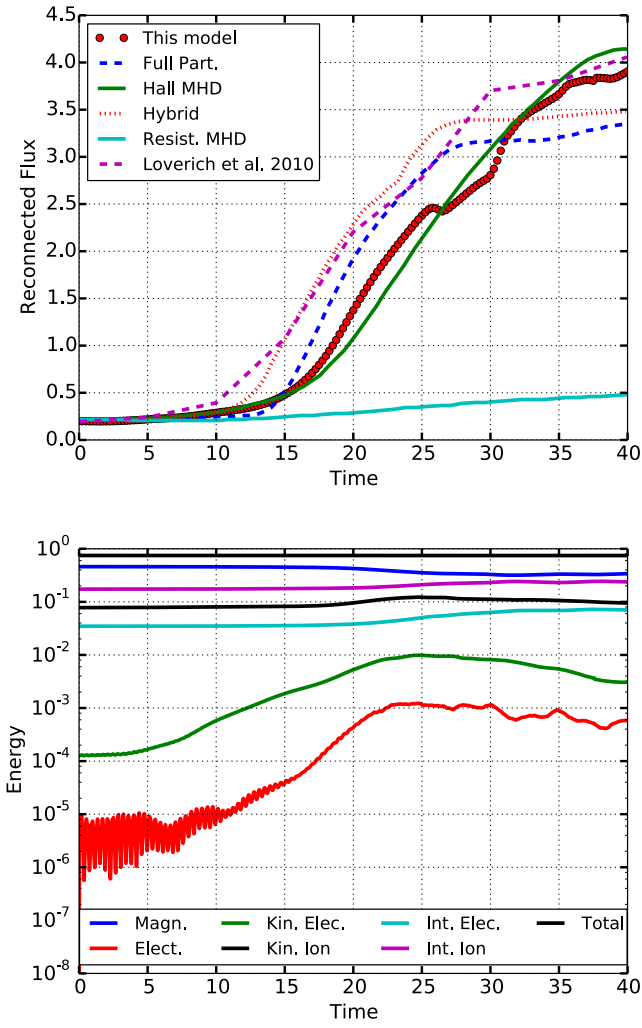

Figure 5.20: Top: Reconnected flux as a function of time in ion cyclotron periods ($1/\Omega_i$) for different models. Our model results are shown in the red dots. Full particle, Hall-MHD, Hybrid, and Resistive MHD results are taken from Birn et al. [9]. We also take the results reported in Loverich et al. [10] to compare to another two-fluid model. Our obtained reconnected flux falls closer to the Hall-MHD and seems to be less resistive than what is reported in the two-fluid model of Loverich et al. [10]. Bottom: Energy as a function of time during the reconnection simulation

$$\Psi(t) = \frac{1}{2L_x B_0} \int_{-L_x}^{L_x} |B_y(x, y = 0, t)| dx \tag{5.14}$$

and display our results in Figure 5.20 (top) in the red dotted line. We overplot the results shown by Birn et al. [9] and Loverich et al. [10] for the GEM configuration obtained with different models to compare the performance of our two-fluid model. Our computation yields a reconnected flux quite similar to that obtained by the Hall-MHD model, but seems to over estimate the reconnected flux at the end of the simulation, compared to the full particle model. We have included the results from Loverich et al. [10] for comparison and our results are qualitatively similar, but with a delay in the onset of reconnection. The difference might be caused by the use of a different initial field, as in Loverich et al.
citeLoverich11 the current is initially carried by the electrons whereas here the initial state starts in equilibrium with a diamagnetic current. In Figure 5.20 (bottom) we also show the evolution of the different energies in the system as a function of time in ion cyclotron periods ($1/\Omega_i$). The figure shows that the electric energy starts increasing early in the simulation, between $t\Omega_i = 5$ and 10 reaching a saturation point at a time of about $t\Omega_i = 22$. The electron kinetic energy seems to follow this behaviour, but decreases a bit towards the end of the simulation. The magnetic energy appears relatively constant until about $t\Omega_i = 20$, when it starts to decrease, while the ion kinetic energy and ion and electron internal energies increase, as expected.

Figures 5.21 and 5.22 show a snapshot of the results for the electron and ion momenta. Figures 5.23 and 5.24 show a snapshot of the results for the electron and ion temperatures. We normalized the temperatures to the initial electron temperature and the momenta to the initial ion momentum at times $t\Omega_i = 25$ and 40, respectively. At $t\Omega_i = 25$ the reconnected flux is almost 2.5 and some shocks are already visible in both momentum and temperature. The electron momentum is significantly higher in the current sheet. At $t\Omega_i = 40$ the current sheet length is significantly smaller, the electrons and ions have been heated due to the conversion of magnetic energy into kinetic and internal energy. Several complex structures and shocks are visible at this time.

Finally, we show the out of plane component of the magnetic field, which is generated by the decoupling between the electron and ion dynamics, not visible in MHD models. The snapshots of B_z at $t\Omega_i = 25$ and 40 are shown in Figure 5.25.

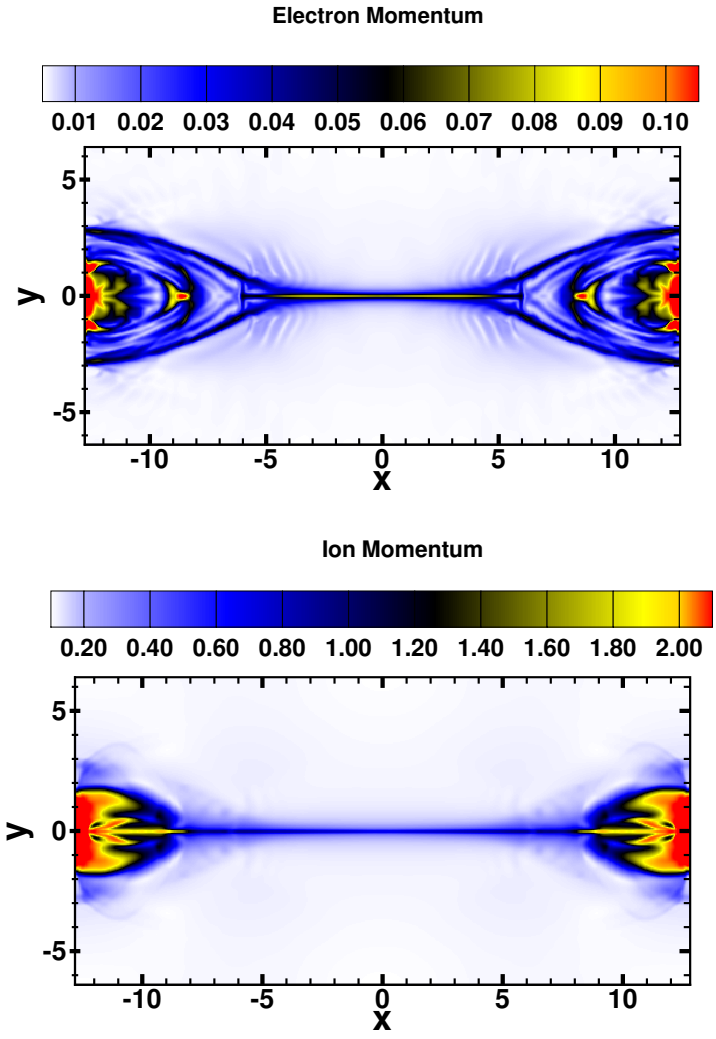

Figure 5.21: Electron (top) and ion (bottom) momentum in normalized units at $t\Omega_i = 25$.

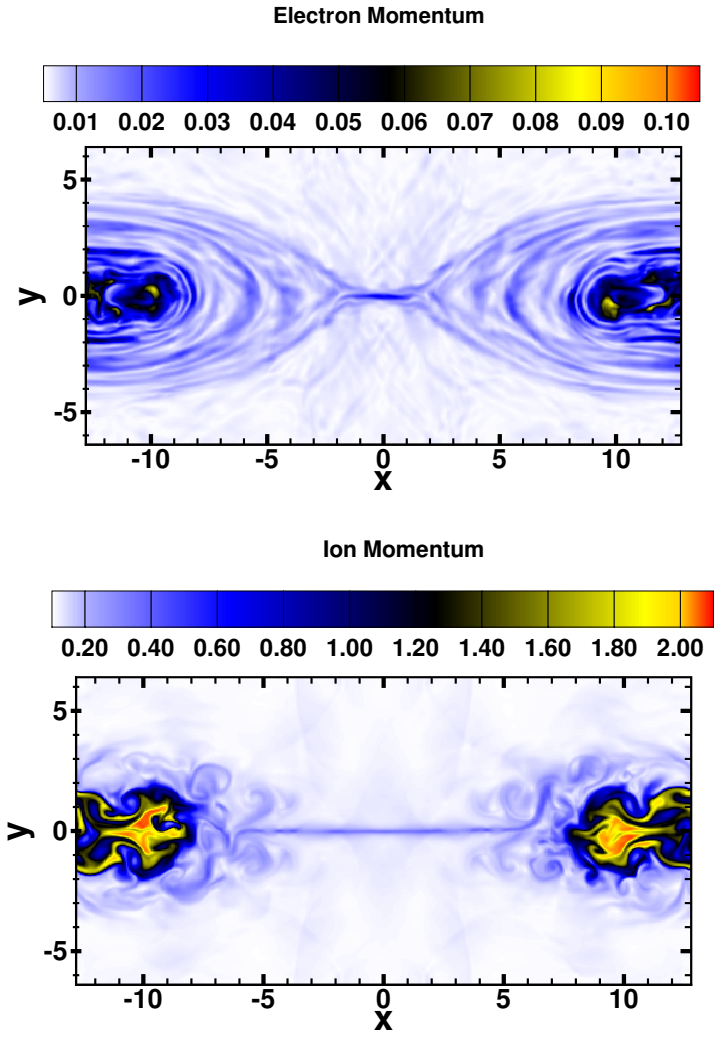

Figure 5.22: Electron (top) and ion (bottom) momentum in normalized units at $t\Omega_i = 40$

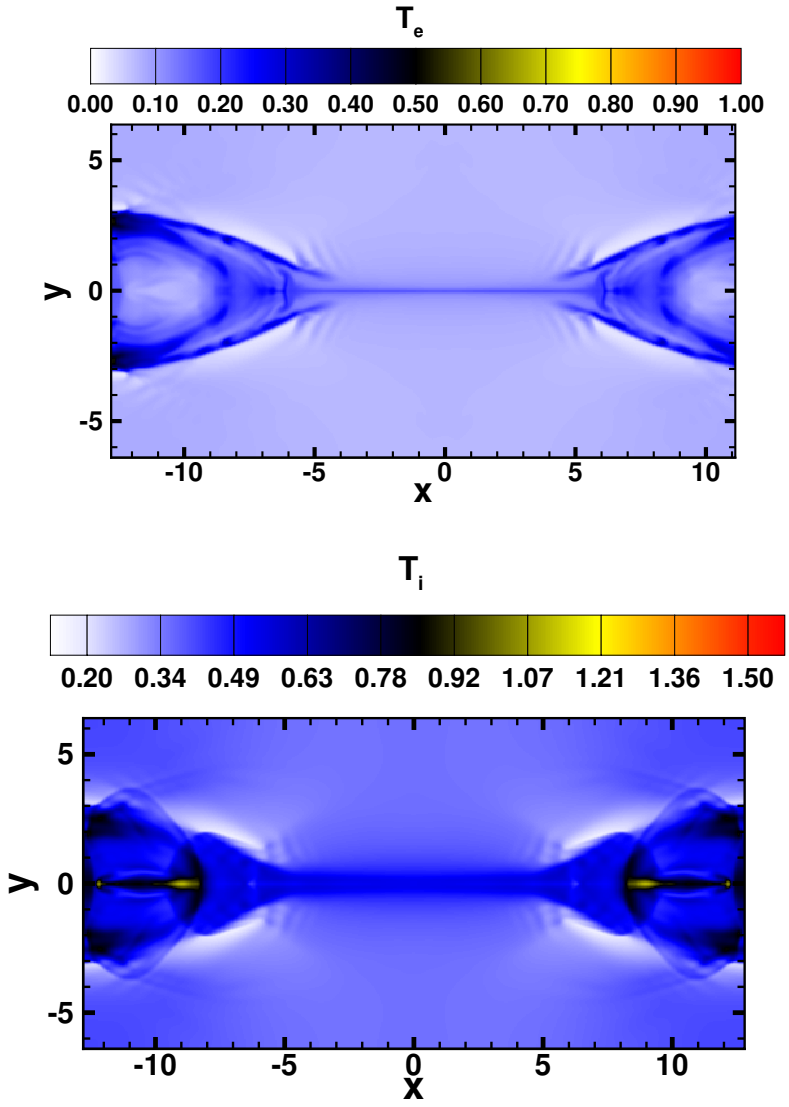

Figure 5.23: Electron (top) and ion (bottom) temperature in normalized units at $t\Omega_i = 25$.

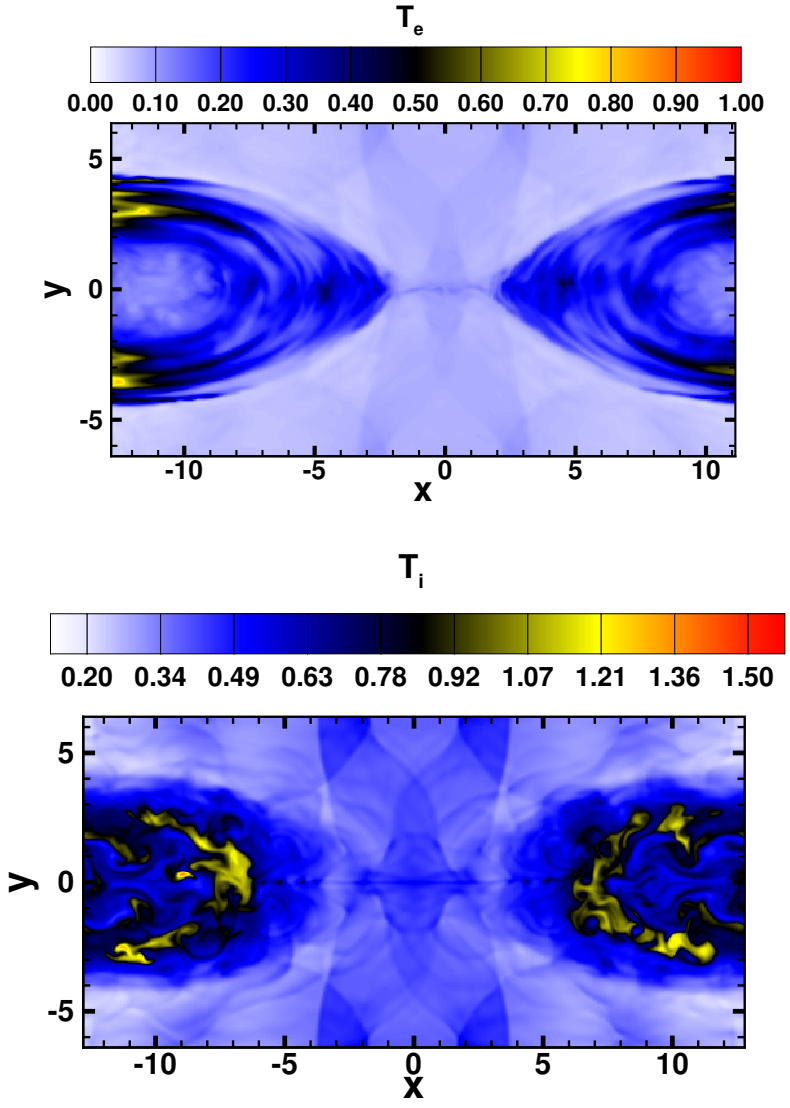

Figure 5.24: Electron (top) and ion (bottom) temperature in normalized units at $t\Omega_i = 40$

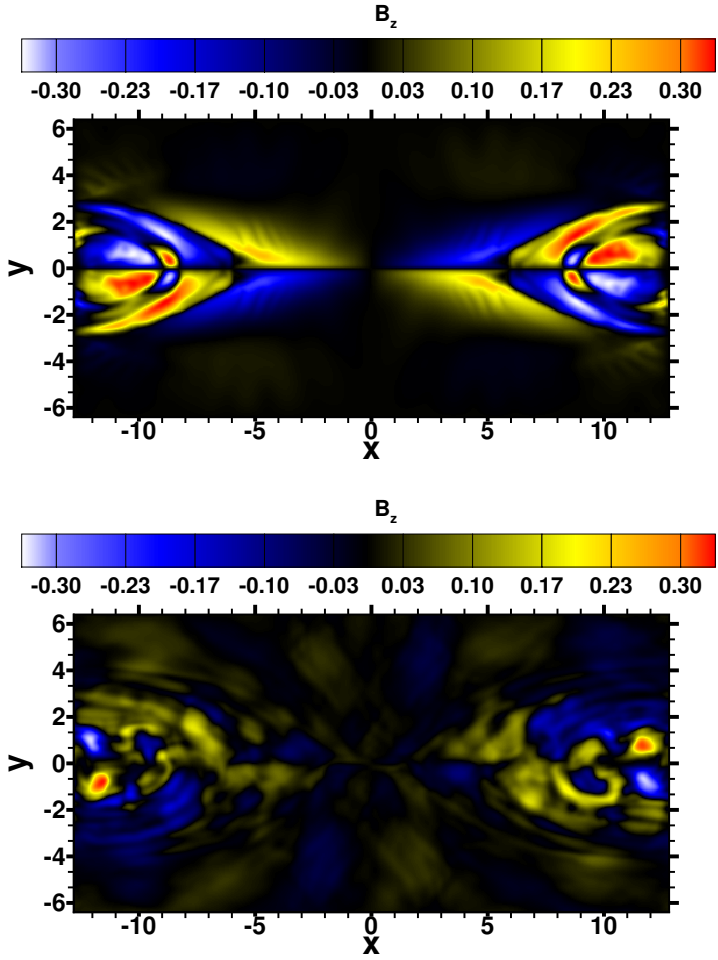

Figure 5.25: Out of plane component of the magnetic field (B_z) at $t\Omega_{ci} = 25$ (left) and $t\Omega_{ci} = 40$ right

Effect of the choice of the limiter in presence of dispersive waves

When running the GEM challenge it is important to notice the importance of the limiter used in the model to treat the behaviour of shocks in a two-fluid model. Unlike in MHD models, in the two-fluid there is a presence of electromagnetic waves in the computational domain that are physical and should not be smoothed out by the limiter used. For this reason, we have chosen to implement the Venkatakrishnan limiter for the treatment of shocks in our computations (see Section 4.4 for details). As it can be seen in Fig. 5.26, this limiter is only active in parts of the domain where a discontinuity/shock is truly present without smoothing out the electromagnetic waves that are formed.

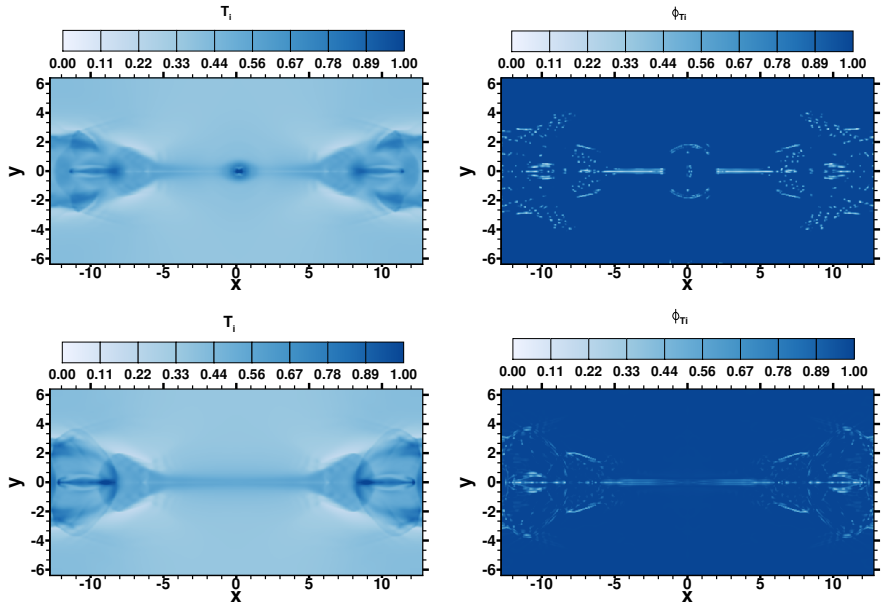

Figure 5.26: Comparison of ion temperature (left) and corresponding limiter (right) in a simulation of magnetic reconnection at time $t\Omega_i = 25$ using a Barth and Jespersen limiter (top) and a Venkatakrishnan limiter (bottom).

5.3 SUMMARY

The accuracy of the proposed second-order scheme is first verified in a two-dimensional test case that reproduces the advection of a magnetized vortex in an iso-density background. The accuracy analysis shows that the proposed method is able to achieve second-order accuracy on ideal MHD cases. Similarly, the accuracy of the solver for the ideal two-fluid plasma model is assessed. The study shows that the rescaling of the numerical dissipation of the magnetic field allows for achieving the second-order accuracy.

The method is validated in four test cases that assume charge neutrality: a viscous resistive MHD case, two ideal MHD cases with presence of shocks and a two-fluid collisional reactive plasma simulation. The first case, the Hartmann flow, is used to verify the performance of the method coupling Maxwell's equations with Navier-Stokes equations. The second and third cases simulate two standard ideal MHD supersonic cases, namely, the Orszag-Tang vortex and the MHD rotor. The last case is used to study a complex multi-fluid case with a reactive, collisional partially ionized model that considers anisotropic transport fluxes.

Alternatively, two additional cases that study the ideal two-fluid (ion + electron) model are analyzed. Firstly, the two-fluid Brio-Wu shock tube is studied for different ion gyroradius. The case shows that the two-fluid plasma model approaches the ideal MHD solution for small non-dimensional gyroradius. Finally, the GEM challenge is studied. This case proves the ability of the code to capture shocks and shock-shock interactions. The obtained reconnection rate is similar to this of Hall-MHD codes, although the flow and magnetic field topology are different. Additionally, we observe that choice of the limiter has an important impact in the dynamics of the reconnection. As the solution contains dispersive waves, the proposed limiter has a correction for near-constant regions in order to activate the limiter only near discontinuities.

The innovative method here proposed shows its versatiliy in a wide a range of plasma phenomena from ideal MHD and partially-ionized ion-neutral models to fully-ionized ion-electron model. Even though the method couples full Maxwell's equations, it is able to reproduce ideal MHD cases by using large time steps comparable to the ideal MHD solvers, thanks to the implicit time stepping method proposed here. The ion-electron solver is not restricted by a CFL condition, but the time step is adapted to the ion time scales in order to resolve the ion dynamics.

CHAPTER 6

Study of the Effect of Radiation on Chromospheric Magnetic Reconnection

The poet's eye, in a fine frenzy rolling, doth glance from heaven to Earth, from Earth to heaven; and as imagination bodies forth the forms of things unknown, the poet's pen turns them to shape, and gives to airy nothing a local habitation and a name; such tricks hath strong imagination.

– *William Shakespeare*

We study magnetic reconnection under chromospheric conditions in five different ionization levels from 0.5% to 50% using a self-consistent two-fluid (ions + neutrals) model that accounts for compressibility, collisional effects, chemical inequilibrium, and anisotropic heat conduction. Results with and without radiation are compared, using two models for the radiative losses: an optically thin radiation loss function, and an approximation of the radiative losses of a plasma with photospheric abundances. Without radiation, reconnection occurs faster for the weakly ionized cases as a result of the effect of ambipolar diffusion and fast recombination. The radiative losses have a strong impact in the reconnection in partially ionized plasmas as the ambipolar diffusion is enhanced and the chemical equilibrium is modified, resulting in thin current sheets and fast reconnection. The results accounting for radiation show time scales and outflows comparable to these observed in spicules and chromospheric jets.

Part of this chapter has been published in:
A. Alvarez Laguna, A. Lani, H. Deconinck, N. N. Mansour, and S. Poedts, **Effect of radiation on chromospheric magnetic reconnection: reactive and collisional multi-fluid simulations**, *The Astrophysical Journal, in press., 2017.*

6.1 MAGNETIC RECONNECTION IN THE SOLAR CHROMOSPHERE

Spicules dominate the dynamics of the chromosphere. They are observed to be ubiquitous at the limb and can be classified into two types [162]. Type I spicules have lifetimes of 3-7 minutes, a length ranging from a few hundred kilometers to 10 Mm, and develop speeds of 10-50 km/s [163, 164, 162, 165, 166]. This type of spicules may be the equivalent of mottles in quiet-Sun regions in the magnetic network that delimits the super granules [167], and fibrils in the active region plage regions [168]. Type I spicules, mottles, and fibrils may be caused by the leakage from the photosphere of flows and waves traveling along the magnetic field lines [165]. Type II spicules appear close to the network or plage regions and have much shorter timescales of 10-60 s, faster velocities from 50-150 km/s, and a length of 1-7 Mm [162]. Type II spicules may be driven by magnetic reconnection resulting from the interaction of photospheric regions with mixed polarity.

Small flare events that are larger than the spicules are observed to be connected with the chromospheric plasma in flux emerging regions, i.e., X-ray jets/SXR microflares, H-α surges, or EUV jets and micro flares. These hot (X-ray and EUV jets) and cool jets (H-α surge or dark EUV jet) are observed to be dynamically related to each other spatially and temporally [169, 170, 171, 172, 173]. Another type of chromospheric jet events are the chromospheric anemones observed in the Ca II H line to have an inverted Y-shape or cusp with a length of 1-4, a width of 100-400 km, a lifetime of 100-500 s, and a velocity of 5-20 km/s [11, 174], as shown in Fig. 6.1. The ejections of these jets are observed to be intermittent with a shorter periodicity of 50-60 s [175, 176, 177]. Magnetic reconnection resulting of a collision between different polarity magnetic fields may be the mechanism that drives these jets [11].

The Ellerman bombs take place in the emerging flux regions, where they create brief bursts with lifetimes of 3-4 min and energies in the range of 10^{26} and 10^{28} erg that may contribute to the heating of the chromosphere in the emerging active regions [178, 179]. More recently, IRIS observations provided evidence of similar bombs occurring in the photosphere and the low-mid chromosphere [180, 181]. These bursts, known as IRIS bombs, locally heat the plasma to $2-8{\cdot}10^4$ K and might be a result of magnetic reconnection.

In the introduction of this dissertation, we discussed how non-ideal processes that are present in partially-ionized plasma affect the dynamics of magnetic reconnection. These non-ideal processes include ambipolar diffusion, chemical and thermal non-equilibrium, radiation, etc. However, to the

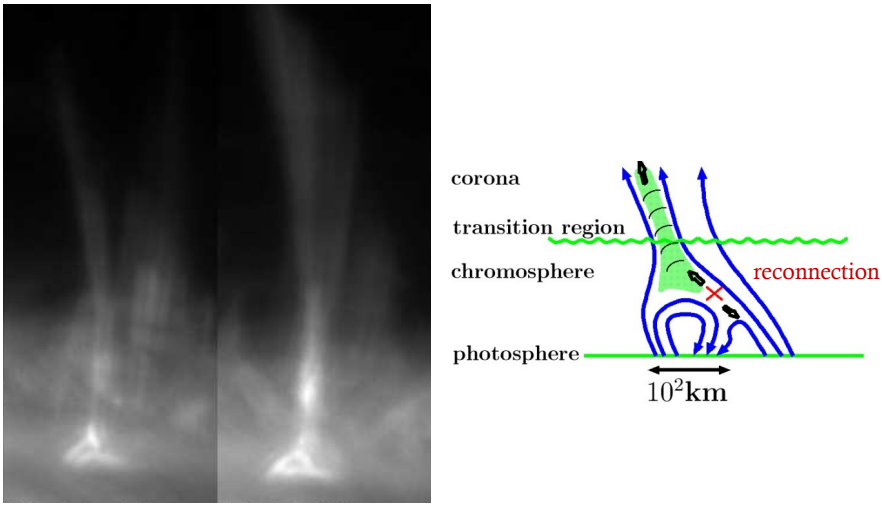

Figure 6.1: Left: observation of a Ca jet (chromospheric anemone) taken by the Hinode/SOT. Right: model of a chromospheric jet that is a result of a reconnection triggered by the collision in the chromosphere of regions with different magnetic polarity (Credits: Shibata et al. [11]).

best of our knowledge, the complex interaction between radiative cooling and multi-fluid effects, i.e., ambipolar diffusion, nonthermal and chemical equilibrium, has not been explored in depth so far. It is the aim of this paper to study this interaction systematically. We build upon the work of Leake et al. [8, 72], Murphy & Lukin [73], Smith & Sakai [182], and Sakai & Smith [183], who previously studied magnetic reconnection with two-fluid simulations. Using a self-consistent non-linear two-fluid (ion + neutral) reactive and collisional model, we study the effect of the partial ionization on the magnetic reconnection for different ionization levels from $\psi = n_i/(n_i+n_n)\cdot 100 = 0.5\%$ to 50% and fixed Lundquist number.

In this chapter, we use the two-fluid (ion+neutral) model for partially ionized plasmas that accounts for chemical reactions, collisions, transport fluxes, and radiation that is discussed in Section 3.2. The structure of the chapter is as follows. In Section 6.3 we present the initial set-up used in the different simulations, in Section 6.4 the results corresponding to the three different cases and five ionization levels are presented. The discussion and conclusions are given in Section 6.5.

6.2 ASSUMPTIONS AND NORMALIZATION

In the results, we will compare the reconnection in five ionization levels, i.e., $\psi_0 = 0.5$, 1, 5, 10, and 50%. In order to limit the complexity of this study, we will consider constant transport properties. The collisional and chemical reaction terms are computed consistently with atomic data and using local plasma conditions. Charge-exchange collisions are neglected in this work in order to compare the results to those of Leake et al. [8]. The plasma is assumed to be composed of hydrogen. Ions and electrons are considered to be in thermal equilibrium, i.e., $T_i = T_e$, and the plasma to be electrically neutral, i.e., $n_i = n_e$. The radiative losses are considered in the plasma (ion + electron) energy equation. The plasma is assumed to be optically thin, i.e., all radiation is instantaneously lost from the system.

The initial conditions are chosen to be representative of the solar chromosphere. The total mass density and the reference length are fixed in all studied cases to $\rho_0 = 5.63 \cdot 10^{-9}$ kg/m^3 and $L_0 = 10^5$ m. The reference temperature, T_0, changes with the ionization level to produce initial chemical equilibrium. The reference plasma beta is also fixed in all the cases, $\beta_0 = \frac{p_0}{B_0^2/\mu_0} = 1$, where B_0 is the reference magnetic field, p_0 the reference total pressure (ion + neutral), and μ_0 the vacuum permeability. The reference values for the different ionization level are summarized in Table 6.1.

The Hall and battery terms are neglected in Ohm's law, as in Leake et al. [8]. The ion skin depth outside the current sheet varies depending on the initial ionization degree from 1.75 m to 0.175 m, with $\psi_0 = 0.5$ and 50%, respectively. These values are small compared to the scales of the problem, and therefore the Hall and battery terms are too small compared to the resistive and ambipolar terms.

The non-dimensional numbers corresponding to the transport properties are fixed to the same constant value for all the ionization levels considered, as follows. The Lundquist number, $\mathrm{S} = v_0 \mu_0 L_0 / \eta = 10^4$, where v_0 is the reference Alfvén speed computed with the total density (ions + neutrals) and η is the resistivity. The Lundquist number is chosen to be close to the critical value, S_{cr}, that determines the development of the tearing mode instability. The Reynolds number of ions and neutrals is $\mathrm{Re}_{i,n} = \rho_0 v_0 L_0 / \xi_{i,n} = 10^4$, where $\xi_{i,n}$ is the viscosity. The neutrals Prandtl number is $\mathrm{Pr}_n = c_{p,n} \xi_n / \kappa_n = 0.625$, where $c_{p,n}$ is the specific heat at constant pressure, and κ_n the thermal conductivity. The anisotropic thermal conductivity of ions is computed with the local properties of the ion fluid, following the expressions provided by Braginskii [5].

6.3 INITIAL CONDITIONS

The initial setup reproduces a Harris sheet in partially ionized plasma in a two-fluid (ion+neutral) model similar to that in Leake et al. [8, 72]. The initial chemical and force equilibrium is studied for five ionization levels, $\psi[\%] = n_i/(n_i + n_n) \cdot 100 = 0.5,\ 1,\ 5,\ 10,$ and 50%.

As in the abovementioned references, when we use the symmetries of the problem, only one quarter of the domain is represented with dimensions $36L_0$ in the horizontal direction and $6L_0$ in the vertical direction, with the outer boundaries placed distant from the reconnection site. The size of the domain is chosen such that the results can be compared to those of Leake et al. [8] and Alvarez Laguna et al. [184]. The computational domain consists of a stretched mesh with 750×400 mesh points with a smallest cell of size 20×5 m.

The initial field is computed to be in chemical and force equilibrium. The initial ionization degree ψ_0 is assumed to be constant in the whole domain. Using the chemical reaction model, we assume $\Gamma_i^{ion} = \Gamma_n^{rec}$, and obtain the initial temperature, T_0. An initial Harris sheet is considered, as follows:

$$\vec{B} = \left(B_0 \tanh\left(\frac{y}{\lambda}\right), 0, 0\right) \tag{6.1}$$

where $\lambda = 0.5L_0$.

Assuming equilibrium of forces in the initial setup, the pressure gradient balances the initial Lorentz force, i.e., $\nabla\left(p_i + p_e + p_n\right) = \vec{j} \times \vec{B}$. With this relation, the initial densities are obtained:

$$n_{n,0} = \frac{B_0^2}{2\mu_0 k_B T_0}\left(\frac{1-\psi_0}{1+\psi_0}\right)\operatorname{sech}^2\left(\frac{y}{\lambda}\right) + n_0\left(\frac{1-\psi_0}{1+\psi_0}\right), \tag{6.2}$$

$$n_{i,0} = \frac{B_0^2}{2\mu_0 k_B T_0}\left(\frac{\psi_0}{1+\psi_0}\right)\operatorname{sech}^2\left(\frac{y}{\lambda}\right) + n_0\left(\frac{\psi_0}{1+\psi_0}\right) \tag{6.3}$$

In order to balance the initial forces of each fluid, an initial frictional force is introduced by a relative velocity between ions and neutrals. The neutrals are chosen to be at rest initially, whereas the ions move in the y-direction at the speed

$$v_i = -\frac{B_0}{\mu_0 \lambda m_{in} n_{i,0} \nu_{in}}\left(\frac{1-\psi_0}{1+\psi_0}\right)\tanh\left(\frac{y}{\lambda}\right)\operatorname{sech}^2\left(\frac{y}{\lambda}\right). \tag{6.4}$$

A perturbation in the initial magnetic field is considered in order to break the previous equilibrium. Defining $\epsilon = 0.01 B_0 L_0$, the perturbation is given

by

$$\tilde{\vec{B}}_0 = \left(-2\epsilon \frac{y}{\lambda^2} e^{-(\frac{x}{4\lambda})^2 - (\frac{y}{\lambda})^2}, \epsilon \frac{x}{8\lambda^2} e^{-(\frac{x}{4\lambda})^2 - (\frac{y}{\lambda})^2}, 0 \right). \tag{6.5}$$

In Table 6.1 we sumarize the initial parameters for the different simulations. The reference values show that the initial ionization level increases as the temperature increases. Furthermore, the magnetic field increases in order to maintain the same β_0 in all simulations. Consequently, the reference Alfvén speed and electric current increases, whereas the Alfvénic time decreases.

The transport coefficients used in all the simulations are presented in dimensional units. The transport coefficients change with the ionization level in order to maintain constant non-dimensional values for all simulations. The heat conduction of the plasma uses the expressions from Braginskii [5] accounting for the anisotropy introduced by the magnetic field. Additionally, the Ohmic resistivity used in the simulations η, is compared to the physical resistivity η_S, which is the result of the collision of electrons with ions and neutrals, and is computed as described in Khomenko et al. [2].

Similarly, the collisional and chemical reaction frequencies are also shown normalized with the Alfvénic transit time. In general, the ion-neutral collisional frequency decreases as the ionization degree increases, whereas the neutral-ion collisions increase. On the other hand, both reaction rates increase with increasing ionization degree, as they are functions that increase as the electron number density increases.

Table 6.1: Reference values, transport coefficients and non-dimensional characteristic frequencies for the different ionization levels studied in this paper. All simulations use the same reference density $\rho_0 = 5.63 \cdot 10^{-9}$ kg/m^3, reference length $L_0 = 10^5$ m and non-dimensional numbers, $\beta_0 = 1$, S $= 10^4$, Re$_{i,n} = 10^4$ and Pr$_n = 0.625$.

	$\psi_0 = 0.5\%$	$\psi_0 = 1\%$	$\psi_0 = 5\%$	$\psi_0 = 10\%$	$\psi_0 = 50\%$
T_0[K]	10390	10855	12131	12808	15296
B_0[T]	$7.81{\cdot}10^{-4}$	$8{\cdot}10^{-4}$	$8.62{\cdot}10^{-4}$	$9.07{\cdot}10^{-4}$	$1.16{\cdot}10^{-3}$
n_0[m^{-3}]	$3.38{\cdot}10^{18}$	$3.4{\cdot}10^{18}$	$3.53{\cdot}10^{18}$	$3.7{\cdot}10^{18}$	$5.05{\cdot}10^{18}$
v_0[m/s]	9281.6	9510.5	10251.1	10781.2	13758.1
j_0[A/m^2]	$6.21{\cdot}10^{-3}$	$6.37{\cdot}10^{-3}$	$6.86{\cdot}10^{-3}$	$7.22{\cdot}10^{-3}$	$7.22{\cdot}10^{-3}$
t_0[s]	10.7	10.5	9.75	9.27	7.27
$\eta[\Omega \cdot \mathrm{m}]$	0.116	0.119	0.129	0.135	0.173
$\eta_S[\Omega \cdot \mathrm{m}]$	$3.55{\cdot}10^{-3}$	$3.10{\cdot}10^{-3}$	$2.42{\cdot}10^{-3}$	$2.18{\cdot}10^{-3}$	$1.62{\cdot}10^{-3}$
$\xi_{i,n}$[Pa $\cdot$ s]	$5.22 \cdot 10^{-4}$	$5.35 \cdot 10^{-4}$	$5.76 \cdot 10^{-4}$	$6.07 \cdot 10^{-4}$	$7.75 \cdot 10^{-4}$
$\kappa_n[\mathrm{W/m \cdot K}]$	17.2	17.7	19.05	20.04	26.6
$\nu_{in}t_0$	$1.06{\cdot}10^{5}$	$1.05{\cdot}10^{5}$	$9.93{\cdot}10^{4}$	$9.19{\cdot}10^{4}$	$4.37 \cdot 10^{4}$
$\nu_{ni}t_0$	$5.34{\cdot}10^{2}$	$1.07{\cdot}10^{3}$	$5.22{\cdot}10^{3}$	$1.02{\cdot}10^{4}$	$4.37 \cdot 10^{4}$
$\nu^{ion}t_0$	$2.50{\cdot}10^{-4}$	$9.61{\cdot}10^{-4}$	$2.19{\cdot}10^{-2}$	$8.58{\cdot}10^{-2}$	2.77
$\nu^{rec}t_0$	$4.98{\cdot}10^{-2}$	$9.5{\cdot}10^{-2}$	0.42	0.77	4.76

6.4 RESULTS

The two-fluid (ion+neutral) model discussed in Section 3.2 that accounts for reactions, collisions, and transport fluxes is used to study magnetic reconnection in five different levels of ionization and radiative cooling models. We first present the results without radiative losses and then we compare the two radiative models: an approximation of the optically thin losses, and an approximation of the chromospheric radiative cooling with and without background heating. For each case, we compare the reconnection rate defined as $M = E_z^*/v_A^* B_{up}$, where E^* is the electric field at the null point, B_{up} is the magnetic field measured at the y-coordinate where the electric current is $j_z^{max}/2$; and $v_A^* = B_{up}/\sqrt{\mu_0(\rho_i^* + \rho_n^*)}$ is the Alfvén speed computed with the total density (ions + neutrals) measured at the latter point. We also compare the evolution in time of the outflow velocity V_{out}, defined as the maximum of the ion velocity in the x-direction along the line $y = 0$, the current sheet width δ^*, defined as the y coordinate of the point where the current is half of its maximum along the vertical line that crosses the null point; the ion-

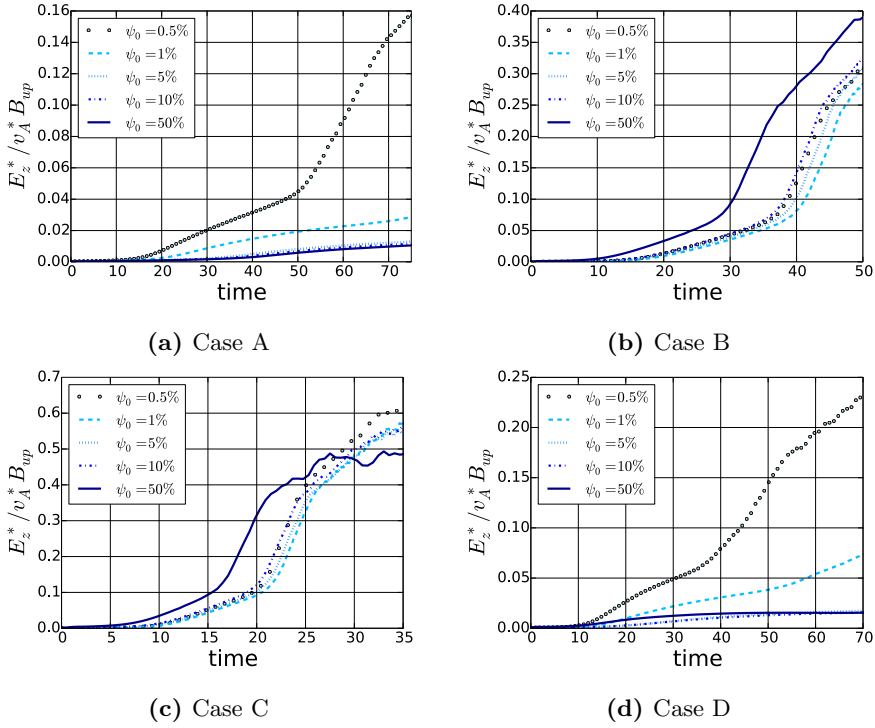

(a) Case A **(b)** Case B

(c) Case C **(d)** Case D

Figure 6.2: Dimensionless reconnection rate of the different cases.

ization degree and the plasma pressure P_p at the null point. Additionally, the evolution of the relative velocity between neutrals and ions is studied in the inflow and outflow (in the following, referred to as "drift" velocity, as in Khomenko et al. [185]) . The evolution in time of the maximum outflow drift velocity is measured as the maximum difference between the horizontal velocities of the fluids at a point along the line $y = 0$ normalized with the horizontal velocity of ions at the same point. Alternatively, the evolution of the maximum inflow drift velocity is measured as the maximum difference between the vertical velocities of the fluids at a point along the vertical line that crosses the null point and it is also normalized with the vertical ion velocity at the mentioned point.

6.4.1 Case A: Study without radiative losses

Figure 6.3 shows the electric current and the magnetic lines for five ionization levels, $\psi_0 = 0.5$, 1, 5, 10, and 50%, at the same non-dimensional time ($t = 45$). All simulations evolve initially with a Sweet-Parker configuration, and only the simulation with the lowest ionization degree, i.e., $\psi_0 = 0.5\%$, develops the tearing mode instability. As predicted by the theory, the current sheet is thinner for low ionization levels as the ambipolar diffusion is stronger. Moreover, the reconnection is faster because of the recombination effect, which removes ions from the reconnection layer, which has a stronger effect in the low-ionization cases.

The evolution of the reconnection rate is shown in Fig. 6.2a. The fastest reconnection corresponds to the weakly ionized case, $\psi_0 = 0.5\%$. At $t = 75$, it is 16 times faster than the Sweet-Parker reconnection rate, i.e., $M_{S-P} = 1/\sqrt{\mathrm{S}} = 0.01$. The reconnection rate increases after $t = 50$ when plasmoids start forming. The cases with $\psi_0 = 5 - 50\%$ evolve very similar, with a reconnection rate that tends to $M = 0.01$, the Sweet-Parker reconnection rate for fully ionized plasmas.

The initiation of the tearing mode instability is strongly affected by the ionization degree inside the current sheet. Even though all simulations have the same Lundquist number, the tearing mode develops earlier in the case of initial ionization $\psi_0 = 0.5\%$, at $t = 55$ with $\sigma = \delta^*/L^* = 1/200$, where L^* is the x-coordinate of the point where the V_{out} is measured.

In Fig. 6.4a the evolution in time of the outflow velocity is shown. The value of the non-dimensional outflow velocity is higher for the lowest ionization level and reaches about half of the Alfvén speed (~ 5.1 km/s) after $t = 80$ (~ 14 minutes). Fig. 6.4b shows the evolution of the current sheet width δ^*. The reconnection layer thins as the simulation evolves in a way that is affected by the ambipolar diffusions. The current sheet width of the simulation with $\psi = 0.5\%$ decreases from $0.5L_0$ (50,000 m) to $4 \cdot 10^{-3} L_0$ (400 m) after 70 transit times.

In Figs. 6.4c and 6.4d, the evolution of the ionization degree and the plasma pressure is shown. Under these conditions, both magnitudes remain almost constant, increasing only in the cases of low ionization through Joule heating.

Figs. 6.4e and 6.4f show the evolution of the maximum inflow and outflow ion-neutral drift velocities. In Fig. 6.4e the maximum outflow drift velocity is much lower than the ion velocity at the same point in all ionization levels. This means that the horizontal motions of the fluids are coupled in the outflow. However, in Fig. 6.4f, the inflow drift velocity is comparable to the ion

h

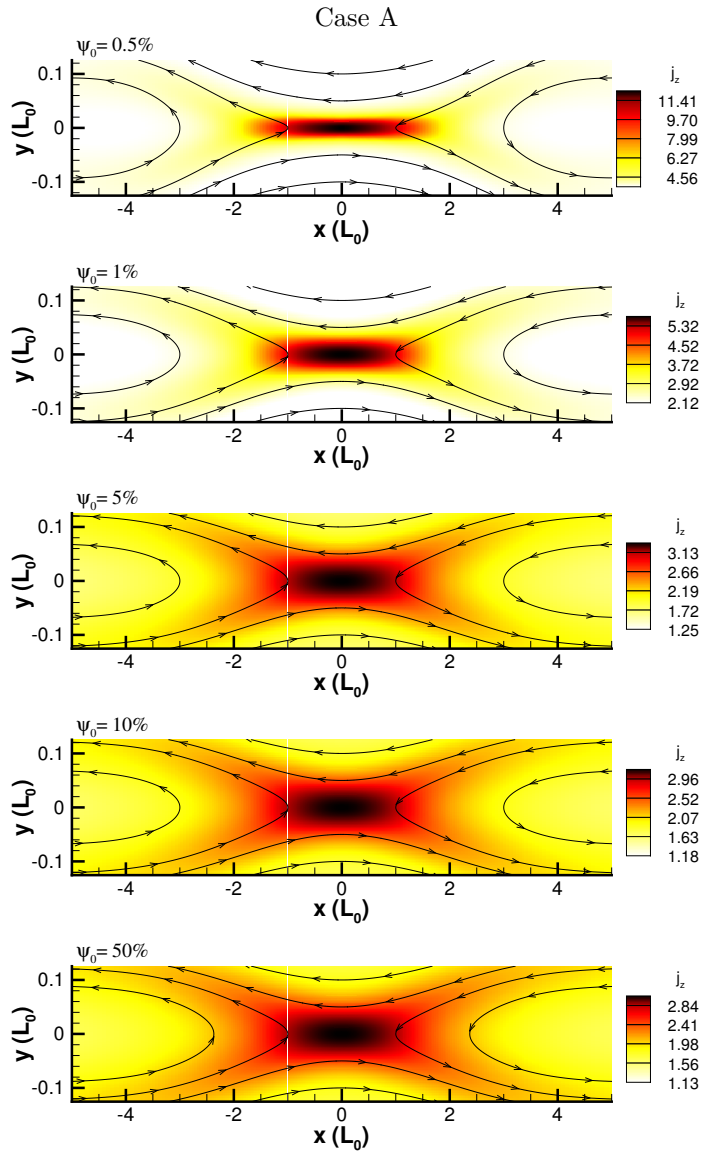

Figure 6.3: Snapshot of the current and the magnetic field lines at $t = 45$ for the initial ionization levels $\psi_0 = 0.5\%$, $\psi_0 = 1\%$, $\psi_0 = 5\%$, $\psi_0 = 10\%$ and $\psi_0 = 50\%$ without radiation model.

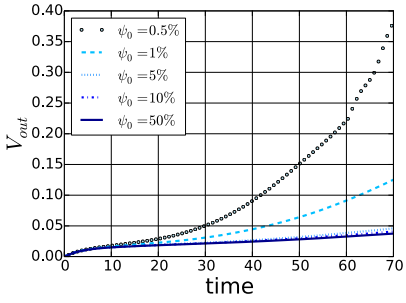

(a) Outflow velocity

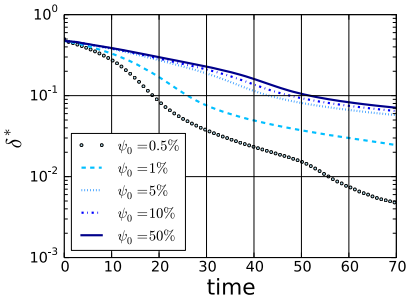

(b) Current sheet width

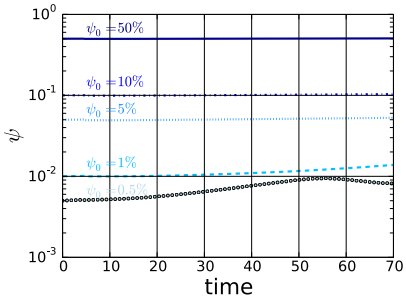

(c) Ionization degree at the X-point

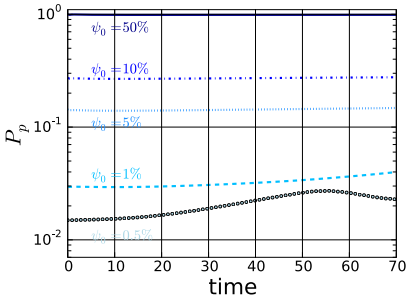

(d) Plasma pressure at the X-point

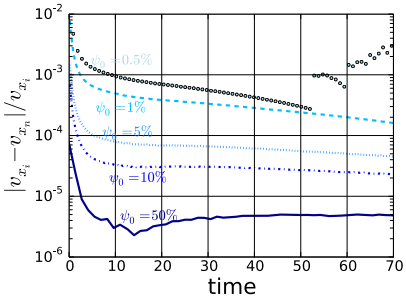

(e) Maximum horizontal drift velocity in the outflow

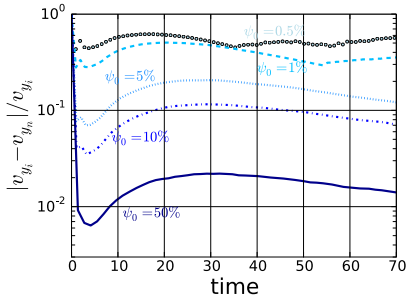

(f) Maximum vertical drift velocity in the inflow

Figure 6.4: Evolution in time of outflow velocity at $x = L^*$, current sheet width δ^*, ionization degree at the X-point, plasma pressure at the X-point, maximum horizontal drift velocity in the outflow and maximum vertical drift velocity in the inflow of Case A.

velocity in the cases with ionization $\psi_0 = 0.5 - 5\%$, as the maximum difference of the inflow velocities reaches $10 - 60\%$ of the ion velocity. The reason of the decoupled inflow motions of the fluids is that the neutral-ion mean free path becomes comparable to the current sheet width. These results are in agreement with Leake et al. [8, 72].

6.4.2 Case B: Optically thin radiative losses in a hydrogen plasma

The same simulations are now studied with the radiation model $Q_R^{(1)}$, described in Sec. 3.2.2, an approximation for the optically thin radiative losses in a hydrogen plasma [8, 98]. The electric current and the magnetic field topology at $t = 45$ is presented in Fig. 6.5.

In Fig. 6.2b, the highest reconnection rate after $t = 50$ corresponds to $\psi_0 = 50\%$, which is around 39 times faster than the Sweet-Parker rate. The evolution of the outflow velocity, Fig. 6.6a, shows that the fastest outflows are produced in the simulation with $\psi_0 = 50\%$, reaching $V_{out} \sim 0.4 v_0$ (5.5 km/s) after 42 Alfvén transit time units ($\sim$ 5 minutes). These scales are closer to the scales observed in chromospheric jets and spicules.

As seen in Fig 6.6b, the current sheet shrinks at a faster rate than without radiation. After 50 transit times, all the simulations reduced the current sheet width to $2 \cdot 10^{-3} L_0 - 4 \cdot 10^{-3} L_0$ ($200 - 400$ m). This thinning is produced by the radiative cooling that reduces the pressure inside the current sheet and decreases the ionization level, as it can be seen in Figs. 6.6c and 6.6d. The radiative losses increase as the temperature increases. For this reason, the simulation with $\psi_0 = 50\%$ experiences the strongest cooling, evolves faster, and develops the tearing mode instability first.

Figs. 6.6e and 6.6f show that the fluids move coupled in the outflow, whereas they are decoupled in the inflow for all ionization levels. The discontinuities that appear after $t = 30$ in the maximum outflow drift velocity are produced by the formation of plasmoids. The appearance of the plasmoid instability enhances the decoupling of the horizontal motion as the small scales of the plasmoids can become comparable to the neutral-ion collisional mean free path.

The initiation of the tearing mode is strongly affected by the radiation and the reactions. As radiation is stronger in $\psi_0 = 50\%$, the tearing mode starts earlier, at $t = 30$. As Fig. 6.5 shows, in the other ionization levels, the current starts to break around $t = 40$. The aspect ratio of the sheet is around $\sigma \sim 1/200$ for all simulations when the instability starts.

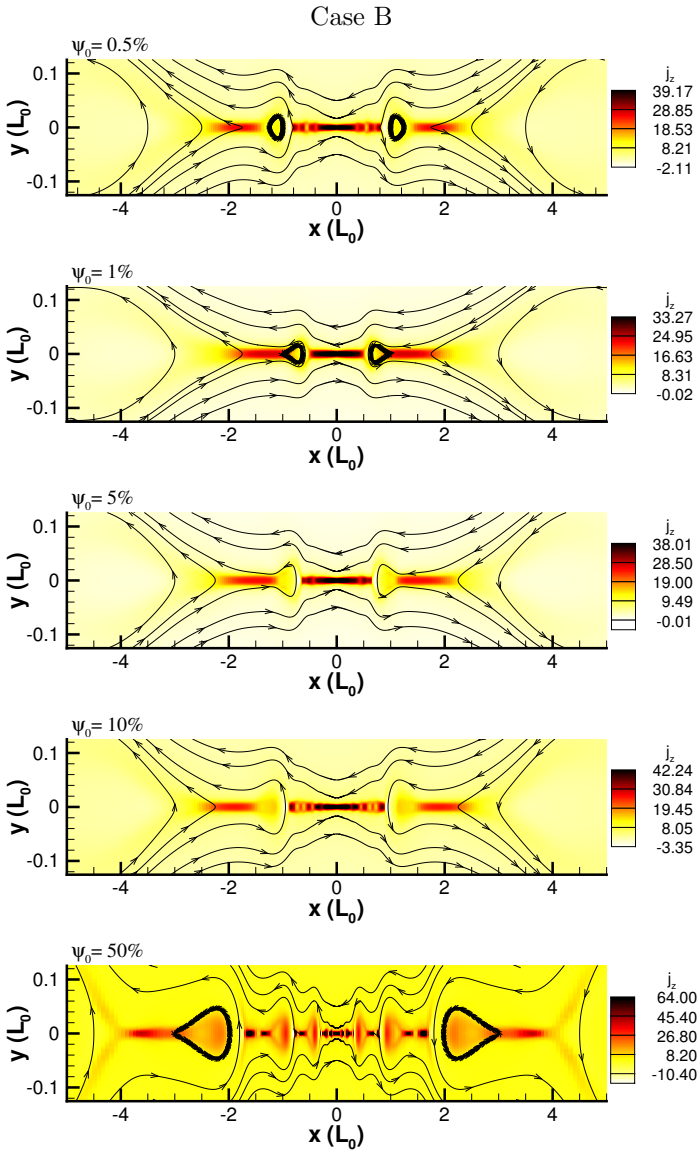

Figure 6.5: Snapshot of the current and the magnetic field lines at $t = 45$ for the initial ionization levels $\psi_0 = 0.5\%$, $\psi_0 = 1\%$, $\psi_0 = 5\%$, $\psi_0 = 10\%$ and $\psi_0 = 50\%$ using the model for optically thin radiative losses in a hydrogen plasma.

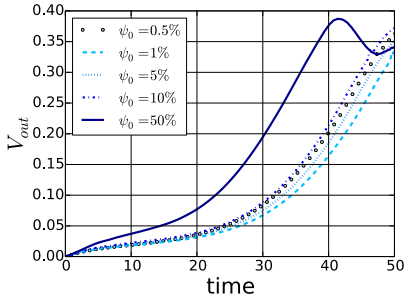

(a) Outflow velocity

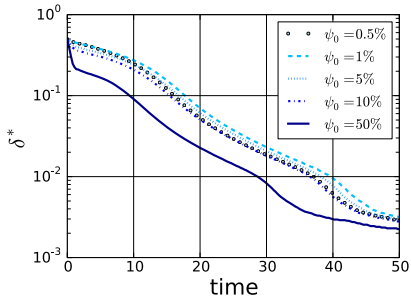

(b) Current sheet width

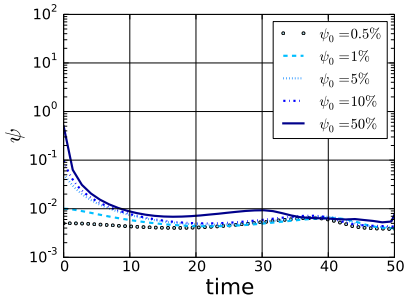

(c) Ionization degree at the X-point

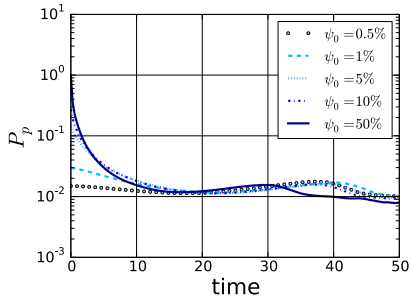

(d) Plasma pressure at the X-point

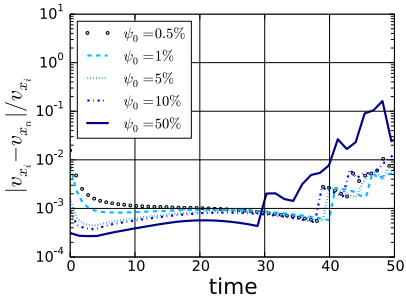

(e) Maximum horizontal drift velocity in the outflow

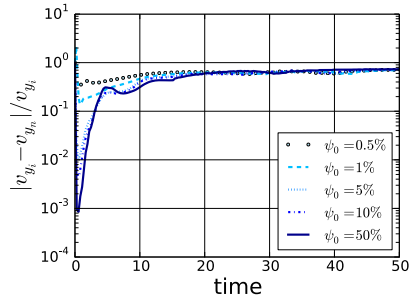

(f) Maximum vertical drift velocity in the inflow

Figure 6.6: Evolution in time of outflow velocity at $x = L^*$, current sheet width δ^*, ionization degree at the X-point, plasma pressure at the X-point, maximum horizontal drift velocity in the outflow and maximum vertical drift velocity in the inflow of Case B.

6.4.3 Case C: Model for radiative losses with photospheric abundances

The radiation model $Q_R^{(2)}$, a more realistic approximation for a plasma with chromospheric composition, is now considered. As this model produces greater radiative losses than $Q_R^{(1)}$, the processes are similar to Case B, but with a faster evolution.

Fig. 6.7 shows the current and magnetic field lines at $t = 25$. All ionization levels have started already the tearing mode instability. The simulations with $\psi_0 = 0.5 - 5\%$ have a similar topology at this time, whereas $\psi_0 = 50\%$ has evolved faster and developed several small plasmoids. The tearing mode is initiated around $t = 20$ for the simulations with $\psi_0 = 0.5 - 5\%$ and slightly earlier, at $t = 17$ for the simulation with $\psi_0 = 50\%$. The instability starts when the aspect ratio of the current sheet is around $\sigma = 1/200$ for all simulations.

In Fig. 6.2c, the maximum reconnection rate is shown for the simulation $\psi_0 = 50\%$ until $t = 25$. After this time, all simulations have similar rates, between $M \sim 0.5 - 0.6$. The outflow velocity in Fig. 6.8a is on the order of $V_{out} = 0.5V_0$ after $t = 25$ for all simulations. In dimensional units, the simulation with $\psi_0 = 50\%$ reaches a speed of 7.6 km/s after 3 minutes, i.e., magnitudes in the range of spicules and flares. In Fig. 6.8b, the width of the current sheets decreases to $2 \cdot 10^{-3}$, which is lower than in the previous cases. The ionization and plasma pressure at the null point, Figs. 6.8c and 6.8d, evolve similarly to Case B, finding small fluctuations in the ionization degree that are caused by the movement of the small plasmoids that are formed. Figs. 6.8e and 6.8f show that the inflow motion is decoupled for all ionization levels, whereas the outflow motion is coupled until the formation of plasmoids, where the horizontal motion can become locally decoupled, i.e., the drift velocity is around the 10% of the ion velocity.

6.4.4 Case D: Model for radiative losses with photospheric abundances with ad hoc background heating

In Case D, we reproduce the simulations of Case C, using $Q_R^{(2)}$ for the radiative losses and including a heating term that balances the radiation of the background plasma at the initial time. The topology of the magnetic field and the current is presented in Fig. 6.9. The magnitudes of the electric current are comparable to those of Case A, as the cooling is not as fast as in

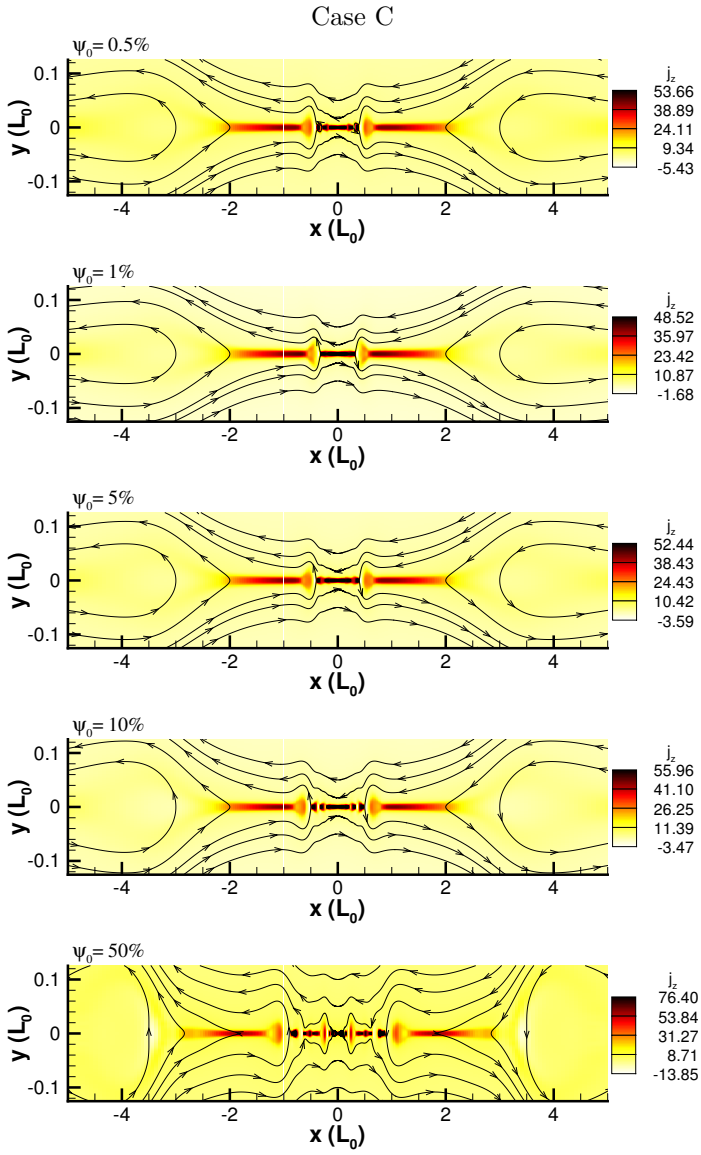

Figure 6.7: Snapshot of the current and the magnetic field lines at $t = 25$ for the initial ionization levels $\psi_0 = 0.5\%$, $\psi_0 = 1\%$, $\psi_0 = 5\%$, $\psi_0 = 10\%$ and $\psi_0 = 50\%$ using the model for radiative losses of a plasma with chromospheric abundances.

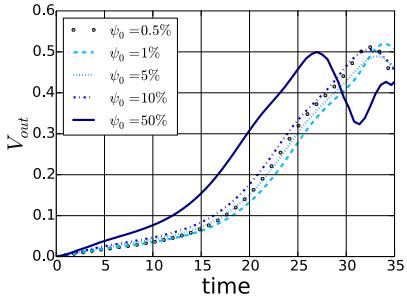

(a) Outflow velocity

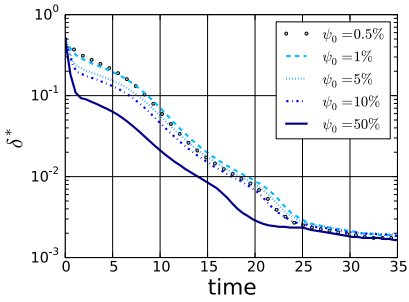

(b) Current sheet width

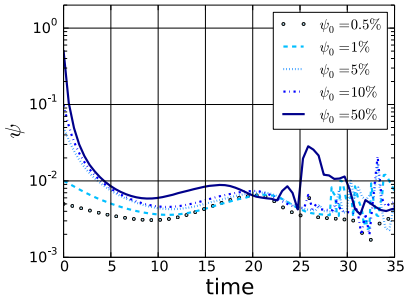

(c) Ionization degree at the X-point

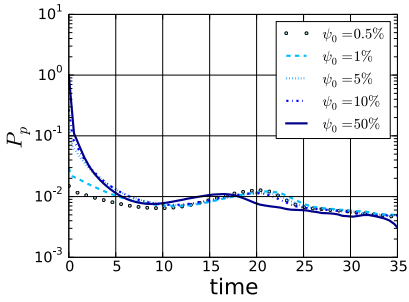

(d) Plasma pressure at the X-point

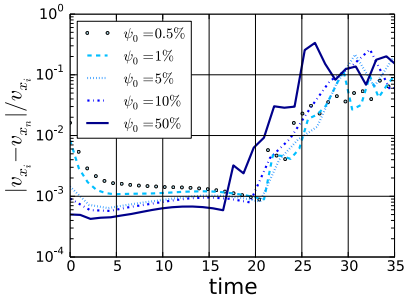

(e) Maximum horizontal drift velocity in the outflow

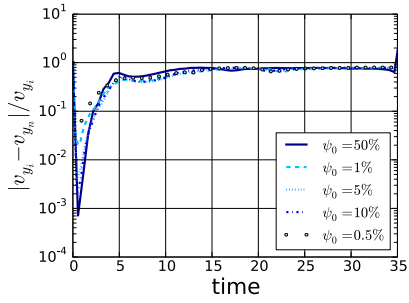

(f) Maximum vertical drift velocity in the inflow

Figure 6.8: Evolution in time of outflow velocity at $x = L^*$, current sheet width δ^*, ionization degree at the X-point, plasma pressure at the X-point, maximum horizontal drift velocity in the outflow and maximum vertical drift velocity in the inflow of Case C.

Case B. The thinnest current sheet corresponds to the case with $\psi_0 = 0.5\%$, which already started developing the tearing mode instability. The tearing mode starts at $t = 38$ in $\psi_0 = 0.5\%$, $t = 65$ in $\psi_0 = 1\%$ with approximately $\sigma = 1/200$.

The reconnection rate of this case is presented in Figure 6.2d. For all the ionization levels, the reconnection rate is faster than Case A and slower than the case without background heating. Owing to the tearing mode instability, the reconnection is faster in the low ionized case, $\psi_0 = 0.5\%$, after $t = 35$. The simulation with $\psi_0 = 50\%$ has an initially enhanced reconnection rate until the radiative cooling is balanced by the Joule heating.

The fastest outflow velocity, in Fig. 6.10a, occurs in the case with $\psi_0 = 0.5\%$. The maximum value is $V_{out} \sim 0.4V_0$ (4.6 km/s), at $t = 70$ (12 minutes). The shrinking of the current sheet width is faster than in Case A, as we show in Fig. 6.10b. It reaches $3 \cdot 10^{-3} L_0$ (300 m) after 70 Alfvénic transit times. In the case of $\psi_0 = 50\%$, the initial loss of ions and plasma pressure at the current sheet produces a thinner current sheet that results in a fast acceleration of the outflow jet. However, when the cooling is compensated for by the Joule heating, the rate at which the current sheet thins decreases. The plasma pressure and the ionization degree are affected by the initial cooling in the cases with higher ionization and remains constant after $t = 10$, as shown in Figs 6.10c and 6.10d. As in Case A, the outflow motion of the fluids is coupled (Fig 6.10e), and the inflow motion (Fig. 6.10e) is decoupled in the low-ionization cases, i.e., $\psi = 0.5 - 5\%$.

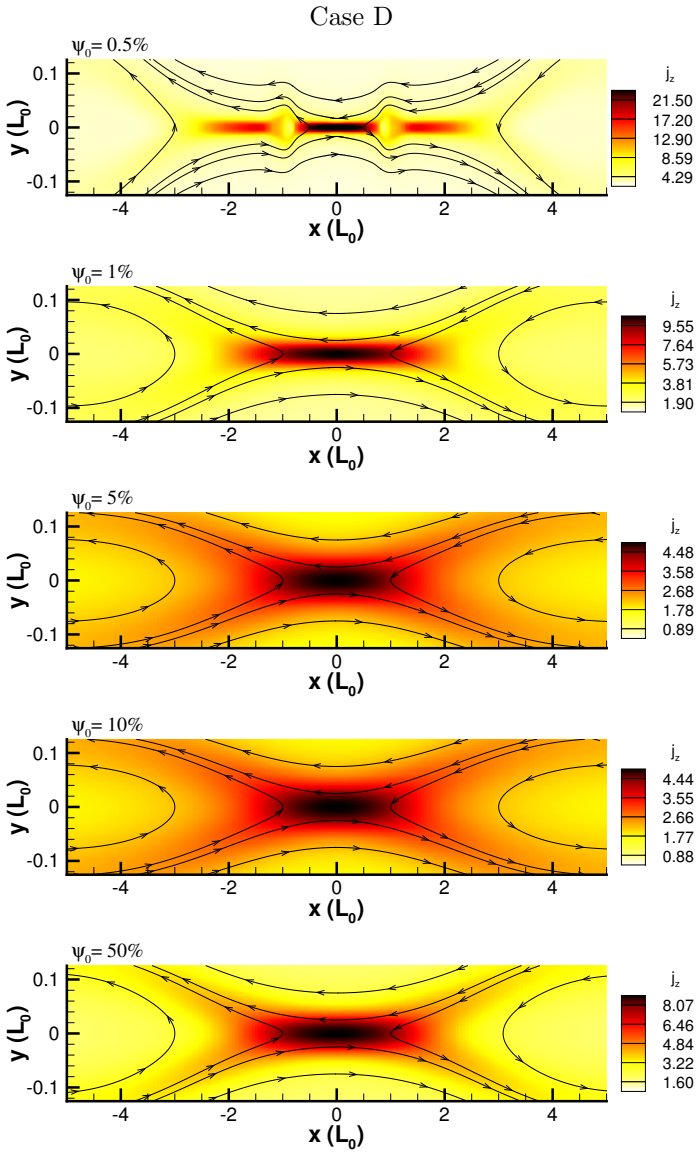

Figure 6.9: Snapshot of the current and the magnetic field lines at $t = 45$ for the initial ionization levels $\psi_0 = 0.5\%$, $\psi_0 = 1\%$, $\psi_0 = 5\%$, $\psi_0 = 10\%$ and $\psi_0 = 50\%$ using the model for radiative losses of a plasma with chromospheric abundances with ad hoc background heating.

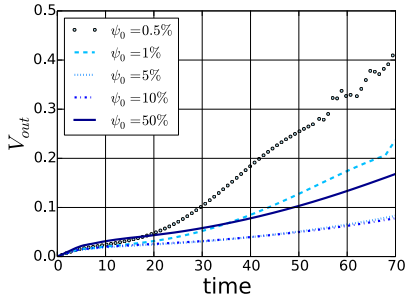

(a) Outflow velocity

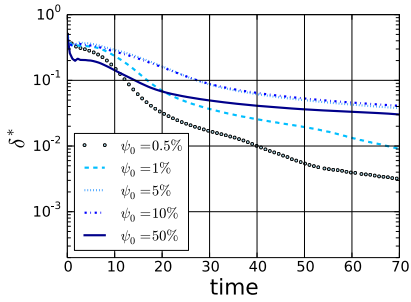

(b) Current sheet width

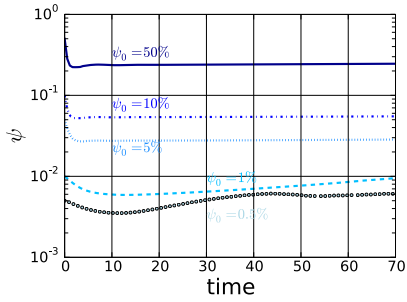

(c) Ionization degree at the X-point

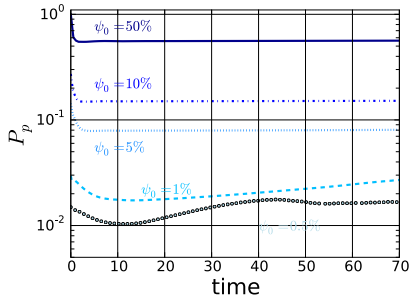

(d) Plasma pressure at the X-point

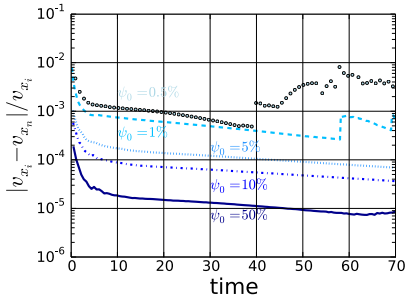

(e) Maximum horizontal drift velocity in the outflow

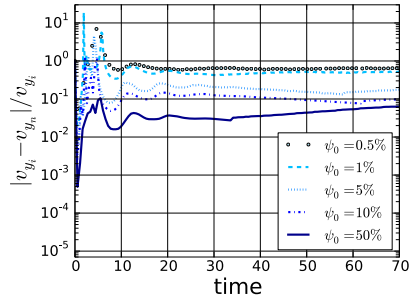

(f) Maximum vertical drift velocity in the inflow

Figure 6.10: Evolution in time of outflow velocity at $x = L^*$, current sheet width δ^*, ionization degree at the X-point, plasma pressure at the X-point, maximum horizontal drift velocity in the outflow and maximum vertical drift velocity in the inflow of Case D.

6.5 DISCUSSION AND CONCLUSIONS

We have studied the magnetic reconnection in partially ionized plasmas under chromospheric conditions in five different ionization levels ranging from 0.5% to 50%. The simulations were obtained using a self-consistent two-fluid model (plasma + neutrals) with fixed Lundquist number and accounting for collisions and chemical reactions consistently with the local plasma conditions. We considered four different cases in order to study systematically the influence of radiation in reconnection in partially ionized plasmas: (A) without radiation; (B) considering a model of radiation for optically thin plasmas; (C) considering a model of radiation based on the chromospheric elemental abundances and (D) the same previous model with a background heating function.

The results without radiation (Case A) are in good qualitative agreement with previous analytical work [56, 65, 57, 58] that predicted reconnection to be faster in lowly ionized plasmas. In our results, the current sheet width is thinner in lowly ionized plasmas because of the ambipolar diffusion that sharpens the magnetic field profile. After 70 Alfvénic transit times, the width of the current sheet of the simulation with $\psi_0 = 0.5\%$ is more than one order of magnitude thinner than in the simulation of $\psi_0 = 50\%$. In addition, the loss of ions produced by recombination enhances reconnection, having a major effect in low ionized plasmas. The reconnection rate of the simulations $\psi_0 = 5{-}50\%$ tends to the Sweet-Parker rate for fully ionized plasmas, whereas the one of $\psi_0 = 0.5\%$ is 16 times faster. The outflow velocity is also higher in the lowly ionized case, reaching a velocity of 4.6 km/s after 963 s ($\approx$ 16 minutes). However, the time taken to reach this speed is much longer than in spicules or chromospheric jets.

Cases B and C studied the same setup with two models for radiative cooling: one for a reactive hydrogen plasma, and the other for a plasma with a chromospheric composition. Radiation is stronger for high ionization levels, as it is an increasing function of the electrons density and the temperature. The fast initial cooling reduces the ionization level at the center of the current sheet, reducing the plasma pressure and producing a fast thinning of the current sheet. The simulation with $\psi_0 = 50\%$ produces the fastest reconnection in Case B. In Case C, since the radiative losses are stronger, magnetic reconnection develops very fast, reaching rates 60 times faster than the Sweet-Parker rate. Moreover, the outflows produced are much faster with radiation, reaching 7.6 km/s after 181 s ($\approx$ 3 minutes), which is closer to the acceleration observed in spicules and chromospheric anemones.

Case D considers the same radiation model as Case C, with background

heating. The external heating suppresses the enhanced reconnection found in the previous results, showing slightly faster rates than the case without radiation.

Partial ionization and radiation affects the formation and growth of the tearing mode instability. In agreement with previous work for fully ionized plasma [66, 67, 68], the tearing mode is initiated when the aspect ratio of the current sheet is around $\sigma \sim 1/200$. Ambipolar diffusion and radiative cooling thin the current sheet efficiently, enhancing the appearance of the tearing mode instability compared to the same conditions in fully ionized plasmas. The latter is in agreement with the observations of intermittent reconnection by Singh et al. [176] and Yan et al. [177]. The formation of plasmoids are also found by Ni et al. [70] in single-fluid simulations with ambipolar diffusion under cromospheric conditions where they are identified as a possible candidate for fast reconnection.

The use of multi-fluid models allows for capturing the relative velocity between ions and neutrals. In our simulations, we observed the ion-neutral drift velocity to reach $60-80\%$ of the ion velocity in the inflow when radiation was strong or when the flow was weakly ionized without radiation. In contrast, the outflow motion is strongly coupled, being the drift velocity around two orders of magnitude smaller than in the inflow. The same has been observed in the two-fluid simulations by Leake et al. [8, 72] and Murphy & Lukin[73]. In addition, recent observational data of prominences [185] confirmed the existence of transients where ions and neutrals flow decouple.

In the present study, the Lundquist number was fixed in all simulations to a value close to the critical value in order to study the effect of radiation and partial ionization in the formation of the tearing mode instability. As shown in Table 6.1, the physical resistivity η_S is around two orders of magnitude smaller than the resistivity imposed in the simulations η. Leake et al. [8] showed that the reconnection rate becomes independent of the Lundquist number, i.e., is in the "fast" reconnection regime, when the recombination scales are comparable to the outflow scales in the reconnection region. As shown in the results, the simulations with strong radiation and the weakly ionized cases ($\psi = 0.5 - 1\%$) without radiation are in this fast-reconnection regime as the recombination dominates or is comparable to the outflow scales. However, in the highly ionized cases without radiation, the ionization imbalance is less important. Therefore, the latter simulations would be slower using the physical resistivity as they scale as the Sweet-Parker reconnection, i.e., $M \sim 1/\sqrt{\mathrm{S}}$.

However, the current sheet width would change using the physical resistivity as the aspect ratio scales as $\sigma \sim 1/\mathrm{S}$ in the fast regime and $\sigma \sim 1/\sqrt{\mathrm{S}}$

in the Sweet-Parker regime [8]. This would produce a stronger decoupling of the fluids in the inflow. However, the inclusion of charge-exchange collisions, with larger cross-sections, can increase this coupling. In addition, in the present work, the Hall effect was neglected as the ion inertial length is much greater than the current sheet thickness. With the physical resistivity, the latter effect can become important, as shown experimentally by Lawrence et al. [186] and in simulations by Murphy et al. [73]. This further study is left to a future follow-up work.

6.6 SUMMARY

The main results of this study can be summarized as follows:

1. Partial ionization and chemical non-equilibrium affect the dynamics and scales of reconnection. Without radiation, the effect is significant only for $\psi_0 \leq 1\%$. Moreover, the tearing mode instability is initiated earlier for lowly ionized plasmas, as the current sheet shrinks at a faster rate.

2. Radiative cooling decreases the plasma pressure and modifies the chemical equilibrium inside the current sheet. Magnetic reconnection is enhanced as the current sheet shrinks very efficiently and ions recombine very fast. The tearing mode instability appears earlier than without radiation.

3. Results with radiative cooling show velocities and time scales comparable to those observed in spicules and chromospheric jets.

4. With background heating, the enhanced reconnection is reduced in the cases with more ionization level, i.e. $\psi_0 = 5 - 50\%$, but is still faster than without radiative loses.

5. The tearing mode instability in reactive and radiating partially ionized plasmas initiates when the aspect ratio of the current sheet is around 1/200, similar value to fully ionized plasmas. However, it appears earlier than in fully ionized plasmas and grows at faster rate.

6. The motion of ions and neutrals decouple in the inflow, whereas they are strongly coupled in the outflow. The coupling in the outflow can be locally weaker when plasmoids are formed.

CHAPTER 7

Multi-fluid Modeling of Magnetosonic Wave Propagation in the Solar Chromosphere: Effects of Impact Ionization and Radiative Recombination

As in nature, all is ebb and tide, all is wave motion...

– Nikola Tesla

We study the effects of ion-neutral interactions on the propagation of magnetosonic waves in the partially ionized solar chromosphere. The dynamic ionization and recombination reactions are studied in gravitationally stratified magnetized collisional media with a two-fluid model for partially-ionized plasma. The initial density and temperature profiles are similar to VAL III chromospheric model in which dynamical, thermal and chemical equilibrium are considered to ensure comparison to existing MHD models. In this initial setup we include a simple homogeneous flux tube magnetic field configuration and an external photospheric velocity driver to simulate the propagation of magnetosonic waves in the partially ionized reactive chromosphere. We study the loss of chemical equilibrium and the plasma heating related to the steepening of fast magnetosonic wave fronts in the gravitationally stratified medium.

Part of this chapter has been published in:
Y. Maneva, A. Alvarez Laguna, A. Lani, and S. Poedts, **Multi-fluid Modeling of Magnetosonic Wave Propagation in the Solar Chromosphere: Effects of Impact Ionization and Radiative Recombination**, *The Astrophysical Journal, Volume 836, Issue 2, article id. 197, 15 pp. (2017).*

7.1 WAVE PROPAGATION IN THE SOLAR CHROMOSPHERE

As mentioned in the introduction of this dissertation, the solar chromosphere and transition region regulate the mass, energy and momentum transfer from the underlying photosphere and convection zones into the upper atmospheric layer, known as the corona. The complexity of the chromosphere is related to its partially ionized plasma, which is not in local thermodynamical equilibrium. As we follow the decreasing plasma density and pressure gradients through the chromosphere, the plasma behavior changes from highly collisional to weakly collisional and the system transitions from gas-pressure dominated to magnetically driven. These observed plasma properties affect the propagation of magneto-hydrodynamic waves through the chromospheric layer and influence the deposition of energy and related plasma heating there.

In Fig. 7.1, we present the frequencies of binary collisions between hydrogen atoms, protons, and electrons as a function of height. In this figure, we consider the temperature and density distribution of Vernazza et al. [1] and a constant magnetic field of 10^{-3} T. We can note that from heights around $z \sim 600$ km, the electron gyrofrequency becomes larger than the largest electron collisional frequency. As a result, the electrons become magnetized and therefore their transport properties are anisotropic. Alternatively, for heights below $z \sim 2300$ km, the ion gyrofrequency is smaller than the ion-electron collisional frequency (note that the latter is the same as the electron-ion frequency). Therefore, the ions do not get magnetized until the transition region. Another important feature is the decrease of seven orders of magnitude of the ion-neutral and electron-neutral collisional frequencies across the atmosphere. This has a strong impact in the properties of the plasma and its interaction with the magnetic field.

Owing to the change of the plasma properties across the atmosphere, more attention has been drawn to the consequences of ion-neutral interactions on the propagation of MHD waves throughout the chromosphere [187, 188]. Analytical calculations have suggested that the dominant presence of neutrals in the chromosphere would lead to an over-damping of the Alfvén waves there, which would change their commonly expected energy deposition in the corona [188]. Nevertheless, there are no rigorous calculations of partial ionization effects on the propagation and damping of Alfvén, fast, and slow magnetosonic waves in a reactive gravitationally stratified collisional media and their interaction with the surrounding plasma. In this respect, the present model provides a first attempt to consider such interactions within chemically reactive multi-fluid simulations.

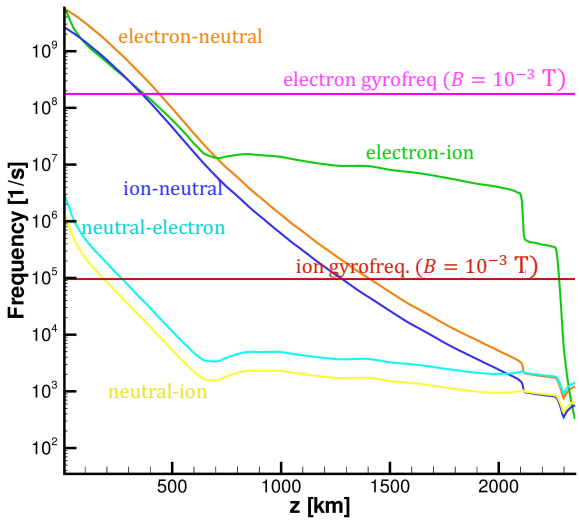

Figure 7.1: Collisional frequencies in the solar atmosphere using the VAL-C model [1].

7.2 ASSUMPTIONS

In this chapter, we use the two-fluid model for partially-ionized hydrogen plasmas that was described in Section 3.2. Unlike Chapter 6 where the transport properties were fixed, here, the viscosity, heat conduction, and resistivity coefficients depend on the local plasma properties. The radiative cooling is not accounted for as there is no heating mechanism included that balances it at the initial time as this heating mechanism is at present unknown. The Hall, battery, and neutral-electron drift terms are disregarded in Ohm's law, Eq. (3.26), as the normalized ion skin depth is considered to be much smaller than the convective and resistive term. Note that, as in Chapter 6, the ambipolar diffusion that results from the drift between ions and neutrals is captured as this is a two-fluid model.

The model for ionization and recombination that was presented in Chapter 6 considers a plasma composed uniquely by hydrogen. However, the lower atmosphere of the Sun contains a small percentage of heavy ions that largely contributes to the electron density. In order to reproduce the ionization level of the VAL-C model [1], the reaction rates of this study are modified as follows. We build upon the ionization and recombination models of Cox &

Tucker [189] and Moore & Fung [190] that read

$$\begin{aligned} \nu^{ion} &= 2.34 \cdot 10^{-14} n_e / (\sqrt{\varphi} \exp(-\varphi)) \quad \text{and} \\ \nu^{rec} &= 5.20 \cdot 10^{-20} n_e \sqrt{\varphi} (0.4288 + 0.5 \log \varphi + 0.4698 \varphi^{-1/3}), \end{aligned} \tag{7.1}$$

where $\varphi = A\phi_{ion}/T_e^\star$ is a dimensionless parameter that takes into account the temperature dependence of the ionization and recombination rates. In this expression, $T_e^\star$ is the electron temperature in eV, $\phi_{ion} = 13.6$ eV is the ionization potential for hydrogen atoms and $A = 0.6$ is a constant, which takes into account the influence of heavy ions and has been introduced to match the expected ionization rates n_i/n_n, as predicted by the VAL-C model [1].

7.3 INITIAL CONDITIONS: THERMAL AND CHEMICAL EQUILIBRIUM

We consider a domain with a physical size of 2000 km by 2000 km where the heliocentric distance is denoted by z and the horizontal direction is represented by x. We use a domain with 200×200 grid points that is stretched in the z-direction in order to have more resolution at photospheric heights.

To model the reactive inhomogeneous chromospheric plasma we initialize the code with a height-dependent temperature profile, given by the original VAL-C chromospheric model [1]. This model, as well as the more recent follow-up chromospheric models [191], do not distinguish between the temperature of molecular hydrogen and protons and provide a single temperature profile for the single ionized hydrogen and the neutrals. Therefore, we assume initially isothermal plasma with $T_e = T_i = T_n$.

In order to compute the initial density profiles, we assume that the total (ion+neutral) pressure gradient balances the gravity force. With this condition, we obtain the total density distribution that decreases exponentially with height. The chemical equilibrium is thus imposed by the condition $\Gamma_i^{ion} = \Gamma_n^{rec}$. With the total density and the chemical equilibrium condition that is function of the temperature, we obtain the ion and neutral density profiles. The initial temperature and densities are shown in Fig. 7.2.

The modified plasma density in our model has shape that is similar to the one of the inferred electron density presented in the chromospheric model by Avrett & Loeser [192]. The initial profiles capture the photospheric temperature minimum around 500 km and the consequent temperature increase in the upper chromosphere. The ionization level increases, as the neutral and

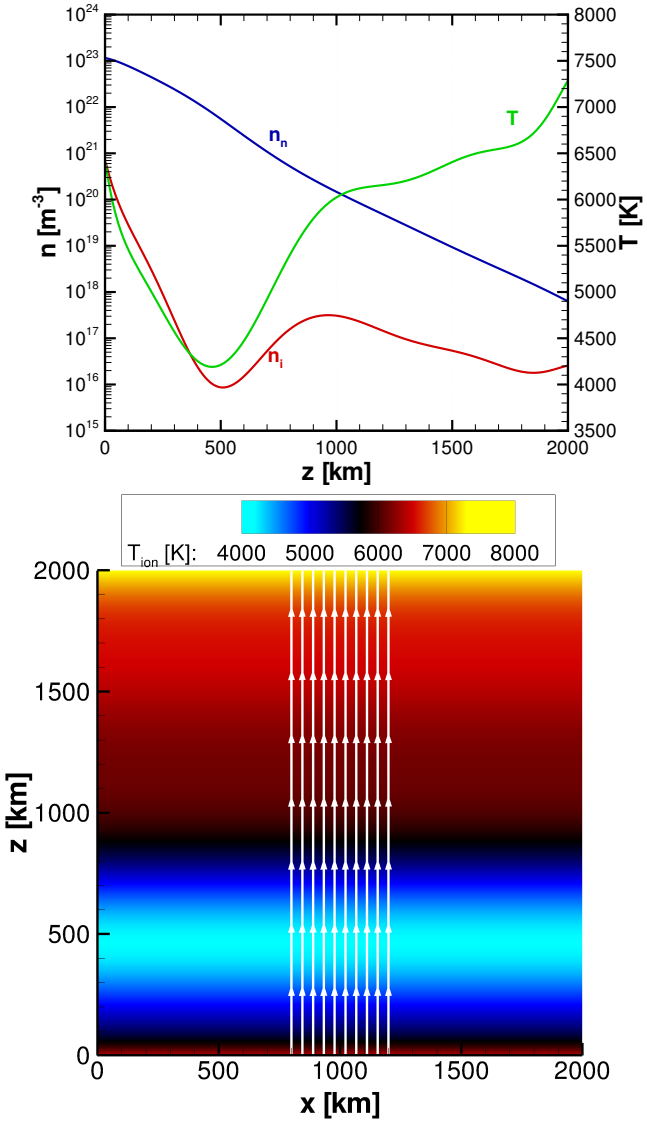

Figure 7.2: Top: Initial temperature and density profiles, based on a modified VAL C atmospheric model in thermal and chemical equilibrium. Bottom: temperature distribution in the computational domain. The white lines represent the magnetic field lines.

ion densities become more comparable in the upper chromosphere. The 2D contour plots of the initial temperature profile is presented in Fig. 7.2.

In order to study the evolution of sound and magnetosonic waves in the chromosphere in all cases here we have adopted a simple Gaussian magnetic field profile and a photospheric foot-point velocity driver used in MHD and improved partially ionized MHD models with ambipolar diffusion terms, as presented for example in Khomenko et al. [193] and Fedun et al. [194, 195].

$$B_y(x) = B_0 \exp\left(-\frac{(x-x_0)^2}{2\sigma^2}\right), \tag{7.2}$$

$$u^n_{x,y}(x,t) = V_0 \sin(2\pi\nu t) \exp\left(-\frac{(x-x_0)^2}{2\sigma^2}\right). \tag{7.3}$$

The magnetic field strength has been set to $B_0 = 18$ G, the flux tube is placed in the center of the domain at $x_0 = 1$ Mm, and the width of the initial magnetic field foot-point has been selected to $\sigma = 40$ km as in Khomenko et al. [196]. The magnitude of the velocity driver is set to 500 m/s as assumed in Fedun et al. [194]. The period of the driver was set to 30s, so that the corresponding frequency is $\omega = 2\pi\nu = 0.06,\ 0.2,\ 0.6$, and 2.1 Hz. The velocity of the neutrals is excited by the driver, although, as the neutrals and ions are coupled through collisions, the ions move together with the neutrals. In the results we will focus on the cases for 30 s period. The time step used for the simulations varies between 10^{-4} s and 10^{-2} s.

We note that the selected initial magnetic field profile is not force-free and it does carry some current. This force becomes significant in the upper chromosphere, where the ions become magnetized and the magnetic pressure becomes comparable to the plasma pressure.

To compare our results to previous MHD and generalized MHD simulations we have used several different initial simulation setups. In order to generate acoustic and magnetosonic waves in the photosphere we have perturbed the horizontal and vertical velocity of the ions, as well as the horizontal and vertical velocities of the neutrals. The main difference between applying the velocity driver on the ions and the neutrals is in the amplitude of the excited perturbations. Since the ions are much less abundant than the neutrals perturbing the ion velocity we input less kinetic energy in the system, which generates smaller pressure gradient and results in less intense waves. However, apart from their amplitude all physical processes, such as the wave properties, the velocity and the temperatures profiles remain the same. Therefore for better representation in the remaining of the paper we will concentrate on the case of velocity driver applied on the neutrals.

In the next section we present in details the results from the simulations and discuss their relation to previous models.

7.4 RESULTS

In Figs. 7.3, 7.4, and 7.5 we show the evolution of the ion vertical and horizontal velocities, and ion temperature with the driver of period 30 s. Similarly, the magnetic field lines are presented in the figures. The plots show the evolution until $t = 438$ s, which corresponds to approximately 15 periods of the driver.

The magnetic field lines, initially straight, open at heights $z > 1000$ km. The reason for that is the initial current that produces a force that pushes the ion fluid horizontally. In Fig. 7.4, we observe two opposite horizontal flows at the upper chromosphere that are caused by the Lorentz force that is only in regions where the plasma beta is smaller than unity. Alternatively, the flux tube diffuses at the temperature minimum $z \sim 500$ km. In this region, the resistivity is larger as it is a function of the temperature, $\eta \propto T^{-3/2}$. In the photosphere $z \sim 100 - 200$ km the field lines are tangled as the amount of ions is very low and they are unmagnetized.

In Figs. 7.3 and 7.4, both horizontal and vertical velocity components show symmetric contours typical for sound waves and fast magnetosonic waves. The vertical velocity component is larger than the horizontal velocity. We observe that the wave fronts have a dimple at the center of the flux tube for heights above $z \sim 1000$. In the simulations, the velocity of neutrals is practically equal to this of ions. We observe small differences in the horizontal velocity that are produced by the initial Lorentz force in the upper chromosphere.

The evolution of the temperature that is presented in Fig. 7.5 shows that heating takes place outside the flux tube in the wavefronts. Alternatively, inside the tube the temperature decreases as a consequence of the advection that is produced by the Lorentz force. Similar to the velocity, the temperatures of ions and neutrals are very similar.

Another aspect is the effect of the induced oscillations on the chemical equilibrium in the system. Fig. 7.6a shows the evolution in time of the ratio between the number densities n_i/n_n at three different altitudes $z = 0$, 1000, and 2000 km in the center of the flux tube. The ionization becomes affected by the waves more quickly than the recombination, which results in local loss of chemical equilibrium. At the photosphere the ionization level oscillates because of this chemical inequilibrium. However, the other altitudes are also

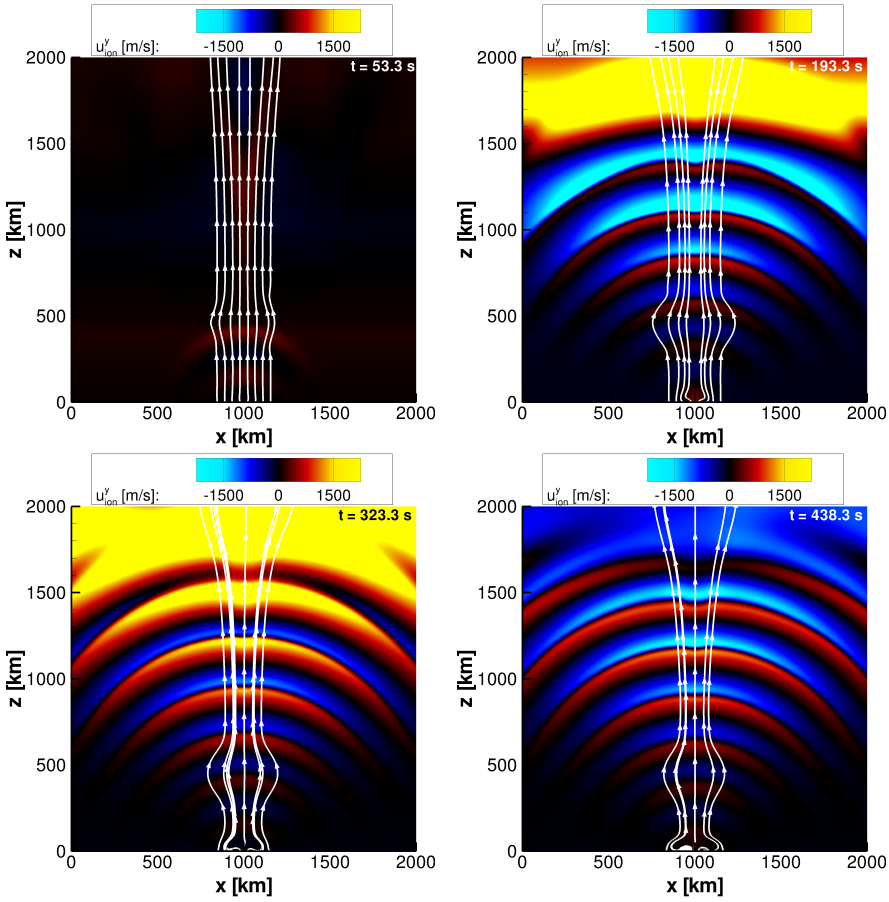

Figure 7.3: Evolution of the ion vertical velocity and the magnetic field lines at times $t = 53.3,\ 193.3,\ 323.3$, and 438.3 s with driver's period of 30 s.

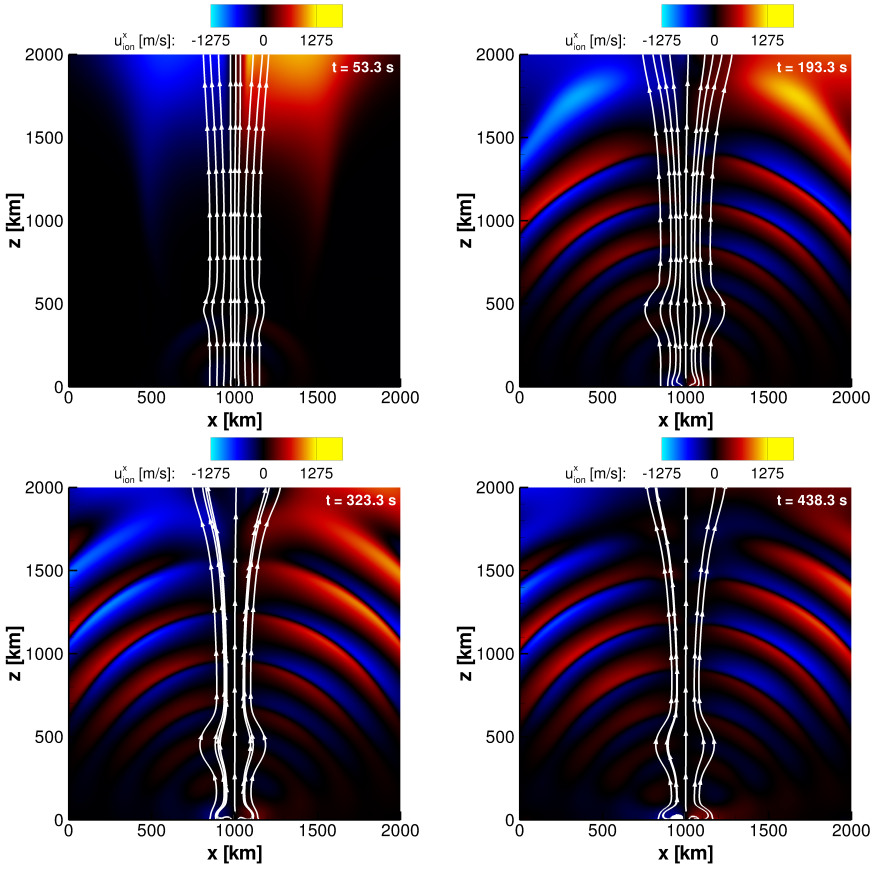

Figure 7.4: Evolution of the ion horizontal velocity and the magnetic field lines at times $t = 53.3,\ 193.3,\ 323.3$, and 438.3 s with driver's period of 30 s.

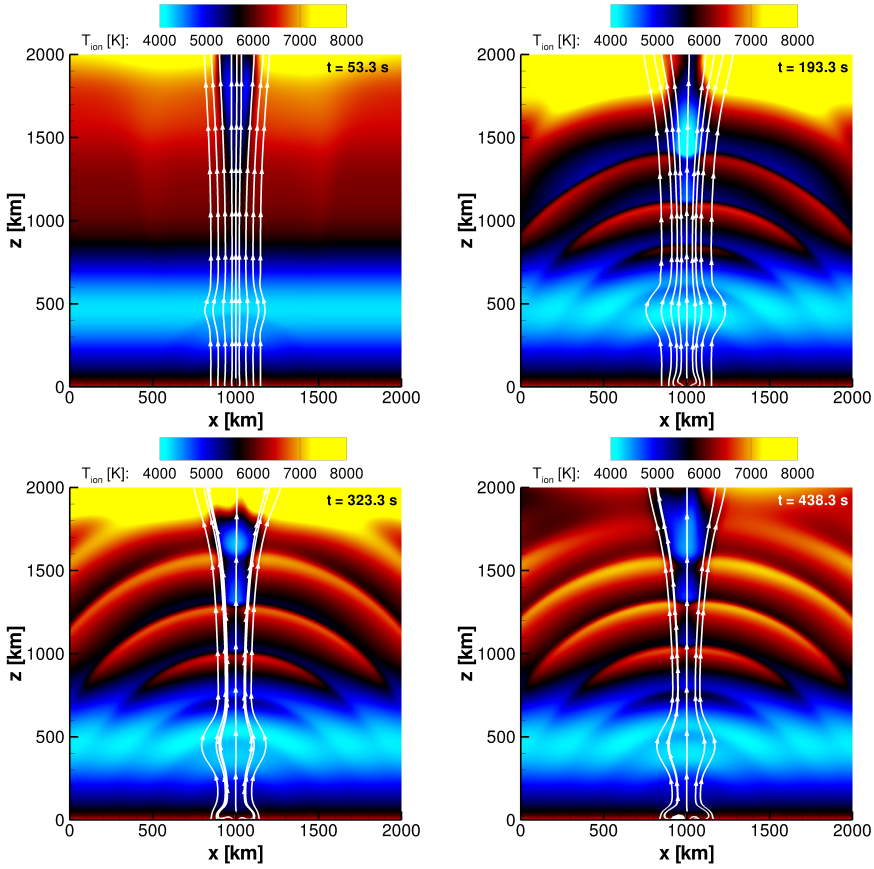

Figure 7.5: Evolution of the ion temperature and the magnetic field lines at times $t =$ 53.3, 193.3, 323.3, and 438.3 s with driver's period of 30 s.

affected by the change of temperature that occurs in the center of the flux because of the advection. After four periods the ionization level oscillates at $z = 1000$ km with larger amplitude and same frequency. However, at the top boundary the ionization level strongly decreases due to the cooling. Nevertheless, after eight periods, an oscillation with a period five times larger than the driver appears.

The same results are observed for the cases of higher and lower frequency drivers, as the ionization and recombination rates are naturally affected by the excited compressible fluctuations.

Fig. 7.6b shows the evolution of the ion temperature in the same three altitudes. We observe that the waves produce oscillations in the temperature due to compression. The oscillations at $z = 0$ km and $z = 1000$ km are in phase, although the oscillations are larger at $z = 1000$. At the top $z = 2000$ km, the variations of temperature are mostly produced by macroscopic motion, i.e., advection because of the Lorentz force. Nevertheless, a mode with larger period than the driver is observed.

Fig. 7.6c shows the evolution in the same three altitudes of the kinetic energy of the neutrals. After four periods the oscillations start at $z = 1000$ km. The oscillations at this altitude have different modes at higher and lower frequency than the driver. At $z = 2000$ km, the oscillations start after six periods and have lower period than the driver. This is an evidence of mode conversion.

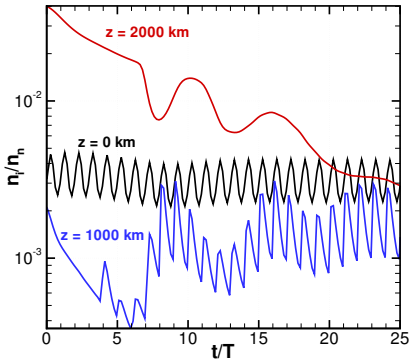

(a) n_i/n_n

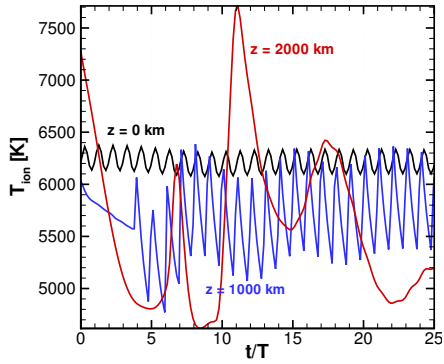

(b) T_i

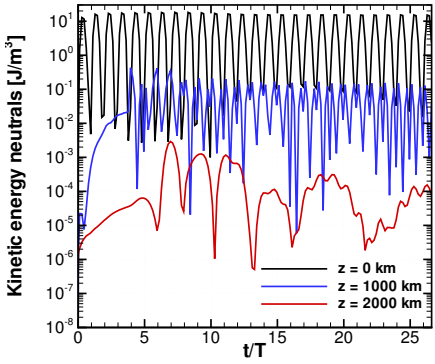

(c) kinetic energy of the neutrals

Figure 7.6: Evolution in time of (a) the ratio between the number densities n_i/n_n, (b) ion temperature, and (c) kinetic energy of the neutrals at three different altitudes $z = 0$, 1000, and 2000 km in the center of the flux tube. The time is normalized to the period of the driver.

7.5 SUMMARY AND CONCLUDING REMARKS

For the first time, a non-linear multi-dimensional multi-fluid simulation of the lower solar atmosphere is studied. We have used a two-fluid numerical simulation setup that treats the charged particles within a generalized MHD approximation and considers a separate fluid of neutrals. The two fluids are coupled through collisions and chemical reactions, such as impact ionization and radiative recombination. The model includes the effects of gravitational force imposed on the initial stratified density and temperature profiles, given by a modified VAL-C chromospheric model. Our simulations take into account Braginskii's collisional transport coefficients with anisotropic heat conduction, Spitzer-type resistivity and accounts for the basic chemical reactions in a hydrogen plasma. We have initialized the simulations with a simple Gaussian magnetic flux tube, which changes in time and opens starting to form a magnetic funnel. Similarly, the magnetic field lines are tangled in the photosphere due to the weakly ionization and magnetization of the plasma.

To compare to existing MHD and generalized MHD models we have imposed initial thermal and chemical equilibrium. We have included a photospheric velocity driver at the foot-point of the magnetic field, and have followed the evolution of the system in the presence of the driven sound and fast magnetosonic waves. Within 5 minutes of simulated real time the initial driver induces loss of chemical equilibrium with dominant recombination in the upper chromosphere and gradual reduction of the ionization fraction in time. Regardless of the selected low magnitude of the magnetic field, we find significant heating of the higher chromospheric layers outside the magnetic flux tube with some overall cooling at low to mid-low altitudes. Significant cooling is also observed in the upper chromospheric layers inside the flux tube, where the temperature can be more than 2000K degrees cooler than the surrounding plasma outside the flux tube. This cooling is partially counter-balanced by the heating due to the convection of the atmosphere.

The plasma heating observed at the wave fronts of the propagating fast magnetosonic fluctuations driven by the initial velocity driver as well as the heating outside the magnetic flux tube in the upper chromosphere account for a temperature increase of 500K up to 1000 K. The observed heating strongly depends on the initial driver: the vertical velocity driver heats the chromospheric plasma more than the horizontal one. The horizontal velocity driver at the selected frequency in our case does not excite waves and does not lead to significant heating. This comparison between the vertical and horizontal drivers significantly differs from the results of previous single fluid

MHD studies of chromospheric wave propagation, where slow magnetosonic waves have been excited by the horizontal velocity driver [197, 193, 195].

Within our model most of the net plasma heating outside the flux tube in the upper chromosphere is wave-based and is related to kinetic to thermal energy conversion as the wave fronts of the fast magnetosonic waves steepen. In the current plasma-neutral interactions we do not observe strong heating along the perpendicular component of the current, as expected from MHD models with partial ionization effect relying on ambipolar diffusion terms [196, 188, 43]. Within the current multi-fluid approach the plasma heating due to the partial ionization effects is either more isotropic and not bound to the direction perpendicular to the external magnetic field profile, or it is fully overcome by the dominant wave-based heating. We should note that the partial ionization effects in our study are not very strong and the main energy source for heating are the excited magnetosonic fluctuations. The role of the partial ionization could perhaps become more prominent for stronger magnetic fields.

Although the redistribution of the different energy types and the conversion from kinetic to thermal energy is not discussed here, we have to mention that there is energy transport from the photosphere throughout the chromosphere. Apart from kinetic energy transported through the chromosphere in the form of waves, there is also an associated electromagnetic energy transfer. The estimated Poynting flux related to the fast magnetosonic waves is much stronger in the horizontal than in vertical direction. However, we expect that to change whenever slow magnetosonic or Alfvén waves are excited in the system, as already suggested by some preliminary model results.

To further improve our model and make it better suitable for longer wave propagation studies we would consider implementing an additional wave damping layer, similar to what had been proposed and implemented for MHD simulations by Khomenko et al. [193].

CHAPTER 8

Multi-fluid modeling of magnetic flux tubes in tokamak conditions

At the time we were all convinced that this work was of vital significance for the balance of power in the world and we were fascinated by the grandeur of the task.

– *Andrei Sakharov*

We study the kink and drift-wave instabilities of magnetic flux tubes under realistic conditions of the DIII-D fusion reactor. We use full-scale three-dimensional two-fluid (ion+electron) simulations that allow for capturing the global MHD scales as well as the separation between the two species occurring at ion scales. We calculate the two-fluid equilibrium for a 'straight tokamak' configuration with the DIII-D conditions. In order to study the kink instability, a perturbation in the $m = 1$, $n = 1$ mode is initially introduced. We investigate traces of secondary magnetic reconnection resulting from the kink instability. Similar to previous kinetic simulations, in the two-fluid simulations, an electron current forms in the reconnection region with opposite direction to the current supporting the flux tube. This behaviour is also observed in magnetic reconnection experiments. Unlike the kink instability, the drift-wave instability forms spontaneously, without initial perturbation, after one Alfvénic transit time. The drift waves produce turbulence that diffuse the current in the direction perpendicular to the flux rope axis. This diffusion triggers localized reconnection in regions close to the resonant surface. Two-fluid simulations prove to be an efficient tool for the study of the physics of magnetically confined nuclear fusion devices as they are able to capture phenomena that take place in both MHD and kinetic scales.

8.1 MAGNETIC FLUX TUBES IN ASTROPHYSICAL AND LABORATORY PLASMAS

Magnetic flux tubes are magnetic configurations that play a fundamental role in astrophysical and nuclear fusion plasmas. They consist of a bundle of magnetic field lines that form tubular structures wherein plasma is confined. Usually, the magnetic field lines are twisted around the axis of the tube forming the so-called flux ropes.

Flux ropes are found in a large number of scenarios both in nature and man-made devices. They are observed in the outer sun atmosphere as coronal loops [198, 21], in planetary magnetospheres, both in the magnetotail [199] and the day-side magnetopause [200], and in astrophysical jets [201, 202]. Similarly, tokamaks and Z-pinch devices can be regarded as closed flux ropes with a toroidal shape [203].

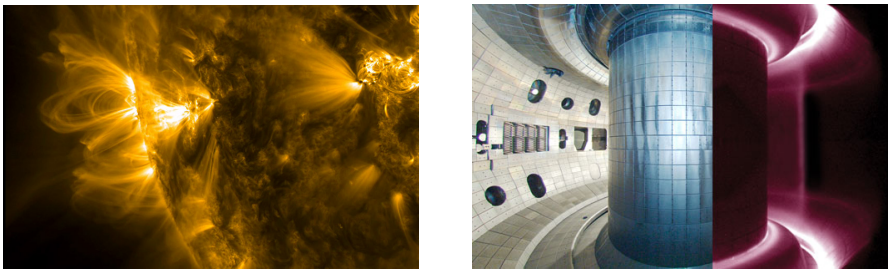

Figure 8.1: Examples of flux ropes. Left: NASA's Solar Dynamics Observatory observation of coronal loops in extreme ultraviolet light from February 8, 2014 (Credits: NASA). Right: DIII-D tokamak in visible light at rest (right left) and during operation (right half) (Credits: General Atomics).

Magnetic flux tubes have been broadly studied with the MHD approach [15, 204]. The MHD theory is able to retrieve the conditions for stability of global modes, such as the kink or the ballooning modes, for different flux rope configurations. However, it is not able to capture the important phenomena produced by the separation of the ion and electron dynamics that are responsible for the drift waves and their associated mass, momentum, and energy transport.

The kinetic theory is widely used by the fusion community to study the physics of flux ropes in nuclear fusion devices. Numerical approaches based on the kinetic equation such as Particle-in-cell (PIC) codes [77, 205] or Eulerian Vlasov solvers [80] are able to describe very accurately the state of the

plasma. However, this approach is computationally very costly to study the global MHD modes. We propose to use the two-fluid modeling that is able to capture the separation between species with a fluid representation and therefore represents a sound alternative to the limitations of both kinetic and MHD models.

8.2 KINK AND DRIFT WAVES INSTABILITIES

The kink instabilities are unstable modes in magnetic flux tubes that are associated to a helical deformation of the plasma column [15]. When the electric current column is bended, an increase of the magnetic pressure occurs in the inside bend of the deformation, while there is a decrease in the outside bend, as shown in Fig. 8.2a. This pressure unbalance tends to magnify the deformation and thus it becomes unstable. The kink modes are divided into internal modes, where the development of the instability does not perturb the vacuum magnetic field that surrounds the plasma, and the external ones where both the plasma and the vacuum magnetic fields are perturbed.

The kink modes are produced by Alfvén waves with low poloidal mode number [15], see Fig. 8.2b. Consequently, they occur in the Alfvén wave transit time scales and are considered as global MHD modes. The MHD theory studies the stability of these modes by defining Fourier series of the form $\exp\left[i(\omega t + m\theta + 2\pi nz/L_z)\right]$ where the mode number m refers to the angular (poloidal) direction θ and n to the axial (toroidal) direction z. Simple current configurations have been studied analytically with vacuum and ideal walls [15, 206, 207], whereas arbitrary geometries can be studied numerically [208, 209].

Here, we will focus on the internal modes $|m| = 1$. The internal mode with $m = 1$ and $n = 1$ is responsible for the sawtooth instability in tokamaks. During this instability, the electron temperature is observed to increase followed by a rapid drop [14]. The drop in temperature does not allow for reaching the necessary temperatures for nuclear reactions.

The stability of the kink modes is linked to the so-called safety factor, defined as:

$$q(r) = \frac{2\pi r B_z}{B_\theta(r) L_z}, \tag{8.1}$$

where B_z is the toroidal magnetic field, $B_\theta(r)$ is the poloidal magnetic field that is a function of the radius r, and L_z is the axial length of the flux tube. Shafranov [210] provides a stability criterion based on the safety factor for a 'straight tokamak', i.e., a flux rope considered to be a cylinder of infinite

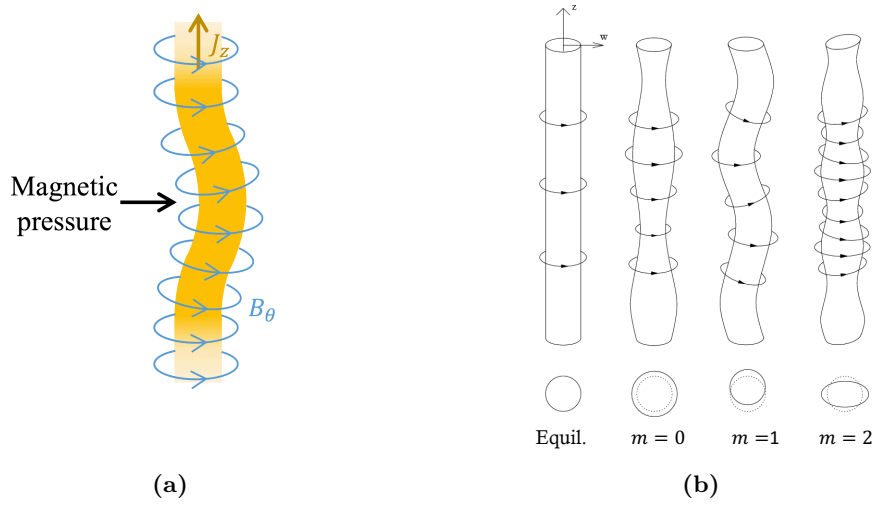

Figure 8.2: (a) Sketch of an external kink of a Z-pinch. (b) lllustration of MHD modes for different poloidal mode numbers.

length. The current is assumed to be maximum at the center of the tube and decrease towards the boundaries, i.e.,

$$q_0 \leq q(r) \leq q_a, \quad \text{with } 0 \leq r \leq a \tag{8.2}$$

where q_o is the safety factor at the center ($r = 0$), and q_a is the safety factor at the plasma outer boundary ($r = a$). In order to design magnetic configurations that are stable against internal modes, the current needs to fulfill the condition known as the Kruskal-Shafranov limit, that reads

$$q_0 > 1. \tag{8.3}$$

When the kink instability reaches the non-linear stage, magnetic reconnection occurs along the surface $q(r) = 1$, also called resonant surface and denoted as $r = r_s$. Secondary plasmoids are observed in the X-point in a number that is proportional to the Lundquist number [211, 212]. The reconnection develops in a regime where the two-fluid effects are important, forming quadripolar structures in pressure and magnetic fields [205, 213]. Similarly, small scale turbulence from ion to electron scales can result in anomalous dissipation that result in fast reconnections [205].

A different type of universal process occurring in magnetized plasmas is the drift waves that are responsible for large transport of mass, momentum, and energy across the magnetic field lines in flux ropes [12]. These waves are produced by the separation of the electron and ion dynamics and therefore cannot be explained by the MHD theory. They arise when density and temperature gradients produce diamagnetic currents that in equilibrium are of the form

$$\vec{j}_{e,i} = \frac{\left(\vec{\nabla} p_{e,i} \times \vec{B}\right)}{B^2}. \tag{8.4}$$

The drift velocity associated to these currents can result in collective oscillations that are called drift waves.

In order for the drift waves to occur, an electric field component along the magnetic field line is necessary, i.e., $E_{\parallel} \neq 0$. This condition implies that the magnetic field lines are not frozen into the plasma. Similarly, a charge imbalance is necessary in order to produce an electric field that creates the $\vec{E} \times \vec{B}$ advection of plasma. The quasi-neutrality principle applies and the densities $n_e = n_i$ to the first order in $\lambda_D^2/\delta x^2$ [12].

We depict the drift-wave mechanism in Fig. 8.3a. In the figure, $n(x)$ is the ambient density that varies in the x-direction, $\vec{B}$ is the magnetic field that points in the z-direction, and ϕ is the electrostatic potential that is created by an excess of positive-ion density δn_i. The electrostatic potential creates a $\vec{E} \times \vec{B}$ advection pattern of velocity $\vec{u}_E$ in the plane perpendicular to the magnetic field.

As shown in Fig. 8.3b, there is an electric field in the direction of the magnetic field. In absence of diffusion, the electric field and, consequently, the electrostatic potential are in phase with the electron density fluctuations. However, when there are diffusive processes in the magnetic field direction, e.g., collisions, viscosity, resonant electron-wave interactions, the density gradients and the electric potential are out of phase in space by $\Psi_{\delta n,\phi}$. The shift in space produces an imbalance of the convective fluxes $\vec{\Gamma}_{\pm}$. This flux imbalance is responsible for a transport of plasma across the magnetic field line.

Drift waves have been measured in laboratory experiments, such as the cylindrical Q machines [214, 215, 216], in toroidal magnetic fusion devices [217, 218], and especifically in the DIII-D tokamak [219]. In the solar corona, they have been proposed as a mechanism producing heating and acceleration of ions at frequencies below the gyrofrequency [30, 31, 32].

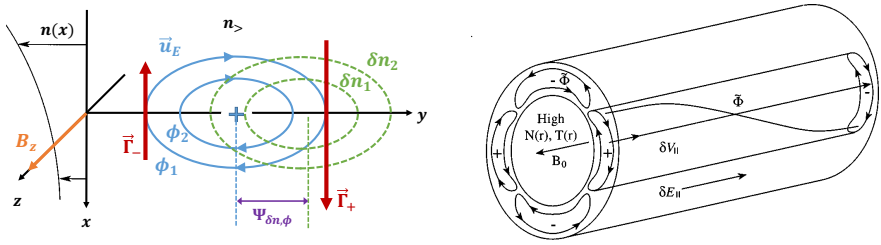

(a) **(b)**

Figure 8.3: (a) Sketch the drift wave mechanism. A positive-ion density perturbation (+) creates an electric potential ϕ. The streamlines of $\vec{u}_E$ that are consequence of the $\vec{E} \times \vec{B}$ particle motion are coincident with the iso-potential lines ϕ_1, ϕ_2. The density variation δn is shifted in phase with the potential by $\Psi_{\delta n,\phi}$ producing a flux imbalance $\vec{\Gamma}_+ > \vec{\Gamma}_-$. (b) Three-dimensional configuration of the $m = 2$ drift mode. (Credits: Horton [12])

8.3 TWO-FLUID EQUILIBRIUM IN A SCREW-PINCH CONFIGURATION

We will describe the two-fluid equilibrium of a flux rope model based on the screw-pinch configuration [203, 209, 205]. This configuration considers a cylindrical flux tube geometry with a magnetic field in cylindrical coordinates (r, θ, z) that reads

$$\begin{aligned} B_r &= 0, \\ B_\theta &= \frac{A_0 r}{r^2 + w^2}, \\ B_z &= B_{z0}. \end{aligned} \tag{8.5}$$

As explained in the previous section, the stability of the kink modes is related to the safety factor, as defined in Eq. (8.1). Therefore, we can write the parameters that define the poloidal magnetic field, i.e., A_0 and w, as function of the safety factor at the axis and at the minor radius, as follows:

$$\begin{aligned} A_0 &= \frac{2\pi a^2 B_{z0}}{(q_a - q_0)\, L_z} \\ w^2 &= \frac{a^2 q_0}{(q_a - q_0)} \end{aligned} \tag{8.6}$$

where a is the minor radius of the flux tube and L_z is the length of the axis of the tokamak. The pressure of the plasma that balances the previous

magnetic configuration reads

$$\nabla p = \frac{(\nabla \times \vec{B}) \times \vec{B}}{\mu_0} \rightarrow \frac{\partial p}{\partial r} = \frac{-2A_0^2 w^2 r}{\mu_0 (r^2 + w^2)^3}. \tag{8.7}$$

Integrating the previous equation, we obtain the total plasma pressure,

$$p(r) = \tilde{p}(r) + p_0 = \frac{A_0^2 w^2}{2\mu_0 (r^2 + w^2)^2} + p_0. \tag{8.8}$$

Here, we will assume that there is no background pressure, $p_0 = 0$ and that the pressure gradient is produced by a density gradient so that the temperature is constant, i.e., $p(r) = n(r) k_B T$. We assume to have charge neutrality, i.e., $n_i(r) = n_e(r) = n(r)/2$, and the temperature of ions and electrons to be different, $T_i = \tau T_e$ where τ is a constant.

Force balance in both fluids is achieved with a diamagnetic current in the z-direction that produces a force in the radial direction compensating the pressure gradient. In mathematical terms,

$$\frac{\partial p_{e,i}}{\partial r} = \left(\vec{j}_{e,i} \times \vec{B} \right) \cdot \vec{e}_r \tag{8.9}$$

With the previous assumptions on the ion and electron densities and temperatures, we obtain the following constant velocities that provide force balance

$$\begin{aligned} u_e^z &= \frac{-4 k_B T_i}{\tau e A_0}, \\ u_i^z &= \frac{4 k_B T_i}{e A_0}. \end{aligned} \tag{8.10}$$

Therefore, the two-fluid equilibrium derived in the present section is a function of the following degrees of freedom $F\,(a, L_z, q_0, q_a, B_{z0}, n(r=0), \tau)$. Note that the pressure at the center is defined by Eq. (8.8) and it can be fixed by choosing either the temperature or the density.

8.3.1 The DIII-D tokamak

We will carry out simulations to study the development of the $m = 1$, $n = 1$ kink mode in the DIII-D tokamak. The simulations aim at studying the experiments that were carried out on July 17th 2017. Towards this goal, the parameters chosen for the equilibrium are as similar as possible as the ones imposed in the experiments. We summarize the conditions in the Table 8.1.

Table 8.1: Parameters defining the initial screw-pinch equilibrium with the DIII-D tokamak conditions.

DIII-D parameters	
a	0.67 m
R_0	1.67 m
$L_z = 2\pi R_0$	10.49 m
B_z	1.1 T
q_0	0.5
q_a	2.2
$n(r=0)$	$4 \cdot 10^{19}$ m^{-3}
τ	1.5
T_i	17.07 keV
T_e	11.38 keV

As it can be seen in the previous table, the safety factor on the axis $q_0 < 1$. Therefore, the initial configuration is unstable against the internal kink modes, as predicted by the Kruskal-Shafranov limit of Eq. (8.3).

8.3.2 Numerical simulations set-up

The numerical set-up comprises a wide span of characteristic scales. In order to save computational time, the speed of light is artificially reduced in the simulations to $c^* = 10 v_{A_\parallel}$, where $v_{A_\parallel}$ is the characteristic Alfvén speed in the z-direction. Similarly, the ion-to-electron mass ratio is reduced to $m_i/m_e = 256$. The divergence cleaning constants are chosen to be $\chi = 1$ and $\gamma = 1$ as no plasma characteristic waves are travelling faster than the numerical speed of light.

In Table 8.2 the characteristic velocity, time, and length scales are summarized. We take the characteristic Alfvén speed in the z-direction as reference velocity, the inverse of the ion gyroradius as reference time and the ion skin depth as reference length.

We use an unstructured mesh of hexahedron elements. The mesh is discretized with 128 elements along the radius at $\theta = 0, \pi/4, \pi, 3\pi/4$, 128 nodes in the poloidal direction at the outer boundary, and 128 equally-spaced nodes in the z-direction. As it is shown in Fig. 8.4, the nodes are equally-spaced in the longitudinal direction and unstructured in the plane perpendicular to

Table 8.2: Characteristic dimensions of the DIII-D simulation

	Dimensional	Dimensionless
$v_{A_\parallel} = B_{z0}/\sqrt{\mu_0 \rho}$	$3.79 \cdot 10^6$ m/s	Ref. velocity
$v_{A_\perp} = B_\theta^{max}/\sqrt{\mu_0 \rho}$	$8.24 \cdot 10^5$ m/s	0.217
$a_i = \sqrt{\gamma p_i/\rho_i}$	$1.67 \cdot 10^6$ m/s	0.436
$a_e = \sqrt{\gamma p_e/\rho_e}$	$2.16 \cdot 10^7$ m/s	5.69
c^*	$3.79 \cdot 10^7$ m/s	10
$\Omega_i^{-1} = m_i/eB_{z0}$	$9.49 \cdot 10^{-9}$ s	Ref. time
$\Omega_e^{-1} = m_e/eB_{z0}$	$3.71 \cdot 10^{-11}$ s	$3.9 \cdot 10^{-3}$
$\omega_{p,i}^{-1} = \sqrt{\epsilon_0^* m_i/ne^2}$	$1.67 \cdot 10^{-9}$ s	0.19
$\omega_{p,e}^{-1} = \sqrt{\epsilon_0^* m_e/ne^2}$	$1.15 \cdot 10^{-10}$ s	$1.2 \cdot 10^{-2}$
$\omega_p^{-1} = 1/\sqrt{\omega_{p,i} + \omega_{p,e}}$	$1.14 \cdot 10^{-10}$ s	$1.2 \cdot 10^{-2}$
$t_A = L_z/v_{A_\parallel}$	$2.77 \cdot 10^{-6}$ s	292
$\delta_i = c^*/\omega_{p,i}$	$3.6 \cdot 10^{-2}$ m	Ref. length
$\delta_e = c^*/\omega_{p,e}$	$2.25 \cdot 10^{-3}$ m	$6.25 \cdot 10^{-2}$
$\lambda_D = \sqrt{\epsilon_0^* k_B T/(ne^2)}$	$1.4 \cdot 10^{-4}$ m	$3.89 \cdot 10^{-3}$
$r_{L_i} = v_{A_\perp}/\Omega_i$	$7.82 \cdot 10^{-3}$ m	0.217
$r_{L_e} = v_{A_\perp}/\Omega_e$	$3.05 \cdot 10^{-5}$ m	$8.48 \cdot 10^{-4}$
a	0.67 m	18.61
L_z	10.49 m	291.43
$\Delta x_{min} = \sqrt[3]{\Delta V_{min}}$	$9.16 \cdot 10^{-3}$ m	0.25
Δt	$7.04 \cdot 10^{-10}$ s	$7.42 \cdot 10^{-2}$
CFL $= c^* \Delta t/\Delta x_{min}$	-	2.91

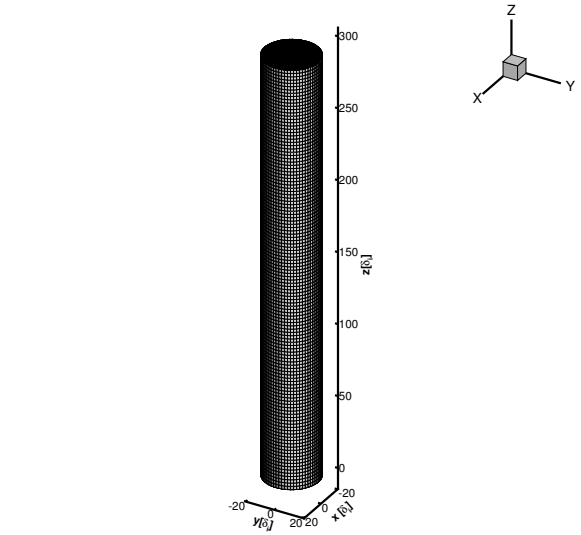

(a)

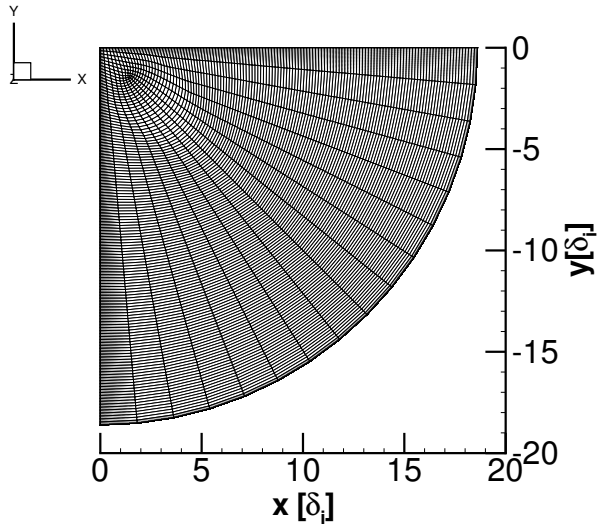

(b)

Figure 8.4: Mesh of $1.01M$ cells used in the simulation of the screw-pinch configuration of the DIII-D tokamak. The length is expressed in ion skin depth units. (a) 3D view. (b) xy-plane view (only one quarter of the mesh is presented).

the axis. The total number of volume cells is around $1.01M$ cells with the minimum volume of $7.7 \cdot 10^{-7}$ m^3.

Two different initial configurations are studied. The first one reproduces the initial equilibrium described in Sect. 8.3 using the dimensional parameters of Table 8.1 with a perturbation in the $m = 1$, $n = 1$ mode in order to induce a kink instability. The perturbation consists in a displacement of the flux tube in the xy-plane following the vector

$$\vec{\xi} = \xi_0 \left[\cos\left(2\pi z/L_z\right)\vec{e}_x + \sin\left(2\pi z/L_z\right)\vec{e}_y\right]. \tag{8.11}$$

We choose the displacement to be 1% of the total minor radius, i.e., $\xi_0 = 0.01a$.

The second configuration studies the same set-up without the perturbation. The initial conditions along the radius in dimensional units are presented in Fig. 8.1.

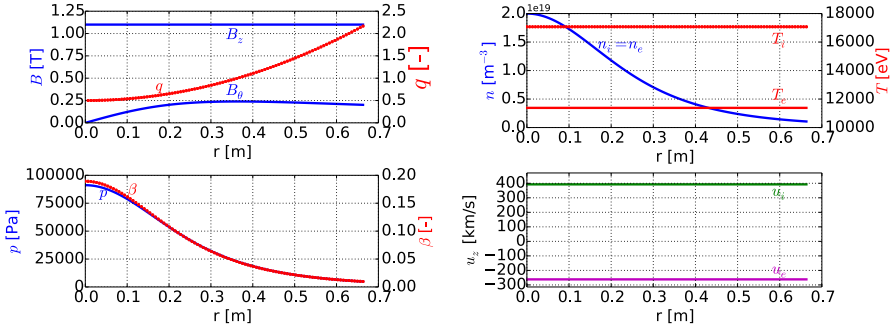

Figure 8.5: Variation along the radius of the initial conditions in dimensional units with the parameters of Table 8.1.

8.4 RESULTS

8.4.1 Initial field with a $m = 1$ $n = 1$ perturbation

We present the evolution of the flux tube with a small initial perturbation in the $m = 1$, $n = 1$ mode. In Fig. 8.6, the isosurface corresponding to $j_z = 0.064 e n_0 v_A$ is presented at four times $t = 0$, $133.5\Omega_i^{-1}$, $163.5\Omega_i^{-1}$, and $207.6\Omega_i^{-1}$. The isosurface corresponds to a value that is 75% of the maximum of the current at the initial time. At $t = 0$, the amplitude of the perturbation is 1% of the minor radius and it cannot be observed. However, at later

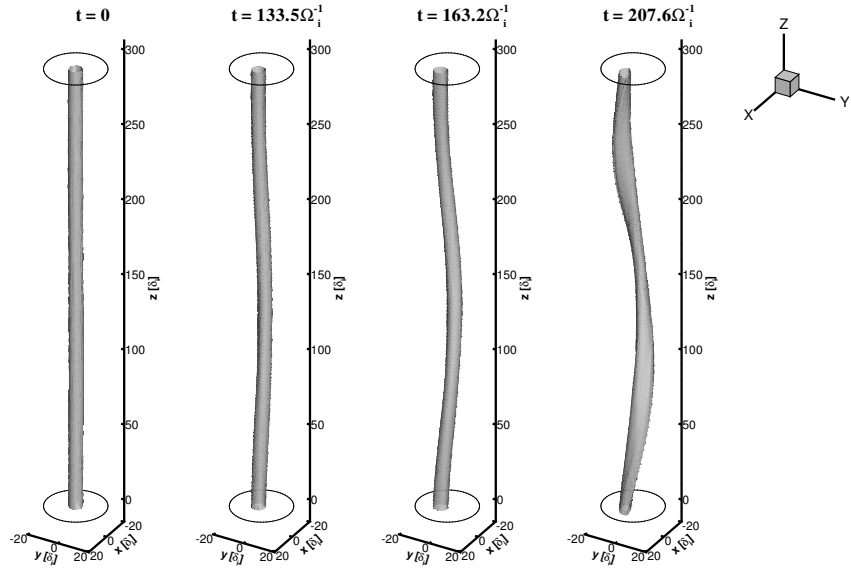

Figure 8.6: Isocontour of the electric current $j_z = 0.064 e n_0 v_A$ at $t = 0, 133.5\Omega_i^{-1}, 163.5\Omega_i^{-1}, 207.6\Omega_i^{-1}$. A visible kink starts at $t = 163.5\Omega_i^{-1}$.

times the current develops a kink instability. The kink in the electric current starts being remarkable around $t = 163.2\Omega_i^{-1}$, i.e., approximately $0.55 t_A$. At $t = 207.6\Omega_i^{-1}$, the kink is in a non-linear phase, but the walls limit the bending of the flux tube.

In Fig. 8.7, the magnetic field lines at $t = 0$, $163.5\Omega_i^{-1}$, $207.6\Omega_i^{-1}$, and $267\Omega_i^{-1}$ are shown. The magnetic field lines untwist because of the secondary reconnection produced by the kink instability.

The magnetic reconnection can occur in regions close to the resonant surface as a result of the kink of the flux tube [15]. As suggested in Markidis et al. [205], the auxiliary magnetic field, defined as $\vec{B}^* = \vec{B} - (2\pi r/L_z) B_z \vec{e}_\theta$, is a useful variable to identify signatures of secondary magnetic reconnection. Fig. 8.8 shows $\vec{B}^*$ at $t = 0$, $163.2\Omega_i^{-1}$, and $207.6\Omega_i^{-1}$. We study this field in the xy-plane at the section $L_z/2$. Initially, two disconnected regions, in blue and red, are separated by the resonant surface, that is shown as a green dashed line. As the current kinks, the inner region crosses the resonant surface. When this happens, magnetic reconnection takes place and a new magnetic topology is formed.

In Fig. 8.9, we plot the current in the z-direction with values $j_z = \pm 0.07 e n_0 v_A$ at the times $t = 163.2\Omega_i^{-1}, 207.6\Omega_i^{-1}$, and $230.3\Omega_i^{-1}$. As magnetic reconnection takes place, a current in the opposite directios to the initial current is formed. The positive current that supports the flux rope is inside the volume with $r < r_s$, where r_s is the resonant surface. The negative current is on the other side of the resonant surface $r > r_s$.

Fig. 8.10 shows the current at $t = 207\Omega_i^{-1}$ in the z-direction on the slice $z = L_z/2$, carried by ions, electrons, and the total current that is the sum of the two. In the initial equilibrium, the current is carried equally by ions and electrons. However, at this stage, the current is mostly carried by electrons as they are much lighter. The negative current outside the resonant surface is fully carried by electrons and has a value comparable to the positive current.

In Fig. 8.11, the electric field in the z-direction is presented at times $t = 230.3\Omega_i^{-1}, 233.3\Omega_i^{-1}$, and $252.1\Omega_i^{-1}$. An electric field with value $E_z = 0.009 B_0 v_A$ (in red) is formed in the reconnection region, the so-called reconnection inductive electric field. Smaller structures with opposite polarities, that are identified as drift waves, appear in other regions with $r > r_s$.

In Fig. 8.12, the density of ions and electrons, and the difference between the two is presented at $t = 207.6\Omega_i^{-1}$ on the slice $z = L_z/2$. Both densities are very similar and are displaced towards the resonant surface. The difference between the densities is small, of the order of $10^{-3} n_0$. Close to the reconnection region, the difference of densities has a quadripolar structure. Close to the boundaries the difference is maximum as the boundary condition does not impose charge neutrality, but electric field $\vec{E} = 0$.

The evolution of the electron temperature at the center ($r = 0$) of the slice at $z = L_z/2$ is shown in Fig. 8.13. The sawtooth crash is captured in this simulation. It starts at $t = 350\Omega_i^{-1}$ when the electron temperature reaches its peak, i.e., $T_e = 12.2$ keV. The sawtooth crash occurs in a timescale of $20\Omega_i^{-1}$. In this disruption, the temperature drops to $T_e = 10.6$ keV.

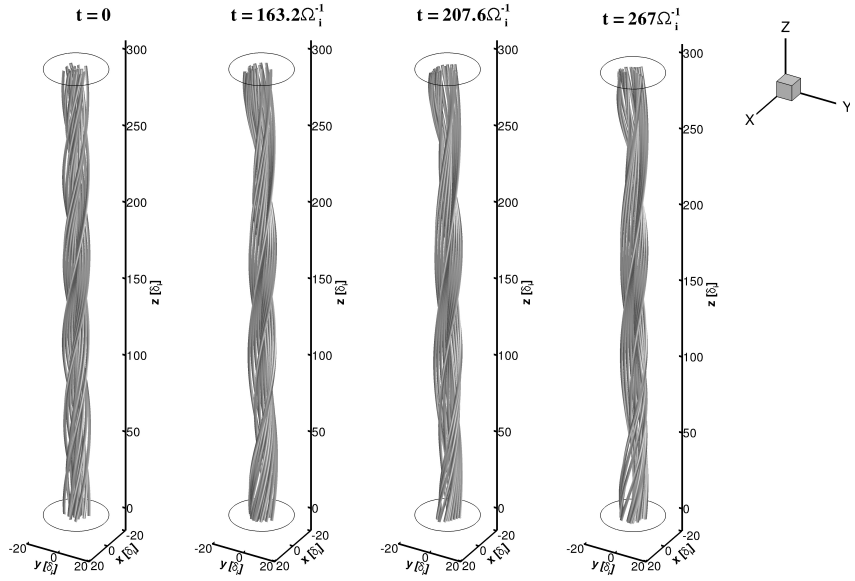

Figure 8.7: Magnetic field lines at $t = 0, 163.5\Omega_i^{-1}, 207.6\Omega_i^{-1}, 267\Omega_i^{-1}$. Magnetic field lines untwist.

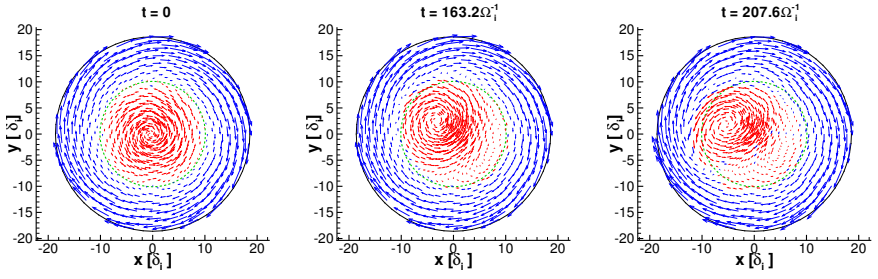

Figure 8.8: Quiver plot of $\vec{B}^*$ on $z = L_z/2$ at $t = 0, 163.5\Omega_i^{-1}, 207.6\Omega_i^{-1}$. Two disconnected regions, in blue and red, are initially present. The resonant surface is plotted as a dashed green line.

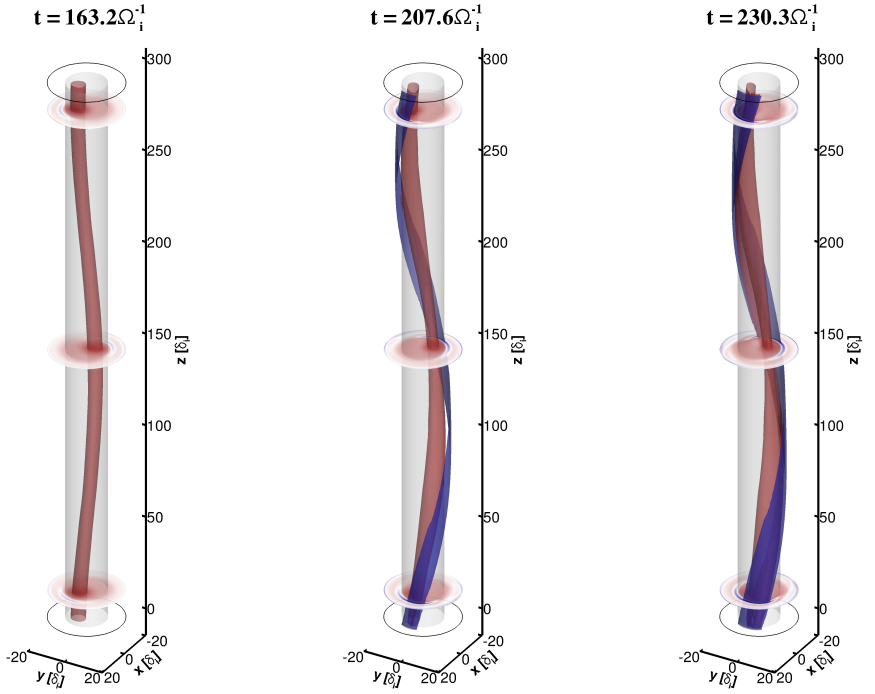

Figure 8.9: Isocontour of the electric current $j_z = 0.07en_0v_A$ (red) and $j_z = -0.07en_0v_A$ (blue) at $t = 163.2\Omega_i^{-1}$, $207.6\Omega_i^{-1}$, and $230.3\Omega_i^{-1}$. The resonant surface is presented in grey.

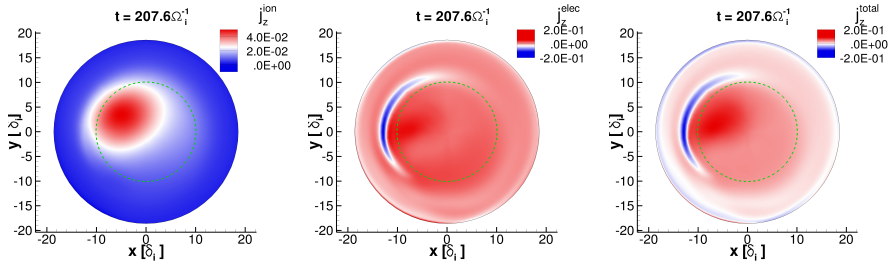

Figure 8.10: Current in the z-direction on the $z = L_z/2$ at $t = 207.6\Omega_i^{-1}$ carried by ions (left), electrons(center) and total current (right). The resonant surface is plotted as a dashed green line.

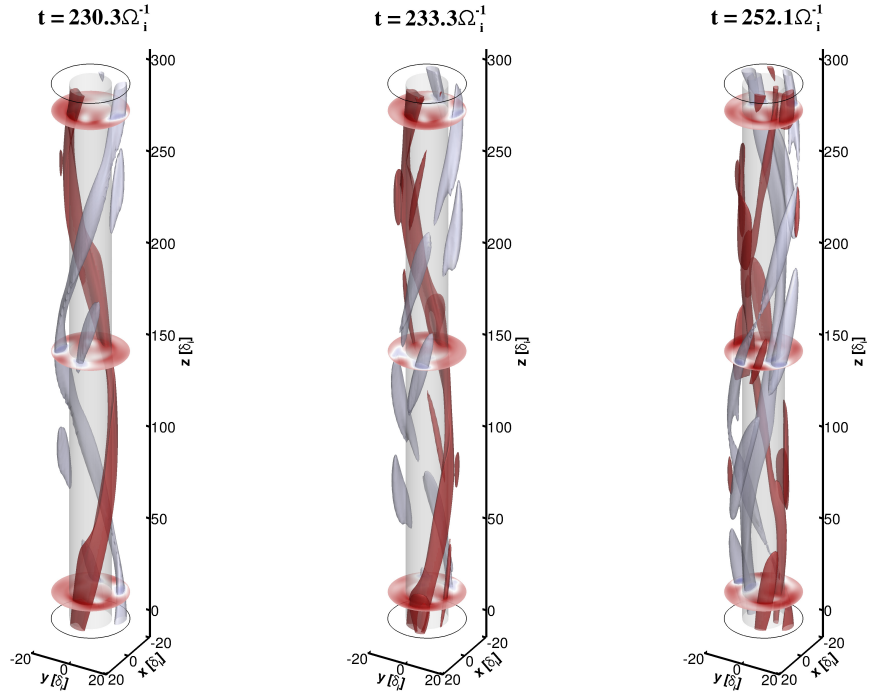

Figure 8.11: Isocontour of the electric field in the z-direction $E_z = 0.009 B_0 v_A$ (red) and $E_z = -0.009 B_0 v_A B_0 v_A$ (blue) at $t = 230.3\Omega_i^{-1}$, $233.3\Omega_i^{-1}$, and $252.1\Omega_i^{-1}$. The resonant surface is presented in grey.

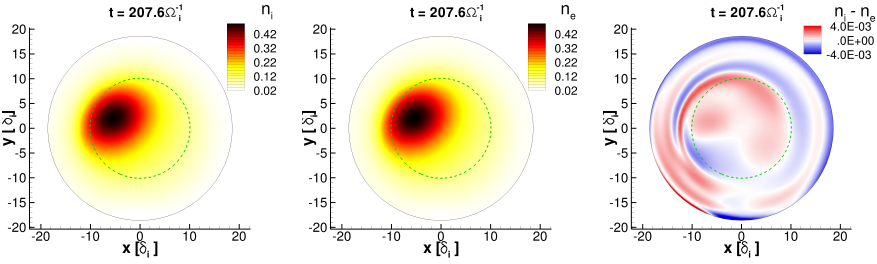

Figure 8.12: Density distribution of the ions (left) and electrons (centre), and difference of the densities (right) at $t = 207.6\Omega_i^{-1}$ in the slice at $z = L_z/2$.

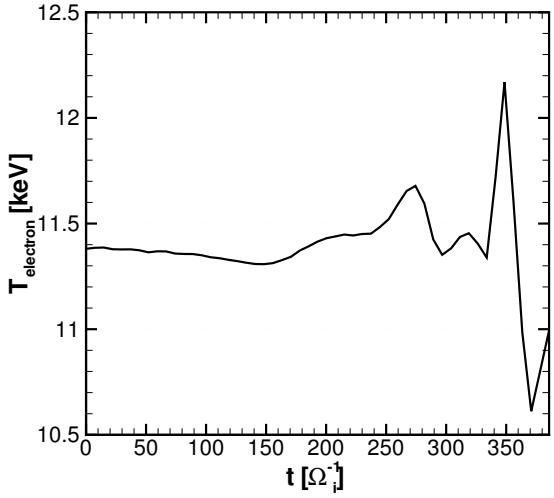

Figure 8.13

Figure 8.14: Evolution of the electron temperature at the center ($r = 0$) of the slice at $z = L_z/2$. The sawtooth crash is observed at $t = 350\Omega_i^{-1}$. The sawtooth crash occurs in a timescale of $20\Omega_i^{-1}$.

8.4.2 Initial field without initial perturbation

The same configuration is studied without the initial perturbation in the current. As the configuration is unstable against internal kink modes, we may expect that numerical noise can induce the kink instability spontaneously. However, as it is shown in Fig. 8.15, a different type of instability develops. In this figure, we present the isosurface corresponding to $j_z = 0.064en_0v_A$ at $t = 0, 207.6\Omega_i^{-1}, 300\Omega_i^{-1}$, and $478.4\Omega_i^{-1}$. Even though we observe a more advanced time than in the perturbed case, no appreciable kink is visible at $t = 478.4\Omega_i^{-1}$. Alternatively, a mode in the poloidal direction with high mode number develops.

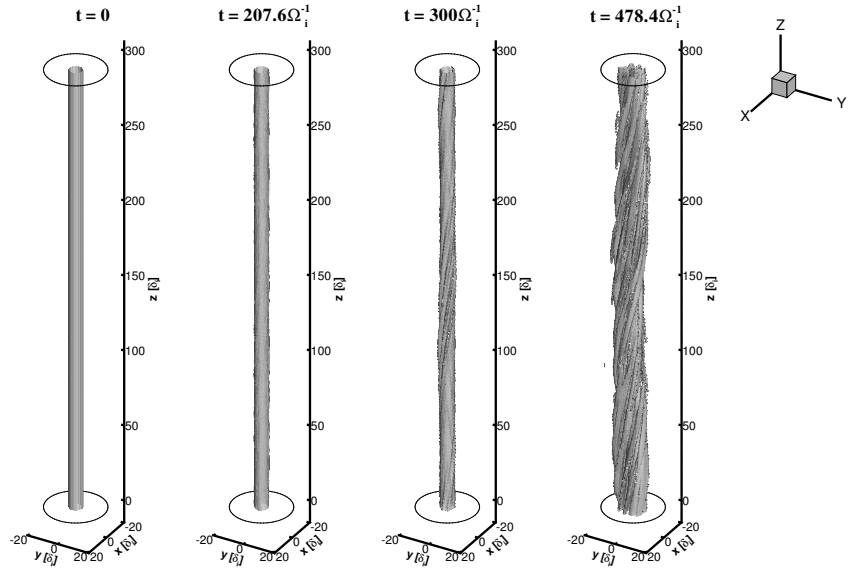

Figure 8.15: Isocontour of the electric current $j_z = 0.064en_0v_A$ at $t = 0, 207.6\Omega_i^{-1}$, $300\Omega_i^{-1}$, and $478.4\Omega_i^{-1}$.

In Fig. 8.16, the electric current in the z-direction is shown in the slice located at $z = L_z/2$ at $t = 300\Omega_i^{-1}, 360\Omega_i^{-1}$, and $405\Omega_i^{-1}$. At $t = 360\Omega_i^{-1}$ and $405\Omega_i^{-1}$, an instability in the poloidal direction with number $m = 4$ is observed. No kink in the current is observed. On the other hand, at $t = 405\Omega_i^{-1}$, a negative current is again formed at the resonant surface.

In order to investigate the origin of this instability, we study the electric

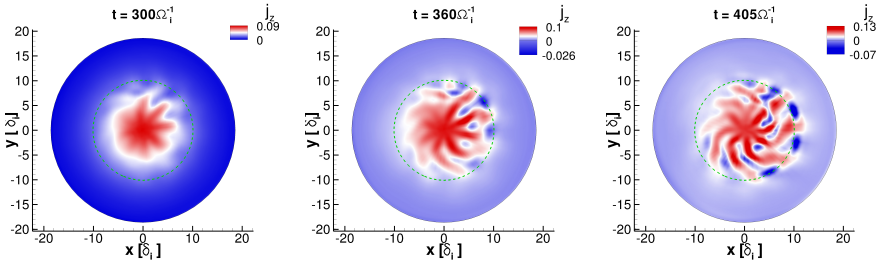

Figure 8.16: Current in the z-direction on the $z = L_z/2$ at $t = 300\Omega_i^{-1}$, $360\Omega_i^{-1}$, and $405\Omega_i^{-1}$ in the slice at $z = L_z/2$. The resonant surface is plotted as a green dashed line.

field in the z-direction. In Fig. 8.17, we present the evolution of the isosurface $E_z = \pm 0.009 B_0 v_A$ between $t = 300\Omega_i^{-1}$ and $t = 405\Omega_i^{-1}$. We can see that electric fields with different polarities rotate around the z axis in the direction of the negative z. Initially, three disconnected regions along the toroidal direction with $m = 3$ in the poloidal direction. As the electric fields rotate, the magnitude grows and the isosurfaces coalescence. The three regions of different sizes are still visible at $t = 405\Omega_i^{-1}$. The instability is therefore identified as the drift-wave instability.

However, in the region of $q < 1$ (inside the grey cylinder representing the resonant surface), the electric field behaves differently. This is due to the fact that the maximum of the gradient in density is located in the same region of the resonant surface. In Fig. 8.18, E_z is plotted on the slice $z = L_z/2$ at the times $t = 300\Omega_i^{-1}$, $360\Omega_i^{-1}$, and $405\Omega_i^{-1}$. The resonant surface is plotted as a green dashed line. An interesting feature is observed. Inside the resonant surface ($r < r_s$), the electric field has a component in the $m = 4$ mode, whereas in the outer region $r > r_s$ the component that is present is the $m = 3$.

The drift-wave instability is responsible for large dissipation and therefore can produce magnetic reconnection. In Fig. 8.19, we present the isosurfaces of electric current with values $j_z = 0.07 e n_0 v_A$ (red) and $j_z = -0.01 e n_0 v_A$ (blue) at $t = 300\Omega_i^{-1}, 375\Omega_i^{-1}$, and $430.2\Omega_i^{-1}$. At $t = 300\Omega_i^{-1}$, the core of the electric current is inside the resonant surface that is represented as a grey cylinder. However, the turbulence that is triggered by the drift waves grows and the current dissipates in the radial direction. This results in a collision of strong currents with the resonant surface. Similar to the case with the kink instability, when a large electric current approaches the resonant surface, magnetic reconnection occurs and an opposite current carried by electrons is

created. In this case, we can see again positive and negative currents that are separated by the resonant surface.

The electric currents carried by ions and electrons are presented in Fig. 8.20. In this case, the initial equilibrium is not completely lost and the ion current is only half of the electron current. The drift wave turbulence affects mostly the electron current. The opposite current is fully carried by electrons. In the right panel of the same figure, the auxiliary magnetic field is presented. Magnetic reconnection can be identified o the vicinity of the resonant surface in the regions where the electron current is negative.

8.5 CONCLUSIONS

In these results, we identify the secondary magnetic reconnection produced by the kink and the drift-wave instabilities of flux ropes in tokamak conditions. In a set of three-dimensional two-fluid simulations, solving for the mass, momentum, and energy conservation laws of ions and electrons coupled to the full Maxwell's equations, we simulate the full-scale dynamics of an infinite straight flux rope with realistic dimensions and conditions of the DIII-D tokamak. The multi-fluid approach, based on the $5M$-approximation, although it is still rather unexplored, proves to be an alternative to MHD and kinetic codes. It is able to capture global MHD modes such as the kink, as well as features that are present in collisionless kinetic simulations, such as the Hall effect and the drift wave turbulence.

Firstly, a flux rope with a small initial perturbation in the $m = 1$, $n = 1$ mode is studied. As the safety factor in the axis is $q_0 < 1$, the flux rope is expected to be unstable against internal modes. Indeed, the flux tube kinks in time scales comparable to the Alfvénic transit time, that is $t_A = 292\Omega_i^{-1}$. At time $t = 163.2\Omega_i^{-1}$ the kink is already visible and at $t = 207 - 230.3\Omega_i^{-1}$ it is in a non-linear stage where signatures of reconnection are observed (See Figs. 8.6 and 8.9).

In the simulation with the initial perturbation, the reconnection is first studied with the auxiliary magnetic field $\vec{B}^*$. The kink drives the inner region of $\vec{B}^*$ towards the resonant surface producing a collision between magnetic fields of different polarity. The kink is stabilized by the wall and therefore the reconnection is very localized in the resonant surface region. Magnetic reconnection produces an untwist of the field lines that can be observed macroscopically (Fig. 8.7).

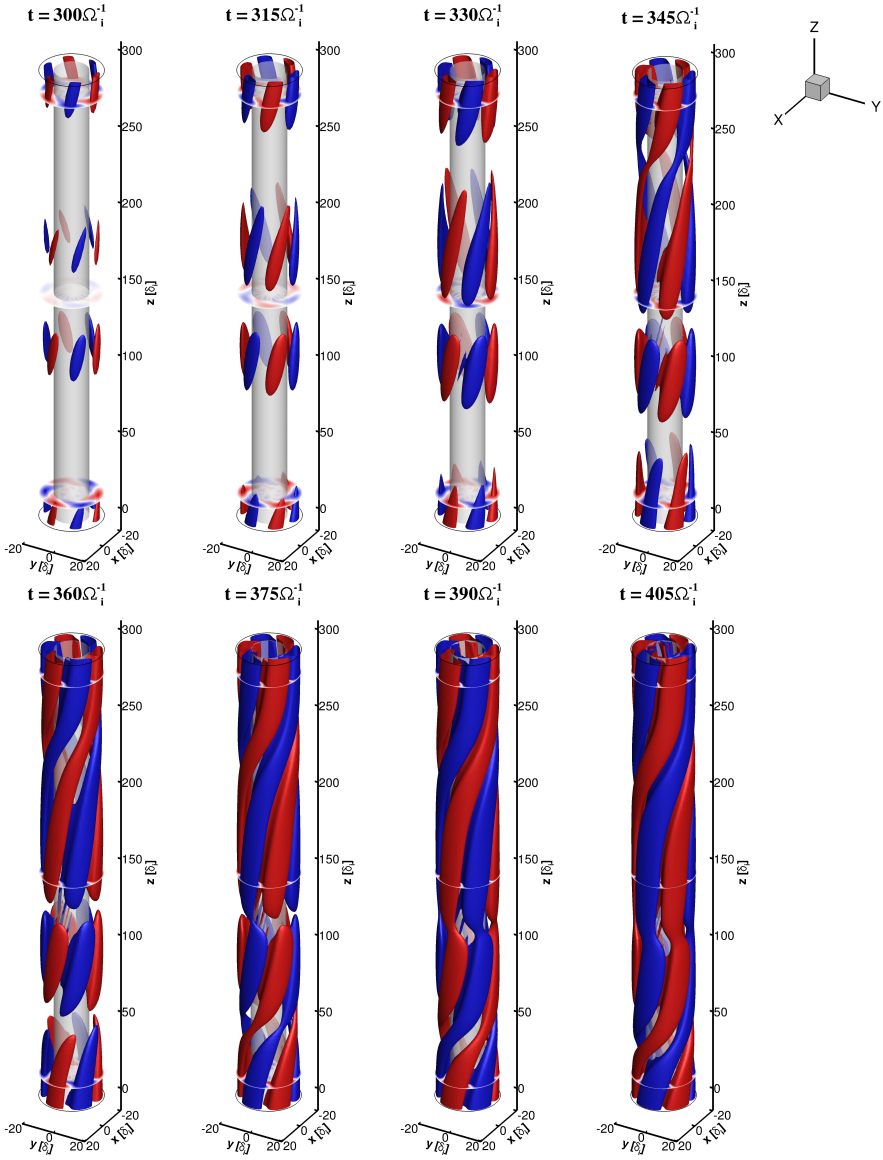

Figure 8.17: Isocontour of the electric field in the z-direction $E_z = 0.009 B_0 v_A$ (red) and $E_z = -0.009 B_0 v_A B_0$ (blue) at $t = 300\Omega_i^{-1}$, $315\Omega_i^{-1}$, $330\Omega_i^{-1}$, $345\Omega_i^{-1}$, $360\Omega_i^{-1}$, $375\Omega_i^{-1}$, $390\Omega_i^{-1}$, $405\Omega_i^{-1}$. The resonant surface is presented in grey.

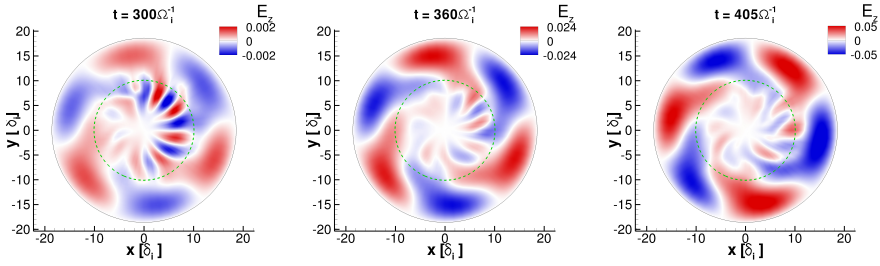

Figure 8.18: E_z distribution $t = 300\Omega_i^{-1}$, $t = 360\Omega_i^{-1}$, and $t = 405\Omega_i^{-1}$ in the slice at $z = L_z/2$.

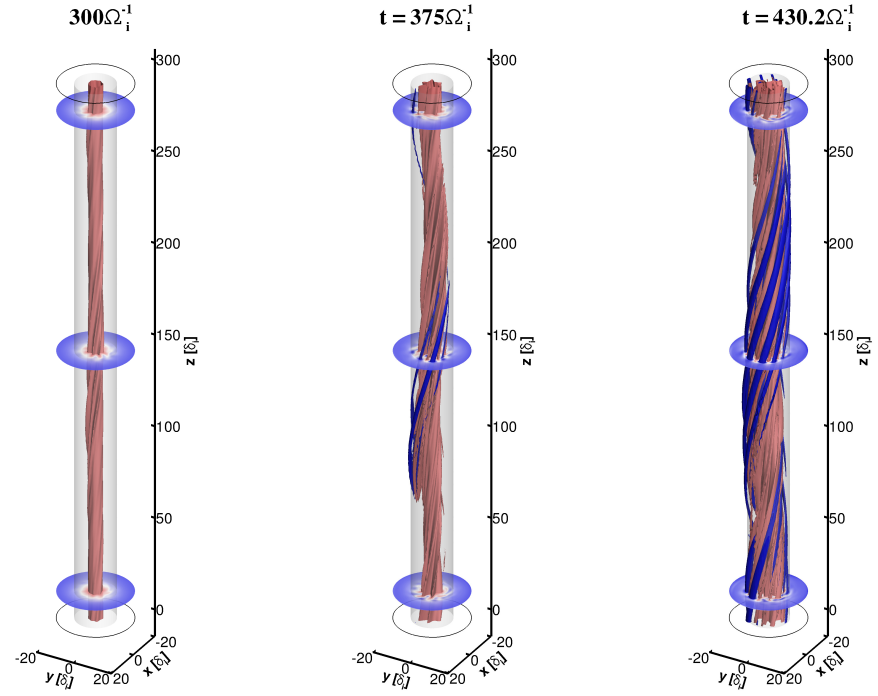

Figure 8.19: Isocontour of the electric current $j_z = 0.07en_0v_A$ (red) and $j_z = -0.01en_0v_A$ (blue) at $t = 300\Omega_i^{-1}$, $375\Omega_i^{-1}$, and $430.2\Omega_i^{-1}$. The resonant surface is presented in grey.

The reconnection generates an electric field $E_z \sim 0.01B_0v_A$ that can be observed as a red surface in Fig. 8.11. This electric field is the reconnection

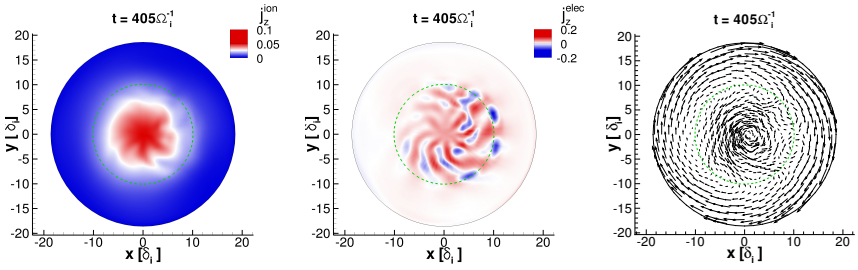

Figure 8.20: Current in the z-direction on the $z = L_z/2$ at $t = 207.6\Omega_i^{-1}$ carried by ions (left) and electrons(center). Right: Quiver plot of the auxiliary magnetic field $\vec{B}^*$ at the same time. The resonant surface is plotted as a dashed green line.

inductive electric field. Similarly, different bi-polar structures are present outside the resonant surface. These structures are identified as drift waves.

The secondary magnetic reconnection creates an opposite current with a magnitude that is approximately the same of the current supporting the flux rope. The opposite current is very localized in the reconnection region and is fully carried by the electrons. This observation agrees with the PIC kinetic simulations by Markidis et al. [205]. Additionally, opposite currents have been observed in the reconnection scaling experiment (RSX) [220, 221]. However, the two-polarity electric field in the reconnection region that is present in the PIC simulations of Markidis et al. [205] is not present in the two-fluid simulations.

The pressure gradient supporting the Lorentz force of the flux rope is produced by a density distribution in the radial direction. Owing to that reason, the density cavities that are characteristic in magnetic reconnections are difficult to be observed in this simulations. Nevertheless, the difference between the densities of ions and electrons show a quadripolar structure in the region where the reconnection takes place. These quadripolar cavities in the plane perpendicular to the flux rope axis have been identified in kinetic simulations as signatures of secondary magnetic reconnection in PIC simulations [205].

Finally, the so-called sawtooth crash is captured in the simulation as a result of the non-linear kink instability. The crash occurs after approximately one Alfvénic transit time. During the simulation, the electron temperature rises until the disruption takes place and it drops around 1.6 keV in a short interval of $20\Omega_i^{-1}$.

The second simulation is initialized with the two-fluid equilibrium derived in Section 8.3, without initial perturbation. Although the configuration is

kink-unstable, the kink instability is not triggered. Instead, an instability with high poloidal mode number develops after one Alfvénic transit time (see Fig. 8.15).

The drift-wave instability is responsible for electric current perturbations in the poloidal direction with high mode number. Electric fields parallel to the magnetic field with different polarities are formed and rotate around the magnetic axis in the direction of the negative z. Two different modes are identified in the electric field E_z. In regions inside the resonant surface ($r < r_s$) $m = 4$ develops, whereas outside ($r > r_s$) it is the mode $m = 3$, as seen in Fig. 8.18. This is due to the fact that the maximum of the density gradient is located in the same region of the resonant surface.

The drift waves produce turbulent in the plane perpendicular to the axis of the flux rope. Consequently, the electric current, initially confined inside the resonant surface, starts diffusing in the radial direction. This dissipation changes the topology of the magnetic field in areas close to the resonant surface. As a result of the magnetic reconnection reconnection an opposite electron current is formed.

The drift-wave instability triggers and grows spontaneously whereas the kink instability needs an initial perturbation to develop. This proves the universal character of the drift-wave instability in configurations with density gradients.

8.6 SUMMARY

Three-dimensional two-fluid simulations of a flux rope in tokamak conditions have been presented. The two-fluid approach is able to capture MHD global modes such as the kink while capturing the separation between ions and electrons that is responsible for the Hall effect and the drift-wave turbulence. These effects play a fundamental role in the development and evolution of the secondary magnetic reconnection.

We propose the two-fluid approach as a sound alternative to MHD and kinetic codes for the study of magnetically confined fusion plasmas. As a fluid model, the multi-fluid approach is able to capture macroscopic dynamics, while representing the separation between the species. The implicit time-stepping does not require a CFL constraint, however, the size of the time step and the mesh cell is chosen according to the ion scales in order to resolve these scales. The present work opens a new opportunity to study flux ropes in astrophysical scenarios where the density is too high to be solved by kinetic codes, but where the two-fluid instabilities may play an important role.

CHAPTER 9

Conclusions and Perspectives

I think and think for months and years. Ninety-nine times, the conclusion is false. The hundredth time I am right.

– Albert Einstein

Plasmas interacting with magnetic fields host a wide variety of complex phenomena. The scientific community is constantly developing new simulation tools that are aimed at analyzing the impact of microscopic processes on the global dynamics of the plasma. The majority of these numerical codes rely on the single-fluid MHD approximation or on particle methods. While the former only captures low-frequency large-scale dynamics, the latter is computationally very costly and is thus restricted to limited domains or low-density and weakly collisional environments. Improved predictive tools would contribute to better understand long-standing problems that puzzle the plasma physics community such as coronal heating or controlled thermonuclear fusion. A better understanding of coronal heating would infer an important improvement of the space weather prediction tools as it would shed light on how energy is transferred in the solar wind expanding from the corona. Alternatively, the achievement of controlled nuclear fusion would potentially meet the energy needs of our society with a nearly unlimited CO_2-free energy source.

The general objective of this thesis was to develop a numerical tool based on the multi-fluid plasma description for both the partially-ionized plasma conditions of the lower solar atmosphere and the fully-ionized conditions of the magnetic confinement fusion reactors. A new numerical method has been developed, implemented into a HPC platform, and extensively validated in a wide range of plasma regimes. The resulting numerical tool has been applied to the study of the effect of radiation on magnetic reconnection under chromospheric conditions, the propagation of magnetosonic waves in the lower solar atmosphere, and the kink and drift-wave instabilities in a tokamak.

As we have seen in this dissertation, multi-fluid modeling is a rather unexplored approach that can contribute to understand the influence of the

microscopic processes that result from the interaction between the species within the plasma on the global plasma dynamics.

9.1 GENERAL CONTRIBUTION

The main contributions of this work can be summarized in three points: 1) the development and implementation of a numerical method for solving the multi-fluid plasma equations coupled to Maxwell's equations, 2) the study of the partially-ionized chromosphere with multi-fluid models, and 3) the study of kink and drift-wave instabilities inside tokamaks with multi-fluid models.

9.1.1 Development of a versatile numerical solver for the multi-fluid plasma model

An innovative numerical method that solves for the multi-fluid plasma equations, including the transport, frictional, and chemical reactions terms, coupled to Maxwell's equations has been proposed. The numerical method features implicit time integration to tackle the stiffness of the system, a scheme that solves flows at all speeds regimes (from subsonic to supersonic), and a scheme for the electromagnetic field with a proper scaling for the numerical dissipation.

The numerical method has been implemented into COOLFluiD, a modern world-class HPC platform that allows a proper efficiency on massively-parallel architectures up to several tens of thousands of cores. The multi-fluid/Maxwell code presented in this dissertation has been tested on a number of supercomputer facilities. These include the ThinKing cluster of the Flemish Supercomputer Centre (VSC), NASA's Pleiades supercomputer, the XC40 Hazel Hen system at HLRS, the Blue Gene/Q JUQUEEN at JSC, and VKI's local clusters. Additionally, in a work that is not included in this dissertation, the algorithm has been ported to graphics processing units (GPUs).

The numerical tool has been extensively verified and proves its versatility to represent a wide range of plasma regimes – from low-subsonic to supersonic, from reactive partially-ionized to fully-ionized, and from collisionally dominated to collisionless and magnetically dominated. The reusable implementation of the code allows for selecting the number of species and the closure models of choice. Hence, the same code can be used to simulate ideal and resistive MHD, reactive and collisional ion-neutral, and ion-electron models. Similarly, three fluid (ion, electron, and neutral species) partially-ionized or

multi-ion fully-ionized models could be explored with this code. This opens the possibility for many new applications of the code in the future.

9.1.2 Multi-fluid study of the partially-ionized solar atmosphere

The non-equilibrium partially-ionized plasma of the lower solar atmosphere has been studied with a multi-fluid model. The model accounts for friction between the fluids, electron impact ionization and radiative recombination reactions, transport fluxes, anisotropic heat conduction, and different radiation models.

Firstly, we have studied magnetic reconnection under chromospheric conditions. In a systematic study of different ionization levels and radiation models, we have shown that the interplay between radiation, chemical equilibrium, and ambipolar diffusion has a great impact in the dynamics of magnetic reconnection in the chromosphere. We observe under realistic circumstances that the current sheet width becomes very narrow and eventually comparable to the neutral-ion mean free path. In order to properly capture the decoupling between the motion of the ions and neutrals that occurs at these scales, multi-fluid models are necessary. The simulations with strong radiative cooling show reconnection outflows and time scales comparable to these observed in spicules.

Secondly, we have studied the propagation of magnetosonic waves in the lower atmosphere of the Sun. To the best of our knowledge, for the first time a global simulation of the lower solar atmosphere was studied with a multi-fluid model that treats separately the ion and the neutral dynamics. The simulations self-consistently develop a funnel-like magnetic topology at the upper chromosphere whereas at the photosphere the magnetic field is tangled. The magnetosonic waves are driven at the footpoint of the flux tube and they travel along the chromosphere changing locally the chemical equilibrium. Multi-fluid global simulations of the lower solar atmosphere can contribute to properly characterize the role of neutrals in the transport of energy from the bottom of the atmosphere to the corona.

9.1.3 Multi-fluid study of plasma instabilities in tokamaks

We have studied the dynamics of a flux rope under typical DIII-D tokamak conditions. The plasma is fully ionized and low collisional and hosts a wide variety of instabilities at different scales, from the kinetic scales to global

MHD scales. We have simulated the kink and the drift-wave instability with a two-fluid model that considers ions and electrons separately.

In our results, we have shown that multi-fluid models are able to capture the dynamics of global MHD instabilities, such as the kink instability, while capturing the separation between the dynamics of ions and electrons. We analyzed the signatures of the secondary magnetic reconnection that occurs in the vicinity of the resonant surface. The multi-fluid model is able to capture the opposite electron current that is also observed in PIC simulations and in the laboratory experiments. Additionally, we have studied the drift-wave instability. Single-fluid MHD codes are not able to capture this instability as it results from the separation between the ion and electron dynamics.

As we have seen in Chapter 2, the multi-fluid equations contain modes relative to both global MHD scales and kinetic scales. Additionally, they are able to capture non-linear dynamics such as the drift turbulence that result from the separation of the motions of ions and electrons. Owing to these reasons, multi-fluid codes are a sound, rather unexplored, alternative to PIC and single-fluid MHD codes for the study of magnetic confinement reactors. In this work, we have proven their ability to capture both small scale turbulence and the global dynamics of the flux ropes.

9.2 SUMMARY

The general multi-fluid plasma equations were derived from kinetic theory, including both elastic and inelastic collisions (Chapter 2). The ideal two-fluid plasma model that considers ions and electrons separately without diffusion and collisions has been presented. The analysis of the propagation of linear waves in an ideal two-fluid plasma (Section 2.4.3) showed that both the kinetic and the MHD waves are contained in the multi-fluid description. The dispersion diagram of these waves was presented for different astrophysical and laboratory conditions. The behaviour of the modes strongly depends on the conditions of the background plasma, especially for wavelengths comparable to the plasma skin depth.

Two closure models were presented in Chapter 3. The partially-ionized plasma multi-fluid model considers plasma (ion+electrons) and neutrals separately. The model considers chemical reactions, frictional energy and momentum exchange, transport fluxes, anisotropic heat conduction, and radiation. The classical transport closure is presented for fully-ionized plasmas.

A novel numerical method was introduced in Chapter 4. The numerical method couples the multi-fluid plasma model with the Maxwell's equations.

The spatial discretization relies on the finite volume method on unstructured meshes with an AUSM$^+$-up scheme for the multi-fluid and a modified-CIR scheme for the Maxwell's equations with hyperbolic divergence cleaning. The time discretization is second-order implicit.

The verification of the model was carried out in Chapter 5. The second-order accuracy in space was demonstrated both in plasmas with the charge neutrality assumption and the two-fluid (ion+electron) model. The ability of the proposed numerical method to capture strong MHD shocks was proven in the Orszag-Tang problem and the MHD rotor. Additionally, the verification of the reactive and collisional terms was carried out by comparing with a result found in the literature. Finally, the fully-ionized two-fluid model was verified on a Brio-Wu type shock tube and the GEM challenge.

The partially-ionized plasma model was applied to the study of chromospheric magnetic reconnection and the propagation of magnetosonic waves in the photosphere and chromosphere (Chapters 6 and 7). The main conclusions drawn from these studies are the following. First, the reconnection in chromospheric conditions occurs faster due to the effect of radiative cooling as it produces a loss of ions through recombination and enhances the ambipolar diffusion. Second, magnetosonic waves can travel through the chromosphere producing localized heating at the wave fronts. The chemical equilibrium is locally modified by the waves, although no visible decoupling of the motion of ion and neutrals is observed.

Finally, the kink and the drift-wave instabilities in flux ropes under tokamak conditions were studied (Chapter 8). The kink instability induces reconnection in the resonant surface region. The signatures of magnetic reconnection, such as the opposite electron current, are similar to others based on PIC simulation results. Additionally, the drift-wave instability is triggered spontaneously in our simulations after one Alfvénic transit time. This instability produces a large dissipation in the perpendicular direction to the magnetic field that eventually can produce localized reconnection in regions close to the resonant surface.

Multi-fluid models represent an alternative to PIC and single-fluid MHD approaches. Our simulations show that multi-fluid models are able to capture both the macroscopic dynamics while taking into account some of the important phenomena that take place at microscopic scales, i.e., elastic and inelastic collisions, charge separation, drift motions, and diffusion of momentum and energy.

9.3 RECOMMENDATIONS AND PERSPECTIVES

As we have seen above, a new numerical tool has been developed for the study of non-equilibrium plasmas. The promising results obtained in this work show that multi-fluid is a description that allows to capture the influence of the microscopic processes on the global dynamics. We propose the following future developments of the numerical code.

The multi-fluid equations need closure models in order to properly characterize the transport and the chemical kinetics terms. As we mentioned in Chapter 3, a closure model for the partially-ionized multi-fluid equations that considers elastic and inelastic collisions and is rigorously derived with Grad's method is, to the best of our knowledge, still not available in literature. A recent effort towards this goal has been developed by Zhdanov & Stepanenko [89, 97]. The accurate characterization of the collisional cross-sections, including the charge-exchange collisions, would contribute to improve the transport models for partially-ionized plasmas.

Similarly, the hypotheses assumed for the classical transport closure for fully-ionized plasmas are not completely fulfilled in plasmas under tokamak conditions. Those plasmas are nearly collisionless and the curvature of the magnetic field should be taken into account by the transport properties (neoclassical transport theory). Alternatively, higher moment multi-fluid equations can provide a more accurate description in nearly-collisionless plasmas. The extension of the present code to higher moment models is feasible and most of the ideas of the numerical method, i.e., scaling of the numerical dissipation, implicit time stepping, AUSM-like schemes, etc, could be applied.

Concerning the study of the magnetic reconnection under chromospheric conditions, the Hall term was neglected in the study we have carried out as in those conditions the ion skin depth was very small as compared to the width of the current sheet. However, as observed by Murphy & Lukin [73], these scales can become comparable in the upper layers of the chromosphere. An interesting extension of the work here presented is the simulation of the chromospheric reconnection with an improved three fluid model.

Similarly, the study of the global dynamics of the lower solar atmosphere with a multi-fluid simulation is a promising tool to understand the role played by the neutrals in the transport of energy through the chromosphere. In Chapter 7, the first steps towards this goal were presented. The numerical tool here developed is able to perform 3D global simulations were the dynamics of waves and reconnection could be studied.

As we saw in Chapter 8, multi-fluid models can capture both microscopic and macroscopic instabilities in flux ropes. The study carried out under

tokamak conditions could be extended to other flux ropes such as the coronal loops. Multi-fluid models could help to understand the relation between drift-wave transport, magnetic braiding, and coronal heating.

In this dissertation we focused on multi-fluid models for two applications, the lower solar atmosphere and tokamaks. However, multi-fluid modeling can be applied to a wide variety of different conditions of interest for astrophysical and technological plasmas. The first steps for the development of a multi-ion global magnetosphere were developed during this work, although they are not included in this dissertation. Similarly, multi-fluid models of the corona and the solar wind could be used in space weather simulations. Finally, other plasma technological applications such as magnetic nozzles or Hall thrusters could be studied with multi-fluid models.

Bibliography

[1] J. E. Vernazza, E. H. Avrett, and R. Loeser. Structure of the solar chromosphere. III - Models of the EUV brightness components of the quiet-sun. *The Astrophysical Journal Supplement Series*, 45:635–725, April 1981. xv, xix, 2, 3, 6, 8, 136, 137, 138

[2] E. Khomenko, M. Collados, A. Díaz, and N. Vitas. Fluid description of multi-component solar partially ionized plasma. *Physics of Plasmas*, 21(9):092901, September 2014. xv, 3, 8, 36, 37, 116

[3] M. L. Goodman and P. G. Judge. Radiating Current Sheets in the Solar Chromosphere. *The Astrophysical Journal*, 751:75, May 2012. xv, 37, 41

[4] Schure, K. M., Kosenko, D., Kaastra, J. S., Keppens, R., and Vink, J. A new radiative cooling curve based on an up-to-date plasma emission code. *Astronomy & Astrophysics*, 508(2):751–757, 2009. xv, 41

[5] S. I. Braginskii. Transport Processes in a Plasma. *Reviews of Plasma Physics*, 1:205, 1965. xvi, 17, 33, 35, 39, 42, 44, 45, 46, 47, 48, 114, 116

[6] V. M. Zhdanov. Transport Processes in Multicomponent Plasma. *Plasma Physics and Controlled Fusion*, 44:2283, October 2002. xvi, 17, 19, 20, 21, 23, 33, 34, 35, 36, 42, 46, 47, 48

[7] Andrew J. Christlieb, James A. Rossmanith, and Qi Tang. Finite difference weighted essentially non-oscillatory schemes with constrained transport for ideal magnetohydrodynamics. *Journal of Computational Physics*, 268:302 – 325, 2014. xvi, 85

[8] J. E. Leake, V. S. Lukin, M. G. Linton, and E. T. Meier. Multi-fluid Simulations of Chromospheric Magnetic Reconnection in a Weakly Ionized Reacting Plasma. *The Astrophysical Journal*, 760:109, December 2012. xvii, 7, 8, 36, 37, 39, 40, 50, 87, 88, 90, 91, 92, 94, 95, 113, 114, 115, 122, 132, 133

[9] J. Birn, J. F. Drake, M. A. Shay, B. N. Rogers, R. E. Denton, M. Hesse, M. Kuznetsova, Z. W. Ma, A. Bhattacharjee, A. Otto, and P. L. Pritchett. Geospace environmental modeling (gem) magnetic reconnection challenge. *J. Geophys. Res.*, 106(A3):3715–3720, 03 2001. xviii, 100, 101, 102

[10] J. Loverich, A. Hakim, and U. Shumlak. A discontinuous galerkin method for ideal two-fluid plasma equations. *Communications in Computational Physics 9*, 240, 2011. xviii, 50, 95, 96, 101, 102

[11] K. Shibata, T. Nakamura, T. Matsumoto, K. Otsuji, T. J. Okamoto, N. Nishizuka, T. Kawate, H. Watanabe, S. Nagata, S. UeNo, R. Kitai, S. Nozawa, S. Tsuneta, Y. Suematsu, K. Ichimoto, T. Shimizu, Y. Katsukawa, T. D. Tarbell, T. E. Berger, B. W. Lites, R. A. Shine, and A. M. Title. Chromospheric Anemone Jets as Evidence of Ubiquitous Reconnection. *Science*, 318:1591, December 2007. xviii, 112, 113

[12] W. Horton. Drift waves and transport. *Reviews of Modern Physics*, 71:735–778, April 1999. xx, 153, 154

[13] D. Biskamp. *Magnetic Reconnection in Plasmas*. Cambridge University Press, 2005. 1, 7, 9

[14] E. Priest and T. Forbes, editors. *Magnetic reconnection : MHD theory and applications*, 2000. 1, 9, 151

[15] J. P. H. Goedbloed and S. Poedts. *Principles of Magnetohydrodynamics*. August 2004. 2, 4, 8, 17, 18, 24, 25, 27, 28, 150, 151, 160

[16] B. De Pontieu, S. W. McIntosh, M. Carlsson, V. H. Hansteen, T. D. Tarbell, P. Boerner, J. Martinez-Sykora, C. J. Schrijver, and A. M. Title. The Origins of Hot Plasma in the Solar Corona. *Science*, 331:55, January 2011. 2

[17] J. A. Klimchuk. Key aspects of coronal heating. *Philosophical Transactions of the Royal Society of London Series A*, 373:20140256–20140256, April 2015. 2

[18] P. Testa, S. H. Saar, and J. J. Drake. Stellar activity and coronal heating: an overview of recent results. *Philosophical Transactions of the Royal Society of London Series A*, 373:20140259–20140259, April 2015. 2

[19] P K Browning. Mechanisms of solar coronal heating. *Plasma Physics and Controlled Fusion*, 33(6):539, 1991. 2

[20] E. R. Priest. Coronal Heating Mechanisms. In J. L. Linsky and S. Serio, editors, *Physics of Solar and Stellar Coronae*, volume 183 of *Astrophysics and Space Science Library*, page 515, 1993. 2

[21] F. Reale. Coronal Loops: Observations and Modeling of Confined Plasma. *Living Reviews in Solar Physics*, 11:4, July 2014. 2, 150

[22] I. De Moortel and P. Browning. Recent advances in coronal heating. *Philosophical Transactions of the Royal Society of London Series A*, 373:20140269–20140269, April 2015. 2

[23] M. Goossens. Magnetohydrodynamic Waves and Wave Heating in Nonuniform Plasmas. In E. R. Priest and A. W. Hood, editors, *Advances in Solar System Magnetohydrodynamics*, page 137, 1991. 2

[24] S. W. McIntosh, B. de Pontieu, M. Carlsson, V. Hansteen, P. Boerner, and M. Goossens. Alfvénic waves with sufficient energy to power the quiet solar corona and fast solar wind. *Nature*, 475:477–480, July 2011. 2

[25] A. K. Srivastava, J. Shetye, K. Murawski, J. G. Doyle, M. Stangalini, E. Scullion, T. Ray, D. P. Wójcik, and B. N. Dwivedi. High-frequency torsional Alfvén waves as an energy source for coronal heating. *Scientific Reports*, 7:43147, March 2017. 2

[26] J. Heyvaerts and E. R. Priest. Coronal heating by phase-mixed shear Alfven waves. *Astronomy & Astrophysics*, 117:220–234, January 1983. 2

[27] P. J. Cargill, I. De Moortel, and G. Kiddie. Coronal Density Structure and its Role in Wave Damping in Loops. *The Astrophysical Journal*, 823:31, May 2016. 2

[28] J. Tataronis and W. Grossmann. Decay of MHD waves by phase mixing. *Zeitschrift fur Physik*, 261:203–216, June 1973. 2

[29] T. J. Okamoto, P. Antolin, B. De Pontieu, H. Uitenbroek, T. Van Doorsselaere, and T. Yokoyama. Resonant Absorption of Transverse Oscillations and Associated Heating in a Solar Prominence. I. Observational Aspects. *The Astrophysical Journal*, 809:71, August 2015. 2

[30] J. Vranjes and S. Poedts. The universally growing mode in the solar atmosphere: coronal heating by drift waves. *Monthly Notices of the Royal Astronomical Society*, 398:918–930, September 2009. 2, 153

[31] J. Vranjes and S. Poedts. Drift waves in the corona: heating and acceleration of ions at frequencies far below the gyrofrequency. *Monthly Notices of the Royal Astronomical Society*, 408:1835–1839, November 2010. 2, 153

[32] J. Vranjes and S. Poedts. Kinetic Instability of Drift-Alfvén Waves in Solar Corona and Stochastic Heating. *The Astrophysical Journal*, 719:1335–1342, August 2010. 2, 153

[33] E. N. Parker. Topological Dissipation and the Small-Scale Fields in Turbulent Gases. *The Astrophysical Journal*, 174:499, June 1972. 2

[34] E. R. Priest, J. F. Heyvaerts, and A. M. Title. A Flux-Tube Tectonics Model for Solar Coronal Heating Driven by the Magnetic Carpet. *The Astrophysical Journal*, 576:533–551, September 2002. 2

[35] E. N. Parker. Nanoflares and the solar X-ray corona. *The Astrophysical Journal*, 330:474–479, July 1988. 2

[36] P. Testa, B. De Pontieu, J. Allred, M. Carlsson, F. Reale, A. Daw, V. Hansteen, J. Martinez-Sykora, W. Liu, E. E. DeLuca, L. Golub, S. McKillop, K. Reeves, S. Saar, H. Tian, J. Lemen, A. Title, P. Boerner, N. Hurlburt, T. D. Tarbell, J. P. Wuelser, L. Kleint, C. Kankelborg, and S. Jaeggli. Evidence of nonthermal particles in coronal loops heated impulsively by nanoflares. *Science*, 346:1255724, October 2014. 2

[37] Bart De Pontieu, Scott W. McIntosh, Viggo H. Hansteen, and Carolus J. Schrijver. Observing the roots of solar coronal heating—in the chromosphere. *The Astrophysical Journal Letters*, 701(1):L1, 2009. 2

[38] B. De Pontieu, L. Rouppe van der Voort, S. W. McIntosh, T. M. D. Pereira, M. Carlsson, V. Hansteen, H. Skogsrud, J. Lemen, A. Title, P. Boerner, N. Hurlburt, T. D. Tarbell, J. P. Wuelser, E. E. De Luca, L. Golub, S. McKillop, K. Reeves, S. Saar, P. Testa, H. Tian, C. Kankelborg, S. Jaeggli, L. Kleint, and J. Martinez-Sykora. On the prevalence of small-scale twist in the solar chromosphere and transition region. *Science*, 346:1255732, October 2014. 2

[39] V. Hansteen, B. De Pontieu, M. Carlsson, J. Lemen, A. Title, P. Boerner, N. Hurlburt, T. D. Tarbell, J. P. Wuelser, T. M. D. Pereira, E. E. De Luca, L. Golub, S. McKillop, K. Reeves, S. Saar, P. Testa, H. Tian, C. Kankelborg, S. Jaeggli, L. Kleint, and J. Martínez-Sykora. The unresolved fine structure resolved: IRIS observations of the solar transition region. *Science*, 346:1255757, October 2014. 2

[40] T. Kosugi, K. Matsuzaki, T. Sakao, T. Shimizu, Y. Sone, S. Tachikawa, T. Hashimoto, K. Minesugi, A. Ohnishi, T. Yamada, S. Tsuneta, H. Hara, K. Ichimoto, Y. Suematsu, M. Shimojo, T. Watanabe, S. Shimada, J. M. Davis, L. D. Hill, J. K. Owens, A. M. Title, J. L. Culhane, L. K. Harra, G. A. Doschek, and L. Golub. The Hinode (Solar-B) Mission: An Overview. *Solar Physics*, 243:3–17, June 2007. 2

[41] B. De Pontieu, A. M. Title, J. R. Lemen, G. D. Kushner, D. J. Akin, B. Allard, T. Berger, P. Boerner, M. Cheung, C. Chou, J. F. Drake, D. W. Duncan, S. Freeland, G. F. Heyman, C. Hoffman, N. E. Hurlburt, R. W. Lindgren, D. Mathur, R. Rehse, D. Sabolish, R. Seguin, C. J. Schrijver, T. D. Tarbell, J.-P. Wülser, C. J. Wolfson, C. Yanari, J. Mudge, N. Nguyen-Phuc, R. Timmons, R. van Bezooijen, I. Weingrod, R. Brookner, G. Butcher, B. Dougherty, J. Eder, V. Knagenhjelm, S. Larsen, D. Mansir, L. Phan, P. Boyle, P. N. Cheimets, E. E. DeLuca, L. Golub, R. Gates, E. Hertz, S. McKillop, S. Park, T. Perry, W. A. Podgorski, K. Reeves, S. Saar, P. Testa, H. Tian, M. Weber, C. Dunn, S. Eccles, S. A. Jaeggli, C. C. Kankelborg, K. Mashburn, N. Pust, L. Springer, R. Carvalho, L. Kleint, J. Marmie, E. Mazmanian, T. M. D. Pereira, S. Sawyer, J. Strong, S. P. Worden, M. Carlsson, V. H. Hansteen, J. Leenaarts, M. Wiesmann, J. Aloise, K.-C. Chu, R. I. Bush, P. H. Scherrer, P. Brekke, J. Martinez-Sykora, B. W. Lites, S. W. McIntosh, H. Uitenbroek, T. J. Okamoto, M. A. Gummin, G. Auker, P. Jerram, P. Pool, and N. Waltham. The Interface Region Imaging Spectrograph (IRIS). *Solar Physics*, 289:2733–2779, July 2014. 2

[42] Elena Khomenko. On the effects of ion-neutral interactions in solar plasmas. *Plasma Physics and Controlled Fusion*, 59(1):014038, 2017. 3

[43] J. Martínez-Sykora, B. De Pontieu, V. Hansteen, and M. Carlsson. The role of partial ionization effects in the chromosphere. *Philosophical Transactions of the Royal Society of London Series A*, 373:20140268–20140268, April 2015. 3, 10, 148

[44] J. Martínez-Sykora, B. De Pontieu, and V. Hansteen. Two-dimensional Radiative Magnetohydrodynamic Simulations of the Importance of Partial Ionization in the Chromosphere. *The Astrophysical Journal*, 753:161, July 2012. 3

[45] M. Carlsson and J. Leenaarts. Approximations for radiative cooling and heating in the solar chromosphere. *Astronomy & Astrophysics*, 539:A39, March 2012. 3

[46] Andreas Lagg, Bruce Lites, Jack Harvey, Sanjay Gosain, and Rebecca Centeno. Measurements of photospheric and chromospheric magnetic fields. *Space Science Reviews*, 210(1):37–76, Sep 2017. 3

[47] David J Rose; Melville Clark. *Plasmas and controlled fusion.* Cambridge, Massachusetts : M.I.T. Press, 1965. 4

[48] R. Pampin, S. Zheng, S. Lilley, B.C. Na, M.J. Loughlin, and N.P. Taylor. Activation analyses updating the iter radioactive waste assessment. *Fusion Engineering and Design*, 87(7):1230 – 1234, 2012. Tenth International Symposium on Fusion Nuclear Technology (ISFNT-10). 4

[49] K. Schindler, M. Hesse, and J. Birn. General magnetic reconnection, parallel electric fields, and helicity. *Journal of Geophysical Research: Space Physics*, 93(A6):5547–5557, 1988. 6

[50] E. N. Parker. Sweet's Mechanism for Merging Magnetic Fields in Conducting Fluids. *Journal of Geophysical Research*, 62:509–520, December 1957. 7

[51] P. A. Sweet. The Neutral Point Theory of Solar Flares. In B. Lehnert, editor, *Electromagnetic Phenomena in Cosmical Physics*, volume 6 of *IAU Symposium*, page 123, 1958. 7

[52] H. E. Petschek. Magnetic Field Annihilation. *NASA Special Publication*, 50:425, 1964. 7

[53] Leonid M Malyshkin and Russell M Kulsrud. On two-dimensional magnetic reconnection with nonuniform resistivity. *Physica Scripta*, 2010(T142):014034, 2010. 7

[54] Z. X. Mei, R. Keppens, I. I. Roussev, and J. Lin. Magnetic reconnection during eruptive magnetic flux ropes. *Astronomy & Astrophysics*, 604:L7, August 2017. 7

[55] D. A. Uzdensky and R. M. Kulsrud. Two-dimensional numerical simulation of the resistive reconnection layer. *Physics of Plasmas*, 7(10):4018–4030, 2000. 7

[56] E. N. Parker. The Solar-Flare Phenomenon and the Theory of Reconnection and Annihiliation of Magnetic Fields. *Astrophysical Journal Supplement Series*, 8:177, July 1963. 7, 131

[57] E. T. Vishniac and A. Lazarian. Reconnection in the Interstellar Medium. *The Astrophysical Journal*, 511:193–203, January 1999. 7, 131

[58] F. Heitsch and E. G. Zweibel. Fast Reconnection in a Two-Stage Process. *The Astrophysical Journal*, 583:229–244, January 2003. 7, 131

[59] A. Brandenburg and E. G. Zweibel. The formation of sharp structures by ambipolar diffusion. *Astrophysical Journal, Part 2 - Letters*, 427:L91–L94, June 1994. 7

[60] A. Brandenburg and E. G. Zweibel. Effects of Pressure and Resistivity on the Ambipolar Diffusion Singularity: Too Little, Too Late. *The Astrophysical Journal*, 448:734, August 1995. 7

[61] V. L. Dorman and R. M. Kulsrud. One-dimensional Merging of Magnetic Fields with Cooling. *The Astrophysical Journal*, 449:777, August 1995. 7

[62] D. A. Uzdensky and J. C. McKinney. Magnetic reconnection with radiative cooling. I. Optically thin regime. *Physics of Plasmas*, 18(4):042105–042105, April 2011. 7

[63] Harold P. Furth, John Killeen, and Marshall N. Rosenbluth. Finiteresistivity instabilities of a sheet pinch. *The Physics of Fluids*, 6(4):459–484, 1963. 7

[64] S.V. Bulanov, J. Sakai, and A.S. Syrovatskii. Tearing mode instability in approximately steady mhd configurations. *Sov. J. Plasma Phys.*, 5:157–63, 1979. 7

[65] E. G. Zweibel. Magnetic reconnection in partially ionized gases. *The Astrophysical Journal*, 340:550–557, May 1989. 7, 131

[66] A. Bhattacharjee, Y.-M. Huang, H. Yang, and B. Rogers. Fast reconnection in high-Lundquist-number plasmas due to the plasmoid Instability. *Physics of Plasmas*, 16(11):112102, November 2009. 7, 132

[67] Y.-M. Huang and A. Bhattacharjee. Scaling laws of resistive magnetohydrodynamic reconnection in the high-Lundquist-number, plasmoid-unstable regime. *Physics of Plasmas*, 17(6):062104–062104, June 2010. 7, 132

[68] N. F. Loureiro, A. A. Schekochihin, and S. C. Cowley. Instability of current sheets and formation of plasmoid chains. *Physics of Plasmas*, 14(10):100703–100703, October 2007. 7, 132

[69] G. Lapenta. Self-Feeding Turbulent Magnetic Reconnection on Macroscopic Scales. *Physical Review Letters*, 100(23):235001, June 2008. 8

[70] L. Ni, B. Kliem, J. Lin, and N. Wu. Fast Magnetic Reconnection in the Solar Chromosphere Mediated by the Plasmoid Instability. *The Astrophysical Journal*, 799:79, January 2015. 8, 132

[71] L. Ni, J. Lin, I. I. Roussev, and B. Schmieder. Heating mechanisms in the low solar atmosphere through magnetic reconnection in current sheets. *ArXiv e-prints*, November 2016. 8

[72] J. E. Leake, V. S. Lukin, and M. G. Linton. Magnetic reconnection in a weakly ionized plasma. *Physics of Plasmas*, 20(6):061202, June 2013. 8, 36, 38, 40, 50, 113, 115, 122, 132

[73] N. A. Murphy and V. S. Lukin. Asymmetric Magnetic Reconnection in Weakly Ionized Chromospheric Plasmas. *The Astrophysical Journal*, 805:134, June 2015. 8, 36, 50, 113, 132, 133, 178

[74] M. R. O'Brien and D. C. Robinson. Tokamak experiments. In R. Dendy, editor, *Plasma Physics: an Introductory Course*, page 189, 1993. 9

[75] J. M. Dawson. Particle simulation of plasmas. *Reviews of Modern Physics*, 55:403–447, April 1983. 9

[76] E. Sonnendrücker, J. Roche, P. Bertrand, and A. Ghizzo. The Semi-Lagrangian Method for the Numerical Resolution of the Vlasov Equation. *Journal of Computational Physics*, 149:201–220, March 1999. 9

[77] Stefano Markidis, Giovanni Lapenta, and Rizwan-uddin. Multi-scale simulations of plasma with ipic3d. *Mathematics and Computers in Simulation*, 80(7):1509 – 1519, 2010. Multiscale modeling of moving interfaces in materials. 9, 150

[78] Giovanni Lapenta. Particle simulations of space weather. *Journal of Computational Physics*, 231(3):795 – 821, 2012. Special Issue: Computational Plasma Physics. 10

[79] S. Ku, C.S. Chang, and P.H. Diamond. Full-f gyrokinetic particle simulation of centrally heated global itg turbulence from magnetic axis to edge pedestal top in a realistic tokamak geometry. *Nuclear Fusion*, 49(11):115021, 2009. 10

[80] F. Filbet and E. Sonnendrücker. Comparison of Eulerian Vlasov solvers. *Computer Physics Communications*, 150:247–266, February 2003. 10, 150

[81] J. P. Goedbloed, R. Keppens, and S. Poedts. *Advanced Magnetohydrodynamics*. April 2010. 10

[82] B. V. Gudiksen, M. Carlsson, V. H. Hansteen, W. Hayek, J. Leenaarts, and J. Martínez-Sykora. The stellar atmosphere simulation code Bifrost. Code description and validation. *Astronomy & Astrophysics*, 531:A154, July 2011. 10

[83] S. Briguglio, F. Zonca, and G. Vlad. Hybrid magnetohydrodynamic-particle simulation of linear and nonlinear evolution of alfvén modes in tokamaks. *Physics of Plasmas*, 5(9):3287–3301, 1998. 10

[84] Lars K.S. Daldorff, Gábor Tóth, Tamas I. Gombosi, Giovanni Lapenta, Jorge Amaya, Stefano Markidis, and Jeremiah U. Brackbill. Two-way coupling of a global hall magnetohydrodynamics model with a local implicit particle-in-cell model. *Journal of Computational Physics*, 268(Supplement C):236 – 254, 2014. 10

[85] Gábor Tóth, Xianzhe Jia, Stefano Markidis, Ivy Bo Peng, Yuxi Chen, Lars K. S. Daldorff, Valeriy M. Tenishev, Dmitry Borovikov, John D. Haiducek, Tamas I. Gombosi, Alex Glocer, and John C. Dorelli. Extended magnetohydrodynamics with embedded particle-in-cell simulation of ganymede's magnetosphere. *Journal of Geophysical Research: Space Physics*, 121(2):1273–1293, 2016. 2015JA021997. 10

[86] K.D. Makwana, R. Keppens, and G. Lapenta. Two-way coupling of magnetohydrodynamic simulations with embedded particle-in-cell simulations. *Computer Physics Communications*, 2017. 10

[87] R. Balescu. *Transport Processes in Plasmas: Classical transport*. Transport Processes in Plasmas. North-Holland, 1988. 17, 18, 23, 34, 35, 36

[88] G. S. Voronov. Kinetic theory of plasmas: Translational energy. *Mathematical Models and Methods in Applied Sciencess*, 19:527–599, 2009. 19, 21

[89] V.M. Zhdanov and A.A. Stepanenko. Kinetic theory of transport processes in partially ionized reactive plasma, ii: Electron transport properties. *Physica A: Statistical Mechanics and its Applications*, 461(Supplement C):310 – 324, 2016. 20, 36, 178

[90] Vincent Giovangigli and Benjamin Graille. Kinetic theory of partially ionized reactive gas mixtures. *Physica A: Statistical Mechanics and its Applications*, 327(3):313 – 348, 2003. 20

[91] G. Lapenta, V. Pierrard, R. Keppens, S. Markidis, S. Poedts, O. Šebek, P. M. Trávníček, P. Henri, F. Califano, F. Pegoraro, M. Faganello, V. Olshevsky, A. L. Restante, Å. Nordlund, J. Trier Frederiksen, D. H. Mackay, C. E. Parnell, A. Bemporad, R. Susino, and K. Borremans. SWIFF: Space weather integrated forecasting framework. *Journal of Space Weather and Space Climate*, 3(27):A05, February 2013. 24

[92] S Poedts, Ch Kanella, and G Lapenta. Coronal heating and solar wind acceleration by drift waves. *Journal of Physics: Conference Series*, 642(1):012021, 2015. 24

[93] D. Bonfiglio, S. Cappello, and D. F. Escande. Dominant Electrostatic Nature of the Reversed Field Pinch Dynamo. *Physical Review Letters*, 94(14):145001, April 2005. 24

[94] G. Lapenta and M. Skender. Role of electric fields in the MHD evolution of the kink instability. *New Journal of Physics*, 19(2):023034, February 2017. 24

[95] Harold Grad. On the kinetic theory of rarefied gases. *Communications on Pure and Applied Mathematics*, 2(4):331–407, 1949. 34

[96] D. Mintzer. Generalized Orthogonal Polynomial Solutions of the Boltzmann Equation. *Physics of Fluids*, 8:1076–1090, June 1965. 34

[97] V.M. Zhdanov and A.A. Stepanenko. Kinetic theory of transport processes in partially ionized reactive plasma, i: General transport equations. *Physica A: Statistical Mechanics and its Applications*, 446(Supplement C):35 – 53, 2016. 36, 178

[98] E. T. Meier and U. Shumlak. A general nonlinear fluid model for reacting plasma-neutral mixtures. *Physics of Plasmas*, 19(7):072508, July 2012. 36, 37, 40, 50, 122

[99] T. V. Zaqarashvili, M. L. Khodachenko, and H. O. Rucker. Magnetohydrodynamic waves in solar partially ionized plasmas: two-fluid approach. *Astronomy & Astrophysics*, 529:A82, May 2011. 37

[100] T. V. Zaqarashvili, M. L. Khodachenko, and H. O. Rucker. Damping of Alfvén waves in solar partially ionized plasmas: effect of neutral helium in multi-fluid approach. *Astronomy & Astrophysics*, 534:A93, October 2011. 37

[101] G. S. Voronov. A Practical Fit Formula for Ionization Rate Coefficients of Atoms and Ions by Electron Impact: Z = 1-28. *Atomic Data and Nuclear Data Tables*, 65:1, 1997. 37, 38

[102] R. W. P. McWhirter. Spectral Intensities. In R. H. Huddlestone and S. L. Leonard, editors, *Plasma Diagnostic Techniques*, page 201, 1965. 38

[103] B. T. Draine and C. F. McKee. Theory of interstellar shocks. *Annual review of astronomy and astrophysics*, 31:373–432, 1993. 39

[104] A. E. Glassgold, P. S. Krstić, and D. R. Schultz. H^++H Scattering and Ambipolar Diffusion Heating. *The Astrophysical Journal*, 621:808–816, March 2005. 39

[105] U. Yusupaliev. Stoletov constant and effective ionization potential of a diatomic gas molecule. *Bulletin of the Lebedev Physics Institute*, 34:334–339, November 2007. 40

[106] J. T. Hogan. Collisional transport of momentum in axisymmetric configurations. *Physics of Fluids*, 27:2308–2312, September 1984. 45

[107] R. J. Mason and C. W. Cranfill. Hybrid Two-Dimensional Electron Transport in Self-Consistent Electromagnetic Fields. *IEEE Transactions on Plasma Science*, 14:45–52, 1986. 50

[108] R. J. Mason. An electromagnetic field algorithm for 2D implicit plasma simulation. *Journal of Computational Physics*, 71:429–473, August 1987. 50

[109] J. Loverich and U. Shumlak. A discontinuous galerkin method for the full two-fluid plasma model. *Computer Physics Communications*, 169(1):251–255, July 2005. 50

[110] B. Srinivasan and U. Shumlak. Analytical and computational study of the ideal full two-fluid plasma model and asymptotic approximations for Hall-magnetohydrodynamics. *Physics of Plasmas*, 18(9):092113, September 2011. 50

[111] E. M. Sousa and U. Shumlak. A blended continuous-discontinuous finite element method for solving the multi-fluid plasma model. *Journal of Computational Physics*, 326:56–75, December 2016. 50

[112] S. Baboolal. Finite-difference modeling of solitons induced by a density hump in a plasma multi-fluid. *Mathematics and Computers in Simulation*, 55(4):309 – 316, 2001. Nonlinear Waves: Computation and Theory. 50

[113] S. Baboolal and R. Bharuthram. Two-scale numerical solution of the electromagnetic two-fluid plasma-maxwell equations: Shock and soliton simulation. *Mathematics and Computers in Simulation*, 76(1–3):3 – 7, 2007. Mathematical Modelling and Computational Methods in Applied Sciences and Engineering. 50

[114] Harish Kumar and Siddhartha Mishra. Entropy stable numerical schemes for two-fluid plasma equations. *Journal of Scientific Computing*, 52(2):401–425, 2012. 50

[115] U. Shumlak and J. Loverich. Approximate riemann solver for the two-fluid plasma model. *J. Comput. Phys.*, 187(2):620–638, May 2003. 50, 95

[116] A. Hakim, J. Loverich, and U. Shumlak. A high resolution wave propagation scheme for ideal two-fluid plasma equations. *J. Comput. Phys.*, 219(1):418–442, November 2006. 50, 93, 95, 96

[117] T. Amano. Divergence-free approximate Riemann solver for the quasi-neutral two-fluid plasma model. *Journal of Computational Physics*, 299:863–886, October 2015. 50, 75, 78, 95, 96, 97

[118] D. S. Balsara, T. Amano, S. Garain, and J. Kim. A high-order relativistic two-fluid electrodynamic scheme with consistent reconstruction of electromagnetic fields and a multidimensional Riemann solver for electromagnetism. *Journal of Computational Physics*, 318:169–200, August 2016. 50

[119] L. Ofman and J. M. Davila. Three-Fluid 2.5-dimensional Magnetohydrodynamic Model of the Effective Temperature in Coronal Holes. *The Astrophysical Journal*, 553:935–940, June 2001. 50

[120] L. Ofman, L. Abbo, and S. Giordano. Multi-fluid Model of a Streamer at Solar Minimum and Comparison with Observations. *The Astrophysical Journal*, 734:30, June 2011. 50

[121] C.-D. Munz, P. Ommes, and R. Schneider. A three-dimensional finite-volume solver for the Maxwell equations with divergence cleaning on unstructured meshes. *Computer Physics Communications*, 130:83–117, July 2000. 51, 52, 58, 62, 63, 70

[122] M.-S. Liou and C. J. Steffen. A New Flux Splitting Scheme. *Journal of Computational Physics*, 107:23–39, July 1993. 51, 64, 66

[123] M.-S. Liou. A sequel to AUSM, Part II: AUSM$^+$-up for all speeds. *Journal of Computational Physics*, 214:137–170, May 2006. 51, 64

[124] M.-S. Liou. A further Development of the AUSM$^+$ Towards Robust and Accurate Solutions for All Speeds. *AIAA paper*, 4116, June 2003. 51, 65, 66

[125] R. Courant, E. Isaacson, and M. Rees. On the solution of nonlinear hyperbolic differential equations by finite differences. *Communication on Pure and Applied Mathematics*, 5:243–255, 1952. 51, 57

[126] A. Lani, T. Quintino, D. Kimpe, H. Deconinck, S. Vandewalle, and S. Poedts. The COOLFluiD framework: Design solutions for high-performance object oriented scientific computing software. In P. M. A. Sloot V. S. Sunderan, G. D. van Albada and J. J. Dongarra, editors, *Computational Science ICCS 2005*, volume 1 of *LNCS 3514*, pages 281–286, Atlanta, GA, USA, May 2005. Emory University, Springer. 52

[127] A. Lani, T. Quintino, D. Kimpe, H. Deconinck, S. Vandewalle, and S. Poedts. Reusable object-oriented solutions for numerical simulation of pdes in a high performance environment. *Scientific Programming. Special Edition on POOSC 2005*, 14(2):111–139, 2006. 52

[128] D. Kimpe, A. Lani, T. Quintino, S. Poedts, and S. Vandewalle. The coolfluid parallel architecture. In D. Kranzlmüller B. Di Martino and J. J. Dongarra, editors, *Proc. 12th European Parallel Virtual Machine and Message Passing Interface Conference*, pages 520–527, Sorrento, Oct 2005. Springer. 52

[129] A. Lani. *An Object Oriented and high performance platform for aerothermodynamics simulation*. Phd thesis, Université Libre de Bruxelles, 2008. 52

[130] T. Quintino. *A Component Environment for High-Performance Scientific Computing. Design and Implementation*. Phd thesis, Katholieke Universiteit Leuven, 2008. 52

[131] A. Lani, N. Villedieu, K. Bensassi, L. Kapa, M. Vymazal, M. S. Yalim, and M. Panesi. COOLFluiD: an open computational platform for multi-physics simulation and research. In *AIAA 2013-2589*, San Diego (CA), Jun 2013. 21th AIAA CFD Conference. 52

[132] G. Degrez, A. Lani, M. Panesi, O. Chazot, and H. Deconinck. REVIEW ARTICLE: Modelling of high-enthalpy, high-Mach number flows. *Journal of Physics D Applied Physics*, 42(19):194004, October 2009. 52

[133] A. Lani, J. Garicano Mena, and H. Deconick. A residual distribution method for symmetrized systems in thermochemical nonequilibrium. In *AIAA-2011-3546*, Honolulu (Hawaii), Jun 2011. 20th AIAA CFD Conference. 52

[134] D. Knight, J. Longo, D. Drikakis, D. Gaitonde, and A. Lani et al. Assessment of CFD capability for prediction of hypersonic shock interactions. *Prog. Aerosp. Sci.*, 48-49:8–26, 2012. 52

[135] A. Lani, M. Panesi, and H. Deconinck. Conservative residual distribution method for viscous double cone flows in thermochemical nonequilibrium. *Commun. Comput. Phys.*, 13:479–501, 2013. 52

[136] M. Panesi and A. Lani. Collisional radiative coarse-grain model for ionization in air. *Physics of Fluids*, 25:057101, 2013. 52

[137] A. Munafo, A. Lani, A. Bultel, and M. Panesi. Modeling of non-equilibrium phenomena in expanding flows by means of a collisional-radiative model. *Physics of Plasma*, 20(7), 2013. 52

[138] M. S. Yalim, D. V. Abeele, and A. Lani. Simulation of field-aligned ideal mhd flows around perfectly conducting cylinders using an artificial compressibility approach. In *Proc. of the 11th International Conference on Hyperbolic Problems*, pages 1085–1092, Lyon, France, July 17-21 2006. Ecole Normale Supérieure, Springer-Verlag. 52

[139] M. S. Yalim, D. Vanden Abeele, A. Lani, T. Quintino, and H. Deconinck. A finite volume implicit time integration method for solving the equations of ideal magnetohydrodynamics for the hyperbolic divergence cleaning approach. *Journal of Computational Physics*, 230:6136–6154, July 2011. 52, 69, 72, 85, 86

[140] A. Lani, M. S. Yalim, and S. Poedts. A GPU-enabled Finite Volume solver for global magnetospheric simulations on unstructured grids. *Computer Physics Communications*, 185:2538–2557, October 2014. 52, 72

[141] G. Tóth. The div.B=0 Constraint in Shock-Capturing Magnetohydrodynamics Codes. *Journal of Computational Physics*, 161:605–652, July 2000. 52, 85, 86

[142] R. Kissmann and J. Pomoell. A semidiscrete finite volume constrained transport method on orthogonal curvilinear grids. *SIAM J. Sci. Comput.*, 34(2):763–791, March 2012. 52

[143] T. Barth. Aspects of unstructured grids and finitevolume solvers for the euler and navier-stokes equations, 1994. 55

[144] V. Venkatakrishnan. On the accuracy of limiters and convergence to steady state solutions, 1993. 55

[145] Timothy Barth and Dennis Jespersen. *The design and application of upwind schemes on unstructured meshes.* American Institute of Aeronautics and Astronautics, 2017/07/11 1989. 56

[146] R. MacCormack. Numerical simulation of aerodynamic flow including induced magnetic and electric fields, 2008. 60, 61, 62, 70

[147] M. Liou. A Sequel to AUSM: AUSM+. *Journal of Computational Physics*, 129:364–382, December 1996. 64

[148] S. E. Kim, B. Makarov, and D. Caraeni. Multi-dimensional linear reconstruction scheme for arbitrary unstructured mesh. In *AIAA-2003-3990*, Orlando, Florida, Jun 2003. 16th AIAA CFD Conference. 67

[149] http://www.mcs.anl.gov/petsc/petsc as/. 69, 94

[150] A. Dedner, F. Kemm, D. Kröner, C.-D. Munz, T. Schnitzer, and M. Wesenberg. Hyperbolic Divergence Cleaning for the MHD Equations. *Journal of Computational Physics*, 175:645–673, January 2002. 69

[151] J. U. Brackbill and D. C. Barnes. The effect of nonzero product of magnetic gradient and B on the numerical solution of the magnetohydrodynamic equations. *Journal of Computational Physics*, 35:426–430, May 1980. 69

[152] R. MacCormack. Flow simulations within induced magnetic and electric fields, 2009. 70

[153] D. S. Balsara. Second-Order-accurate Schemes for Magnetohydrodynamics with Divergence-free Reconstruction. *Astrophysical Journal Supplement Series*, 151:149–184, March 2004. 72

[154] D. S. Balsara. Divergence-free reconstruction of magnetic fields and WENO schemes for magnetohydrodynamics. *Journal of Computational Physics*, 228:5040–5056, August 2009. 72

[155] D. S. Balsara, T. Rumpf, M. Dumbser, and C.-D. Munz. Efficient, high accuracy ADER-WENO schemes for hydrodynamics and divergence-free magnetohydrodynamics. *Journal of Computational Physics*, 228:2480–2516, April 2009. 72

[156] Y. Shen, G. Zha, and M. A. Huerta. E-CUSP scheme for the equations of ideal magnetohydrodynamics with high order WENO Scheme. *Journal of Computational Physics*, 231:6233–6247, August 2012. 72, 74

[157] A. Mignone, P. Tzeferacos, and G. Bodo. High-order conservative finite difference GLM-MHD schemes for cell-centered MHD. *Journal of Computational Physics*, 229:5896–5920, August 2010. 72

[158] Mitchner M. and Kruger C. H. Jr. *Partially Ionized Gases*. Department of Mechanical Engineering, Stanford Engineering, Wiley-Interscience Publication, 1973. 80

[159] S. A. Orszag and C.-M. Tang. Small-scale structure of two-dimensional magnetohydrodynamic turbulence. *Journal of Fluid Mechanics*, 90:129–143, January 1979. 83

[160] R. B. Dahlburg and J. M. Picone. Evolution of the Orszag-Tang vortex system in a compressible medium. I - Initial average subsonic flow. *Physics of Fluids B*, 1:2153–2171, November 1989. 83

[161] D. S. Balsara and D. S. Spicer. A Staggered Mesh Algorithm Using High Order Godunov Fluxes to Ensure Solenoidal Magnetic Fields in Magnetohydrodynamic Simulations. *Journal of Computational Physics*, 149:270–292, March 1999. 85

[162] B. de Pontieu, S. McIntosh, V. H. Hansteen, M. Carlsson, C. J. Schrijver, T. D. Tarbell, A. M. Title, R. A. Shine, Y. Suematsu, S. Tsuneta, Y. Katsukawa, K. Ichimoto, T. Shimizu, and S. Nagata. A Tale of Two Spicules: The Impact of Spicules on the Magnetic Chromosphere. *Publications of the Astronomical Society of Japan*, 59:S655–S662, November 2007. 112

[163] J. M. Beckers. Solar Spicules (Invited Review Paper). *Solar Physics*, 3:367–433, March 1968. 112

[164] B. De Pontieu, R. Erdélyi, and S. P. James. Solar chromospheric spicules from the leakage of photospheric oscillations and flows. *Nature*, 430:536–539, July 2004. 112

[165] B. De Pontieu, S. W. McIntosh, M. Carlsson, V. H. Hansteen, T. D. Tarbell, C. J. Schrijver, A. M. Title, R. A. Shine, S. Tsuneta, Y. Katsukawa, K. Ichimoto, Y. Suematsu, T. Shimizu, and S. Nagata. Chromospheric Alfvénic Waves Strong Enough to Power the Solar Wind. *Science*, 318:1574, December 2007. 112

[166] A. C. Sterling. Solar Spicules: A Review of Recent Models and Targets for Future Observations - (Invited Review). *Solar Physics*, 196:79–111, September 2000. 112

[167] B. De Pontieu, V. H. Hansteen, L. Rouppe van der Voort, M. van Noort, and M. Carlsson. High-Resolution Observations and Modeling of Dynamic Fibrils. *The Astrophysical Journal*, 655:624–641, January 2007. 112

[168] V. H. Hansteen, B. De Pontieu, L. Rouppe van der Voort, M. van Noort, and M. Carlsson. Dynamic Fibrils Are Driven by Magnetoacoustic Shocks. *The Astrophysical Journal Letters*, 647:L73–L76, August 2006. 112

[169] K. Shibata, M. Shimojo, T. Yokoyama, and M. Ohyama. Theory and observations of X-ray jets. In R. D. Bentley and J. T. Mariska, editors, *Astronomical Society of the Pacific Conference Series*, volume 111 of *Astronomical Society of the Pacific Conference Series*, pages 29–38, 1996. 112

[170] T. Yokoyama and K. Shibata. Magnetic reconnection as the origin of X-ray jets and Hα surges on the Sun. *Nature*, 375:42–44, May 1995. 112

[171] N. Nishizuka, M. Shimizu, T. Nakamura, K. Otsuji, T. J. Okamoto, Y. Katsukawa, and K. Shibata. Giant Chromospheric Anemone Jet Observed with Hinode and Comparison with Magnetohydrodynamic Simulations: Evidence of Propagating Alfvén Waves and Magnetic Reconnection. *The Astrophysical Journal Letters*, 683:L83–L86, August 2008. 112

[172] Y. C. Jiang, H. D. Chen, K. J. Li, Y. D. Shen, and L. H. Yang. The Hα surges and EUV jets from magnetic flux emergences and cancellations. *Astronomy & Astrophysics*, 469:331–337, July 2007. 112

[173] T. Shimizu, R. A. Shine, A. M. Title, T. D. Tarbell, and Z. Frank. Photospheric Magnetic Activities Responsible for Soft X-Ray Point-like Microflares. I. Identifications of Associated Photospheric/Chromospheric Activities. *The Astrophysical Journal*, 574:1074–1088, August 2002. 112

[174] N. Nishizuka, T. Nakamura, T. Kawate, K. A. P. Singh, and K. Shibata. Statistical Study of Chromospheric Anemone Jets Observed with Hinode/SOT. *The Astrophysical Journal*, 731:43, April 2011. 112

[175] L. Yang, J. He, H. Peter, C. Tu, L. Zhang, X. Feng, and S. Zhang. Numerical Simulations of Chromospheric Anemone Jets Associated with Moving Magnetic Features. *The Astrophysical Journal*, 777:16, November 2013. 112

[176] K. A. P. Singh, H. Isobe, N. Nishizuka, K. Nishida, and K. Shibata. Multiple Plasma Ejections and Intermittent Nature of Magnetic Reconnection in Solar Chromospheric Anemone Jets. *The Astrophysical Journal*, 759:33, November 2012. 112, 132

[177] L. Yan, J. He, L. Xia, and F. Jiao. Observational Evidence for the Causes and Consequences of Chromospheric Reconnection. *The Astrophysical Journal*, 804:69, May 2015. 112, 132

[178] E. Pariat, B. Schmieder, A. Berlicki, Y. Deng, N. Mein, A. López Ariste, and S. Wang. Spectrophotometric analysis of Ellerman bombs in the Ca II, Hα, and UV range. *Astronomy & Astrophysics*, 473:279–289, October 2007. 112

[179] E. Pariat, G. Aulanier, B. Schmieder, M. K. Georgoulis, D. M. Rust, and P. N. Bernasconi. Resistive Emergence of Undulatory Flux Tubes. *The Astrophysical Journal*, 614:1099–1112, October 2004. 112

[180] P. G. Judge. UV Spectra, Bombs, and the Solar Atmosphere. *The Astrophysical Journal*, 808:116, August 2015. 112

[181] H. Tian, Z. Xu, J. He, and C. Madsen. Are IRIS Bombs Connected to Ellerman Bombs? *The Astrophysical Journal*, 824:96, June 2016. 112

[182] P. D. Smith and J. I. Sakai. Chromospheric magnetic reconnection: two-fluid simulations of coalescing current loops. *Astronomy & Astrophysics*, 486:569–575, August 2008. 113

[183] J. I. Sakai and P. D. Smith. Two-Fluid Simulations of Coalescing Penumbra Filaments Driven by Neutral-Hydrogen Flows. *The Astrophysical Journal Letters*, 691:L45–L48, January 2009. 113

[184] A. Alvarez Laguna, A. Lani, H. Deconinck, N. N. Mansour, and S. Poedts. A fully-implicit finite-volume method for multi-fluid reactive and collisional magnetized plasmas on unstructured meshes. *Journal of Computational Physics*, 318:252–276, August 2016. 115

[185] E. Khomenko, M. Collados, and A. J. Díaz. Observational Detection of Drift Velocity between Ionized and Neutral Species in Solar Prominences. *The Astrophysical Journal*, 823:132, June 2016. 118, 132

[186] E. E. Lawrence, H. Ji, M. Yamada, and J. Yoo. Laboratory Study of Hall Reconnection in Partially Ionized Plasmas. *Physical Review Letters*, 110(1):015001, January 2013. 133

[187] S. Shelyag, E. Khomenko, A. de Vicente, and D. Przybylski. Heating of the Partially Ionized Solar Chromosphere by Waves in Magnetic Structures. *The Astrophysical Journal Letters*, 819:L11, March 2016. 136

[188] R. Soler, J. L. Ballester, and T. V. Zaqarashvili. Overdamped Alfvén waves due to ion-neutral collisions in the solar chromosphere. *Astronomy & Astrophysics*, 573:A79, January 2015. 136, 148

[189] D. P. Cox and W. H. Tucker. Ionization Equilibrium and Radiative Cooling of a Low-Density Plasma. *The Astrophysical Journal*, 157:1157, September 1969. 138

[190] R. L. Moore and P. C. W. Fung. Structure of the Chromosphere-Corona Transition Region. *Solar Physics*, 23:78–102, March 1972. 138

[191] J. M. Fontenla, E. H. Avrett, and R. Loeser. Energy balance in the solar transition region. III - Helium emission in hydrostatic, constant-abundance models with diffusion. *The Astrophysical Journal*, 406:319–345, March 1993. 138

[192] E. H. Avrett and R. Loeser. Models of the Solar Chromosphere and Transition Region from SUMER and HRTS Observations: Formation of the Extreme-Ultraviolet Spectrum of Hydrogen, Carbon, and Oxygen. *Astrophysical Journal Supplement Series*, 175:229–276, March 2008. 138

[193] E. Khomenko, M. Collados, and T. Felipe. Nonlinear Numerical Simulations of Magneto-Acoustic Wave Propagation in Small-Scale Flux Tubes. *Solar Physics*, 251:589–611, September 2008. 140, 148

[194] V. Fedun, R. Erdélyi, and S. Shelyag. Oscillatory Response of the 3D Solar Atmosphere to the Leakage of Photospheric Motion. *Solar Physics*, 258:219–241, September 2009. 140

[195] V. Fedun, S. Shelyag, and R. Erdélyi. Numerical Modeling of Footpoint-driven Magneto-acoustic Wave Propagation in a Localized Solar Flux Tube. *The Astrophysical Journal*, 727:17, January 2011. 140, 148

[196] E. Khomenko and M. Collados. Heating of the Magnetized Solar Chromosphere by Partial Ionization Effects. *The Astrophysical Journal*, 747:87, March 2012. 140, 148

[197] E. Khomenko and M. Collados. Numerical Modeling of Magnetohydrodynamic Wave Propagation and Refraction in Sunspots. *The Astrophysical Journal*, 653:739–755, December 2006. 148

[198] J. T. Gosling. Coronal mass ejections and magnetic flux ropes in interplanetary space. *Washington DC American Geophysical Union Geophysical Monograph Series*, 58:343–364, 1990. 150

[199] J. P. Eastwood, D. G. Sibeck, J. A. Slavin, M. L. Goldstein, B. Lavraud, M. Sitnov, S. Imber, A. Balogh, E. A. Lucek, and I. Dandouras. Observations of multiple X-line structure in the Earth's magnetotail current sheet: A Cluster case study. *Geophysical Research Letters*, 32:L11105, June 2005. 150

[200] G. Paschmann, I. Papamastorakis, N. Sckopke, G. Haerendel, B. U. O. Sonnerup, S. J. Bame, J. R. Asbridge, J. T. Gosling, C. T. Russel, and R. C. Elphic. Plasma acceleration at the earth's magnetopause - Evidence for reconnection. *Nature*, 282:243–246, November 1979. 150

[201] R. V. E. Lovelace. Dynamo model of double radio sources. *Nature*, 262:649–652, August 1976. 150

[202] H. Li, G. Lapenta, J. M. Finn, S. Li, and S. A. Colgate. Modeling the Large-Scale Structures of Astrophysical Jets in the Magnetically Dominated Limit. *The Astrophysical Journal*, 643:92–100, May 2006. 150

[203] J.P. Freidberg. *Plasma Physics and Fusion Energy.* Cambridge University Press, 2008. 150, 154

[204] W. A. Newcomb. Hydromagnetic stability of a diffuse linear pinch. *Annals of Physics*, 10:232–267, June 1960. 150

[205] S Markidis, G Lapenta, G L Delzanno, P Henri, M V Goldman, D L Newman, T Intrator, and E Laure. Signatures of secondary collisionless magnetic reconnection driven by kink instability of a flux rope. *Plasma Physics and Controlled Fusion*, 56(6):064010, 2014. 150, 152, 154, 160, 171

[206] B. B. Kadomtsev. Self-organization and transport in tokamak plasma. *Plasma Physics and Controlled Fusion*, 34:1931–1938, December 1992. 151

[207] R.B. White. *The Theory of Toroidally Confined Plasmas.* Imperial College Press, 2006. 151

[208] J Wesson. Tokamaks—third edition. *Oxford University Press*, 2004. 151

[209] Giovanni Lapenta, Ivo Furno, Thomas Intrator, and Gian Luca Delzanno. Kink instability of flux ropes anchored at one end and

free at the other. *Journal of Geophysical Research: Space Physics*, 111(A12):n/a–n/a, 2006. A12S06. 151, 154

[210] V. D. Shafranov. Hydrodynamic stability of a current-carrying pinch in a strong longitudinal field. *Sov. Phys.–Tech. Phys.*, 15:175–183, 1970. 151

[211] Q. Yu, S. Günter, and K. Lackner. Numerical modelling of sawtooth crash using two-fluid equations. *Nuclear Fusion*, 55(11):113008, 2015. 152

[212] S Günter, Q Yu, K Lackner, A Bhattacharjee, and Y-M Huang. Fast sawtooth reconnection at realistic lundquist numbers. *Plasma Physics and Controlled Fusion*, 57(1):014017, 2015. 152

[213] M T Beidler, P A Cassak, S C Jardin, and N M Ferraro. Local properties of magnetic reconnection in nonlinear resistive- and extended-magnetohydrodynamic toroidal simulations of the sawtooth crash. *Plasma Physics and Controlled Fusion*, 59(2):025007, 2017. 152

[214] H. W. Hendel, T. K. Chu, and P. A. Politzer. Collisional Drift Waves-Identification, Stabilization, and Enhanced Plasma Transport. *Physics of Fluids*, 11:2426–2439, November 1968. 153

[215] H. L. Pecseli, J. J. Rasmussen, H. Sugai, and K. Thomsen. Evolution of externally excited convective cells in plasmas. *Plasma Physics and Controlled Fusion*, 26:1021–1034, August 1984. 153

[216] H. L. Pecseli, J. J. Rasmussen, and K. Thomsen. Nonlinear interaction of convective cells in plasmas. *Plasma Physics and Controlled Fusion*, 27:837–846, August 1985. 153

[217] S. C. Prager, A. K. Sen, and T. C. Marshall. Dissipative Trapped-Electron Instability in Cylindrical Geometry. *Physical Review Letters*, 33:692–695, September 1974. 153

[218] G. A. Navratil, J. Slough, and A. K. Sen. A steady state linear machine for collisionless plasma studies. *Plasma Physics*, 24:185–196, February 1982. 153

[219] D L Rudakov, J A Boedo, R A Moyer, S Krasheninnikov, A W Leonard, M A Mahdavi, G R McKee, G D Porter, P C Stangeby, J G Watkins, W P West, D G Whyte, and G Antar. Fluctuation-driven transport in

the diii-d boundary. *Plasma Physics and Controlled Fusion*, 44(6):717, 2002. 153

[220] I. Furno, T. Intrator, E. Torbert, C. Carey, M. D. Cash, J. K. Campbell, W. J. Fienup, C. A. Werley, G. A. Wurden, and G. Fiksel. Reconnection scaling experiment: A new device for three-dimensional magnetic reconnection studies. *Review of Scientific Instruments*, 74(4):2324–2331, 2003. 171

[221] T. P. Intrator, X. Sun, G. Lapenta, L. Dorf, and I. Furno. Experimental onset threshold and magnetic pressure pile-up for 3d reconnection. *Nat Phys*, 5(7):521–526, 07 2009. 171

FACULTY OF SCIENCE
DEPARTMENT OF MATHEMATICS
CENTRE FOR MATHEMATICAL PLASMA-ASTROPHYSICS
Celestijnenlaan 200A box 2400
B-3001 Leuven
alejandro.alvarezlaguna@kuleuven.be
https://wis.kuleuven.be/CmPA